

# The Structure of Galaxy Clusters and their Intracluster Medium as Observed with XMM-Newton

DISSERTATION

der Fakultät für Physik  
der Ludwig-Maximilians-Universität München  
zur Erlangung des Grades  
Doktor der Naturwissenschaften  
Dr. rer. nat.

vorgelegt von

Yu-Ying Zhang  
aus Nei Mongol, China

München, den 29. Juli 2005



1. Evaluator: Prof. Dr. Hans Böhringer  
2. Evaluator: Prof. Dr. Andreas M. Burkert  
Date of the oral exam: 27. October 2005



# Zusammenfassung

Galaxienhaufen sind die größten, gravitativ gebundenen und nahezu virialisierten Systeme im Universum. Sie werden in verschiedener Weise zu kosmologischen und astrophysikalischen Untersuchungen genutzt. Eine wichtige Voraussetzung für die Nutzung von Galaxienhaufen für kosmologische Studien ist eine genaue Kenntnis der Struktur und Masse von Galaxienhaufen. Die weitentwickelten, modernen Röntgenobservatorien, XMM-Newton (mit hoher spektraler Auflösung, großer effektiver Fläche, und relativ großem Blickfeld) und Chandra (mit sehr guter Winkelauflösung) ermöglichen zum ersten Mal eine ideale Diagnostik, um im Detail die Struktur des Innerhaufenmediums in Galaxienhaufen zu untersuchen. Wir nutzen XMM-Newton und Chandra, um eine repräsentative Stichprobe von Galaxienhaufen bei einer mittleren Rotverschiebung ( $z \sim 0.3$ ) zu untersuchen.

Im kosmologischen Standardmodell ist die Selbstähnlichkeit der Objekte, die sich aus der großräumigen Struktur gebildet haben, eine der wichtigsten Voraussagen, die auch zu einer sehr engen Korrelation von Haufenmasse und Beobachtungsgrößen führt. Daher kann man röntgenastronomische Beobachtungsgrößen dazu benutzen, die wichtigsten physikalischen Größen von Galaxienhaufen vorauszusagen. Astrophysikalische und kosmologische Anwendungen von Studien von Galaxienhaufen basieren auf diesem selbstähnlichen Verhalten. Ein umfassendes Verständnis des selbstähnlichen Verhaltens von Galaxienhaufen macht sie daher zu idealen Studienobjekten der Bildung und Entwicklung der großräumigen Struktur.

Für die Untersuchungen wurde eine statistisch exakte röntgenflussbegrenzte, und im Volumen komplette Stichprobe von 14 Galaxienhaufen bei mittlerer Rotverschiebung aus dem REFLEX Durchmusterungs-Katalog ausgewählt (die REFLEX-DXL Stichprobe). Die Analyse der XMM-Newton Beobachtungsdaten dieser Stichprobe und ihre astrophysikalische und kosmologische Anwendung bilden den Hauptteil dieser Dissertation. Um die Selbstähnlichkeit der Galaxienhaufen zu untersuchen und die Kenntnis der Masse–Beobachtungsgrößen Relation bei mittleren Rotverschiebungen zu verbessern, wurde ein Satz verlässlicher Datenauswertungsprozeduren entwickelt. Die abgeleiteten Werte für den Masseanteil des Haufengases stimmt sehr gut mit den Ergebnissen früherer Galaxienhaufenstudien für nahe Stichproben und der weiter entfernter Haufen überein. Auch mit dem kosmischen Baryonenanteil, der aus der Beobachtungen des Mikrowellenhintergrundes bestimmt wurde (z.B. mit dem WMAP Satelliten), besteht gute Übereinstimmung. Die Massenbestimmungen der Haufen besitzen eine höhere Genauigkeit als frühere Analysen und helfen die Relationen der Masse und Beobachtungsgrößen genauer und enger zu machen. Diese Ergebnisse zu den Masse–Beobachtungsgrößen Relationen sind in guter Übereinstimmung mit früheren Studien, aber die Unsicherheit in der Normalisierung dieser Relationen konnte erheblich reduziert werden. Eine interessante Abweichung vom

selbstähnlichen Verhalten konnte in der Zentralregion der Haufen beobachtet werden. Das deutet auf wichtige physikalische Prozesse hin, die die Zentralregion beeinflussen, und beruht nicht nur auf statistischen Fluktuationen in den Messungen. Die REFLEX-DXL Galaxienhaufen wurden auch mit Chandra, ESO/MPIA WFI, ESO-NTT und ESO-VLT-VIMOS beobachtet. Eine gemeinsame Auswertung dieser Daten aus verschiedenen Wellenlängen bildet eine zukünftige Erweiterung dieser Arbeit.

Die gleiche Datenanalyse wurde auch auf einen prominenten Galaxienhaufen angewandt, CL0024+17 bei einer Rotverschiebung von  $z = 0.395$ , der als Gravitationslinse wirkt. Diese Studie illustriert insbesondere die Analyse der Morphologie und Komplexität individueller Galaxienhaufen. CL0024+17 ist der klassische Fall einer Diskrepanz in der Massenbestimmung eines Haufens aus den Röntgendaten einerseits und der Wirkung als Gravitationslinse für Galaxien im Hintergrund andererseits. Es ist der einzige Haufen, der mit hoher Winkelauflösung für eine Linsenanalyse bis zu großen Radien beobachtet wurde (25 HST Aufnahmen in verschiedenen Feldern). In der vorliegenden Arbeit wurde die gravitative Massenverteilung im Detail aus den spektroskopischen und Abbildungs-Daten von XMM-Newton bestimmt. Es bleibt eine Diskrepanz von einem Faktor 4 zwischen der mit Hilfe der Röntgendaten bestimmten totalen Masse und der Masse, die aus dem starken Gravitationslinseneffekt gewonnen wurde. Mit den Ergebnissen der schwachen Linsenwirkung bei größeren Radien sind die Röntgenergebnisse daher innerhalb von  $2\sigma$  Fehlgrenzen vereinbar. Die Haufensubstruktur, die in den HST-Bildern zu sehen ist, wird durch ein Röntgenbild bestätigt, das die Winkelverteilung des mittleren Härtegrades der Röntgenstrahlung zeigt. Diese Ergebnisse zeigen, dass die komplexe Struktur im Zentrum des Galaxienhaufens den Schlüssel zur Erklärung der Massendiskrepanz zwischen Röntgen- und Gravitationslinsenanalyse bildet. Die Diskrepanz ist somit darauf zurückzuführen, dass der Haufen ein komplexes System zusammenstoßender Systeme bildet, wobei die Hauptachse des Zusammenstoßes in der Sichtlinie liegt und in ein ebenso ausgerichtetes Filament der großräumigen Struktur eingebettet ist. Diese Ausrichtung der Stoßachse in der Sichtlinie macht es schwer, den Zusammenstoß im Detail in den Röntgendaten zu untersuchen, aber diese Geometrie führt auf der anderen Seite zu einer Verstärkung der Gravitationslinsenwirkung.

XMM-Newton und Chandra liefern Abbildungs- und Spektroskopiedaten von höchster Qualität für das detaillierte Studium von Galaxienhaufen. Die gut räumlich und spektroskopisch aufgelösten Beobachtungsdaten bieten uns die Möglichkeit, Galaxienhaufen astrophysikalisch zu untersuchen, wie in dieser Arbeit gezeigt wird. Aus dem Vergleich der hier für die REFLEX-DXL Stichprobe gewonnenen Ergebnisse zu den Beobachtungen von Galaxienhaufen bei geringer und hoher Rotverschiebung können wir schließen, dass sich die Entwicklung von massiven Galaxienhaufen ( $T > 5$  keV) von einer Rotverschiebung von  $z \sim 1.2$  bis in die Gegenwart sehr gut mit einem selbstähnlichen Strukturentstehungsmodell erklären lassen. Es gibt aber auch Abweichungen der einzelnen Galaxienhaufen von selbstähnlichen Modellen, die auf die Wirkung interessanter, zusätzlicher physikalischer Prozesse schließen lassen.

# Summary

Clusters of galaxies are the largest gravitationally bound and nearly virialized systems in the Universe. They are used in a variety of ways to perform both cosmological and astrophysical studies. A prime requisite for the use of galaxy clusters for cosmology is a precise knowledge of cluster structure and cluster mass. The two currently most advanced X-ray observatories, XMM-Newton (with high spectral resolution, large effective area, and large field-of-view) and Chandra (with high spatial resolution), provide for the first time ideal diagnostics to investigate in detail the structure of the intracluster medium in galaxy clusters. We make use of XMM-Newton and Chandra to investigate a representative sample of galaxy clusters at medium redshift ( $z \sim 0.3$ ).

In a standard cosmology, self-similarity of the objects forming out of large-scale structure such as clusters of galaxies is the most important prediction by hierarchical structure formation models, and leads to tight mass–observable correlations. The X-ray observables can thus in principle be used to predict the major physical properties of galaxy clusters. Astrophysical and cosmological applications of galaxy clusters are on the basis of the self-similar behavior. A comprehensive understanding of the self-similar behavior of galaxy clusters makes them ideal objects to study structure formation and evolution.

An unbiased, flux-limited and almost volume-complete sample of 14 galaxy clusters at medium redshift, the REFLEX-DXL sample, has been selected from the REFLEX catalog. The analysis of the XMM-Newton data of this sample including its astrophysical and cosmological applications is the main topic of this thesis. A set of reliable data analysis procedures have been developed to investigate the self-similarity of galaxy clusters and to tighten mass–observable correlations at moderate redshift. The derived gas mass fractions agree with previous cluster studies for the nearby samples and more distant samples, and with the baryon fraction based on the cosmic microwave background measurements (e.g. the WMAP satellite). The cluster mass measurements have improved accuracy and help to tighten scaling relations. The profiles of the surface brightness, temperature, entropy, and mass are well characterized by self-similar behavior at radii above 0.1 times the virial radius, which tightens mass–observable correlations. The results regarding mass–observable correlations at medium redshift confirm previous studies, but reduce the uncertainties on the normalizations. An interesting deviation about the self-similar model has been observed in the central region. This reveals some physical processes affecting the intracluster medium rather than simply being statistical fluctuations in the measurements. The REFLEX-DXL clusters were also observed by Chandra, ESO/MPIA WFI, ESO-NTT and ESO-VLT-VIMOS. A joint analysis based on the multi-wavelength observations will be performed as an extension of this work.

These procedures have also been used to analyze one lensing cluster, CL0024+17, at

## Summary

---

redshift  $z \sim 0.395$  to trace the cluster morphology and to illustrate the complexity of individual clusters. CL0024+17 is a classic case of significant mass discrepancy between lensing and X-ray studies. It is the only cluster so far observed up to large radii with a high optical resolution (25 HST observations). A detailed gravitational mass measurement has been deduced based on the XMM-Newton imaging spectroscopy analysis. The discrepancy of up to a factor of 4 remains between the X-ray measured total mass and strong lensing mass. The XMM-Newton results are marginally consistent with the weak lensing measure within  $2\sigma$ . The substructure observed by HST is confirmed in the X-ray hardness ratio map. These results show that the complex structure in the core region is key to explaining the discrepancy in gravitational mass determined from the X-ray observations and optical lensing data at the strong lensing arc radii. This disagreement is most probably due to a complex merger configuration with a long filament along the line-of-sight. The line-of-sight orientation makes it difficult to reveal the merger structure in the X-ray data, but on the other hand it enhances the probability of finding strong lensing features.

XMM-Newton and Chandra provide us the best quality imaging spectroscopic data so far for studies of X-ray galaxy clusters. A high resolution view of the complexity in galaxy clusters opens an interesting field to study the astrophysics. Comparing the REFLEX-DXL sample to the nearby and more distant samples, we conclude that the evolution of galaxy clusters up to redshift  $z \sim 1.2$  is well described by a self-similar model for massive clusters ( $T > 5$  keV), although deviations around the self-similar model exist for individual clusters, which point to a number of important physical processes.



# Contents

<b>Zusammenfassung (Summary in German)</b>	<b>i</b>
<b>Summary</b>	<b>iii</b>
<b>List of Figures</b>	<b>ix</b>
<b>List of Tables</b>	<b>xi</b>
<b>1 Introduction</b>	<b>1</b>
1.1 Galaxy clusters . . . . .	1
1.2 Primary motivation and the REFLEX-DXL sample . . . . .	4
1.2.1 REFLEX sample . . . . .	4
1.2.2 REFLEX-DXL sample . . . . .	4
1.3 Outline . . . . .	6
<b>2 Theoretical framework</b>	<b>9</b>
2.1 Standard cosmological model . . . . .	9
2.2 Linear and quasi-linear theory . . . . .	11
2.2.1 Primordial density fluctuations and the transfer function . . . . .	11
2.2.2 Dynamics of linear perturbations . . . . .	12
2.2.3 Spherical “Top-Hat” collapse . . . . .	14
2.3 Mass function . . . . .	14
2.4 X-ray emission . . . . .	16
2.5 Mass distribution in galaxy clusters . . . . .	16
2.6 Cooling time . . . . .	17
2.7 Self-similar model and empirical scaling relations . . . . .	18
<b>3 Scientific motivation</b>	<b>21</b>
3.1 Scientific rationale . . . . .	21
3.1.1 Cluster total mass and gas mass fraction . . . . .	21
3.1.2 Scaling relations and correlations . . . . .	23
3.1.3 Cluster number density . . . . .	24
3.1.4 Complexity in galaxy clusters . . . . .	27
3.1.5 Summary . . . . .	28
3.2 Current status . . . . .	28
3.2.1 Cluster total mass and gas mass fraction . . . . .	28
3.2.2 Scaling relations and correlations . . . . .	28

## Contents

---

3.2.3	Cluster number density . . . . .	30
3.2.4	Complexity in galaxy clusters . . . . .	30
3.3	Major goals . . . . .	31
3.3.1	Cluster total mass and gas mass fraction . . . . .	31
3.3.2	Scaling relations and correlations . . . . .	32
3.3.3	Cluster number density . . . . .	32
3.3.4	Complexity in galaxy clusters . . . . .	33
<b>4</b>	<b>XMM-Newton observatory</b>	<b>35</b>
4.1	X-ray observations and XMM-Newton . . . . .	35
4.2	Data reduction technique . . . . .	38
<b>5</b>	<b>Temperature gradients in the REFLEX-DXL galaxy clusters</b>	<b>41</b>
5.1	Introduction . . . . .	41
5.2	Method . . . . .	43
5.2.1	Data preparation . . . . .	43
5.2.2	Background analysis . . . . .	45
5.3	Results . . . . .	49
5.3.1	Redshift, mean temperature, and metallicity . . . . .	49
5.3.2	Temperature profiles . . . . .	54
5.3.3	Modeling RXCJ0307.0–2840 . . . . .	57
5.4	Summary and Conclusions . . . . .	62
<b>6</b>	<b>X-ray properties in massive galaxy clusters</b>	<b>67</b>
6.1	Introduction . . . . .	67
6.2	Data reduction . . . . .	69
6.2.1	Data preparation . . . . .	69
6.2.2	Source detection . . . . .	69
6.2.3	Background subtraction . . . . .	70
6.2.4	PSF and deprojection . . . . .	75
6.3	X-ray properties . . . . .	75
6.3.1	Metallicity and temperature . . . . .	75
6.3.2	Surface brightness . . . . .	79
6.3.3	Cooling time . . . . .	83
6.3.4	Overdensity . . . . .	84
6.3.5	Gas entropy . . . . .	84
6.3.6	Mass distribution . . . . .	85
6.3.7	Gas mass fraction distribution . . . . .	87
6.4	Scaling relations . . . . .	89
6.4.1	Scaled metallicity profiles . . . . .	90
6.4.2	Scaled temperature profiles . . . . .	90
6.4.3	Scaled surface brightness profiles . . . . .	91
6.4.4	Scaled entropy profiles . . . . .	93
6.4.5	Scaled total mass profiles . . . . .	93
6.5	Correlations . . . . .	94

6.5.1	Core radius . . . . .	94
6.5.2	Gas mass fraction . . . . .	94
6.5.3	$\delta_c$ - $M_{\text{vir}}$ and $c_{\text{vir}}$ - $M_{\text{vir}}$ relations . . . . .	95
6.5.4	$L$ - $T$ , $L$ - $M$ , $M$ - $T$ , $M_{\text{gas}}$ - $T$ and $L$ - $Z$ relations . . . . .	97
6.5.5	Intrinsic scatter in the correlations . . . . .	102
6.6	Discussion . . . . .	105
6.6.1	Mass infalling from the outskirts . . . . .	105
6.6.2	Additional physical processes . . . . .	106
6.7	Summary and conclusions . . . . .	106
<b>7</b>	<b>XMM-Newton study of the lensing cluster of galaxies CL0024+17</b>	<b>109</b>
7.1	Introduction . . . . .	109
7.2	Method . . . . .	113
7.2.1	Data preparation . . . . .	113
7.2.2	Background analysis . . . . .	114
7.2.3	Point source subtraction . . . . .	117
7.3	Results . . . . .	118
7.3.1	Image analysis . . . . .	118
7.3.2	Chandra observation of the center . . . . .	122
7.3.3	Optical observations . . . . .	122
7.3.4	Hardness ratio maps . . . . .	122
7.3.5	Temperature and metallicity profiles . . . . .	123
7.3.6	Surface brightness . . . . .	124
7.3.7	Cooling time of the gas . . . . .	125
7.3.8	Gas entropy . . . . .	126
7.3.9	Mass modeling . . . . .	126
7.3.10	Gas mass fraction . . . . .	129
7.4	Discussion . . . . .	129
7.4.1	Metallicity . . . . .	129
7.4.2	Temperature gradient . . . . .	130
7.4.3	Complex structure . . . . .	131
7.4.4	Comparison to lensing measurements . . . . .	131
7.4.5	Comparison to velocity dispersion measurement . . . . .	132
7.4.6	X-ray properties . . . . .	132
7.4.7	Central cooling . . . . .	132
7.5	Summary and Conclusions . . . . .	132
<b>8</b>	<b>Summary and conclusions</b>	<b>135</b>
8.1	Summary of the REFLEX-DXL sample . . . . .	135
8.1.1	Mass and gas mass fraction . . . . .	135
8.1.2	Self-similar behavior of the X-ray properties at $r > 0.1r_{\text{vir}}$ . . . . .	135
8.1.3	Correlations of the cluster properties . . . . .	137
8.2	Summary of CL0024+17 . . . . .	137
8.2.1	X-ray properties of CL0024+17 . . . . .	138
8.2.2	Mass estimates and the discrepancy . . . . .	138

## Contents

---

8.3 Conclusions and future prospective . . . . .	139
<b>Bibliography</b>	<b>141</b>
<b>Acknowledgements</b>	<b>I</b>
<b>Curriculum Vitae</b>	<b>III</b>
<b>Publications and Proceedings</b>	<b>V</b>

# List of Figures

1.1	Cosmic matter density contained in galaxy clusters vs. minimum mass . . . . .	2
1.2	X-ray luminosity and redshift distribution of the REFLEX survey . . . . .	6
3.1	Mass definition of a halo vs. $\Omega_m$ . . . . .	22
3.2	Evolution of the cluster mass function . . . . .	25
3.3	Dependence of $\sigma_8$ on the $M$ - $T$ normalization . . . . .	26
4.1	XMM-Newton and Chandra images of A2744 . . . . .	36
4.2	XMM-Newton spectra of RXCJ0547.6-3152 . . . . .	37
4.3	A comparison of the effective area . . . . .	38
5.1	Light curve of RXCJ0658.5-5556 for pn . . . . .	44
5.2	Residual background and the best fits . . . . .	45
5.3	Temperature profiles for RXCJ0307.0-2840 . . . . .	47
5.4	Comparison of the temperature estimates from MOS1, MOS2 and pn . . . . .	47
5.5	XMM-Newton spectra of RXCJ0307.0-2840 . . . . .	53
5.6	Temperature profiles of 9 REFLEX-DXL clusters . . . . .	54
5.7	Temperature measurements vs. low-energy cut-off . . . . .	55
5.8	Projected and deprojected temperature profiles for RXCJ0307.0-2840 . . . . .	58
5.9	Image for RXCJ0307.0-2840 in the 0.5-2 keV band . . . . .	60
5.10	Electron number density profiles of RXCJ0307.0-2840 . . . . .	61
5.11	Temperature profiles of RXCJ0307.0-2840 . . . . .	62
5.12	Mass and gas mass profiles of RXCJ0307.0-2840 . . . . .	63
5.13	Gas mass fraction distributions of RXCJ0307.0-2840 . . . . .	64
6.1	XMM-Newton spectra of RXCJ0303.8-7752 . . . . .	73
6.2	Projected and deprojected temperature profiles for 9 REFLEX-DXL clusters . . . . .	74
6.3	Temperature profiles using DBS II for 4 REFLEX-DXL clusters . . . . .	78
6.4	Surface brightness profiles of the REFLEX-DXL NCCCs . . . . .	80
6.5	Surface brightness profiles of the REFLEX-DXL CCCs . . . . .	81
6.6	Surface brightness profile and its double $\beta$ -model fit of RXCJ0307.0-2840 . . . . .	82
6.7	Central mass distributions of RXCJ0307.0-2840 . . . . .	83
6.8	$S_{0.1r_{200}}$ vs. $T_{\text{gmw}}$ . . . . .	85
6.9	Gas mass fraction profiles of the REFLEX-DXL sample . . . . .	88
6.10	A comparison of $T_{\text{spec}}$ to $T_{\text{emw}}$ and $T_{\text{gmw}}$ . . . . .	90
6.11	Metallicity profiles of the REFLEX-DXL sample . . . . .	91
6.12	Scaled temperature profiles of the REFLEX-DXL sample . . . . .	92

## List of Figures

---

6.13	Scaled surface brightness profiles of the REFLEX-DXL sample . . . . .	92
6.14	Scaled entropy profiles of the REFLEX-DXL sample . . . . .	93
6.15	Scaled total mass profiles of the REFLEX-DXL sample . . . . .	94
6.16	Gas mass fraction profiles of the REFLEX-DXL sample . . . . .	95
6.17	$c_{\text{vir}}$ vs. $M_{\text{vir}}$ . . . . .	96
6.18	A comparison of the XMM-Newton and ROSAT luminosities . . . . .	97
6.19	$L_X^{0.1-2.4\text{keV}}$ vs. $T$ . . . . .	100
6.20	$L_X^{\text{bol}}$ vs. $T$ . . . . .	100
6.21	$L_X^{\text{bol}}$ vs. $M$ . . . . .	101
6.22	$M$ vs. $T$ . . . . .	101
6.23	$M_{\text{gas}}$ vs. $T$ . . . . .	103
6.24	$L_X^{0.1-2.4\text{keV}}$ vs. $Z$ . . . . .	104
6.25	Histogram of the Gaussian distributed $\sigma_{\text{int}}$ . . . . .	105
7.1	XMM-Newton image of CL0024+17 in the 0.5–2 keV band . . . . .	110
7.2	Chandra image and surface brightness profiles . . . . .	111
7.3	HST mosaic image of the center of CL0024+17 . . . . .	112
7.4	XMM-Newton HRM of CL0024+17 . . . . .	113
7.5	XMM-Newton spectra of CL0024+17 . . . . .	114
7.6	Projected temperature and metallicity profiles . . . . .	115
7.7	XMM-Newton surface brightness profiles for CL0024+17 . . . . .	116
7.8	Contour plot of $r_c$ and $\beta$ . . . . .	117
7.9	Cooling time . . . . .	118
7.10	Entropy profiles of CL0024+17 . . . . .	119
7.11	Density and mass profiles . . . . .	120
7.12	Projected density and mass profiles truncated at 2.5 Mpc . . . . .	120
7.13	Projected density and mass profiles truncated at 1.7 Mpc . . . . .	121
7.14	Gas mass fraction profiles . . . . .	121
8.1	Preliminary temperature function of the REFLEX-DXL sample . . . . .	140

# List of Tables

3.1	Some published correlations . . . . .	29
5.1	Observational information on 9 REFLEX-DXL clusters . . . . .	42
5.2	Parameters of the residual background models . . . . .	43
5.3	Region list of the substructures and point sources . . . . .	51
5.4	Global temperatures, metallicities and redshifts . . . . .	52
5.5	Temperature profiles . . . . .	56
5.6	Parameters from the best $\chi^2$ fits . . . . .	65
6.1	Properties of the point-like sources in the cluster center . . . . .	70
6.2	Primary parameters of the REFLEX-DXL clusters . . . . .	76
6.3	Results of the XMM-Newton spectral analysis . . . . .	76
6.4	Temperature and metallicity profiles . . . . .	77
6.5	Parameters of Model I . . . . .	79
6.6	Parameters of Model II . . . . .	81
6.7	REFLEX-DXL catalogue part I . . . . .	84
6.8	REFLEX-DXL catalogue part II . . . . .	88
6.9	REFLEX-DXL catalogue part III . . . . .	89
6.10	REFLEX-DXL catalogue part IV . . . . .	96
6.11	Luminosities of the substructure and point-like sources . . . . .	98
6.12	$L-T$ relations . . . . .	99
6.13	$L-M$ relations . . . . .	102
6.14	$M-T$ and $M_{\text{gas}}-T$ relations . . . . .	103
6.15	Logarithmic intrinsic scatter measured for 4 main correlations . . . . .	105
7.1	Parameters of the residual background model . . . . .	116
7.2	Brightest point source list . . . . .	119
7.3	Parameters of the $\beta$ -model . . . . .	125
7.4	Comparison of the gravitational mass from the X-ray and optical lensing . .	127
7.5	Parameters of each profile model for the best $\chi^2$ fit . . . . .	128
7.6	Measured parameters for CL0024+17 . . . . .	129
7.7	Temperature and metallicity measurements . . . . .	130

## List of Tables

---



# 1 Introduction

## Abstract

In this chapter, I give an introduction to galaxy clusters and the construction of a flux-limited and almost volume-complete sample, consisting of 14 distant ( $z \sim 0.3$ ), X-ray luminous (DXL) galaxy clusters selected from the REFLEX survey (the REFLEX-DXL sample). The scientific objective for each individual project is presented in the last section.

## 1.1 Galaxy clusters

In the current structure formation paradigm, the hierarchical structure formation model, galaxy clusters are the largest gravitationally collapsed systems in the Universe formed from smaller mass systems along large-scale filaments (e.g. Springel et al. 2001). Galaxy clusters are the most massive ( $\sim 10^{14}$ – $10^{15} M_{\odot}$ ) systems, and almost approach gravitational relaxation and virial equilibrium. Galaxy clusters are relatively young, with dynamical time scales of order  $10^9$  yrs (e.g. Forman 2003). Up to 10% of the total mass in the Universe is bound in virialized galaxy clusters (e.g. Reiprich & Böhringer 2002). The cosmic matter density derived in galaxy clusters decreases as a function of minimum cluster mass as shown in Fig. 1.1.

Galaxy clusters consist of three main components, dark matter (DM), galaxies and hot diffuse intracluster medium (ICM). For Hubble constant  $H_0 = 70 \text{ km s}^{-1} \text{ Mpc}^{-1}$ , galaxies and hot gas account for approximately 3% and 10% of the cluster gravitational mass, respectively. The remaining matter is supposed to be DM, which is the most important component for structure formation of the Universe.

The existence of DM has been indicated by many observations. Observations of gravitationally bound systems, such as groups, clusters and superclusters, show large mass-to-light ratios. The flat rotation curves of galaxies suggest a high mass density distribution up to the very large radii (Davis et al. 1978). As shown in Yang et al. (1979), the combination of the standard big bang nucleosynthesis (BBN) theory and the observed deuterium and helium abundances implies the so called “missing mass”. DM has not been detected directly, but it has been measured indirectly by its gravitational effect. DM can be probed by its gravitational potential by, e.g. the dynamics of galaxies, gravitational lensing distortions of background galaxies by potential wells of galaxy clusters, hydrodynamics of the hot intracluster gas, and the cosmic microwave background (CMB) anisotropy spectrum (e.g. Colafrancesco 2003). Detailed studies were started very early to measure the DM distribution in galaxy clusters. Zwicky (1933) gave the first evidence for the presence of DM in the Coma cluster. Bailey (1982) investigated the mass-to-light ratio of Coma and

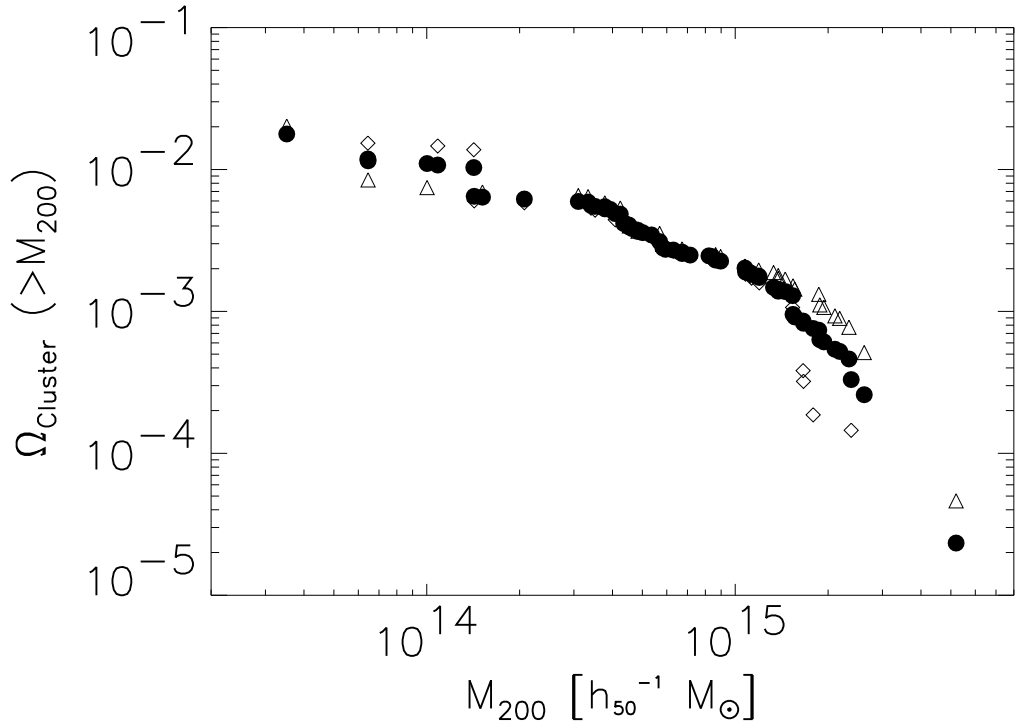


**Figure 1.1:** Cosmic matter density contained in galaxy clusters normalized to critical density ( $\Omega_{\text{Cluster}}$ ) as function of minimum value of the cluster masses ( $M_{200}$ ) measured at the radii with an overdensity of 200 (Reiprich & Böhringer 2002). Filled circles indicate the complete sample in their paper, open triangles indicate the 34 clusters north of the Galactic plane, and open diamonds the 29 clusters at southern Galactic latitudes included in their sample.

determined the DM density using the velocity dispersion. Tyson (1988) suggested that background galaxies lensed by galaxy clusters can be used to set limits to the DM halo mass distributions. Based on a spectral image of the Coma cluster observed by a coded mask telescope flown as part of the *Spacelab 2* mission, Watt et al. (1992) derived the temperature and density of the ICM as a function of radius and determined the total cluster mass profile assuming hydrostatic equilibrium. They deduced the DM distribution by subtracting the contributions due to visible matter in galaxies and X-ray emitting gas. The multi-pole structure of the CMB anisotropy power spectrum depends on the normalized overall amount of DM in the Universe. From the CMB experiments (e.g. BOOMERANG and WMAP), the overall DM density in the Universe has been measured from the CMB data to be  $\Omega_{\text{DM}} = 0.27 \pm 0.04$  (e.g. Bennett et al. 2003; Spergel et al. 2003).

From optical observations, it is well known that normal clusters contain  $\sim 100$  galaxies, and rich clusters  $\sim 1000$  galaxies. The number of the galaxy in a cluster varies from 30–300 for rich clusters, to 3–30 for poor groups and clusters. 5% of the bright galaxies ( $> L_*$ , where  $L_*$  is the characteristic luminosity of the luminosity function) are found in rich

clusters, while more than 50% are found in groups (e.g. Schuecker 2005). For rich clusters, typical surface number densities of cluster galaxies of the outskirts drops to 1% of the value at the cluster center.

The hot ICM (1–15 keV) in galaxy clusters emits X-rays. Typical luminosities are in the range  $10^{42}$ – $10^{45}$  erg s<sup>-1</sup> in the 0.1–2.4 keV energy band. The electron number density in the center of galaxy clusters is around  $10^{-3}$ – $10^{-1}$  cm<sup>-3</sup>, which means the ICM is optically thin. This enables us to directly interpret the spectra from known emission mechanisms (e.g. thermal Bremsstrahlung) without considering radiation transfer. The X-ray emission per volume element in galaxy clusters is proportional to the square of the ICM density. X-ray observations are thus less affected by small objects along the line-of-sight than optical images. X-ray emission per volume element in galaxy clusters is also proportional to the square root of the ICM temperature. Smaller clusters show lower temperatures, which are thus significantly less luminous. This makes the projection effect by smaller systems less significant in X-rays than in the optical. Therefore, X-ray observations of the ICM in galaxy clusters provide a unique means to investigate the thermodynamics of the ICM and its evolution. The shape of the X-ray spectrum can be used to measure the ICM temperature. The X-ray surface brightness can be used to measure the ICM density distribution (Henriksen & Mushotzky 1986). As mentioned above, the DM distribution can thus be determined assuming hydrostatic equilibrium. The ICM in galaxy clusters can also be observed by the distortion of the CMB spectrum due to Compton scattering, which is known as the Sunyaev-Zeldovich (SZ) effect (Sunyaev & Zeldovich 1972).

The evolution of the three main components of galaxy clusters is interactive and interconnected. The DM component is the main driver of gravity which heats the ICM via hydrodynamical shocks and produces the “thermal” motion of the galaxies. The ICM contributes to the galaxies by forming stars once it is cool. At the same time, star formation and supernova explosions provide feedback to the ICM by changing the metallicities and heating the ICM. In general, galaxy clusters can be considered to be well defined laboratories.

Galaxy clusters can be used not only to trace the cosmic evolution of the baryons in the Universe, but also to constrain the cosmological model independently. For example, galaxy clusters provide one of the most important proofs of a low density Universe basically independent of dark energy (e.g. Reiprich & Böhringer 2002).

Galaxy clusters are rare objects in the Universe with number densities of  $10^{-5} h^3$  Mpc<sup>-3</sup> (e.g. Böhringer et al. 2002a). Most of them are dynamically young, at redshifts below 2. More than 5000 galaxy clusters have been identified by the optical galaxy concentrations, and more than 2000 by the extended X-ray emission (e.g. Schuecker 2005).

The following principal cluster measurements can be used for critical tests of the underlying cosmological model (i) the power spectrum of the cluster distribution (e.g. Schuecker et al. 2003), (ii) the baryon fraction and its evolution (e.g. Ettori et al. 2002a), and (iii) the cluster mass/temperature/luminosity function and its evolution (e.g. Reiprich & Böhringer 2002; Henry 1997, 2004). Galaxy clusters also link the transition between astrophysical processes on small scales and structure formation on large scales. The gas mass fraction, the ratio of the ICM mass to total mass, in galaxy clusters can be used to test the BBN theory (e.g. White et al. 1993). In the hierarchical structure formation models, galaxy

## 1 Introduction

---

clusters form after smaller objects such as galaxies. The merger rate of galaxy clusters can be used to constrain the cosmic matter density parameter and consequently the other cosmological parameters (e.g. Schuecker et al. 2001).

In massive galaxy clusters, gravity plays a dominant role in the overall distribution and evolution of the hot gas. Therefore, massive galaxy clusters provide a clean and effective means to compare observations with simulations and theory and thus to test the cosmological models (e.g. Reiprich & Böhringer 2002) and to study astrophysical processes.

### 1.2 Primary motivation and the REFLEX-DXL sample

Since cluster temperatures and X-ray luminosities show strong correlations with cluster mass (e.g. Markevitch 1998), the X-ray selection is the most efficient selection procedure to select a sample by cluster mass.

Galaxy clusters have been probed up to  $z \sim 1.2$  (e.g. Vikhlinin et al. 1999, 2005a; Rosati et al. 2002). However, temperature measurements of a handful of galaxy clusters at high redshifts have shown that the temperature evolution remains modest at these redshifts (Voit 2005). The sampling volume in those surveys is relatively small and does not necessarily contain enough of the most massive clusters to constrain the cosmological parameters by the strong evolutionary effect of the mass function. Also a collection of observed individual galaxy clusters does not provide an unbiased basis for statistical studies.

#### 1.2.1 REFLEX sample

The ROSAT-ESO Flux-Limited X-ray (REFLEX, Böhringer et al. 2001a, 2002a, 2004a) galaxy cluster survey was constructed based on the ROSAT All-Sky Survey (RASS, Voges et al. 1999). The total survey covers  $13,924 \text{ deg}^2$  in the southern sky with a completeness in excess of 90% above a flux limit of  $3 \times 10^{12} \text{ erg s}^{-1} \text{ cm}^{-2}$  (0.1–2.4 keV). It provides the largest, statistically complete, published catalog of X-ray selected clusters of galaxies so far. A well understood three-dimensional selection function was provided for the REFLEX survey (Böhringer et al. 2004a). Therefore, it provides the basis to construct an unbiased subsample of clusters with specific selection criteria.

#### 1.2.2 REFLEX-DXL sample

A comprehensive study of a representative, unbiased sample will provide a unique constraint to the scaling relations and cosmological parameters. The selection criteria of the subsample are determined by the following properties.

##### 1.2.2.1 Luminosity

The most useful sample is a sample with a homogeneous coverage of the luminosity space. The massive (luminous,  $> 5 \text{ keV}$ ) clusters are selected since (i) the volume completeness correction of a sample is not very dramatic for massive clusters with  $T > 5 \text{ keV}$  (e.g. Pierpaoli et al. 2001), and (ii) the evolutionary effect of the cluster number density is expected to be most dramatic for massive clusters (details see Chapter 3).

### 1.2.2.2 Redshift

The medium distant redshift baseline is selected since such a sample can be compared with nearby and distant samples to study the evolutionary effect.

The cluster size at these redshifts optimally exploits the capabilities of XMM-Newton, e.g. field of view (FOV) and spectral sensitivity. For the clusters above 5 keV at redshift  $z \sim 0.3$ , the cluster radii with overdensity 500 ( $r_{500}$ ) correspond to 6'–10'. These clusters can thus optimally cover the sensitive region of the FOV ( $30' \times 30'$ ) of XMM-Newton with a sufficient area left for a reliable subtraction of the background.

At the same time, the flux corresponding to these redshifts optimizes the collection of sufficient photons using a reasonable exposure time ( $\sim 10$  ks). These data can be used to approach an uncertainty of 10–15% in the temperature measurement and to derive a spatially resolved abundance (for Fe) profile within  $r_{500}$ .

### 1.2.2.3 Morphology

In most of the previous studies (e.g. Allen et al. 2002), only the regular, relaxed clusters were chosen to calibrate the mass–observable relations to avoid the enhancement of the uncertainty by merging clusters. For a correct calibration of the scaling relations referring to the whole galaxy cluster population or a representative part, the sample should not be biased towards a particular type of cluster morphology (e.g. very relaxed clusters). All the clusters fulfilled the luminosity and redshift selection criteria will be selected from the REFLEX sample.

### 1.2.2.4 Selection criteria

Therefore, the sample is constructed from the REFLEX survey with X-ray luminosity and redshift as the only characteristic parameters (Fig 1.2). It is a flux-limited and almost volume-complete sample constructed strictly with the following numerical prescription to introduce a minimal bias.

- luminosities<sup>1</sup>  $L_X \geq 10^{45}$  erg s<sup>-1</sup> for the 0.1–2.4 keV band,
- redshifts in the range,  $z = 0.26$  to  $0.31$ .

This unbiased sample of 13 distant, X-ray luminous (DXL) galaxy clusters at  $z \sim 0.3$ , and one supplementary cluster at  $z = 0.2578$  (the REFLEX-DXL sample) provides a homogeneous luminosity distribution which is ideal to study scaling relations. Additionally, the REFLEX-DXL sample is tightly related with the “XMM-Newton Legacy-Type Program for the Study of Galaxy Cluster Structure” (XMM-LP, PI: Hans Böhringer) which consists of 32 galaxy clusters in the redshift range of 0.05–0.2.

---

<sup>1</sup>A flat cosmological model with the normalized cosmic matter density  $\Omega_m = 1$  and the Hubble constant  $H_0 = 50$  km s<sup>-1</sup> Mpc<sup>-1</sup> was used for the  $L_X$  threshold in the sample construction. This luminosity threshold corresponds to  $L_X \geq 5.9 \times 10^{44}$  erg s<sup>-1</sup> for a  $\Lambda$ CDM cosmology with the density parameter  $\Omega_m = 0.3$  and the Hubble constant  $H_0 = 70$  km s<sup>-1</sup> Mpc<sup>-1</sup>

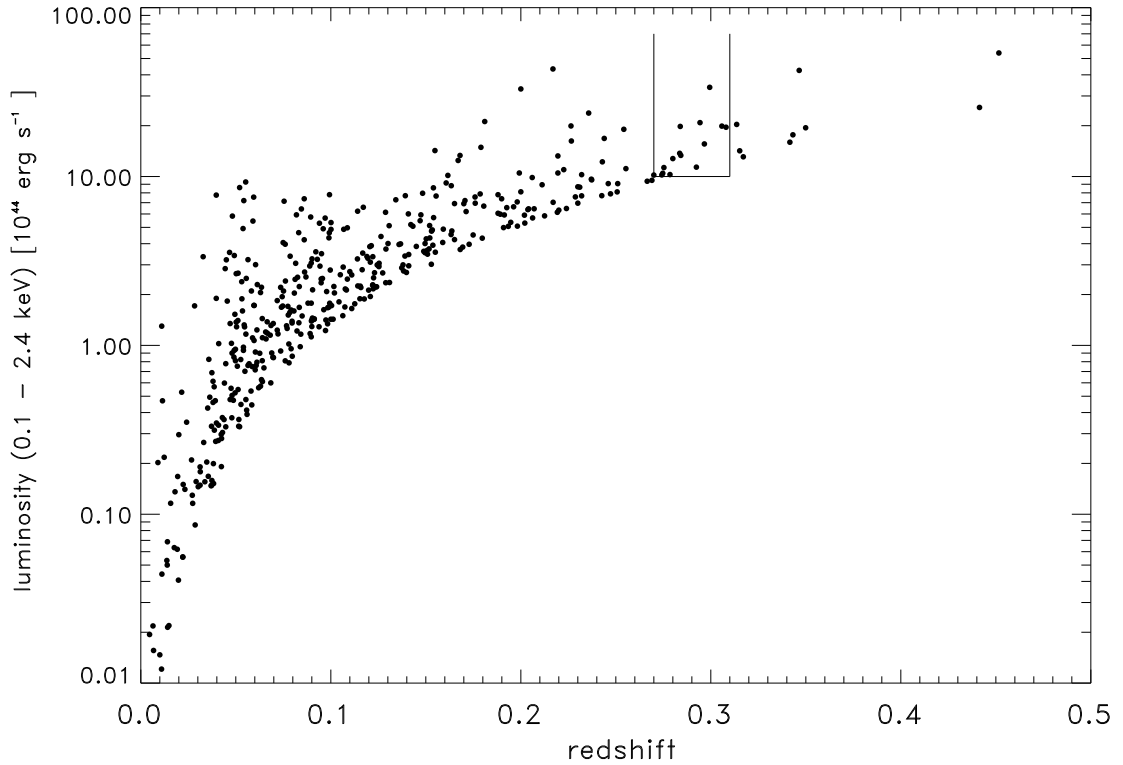


**Figure 1.2:** X-ray luminosity and redshift distribution of the galaxy clusters of the REFLEX survey. The box shows the flux-limited and almost volume-complete sample, the REFLEX-DXL sample (Böhringer et al. 2005a).

## 1.3 Outline

In this thesis, detailed studies of the ICM properties of massive galaxy clusters and their astrophysical and cosmological applications are provided. The results were also published in Zhang et al. (2004a, 2004b, 2005a, 2005b, 2005c), Böhringer et al. (2005a) and Finoguenov et al (2005). Chapter 2 describes the theoretical framework of this work. Chapter 3 is the detailed description of the scientific motivation, basic goals and main approaches of this work and the current status in this field. Chapter 4 gives a simple introduction of the XMM-Newton observatory and data reduction technique. The main work of this thesis is summarized in three refereed papers with the present author as the first author (Zhang et al. 2004a, 2005a, 2005c).

Chapter 5 is a copy of the article *Exploring the Structure of Galaxy Clusters: XMM-Newton observations of the REFLEX-DXL clusters at  $z \sim 0.3$*  by Zhang, Y. -Y., Finoguenov, A., Böhringer, H., Ikebe, Y., Matsushita, K., and Schuecker, P. 2004, A&A, 413, 49. In this article, the XMM-Newton observations of 9 galaxy clusters of a flux-limited and almost volume-complete sample (observed in the AO-1 observing period) are applied to study the temperature profiles. Robust cluster mass measurements are very important to study the X-ray galaxy cluster scaling relations and their intrinsic scatter, which is key to the use

of clusters of galaxies as cosmological probes. The main uncertainty of the mass estimate comes from the uncertainty of the temperature measure. To achieve a precise mass determination of galaxy clusters, one has to obtain very reliable temperature distributions. The advanced XMM-Newton X-ray observatory has a high energy resolution and a large FOV allowing such a detailed study. An almost volume complete sample, the REFLEX-DXL sample, has been selected from the REFLEX survey. A set of reliable procedures have been developed and tested to obtain precise temperature profiles of 9 REFLEX-DXL clusters of galaxies.

Chapter 6 is a copy of the article *X-ray Properties in Galaxy Clusters: XMM-Newton observations of the REFLEX-DXL sample* by Zhang, Y. -Y., Böhringer, H., Finoguenov, A., Ikebe, Y., Matsushita, K., Schuecker, P., Guzzo, L., and Collins, C. A. 2005, A&A, in press. This is an extension of Chapter 5. In this article, a detailed study of the X-ray properties has been performed for all of the REFLEX-DXL clusters based on the XMM-Newton observations in the AO-1 and AO-4 observing periods. The X-ray properties of the most massive clusters are well described in hierarchical modeling since the structure of the X-ray emitting intracluster plasma is essentially determined by gravitational effects and shock heating. Therefore the most massive clusters provide the cleanest results in comparing theory with observations. Robust cluster masses were derived based on precise gas density and temperature distributions. The gas mass fractions are in a narrow range of 0.06–0.15. This agrees with previous cluster studies and the WMAP baryon fraction measurement (Spergel et al. 2003). The cluster mass measurements with improved accuracy tighten scaling relations. The profiles of the surface brightness, temperature, entropy, and mass are well characterized by a self-similar behavior. This is the origin of the small scatter of the correlations of various cluster properties. A reduced uncertainty of the normalization was obtained for the correlations such as  $L-T$ ,  $L-M$ ,  $M-T$  and  $M_{\text{gas}}-T$  relations. The evolution of the correlations can be accounted for by a redshift evolution correction. A detailed study of the intrinsic scatter of the correlations was also performed for a better understanding of the correlations.

Chapter 7 is a copy of the article *XMM-Newton study of the lensing cluster of galaxies CL0024+17* by Zhang, Y.-Y., Böhringer, H., Mellier, Y., Soucail, G., and Forman, W. 2005, A&A, 431, 433. In this article, we compared the X-ray measured gravitational mass based on the XMM-Newton observations with the optical lensing mass for CL0024+17. One of the optically most prominent, but also most puzzling distant lensing galaxy clusters, is CL0024+17 at redshift  $z = 0.395$  (Gunn & Oke 1975), which shows a significantly higher lensing mass than X-ray mass. This cluster has been the subject of many studies since its discovery by Humason & Sandage (1957). Schneider et al. (1986) described it as a very rich optical cluster. The capability of XMM-Newton to perform imaging spectroscopy at high angular resolution allows us to study the density and temperature structure of the ICM. Therefore XMM-Newton observations of CL0024+17 have been performed to shed new light on this enigmatic system. The emission appears approximately symmetric in the XMM-Newton image. However, some indication of elongation is visible in the northwest-southeast direction from the hardness ratio map. The temperature distribution shows an isothermal temperature in the central region and a temperature gradient in the outskirts. Assuming hydrostatic equilibrium, the gravitational mass and gas mass fraction are  $2.0 \pm$

## 1 Introduction

---

$0.3 \times 10^{14} h_{70}^{-1} M_{\odot}$  and  $0.20 \pm 0.03 h_{70}^{-3/2}$ , respectively, at the radius with overdensity 200. The X-ray total mass based on the advanced XMM-Newton data marginally agrees with the weak lensing results but not with the strong lensing measurements. A hint towards an explanation for this mass discrepancy came from the detailed analysis of the galaxy dynamics in CL0024+17 based on  $\sim 300$  redshifts of galaxy members (Czoske et al. 2001, 2002). Czoske et al. (2001, 2002) found that the line-of-sight velocity distribution is not that of a relaxed cluster and is at least bimodal. They also demonstrated that the redshifts can approximately be explained by a line-of-sight merger of two systems with a mass ratio of the order of 1:2. Therefore, filamentary structures could also contribute to the projected mass detected by lensing. The X-ray hardness ratio map confirms the complex structure in the cluster center found in optical. However, since this mass does not lie within the cluster core, it would not be included in the X-ray mass measurement. The line-of-sight orientation makes it difficult to reveal the merger structure in the X-ray data, but on the other hand it enhances the probability of finding strong lensing features.

Chapter 8 gives the summary and main conclusions of this work.



# 2 Theoretical framework

## Abstract

In this chapter, I provide the theoretical framework of large-scale structure (LSS) and galaxy cluster formation including a detailed description of the self-similar model and various empirical scaling relations for galaxy clusters.

## 2.1 Standard cosmological model

The current standard cosmological model is based on the assumption that the Universe is homogeneous and isotropic on large scales ( $> 100$  Mpc) (e.g. Peebles 1980; Padmanabhan 1993). The space-time for such a universe can be described by the Robertson-Walker metric:

$$ds^2 = c^2 dt^2 - a^2(t) \left[ \frac{dr^2}{1 - \kappa r^2} + r^2(d\theta^2 + \sin^2 \theta d\phi^2) \right], \quad (2.1)$$

where  $c$  is the speed of light,  $(r, \theta, \phi)$  the comoving spherical coordinates,  $s$  the proper time, and  $t$  the cosmic time.  $a(t)$  is independent of spatial coordinates. It denotes the overall scale of the spatial metric as a function of time.  $\kappa$  is the curvature index, a constant scaled so that it takes the values 1, 0 or  $-1$  for a closed, flat and open universe, respectively.

The energy of photons emitted by distant sources is reduced by the expansion of the Universe. The redshift,  $z(t) = a(t_0)/a(t) - 1$ <sup>1</sup>, is often used as a time indication in the cosmological studies.

The assumption of the Robertson-Walker Metric results simplifies *Einstein's field equations* to give the dynamical evolution of the Universe in form of the *Friedmann-Lemaître equations*,

$$\ddot{a} = -\frac{4\pi G a}{3} \left( \rho + \frac{3p}{c^2} \right) + \frac{\Lambda a c^2}{3}, \quad (2.2)$$

$$\dot{a}^2 = \left( \frac{8\pi G \rho}{3} + \frac{\Lambda c^2}{3} \right) a^2 - \kappa. \quad (2.3)$$

Here, overdots denote derivations with respect to cosmic time,  $\rho = \rho(t)$  the cosmic matter density,  $p = p(\rho)$  the pressure, and  $\Lambda$  the cosmological constant. Eq.(2.3) can be re-written as

$$H^2(t) = \left( \frac{\dot{a}}{a} \right)^2 = \frac{8\pi G \rho}{3} + \frac{\Lambda c^2}{3} - \frac{\kappa}{a^2}. \quad (2.4)$$

---

<sup>1</sup> $a(t)$  is normalized to the present day that  $a(t_0) = 1$ .

## 2 Theoretical framework

It is referred to the *Friedmann equation* and indicates that the expansion of the Universe is determined by relativistic and non-relativistic matter, and the cosmological constant or more general, dark energy.  $H = H(t) = H(z)$  is the Hubble parameter which represents the expansion rate of the Universe at the cosmic time  $t$ . It has the measured value of  $H_0 = 72 \pm 8 \text{ km s}^{-1} \text{ Mpc}^{-1}$  at the present day (Freedman et al. 2001) known as the Hubble constant. In general,  $H_0 = 70 \text{ km s}^{-1} \text{ Mpc}^{-1}$  is used in this work, unless explicitly stated otherwise. By convention,  $H_0$  is usually parameterized as  $H_0 = 70 h_{70} \text{ km s}^{-1} \text{ Mpc}^{-1}$  with the dimensionless factor  $h_{70}$ . Once the equation of state  $p = p(\rho)$  is specified, one can solve for  $a(t)$ . For example, for non-relativistic matter, the pressure can be replaced so that the solution is  $\rho \propto a^{-3}$ ; for relativistic matter like photons or neutrinos, the pressure is  $p = \rho c^2/3$  so that the solution is  $\rho \propto a^{-4}$ .

The matter density of the Universe at redshift  $z$  is usually expressed in units of the critical density at that epoch,

$$\rho_c(z) = \frac{3H^2(z)}{8\pi G}, \quad (2.5)$$

which is used to define three cosmological parameters, the normalized cosmic matter density, the normalized cosmological constant and the normalized curvature index, at epoch  $z$ :

$$\Omega_m(z) = \frac{\rho(z)}{\rho_c(z)}, \quad \Omega_\Lambda(z) = \frac{\Lambda c^2}{3H^2(z)}, \quad \text{and} \quad \Omega_\kappa(z) = -\frac{\kappa}{a^2 H^2(z)}. \quad (2.6)$$

$\Omega_m$ ,  $\Omega_\Lambda$  and  $\Omega_\kappa$  denote the corresponding parameters at the present day,  $t = t_0$ . The cosmological dynamic equation can thus be simplified to  $\Omega_m(z) + \Omega_\Lambda(z) + \Omega_\kappa(z) = 1$ . For a flat Universe,  $\Omega_m(z) + \Omega_\Lambda(z) = 1$ . The deceleration parameter is given by

$$q = -\left(\frac{\ddot{a}a}{\dot{a}^2}\right) = \frac{\Omega_m(z)}{2} - \Omega_\Lambda(z). \quad (2.7)$$

$w = p/\rho c^2$  describes the phenomenological ratio of the pressure of the dark energy component and rest energy density.  $w = -1$  corresponds to the Einstein's cosmological constant.

The WMAP collaboration (Spergel et al. 2003) combined the WMAP experimental results with many other observations and obtained the following cosmological parameters:  $\Omega_m = 0.29 \pm 0.087$ ,  $\Omega_\Lambda = 0.69 \pm 0.05$ ,  $\Omega_\kappa \simeq 0$ , and  $w = -0.998 \pm 0.038$ . Since the critical density is a function of the Hubble parameter, it also evolves with time. At the present day, it has the value

$$\rho_{c0} \equiv 2.7755 \times 10^{11} h^2 M_\odot \text{ Mpc}^{-3}. \quad (2.8)$$

The *Friedmann equation* can thus be transformed into

$$E^2(z) = \frac{H^2(z)}{H_0^2} = \Omega_m(1+z)^3 + \Omega_\kappa(1+z)^2 + \Omega_\Lambda. \quad (2.9)$$

Once the density parameters of Universe of the present day is known, one can integrate this equation to derive the age of the Universe at redshift  $z$

$$t(z) = \int \frac{da}{\dot{a}} = \frac{1}{H_0} \int_z^\infty \frac{d\bar{z}}{(1+\bar{z})\sqrt{\Omega_m(1+\bar{z})^3 + \Omega_\kappa(1+\bar{z})^2 + \Omega_\Lambda}}. \quad (2.10)$$

For  $z = 0$ , the integration gives the age of the Universe. The WMAP results (Spergel et al. 2003) suggest that the age of the Universe is  $13.4 \pm 0.3 \text{ Gyr}$ .

## 2.2 Linear and quasi-linear theory

The standard cosmological model assumes that structures in the Universe originate from small amplitude quantum fluctuations possibly imprinted as an initially homogeneous and isotropic Gaussian random field during an epoch of inflationary expansion shortly after the big bang. The linear growth of the density fluctuations is thus completely determined by its power spectrum, or equivalently determined by its two-point correlation function. For small fluctuations (i.e. the density contrast  $\delta\rho = (\rho - \bar{\rho})/\bar{\rho} \ll 1$ ), linear and quasi-linear theories have been used to study the formation and evolution of LSS.

### 2.2.1 Primordial density fluctuations and the transfer function

The initial matter perturbation spectrum is assumed to be a power law,

$$P(k) \propto k^n, \quad (2.11)$$

where  $k$  is a comoving wavenumber, and  $n$  is an effective power index also when  $P(k)$  is not a pure power law. For the special case  $n = 1$ , i.e. the Harrison-Zeldovich scale-invariant spectrum, Eq.(2.11) implies that the density contrast has the same amplitude on all scales when the perturbations enter the particle horizon.

Inflation is produced by the dominant presence of a quantum scalar field (inflaton) which slowly rolls down its potential, maintaining an approximately constant energy density and causing the early Universe to expand exponentially for a brief period of time. In Einstein-de Sitter phase, quantum fluctuations in the inflaton field are thus blown up to cosmologically interesting macroscopic scales. Models of inflation predict the general properties of the resulting fluctuation field. This field has Gaussian distributed amplitudes and a near scale-invariant power spectrum.

The primordial power spectrum changes during the evolution of the early Universe until the end of the epoch of recombination by various processes including growth under self-gravitation, effects of pressure, and dissipative processes. In general, modes of short wavelength have their amplitudes reduced relative to those of long wavelength. The overall effect can be encapsulated in the transfer function,  $T(k)$ , which gives the ratio of the later-time amplitude of a mode to its initial value:

$$P(k) \propto k^n T^2(k). \quad (2.12)$$

Accurate results for transfer functions require a solution of the *Boltzmann equation* to follow the evolution in detail. CMBFAST is commonly considered one of the best publicly available multi-fluid Boltzmann codes for this task (Seljak & Zaldarriaga 1996). There are also several fitting formulae available for the transfer function of the CDM model. For adiabatic CDM, one of the most widely used ones is given by Bardeen et al. (1986),

$$T(k) = \frac{\ln(1 + 2.34q)}{2.34q} [1 + 3.89q + (16.1q)^2 + (5.46q)^3 + (6.71q)^4]^{-1/4}, \quad (2.13)$$

with  $q = k(\Omega_m h^2)^{-1}$  Mpc. This formula can be modified for an adiabatic CDM model with a mixture of baryons,  $\Omega_b$ , by setting  $q = k/h/\Gamma$  Mpc and the shape parameter

## 2 Theoretical framework

---

$\Gamma = \Omega_m h \exp[-\Omega_b(1 + \sqrt{2h}/\Omega_m)]$  (Sugiyama 1995). This transfer function fitting formula considering baryons gives a good approximation on scales below  $\sim 200 h^{-1}$  Mpc (e.g. Hu & Sugiyama 1996; Eisenstein & Hu 1998), which well recover the cluster scales. On scales above  $\sim 200 h^{-1}$  Mpc, the approximation can not precisely recover the observational transfer function since the acoustic oscillations become significant (e.g. Hu & Sugiyama 1996; Eisenstein & Hu 1998).

To completely specify  $P(k)$  with a given shape, one has to fix the amplitude by calculating the value of  $P(k)$  at any  $k$ , or the value of any statistic that depends on  $P(k)$ . The variance of the galaxy distribution sampled with randomly placed spheres of radius  $R$  can be used to normalize a theoretical power spectrum,

$$\sigma^2(R) = \frac{1}{2\pi^2} \int_0^\infty k^3 P(k) W^2(kR) \frac{dk}{k}, \quad (2.14)$$

where  $W(kR) = 3[\sin(kR) - kR \cos(kR)]/(kR)^3$  is the Fourier transform of a spherical top-hat filter with radius  $R$ . The value of  $\sigma(R)$  derived from the distribution of normal galaxies is approximately unity in spheres of radius  $R_8 = 8 h^{-1}$  Mpc, which is known as  $\sigma_8$ . In general,  $\sigma_8$  is used to normalize the power spectrum,

$$\sigma^2(R) = \sigma_8^2 \frac{\int_0^\infty k^2 k^n T^2(k) W^2(kR) dk}{\int_0^\infty k^2 k^n T^2(k) W^2(kR_8) dk}. \quad (2.15)$$

$\sigma_8$  is thus called the normalization. Alternatively, the normalization can be obtained from the CMB anisotropy based on the COBE or WMAP observations (e.g. Bennett et al. 2003; Spergel et al. 2003).

### 2.2.2 Dynamics of linear perturbations

Jeans (1902) applied first order perturbation theory to study the instabilities in evolving clouds of gas in the context of a static background fluid. Since the evolution of DM in an expanding background behaves similarly to a collisionless fluid, Jeans theory can also be used to discuss the time evolution of perturbations in an expanding Universe. Using the comoving coordinates,  $\vec{x}$ , defined as

$$\vec{r} = a(t) \vec{x}, \quad (2.16)$$

the proper velocity,  $\vec{v} = d\vec{r}/dt$ , at point  $\vec{x}$  can be written as

$$\vec{v} = \dot{a}(t) \vec{x} + a(t) \vec{u}, \quad (2.17)$$

where  $\vec{u}$  is the peculiar velocity describing the motion of the fluid relative to the fundamental observer (comoving with the background) at  $\vec{x}$ . The density,  $\rho$ , is in terms of the density perturbation against the background,

$$\rho(\vec{x}, t) = \bar{\rho}(t) [1 + \delta(\vec{x}, t)]. \quad (2.18)$$

The time evolution of an ideal fluid is given by the continuity equation describing mass conservation (below horizon), the *Euler's equation* describing momentum conservation, and

the *Poisson's equation* describing the relation between the gravitational field and the matter density,

$$\frac{\partial \delta}{\partial t} + \nabla \cdot [(1 + \delta) \vec{u}] = 0, \quad (2.19)$$

$$\frac{\partial \vec{u}}{\partial t} + (\vec{u} \nabla) \vec{u} = -\nabla \phi - \frac{\nabla P}{\bar{\rho}(1 + \delta)}, \quad (2.20)$$

$$\nabla^2 \phi = 4\pi G \bar{\rho} \delta, \quad (2.21)$$

where  $\nabla \equiv \nabla_x$  and  $\partial/\partial t$  is in Eulerian space,  $\phi$  denotes the Newtonian potential, and  $\bar{\rho}$  is the mean background density.

In the cases where both  $\delta$  and  $\vec{u}$  are small and the pressure is negligible, nonlinear terms can be neglected and one obtains:

$$\frac{\partial^2 \delta}{\partial t^2} + 2 \frac{\dot{a}}{a} \frac{\partial \delta}{\partial t} = 4\pi G \bar{\rho} \delta. \quad (2.22)$$

Solutions of Eq.(2.22) depend on the cosmological model through the Hubble parameter  $H(t) = \dot{a}/a$  and the defined perturbations. For the simplest matter-dominated universe, the Einstein-de Sitter universe, one obtains the exact solution with two modes, a growing mode,

$$\delta_+ \propto t^{2/3} \propto \frac{1}{1+z}, \quad (2.23)$$

and a decaying mode,

$$\delta_- \propto t^{-1}. \quad (2.24)$$

Given a density field of perturbations, its late time growth is described by the growth factor as long as  $\delta \ll 1$

$$\frac{\delta(x, z)}{\delta_0(x, 0)} = \frac{D(z)}{D(0)}. \quad (2.25)$$

Setting  $D(0) = 1$ , the normalized growth factor is given by,

$$D(z) = \frac{1}{1+z} \cdot \frac{g(z)}{g(0)}. \quad (2.26)$$

For adiabatic perturbations, the approximate expression of  $g(z)$  is given by Carroll et al. (1992),

$$g(z) = \frac{5}{2} \cdot \frac{\Omega_m(z)}{\Omega_m^{4/7}(z) - \Omega_\Lambda(z) + [1 + \frac{1}{2}\Omega_m(z)][1 + \frac{1}{70}\Omega_\Lambda(z)]}. \quad (2.27)$$

The redshift normalization is arbitrary, as long as it refers to a time before any scale of interest has entered the horizon. The evolution of linear perturbations back to the last scattering surface obeys the simple growth law given by Eq.(2.25), which shows the change of the structure in the Universe during the matter-dominated epoch.

### 2.2.3 Spherical “Top-Hat” collapse

The spherical “Top-Hat” collapse model is a simple and useful approximation to study the nonlinear evolution of the cosmic density field. For a spherical perturbation in a flat Einstein-de Sitter universe, the Eulerian radius  $R$  of a mass shell with initial Lagrangian radius  $R_0$  and mean linear density contrast  $\delta_0$  is given by

$$\frac{R(z)}{R_0} = \frac{3}{5} \cdot \frac{1+z}{|\delta_0|} \cdot \frac{(1-\cos\theta)}{2}, \quad (2.28)$$

$$1+z = \frac{5}{3} \left(\frac{4}{3}\right)^{\frac{2}{3}} \frac{|\delta_0|}{(\theta - \sin\theta)^{\frac{2}{3}}}, \quad (2.29)$$

where  $\delta_0$  is the initial density contrast  $\delta_{\text{init}}$  extrapolated to the present time by Eq.(2.25). In the case  $\delta_{\text{init}} < 0$ ,  $(1 - \cos\theta)$  should be replaced by  $(\cosh\theta - 1)$  and  $(\theta - \sin\theta)$  by  $(\sin\theta - \theta)$ .

In the spherical collapse model, initially overdense regions begin their collapse at  $\theta = 0$ , turnaround at  $\theta = \pi$ , and collapse at  $\theta = 2\pi$ . With the above equations, an overdense region evolves as

$$\frac{R_0}{R(z)} = \frac{6^{\frac{2}{3}} (\theta - \sin\theta)^{\frac{2}{3}}}{2 (1 - \cos\theta)}. \quad (2.30)$$

At the point of turnaround the density contrast is given by  $\delta = (R_0/R_z)^3 - 1 = (3\pi/4)^2 - 1 \sim 4.55$ .  $R_0/R(z)$  at the epoch of collapse is infinite, and so the density of this region is infinite as well. Actually, the region virializes at some non-zero size rather than collapses to infinite density. The average density within the virialized object is usually estimated by assuming that the object virializes at half the value of the turnaround radius. For a flat universe, this occurs when the average density reaches  $\Delta_{c,z}\rho_c$ , where the overdensity is given by

$$\Delta_{c,z} = 18\pi^2 + 82[\Omega_m(z) - 1] - 39[\Omega_m(z) - 1]^2. \quad (2.31)$$

According to Eq.(2.28), the extrapolated linear density contrast of such a collapsed object has a critical value,  $\delta_{\text{sc}}$ , given by

$$\delta_{\text{sc}}(z) = \frac{3}{5} \left(\frac{3\pi}{2}\right)^{\frac{2}{3}} \simeq 1.686 \quad (2.32)$$

at the epoch of collapse. The critical density can be extrapolated by linear theory to the present day,  $\delta_{\text{sc}}(z)/D(z) = 1.686/D(z)$ .

## 2.3 Mass function

In the Cold Dark Matter (CDM) scenario, galaxies and LSS are built up by the process of hierarchical clustering. A simple but quite useful description of this process was first developed by Press & Schechter (1974). This provides an analytic formalism for the process of structure formation once the density perturbations have reached such an high enough amplitude that they can be considered to have formed virialized objects.

The primordial density perturbations are Gaussian fluctuations. Therefore the phases of the waves which make up the density distribution are random and the distribution of the amplitudes of the perturbations of a given mass  $M$  can be described by a Gaussian distribution,

$$p(\delta) = \frac{1}{\sqrt{2\pi}\sigma(M)} \exp\left(-\frac{\delta^2}{2\sigma^2}\right), \quad (2.33)$$

where  $\delta = \delta\rho/\rho$  is the density contrast associated with perturbations of mass  $M$ . For a Gaussian distribution, the mean value is zero and the variance,  $\sigma^2(M)$ , i.e the mean square fluctuation, is

$$\langle \delta^2 \rangle = \left\langle \left( \frac{\delta\rho}{\rho} \right)^2 \right\rangle = \sigma^2(M). \quad (2.34)$$

At time  $t$ , the fraction of points within a sphere of radius  $R$ , where the mean overdensity exceeds  $\delta_c$  is given by

$$f(\delta > \delta_c) = \frac{1}{2} \left[ 1 - \operatorname{erf} \left( \frac{\delta_c}{\sqrt{2}\sigma(R)} \right) \right]. \quad (2.35)$$

Press & Schechter suggested that this fraction is identical to the fraction of particles collapsed with masses exceeding  $M = 4\pi\bar{\rho}a^3R^3/3$ . However, when  $M \rightarrow 0$ ,  $\sigma(R) \rightarrow \infty$  and thus  $f \rightarrow 1/2$ . This prediction only includes half of the particles collapsed above any mass. Press & Schechter solved this by multiplying the mass fraction by an arbitrary factor of 2. It is often argued that this accounts for additional mass accretion. Bond et al. (1991) developed a solution to this procedure based on excursion sets and gave an explanation to the origin of the arbitrary factor of 2 known as the extended PS formalism. The number density of collapsed clumps within the mass range  $M \rightarrow M + dM$  at redshift  $z$  is

$$n(M, z) = -2 \frac{\bar{\rho}}{M} \cdot \frac{\partial f}{\partial R} \cdot \frac{dR}{dM} dM \quad (2.36)$$

$$= -\sqrt{\frac{2}{\pi}} \cdot \frac{\bar{\rho}}{M} \cdot \frac{\delta_c(z)}{\sigma^2} \exp\left[-\frac{\delta_c^2(z)}{2\sigma^2}\right] dM. \quad (2.37)$$

A substantially better fit to the mass function in  $N$ -body simulations is obtained if the error function in Eq.(2.35) is replaced by a function of slightly different shape. Sheth & Tormen (1999) suggested the following modification:

$$n(M, z)dM = A \left( 1 + \frac{1}{\nu'^{2q}} \right) \sqrt{\frac{2}{\pi}} \frac{\bar{\rho}}{M} \frac{d\nu'}{dM} \exp\left(-\frac{\nu'^2}{2}\right) dM, \quad (2.38)$$

where  $\nu = \delta_c/\sigma$ ,  $\nu' = \sqrt{a}\nu$ ,  $a = 0.707$ ,  $A = 0.322$  and  $q = 0.3$ . In a detailed comparison with a wide range of simulations, Jenkins et al. (2001) confirmed that the model is indeed a good fit providing that halos are defined at the same density contrast relative to the mean in all cosmologies. However, Jenkins et al. (2001) pointed out that the Sheth & Tormen model does overestimate the number density of extremely rare objects. A more accurate fitting formula was provided in Jenkins et al. (2001).

The above describes how the cluster mass function is related to the cosmological models in the LSS theory. However, the total mass in galaxy clusters can not be observed directly,

## 2 Theoretical framework

---

but can be calculated using various mass-observable relations. Therefore, an observable calculation of the whole cluster population (i.e. luminosity function, temperature function, and gas mass function) in terms of the mass function provides an alternative solution in the LSS theory. This provides the same strong and direct link between the observable function and the cosmological models as between the mass function and the cosmological models. The various observable functions thus provide a powerful and relatively direct test of the cosmological models. To make use of this link, we do need a broad knowledge of cluster observables and cluster structure.

### 2.4 X-ray emission

The ICM is trapped and shock heated in the cluster gravitational potential, and emits X-ray emission. The prime emission process is thermal Bremsstrahlung (e.g. Sarazin 1988). The emissivity is given by

$$\varepsilon_\nu \equiv \frac{dL}{dV d\nu} \quad (2.39)$$

$$= \frac{2^4 e^6}{3m_e \hbar c^2} \left( \frac{2\pi k_B T}{3m_e c^2} \right)^{1/2} \mu_e n_e^2 g(Z, T, \nu) \exp\left(-\frac{h_P \nu}{k_B T}\right) (k_B T)^{-1}, \quad (2.40)$$

where  $\hbar = h_P/(2\pi)$ . Here  $\nu$  denotes frequency,  $Z$  iron charge,  $T$  electron temperature,  $e$  electron charge,  $m_e$  electron mass,  $n_e$  electron number density,  $h_P$  Planck constant,  $k_B$  Boltzmann constant,  $\mu_e = 2/(1+X) = 1.18$  mean molecular weight per electron, and  $g(Z, T, \nu)$  Gaunt factor.

Most models of the X-ray emission in galaxy clusters consist of thermal Bremsstrahlung continuum and strong line emission including the strongest lines, iron line complex around 6.8 keV. The X-ray spectral shape can be used to determine the ICM temperature (e.g. Henriksen & Mushotzky 1986). Under the assumption of spherical symmetry, the X-ray surface brightness profile,  $S_X$ , can be inversed to derive the gas distribution of clusters (e.g. Henriksen & Mushotzky 1986).

### 2.5 Mass distribution in galaxy clusters

The ICM distribution can be used to trace the cluster potential. Under the assumption of spherical symmetry, the cluster mass can be obtained from the X-ray measured ICM density and temperature distributions using the hydrostatic equilibrium,

$$\frac{1}{\mu m_p n_e} \frac{d(n_e k_B T)}{dr} = -\frac{GM(r)}{r^2}. \quad (2.41)$$

For a fully ionized plasma with a hydrogen mass percentage of  $X = 0.70$ , the mean molecular weight per hydrogen atom is  $\mu = 4/(3+5X) = 0.62$ .

Massive galaxy clusters are the largest virialized system in the Universe. The main component of galaxy clusters is DM. A DM halo may be defined as a virialized system which has mean density  $\Delta_{c,z}$  times the critical density of the Universe, as suggested by the



“top-hat” spherical collapse model. Regardless of the detailed initial conditions, numerous numerical simulations indicated that the radial mass distribution of the DM halos follows a universal profile (e.g. Navarro et al. 1996, 1997) in the hierarchical model with the initial power spectrum,

$$\frac{\rho(r)}{\rho_c} = \frac{\delta_c}{(r/r_s)(1+r/r_s)^2}, \quad (2.42)$$

where  $r_s$  is a characteristic radius, and  $\delta_c$  a characteristic density. The NFW profile has a logarithmic slope changing gradually from  $-1$  near the center to  $-3$  at large radii, and is close to  $-2$  in the range between the center and large radii. The gravitational mass within radius  $r$  is thus determined by

$$M(r) = 4\pi\rho_s r_s^3 \left[ \ln(1+r/r_s) - \frac{r/r_s}{1+r/r_s} \right]. \quad (2.43)$$

However, recent studies using numerical simulations show that the inner DM density profile has  $\rho \propto r^{-1.5}$  (e.g. Moore et al. 1999; Navarro et al. 2004; Reed et al. 2003; Diemand et al. 2004). A universal profile was thus suggested (e.g. Moore et al. 1999),

$$\frac{\rho(r)}{\rho_c} = \frac{\delta_c}{(r/r_s)^\alpha(1+r/r_s)^{3-\alpha}}, \quad (2.44)$$

where  $\alpha$  and  $3-\alpha$  denote the inner and outer slopes, respectively, and  $r_s$  specifies the radius where the profile steepens. This transition of the density profile gradient can be characterized by a concentration parameter,  $c = r_{\text{vir}}/r_s$ . Simulations (Jing 2000) indicate a range of  $c \sim 4-10$  in which low mass clusters tend to have high concentration parameters. Some studies (e.g. Wu & Xue 2000; Xue & Wu 2000b; Zhang 2001) based on ROSAT observations of 45 clusters indicate that the density distributions in DM halos showing flat cores can be well fitted over the whole observed radius range by purely phenomenological models, e.g. the Burkert profile (Burkert 1995, 2000) and the TIS profile (the truncated isothermal sphere model, Shapiro et al. 1999). Therefore high resolution observations of the inner profiles of DM halos is key to constraining the DM model. In later chapters, the assembly of the central flatness or cusp of the DM distributions will be discussed. Since the global properties on cluster scales are almost independent of the inner slope, the mass can still be modeled by an NFW model at  $r > 0.1r_{\text{vir}}$  (e.g. Zhang 2001; Zhang et al. 2005c).

## 2.6 Cooling time

Once gas begins to fall into a DM halo, shocks will heat it up to the virial temperature. The gas releases the thermal energy to form stars by radiative cooling. It is useful to introduce three time-scales as follows. The cooling time scale is the time scale on which gas radiates thermal energy and falls into the gravitational potential,

$$t_c = -\frac{E}{\dot{E}} \propto \frac{\rho k_B T}{\mu \tilde{\Lambda}(T)}. \quad (2.45)$$

The dynamical time scale is the time scale to collapse to form a gas cloud with density  $\rho$ ,

$$t_{\text{dyn}} = 1/\sqrt{G\rho}. \quad (2.46)$$

## 2 Theoretical framework

---

These two time-scales together with the Hubble time  $\tau_H = H^{-1}$ , determine the collapse of a protocluster. If  $t_c > \tau_H$ , radiative cooling is not important. If  $\tau_H > t_c > t_{\text{dyn}}$ , gas can cool on a cosmological timescale, but it cools so slowly that the gas cloud can adjust its pressure distribution to maintain a relatively quiescent quasi-static collapse on a timescale  $t_c$ . If  $t_c < t_{\text{dyn}}$ , the cloud cools so rapidly that it loses pressure support and undergoes a rapid collapse on the free-fall timescale, accompanied by fragmentation to smaller and smaller scales as instabilities develop in the cloud. Recent X-ray observations of cooling flow clusters indicate AGN-ICM interaction (e.g. Fabian et al. 2003). Chandra observations of RXCJ1504+0248 show a central AGN heating of the cooling core in a self-regulated way to prevent a massive cooling of the gas at a very extreme condition (e.g. Böhringer et al. 2005b).

### 2.7 Self-similar model and empirical scaling relations

A self-similar model can be naturally deduced from the theoretical framework described above (e.g. Kaiser 1986, 1991). It is supported by simulations (e.g. Navarro et al. 1997) in hierarchical structure formation scenarios which show that the relative shape of all relaxed clusters is very similar. The characteristic density and scale of a halo should be correlated with the virial mass of the DM halo (e.g. Navarro et al. 1997).

The self-similar model is based on the following assumptions (e.g. Arnaud & Evrard 1999): (i) thermal Bremsstrahlung emissivity,  $\tilde{\Lambda}(T) \propto T^{1/2}$ , (ii) virial equilibrium,  $M \propto r_\Delta^3$  giving  $T \propto \sigma_r^2 \propto M/r_\Delta \propto M^{2/3}$ , (iii) self-similar halos, the characteristic density and scale of a halo correlated with the halo mass, and (iv) constant gas mass fraction. The assumptions give  $L \propto n_e^2 r_\Delta^3 T^{0.5} \propto f_b M^2 r_\Delta^{-3} T^{0.5} \propto T^2$  and  $M_{\text{gas}} \propto T^{3/2}$ . The thermal Bremsstrahlung model is applicable for massive clusters ( $> 5$  keV). The virial equilibrium has been checked by cosmological, gas dynamical simulations (e.g. Bryan & Norman 1998).

The mean cluster overdensity is the average density with respect to  $\rho_c(z) = \rho_{c0} E^2(z)$ . At redshift  $z$  within virial radius ( $r_{\text{vir}}$ ) the average overdensity ( $\Delta_{c,z}$ ) can be determined by the cosmological model. In the mass modeling, the virial radius,  $r_{\text{vir}}$ , is generally defined to be the radius where the overdensity is  $\Delta_{c,z}$ . The dependence on the evolution of the cosmological parameters gives the redshift evolution corrections of the correlations (e.g. Arnaud et al. 2002a; Ettori et al. 2004),

$$\begin{aligned} S_X \cdot E^3(z) (\Delta_{c,z}/\Delta_{c,0})^{3/2} &\propto f(T) , \\ S \cdot E^{4/3}(z) (\Delta_{c,z}/\Delta_{c,0})^{2/3} &\propto f(T) , \\ L \cdot E^{-1}(z) (\Delta_{c,z}/\Delta_{c,0})^{-0.5} &\propto f(T) , \\ M \cdot E(z) (\Delta_{c,z}/\Delta_{c,0})^{0.5} &\propto f(T) , \\ M_{\text{gas}} \cdot E(z) (\Delta_{c,z}/\Delta_{c,0})^{0.5} &\propto f(T) . \end{aligned}$$

The mass-observable correlations predicted by the self-similar model agree with the observations for massive galaxy clusters ( $> 5$  keV). While some observations deviate from the self-similar prediction and give rise to deeper concern (e.g.  $L \propto T^3$ , Arnaud & Evrard 1999). Many studies (e.g. Ponman et al. 1999; Borgani et al. 2004) suggested that heating and cooling plays an important role in low mass systems. In such a scenario, the thermal energy gained from the gravitational heating is proportional to  $M^{2/3}$ , while the heating related to galaxy population is optical luminosity dependent but almost mass independent.

## 2.7 Self-similar model and empirical scaling relations

---

Supernovae in early starbursts and AGN activities are considered to be the major source of heating. The radiative cooling effect is thus suppressed by heating. The heating and cooling processes increase the entropy in the cluster center, which means a lower ICM density according to hydrostatic equilibrium. The central entropy modified by the effect of heating and cooling gives  $S \propto 120 \text{ keV cm}^2 (T/\text{keV})^{0.65 \pm 0.05}$  as shown in the observations (e.g. Voit & Bryan 2001; Ponman et al. 2003).

This scenario can reproduce the empirical scaling of  $S_X \propto T^{1.38}$  of the X-ray surface brightness profiles (Arnaud & Evrard 1999). This scenario is also encouraged by recent, high resolution observations. For example, the XMM-Newton RGS data of A1835 (Peterson et al. 2001) and M87 (Böhringer et al. 2002b) lack of evidence of a cooler temperature phase of the ICM. The Chandra observations of the Perseus cluster show clear cavities in the region covered by the radio lobes (Fabian et al. 2003). Deep X-ray observations of those regions reveal sound waves or weak shock waves produced by the interaction of the expanding radio bubbles and the ambient ICM (Fabian et al. 2003). A rough estimate from the X-ray observations (e.g. Fabian et al. 2003) shows that the values of the energy injection by AGNs in galaxy clusters are in the range of  $10^{44}$ – $10^{45} \text{ erg s}^{-1}$ , which are sufficient to make up the energy loss due to radiative cooling in the the cooling cores. The XMM-Newton spectra of M87 display lines of several heavy elements (Böhringer et al. 2001b). This reveals the heavy element enrichment, involving mostly Fe and Si, which agrees with the yields of type Ia and type II supernovae (Böhringer et al. 2001b).

Recent studies based on the Chandra observations imply that massive galaxy clusters ( $> 5 \text{ keV}$ ) are well described by a self-similar model up to redshift 1.2 (e.g. Ettori et al. 2004; Vikhlinin et al. 2005a).

## 2 Theoretical framework

---

# 3 Scientific motivation

## Abstract

In this chapter, I give a complete view of the scientific rationale, basic goals and main approaches of this work and the current status in this field.

## 3.1 Scientific rationale

Observational cosmology is one of the most important fields of astrophysical studies. Various objects observed in various wavelengths have been used to study all kinds of astrophysical mechanisms and to extract cosmological parameters. Two main possibilities to test a cosmological model are listed as follows. One is to test the expansion history of the Universe and thus to determine the metric using the luminosity distance and/or volume. The other is to test the gravitational growth of the fluctuation using the evolution of the cluster number density (e.g. Schuecker et al. 2003). X-ray observations of massive galaxy clusters provide a unique means for both approaches, where the determination of the gravitational mass of a cluster plays a central role. A recent review is given in Voit (2005).

### 3.1.1 Cluster total mass and gas mass fraction

The mass of a cluster can be determined in a variety of ways using: (i) the X-ray gas density and temperature distributions under the assumptions of hydrostatic equilibrium and spherical symmetry, (ii) the velocity dispersion of cluster galaxies, (iii) the distortion of background galaxies caused by the gravitational lensing effect, and (iv) the SZ effect (Sunyaev & Zeldovich 1972). The methods to measure cluster mass using velocity dispersion of cluster galaxies and gravitational lensing are improving (Girardi et al. 1998). However, the cluster mass measured from the precise ICM temperature and density profiles using X-ray observations is still the most reliable (Pierpaoli et al. 2001). A precise determination of the cluster mass and gas mass fraction is important for the study of the X-ray scaling relations and correlations, and to understand their intrinsic scatter.

An accurate determination of the total mass is key to the applications in astrophysical and cosmological studies. Voit (2005) pointed out that all correlations between cluster mass and observables evolve with redshift, partly because the definition of total mass is pinned to the critical density and partly due to galaxy-formation physics. Pierpaoli et al. (2001) investigated the relations between various definitions of cluster mass as a function of the normalized cosmic matter density ( $\Omega_m$ ) of the Universe (Fig. 3.1). They confirmed that the mass definitions of massive systems (e.g. rich clusters) can be related and converted

### 3 Scientific motivation

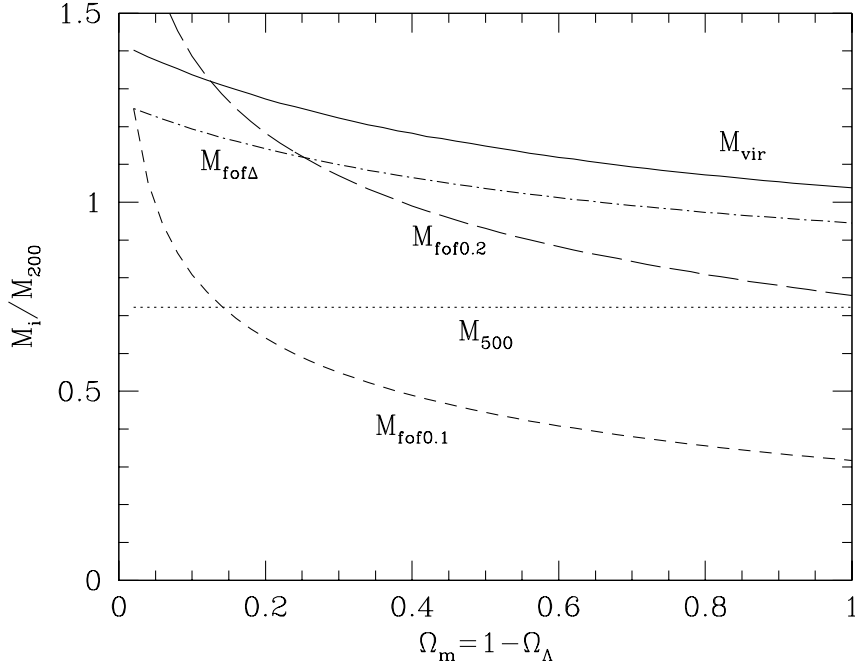


**Figure 3.1:** Relations between various definitions of the mass of a halo as a function of  $\Omega_m$  assuming the halo density profile follows the Navarro-Frenk-White (NFW, see Eq. 2.42) model (Navarro et al. 1997) with concentration parameter  $c = 5$  (Pierpaoli et al. 2001).  $M_{\text{vir}}$  is the cluster virial mass,  $M_{200}$  the cluster total mass at the radius with overdensity 200,  $M_{500}$  the cluster total mass at the radius with overdensity 500.  $M_{\text{fof}\Delta}$ ,  $M_{\text{fof}0.2}$ , and  $M_{\text{fof}0.1}$  are the cluster masses defined by using different linking lengths of the friend-of-friend (fof) method in numerical simulations.

simply by a constant factor. For low mass systems, such as groups, they concluded that the definition of mass is a significant source of uncertainty in the cosmological applications.

Clusters of galaxies provide the only means to approach a complete accounting of intergalactic baryons, their thermal state, and their metal enrichment (e.g. Voit 2005). Therefore X-ray observations of the ICM provide a unique approach to study the cooling and feedback processes that govern galaxy formation. How the thermodynamic properties of today's clusters are linked to the physics of the intergalactic baryons at the epoch of galaxy formation is key to the knowledge of galaxy formation in the ICM (e.g. Voit 2005).

The gas mass fraction ( $f_{\text{gas}}$ ) and its evolution provides a direct and complementary probe of the matter composition of the Universe since the baryons in galaxy clusters reside mostly in hot gas together with a fraction (15%  $f_{\text{gas}}$ ) in stars as implied by simulations (e.g. Eke et al. 1998; Kravtsov et al. 2005). The normalized cosmic matter density ( $\Omega_m$ ) can be determined from the baryon fraction,  $f_b = f_{\text{gas}} + f_{\text{gal}}$ , in which a contribution from stars in galaxies is given by  $f_{\text{gal}} = 0.02 \pm 0.01 h_{50}^{-1}$  (e.g. White et al. 1993). The gas mass fraction thus provides a robust and complementary method to the other approaches to constrain the normalized cosmic matter density ( $\Omega_m$ ). Vikhlinin et al. (2005b) found that the gas mass fraction and temperature profiles exhibit significant scatter and trends with mass in

the inner region ( $r < 0.1r_{500}$ ). They also found that the gas mass fraction dependence on mass becomes weaker and its values closer to a universal value at larger radii, in particular, in spherical shells  $r_{2500} < r < r_{500}$ . Therefore, it is very important to push the cluster mass and thus gas mass fraction measurements to large radii above  $r_{2500}$ .

#### 3.1.2 Scaling relations and correlations

Two approaches can be used to investigate the cluster structure and thermodynamics and the evolution of the ICM X-ray properties. One is to study the self-similar scaling relations by investigating the scaled distributions of various observables of the ICM. The other is to study the correlations of the cluster mass with various observational parameters such as ICM temperature, X-ray luminosity, metallicity, and gas mass fraction.

Self-similar scaling relations of the ICM properties, such as the temperature, density, and entropy of massive clusters, are predicted by the hierarchical structure formation model (e.g. Navarro et al. 1997). In the hierarchical scenario, less massive halos form at earlier epochs and are thus denser than massive halos. The low mass halos subsequently merge to form higher mass systems. As indicated by simulations, the DM distributions in galaxy clusters have a universal form, e.g. the NFW model (Navarro et al. 1997) and the extended NFW (ext-NFW, see Eq. 2.44) model (e.g. Navarro et al. 2004). The characteristic density and scale of a halo should be correlated with the virial mass of the DM halo (e.g. Navarro et al. 1996, 1997, 2004; Morre et al. 1999; Diemand et al. 2004).

The correlations of the various observational parameters are the most important input in modeling the galaxy cluster population and understanding the cluster formation process. Three important correlations are: X-ray luminosity–temperature ( $L$ – $T$ ), luminosity–mass ( $L$ – $M$ ), and mass–temperature ( $M$ – $T$ ) relations. The deviation of the correlations from the prediction of the self-similar model reflects non-gravitational effects. A detailed study of the correlations and their scatter, in combination with the study of the enrichment of the ICM by heavy elements, sheds light on the star formation history and the effect of the galaxy population (e.g. Voit 2005). The intrinsic scatter, which is due to the multi-variate dependencies and random processes, has been investigated to understand the efficiency of the correlations and the bias caused by the variety of cluster morphologies, e.g. mergers. Additionally,  $N$ -body/hydrodynamical simulations can be used to reproduce the observational results to reveal the relative effects of various underlying processes.

A better understanding of the scaling relations and correlations of the observables is of prime importance for galaxy clusters as a unique means to study the large-scale structure (LSS) and to constrain the cosmological parameters.

Voit (2005) gave an example of how mass–observable evolution affects observations of the mass function evolution by considering its effects on X-ray surveys (Fig. 3.2). Two cold DM (CDM) models were used in his work:  $\Lambda$ CDM<sup>1</sup> ( $\Omega_m = 0.3$ ,  $\Omega_\Lambda = 0.7$ ,  $w = -1$ ,

---

<sup>1</sup>It is a standard paradigm, in which the Universe is determined by a normalized cosmic matter density term ( $\Omega_m$ ) and a normalized cosmological constant term ( $\Omega_\Lambda$ ) as shown in Eq. 2.6.  $w = p/\rho c^2$  describes the phenomenological ratio of the pressure of the dark energy component and rest energy density.  $w = -1$  corresponds to the Einstein's cosmological constant.  $\sigma_8$  is the variance derived from the distribution of normal galaxies in spheres of radius  $R = 8h^{-1}$  Mpc.

### 3 Scientific motivation

---

$\sigma_8 = 0.9$ ) and  $\tau\text{CDM}^2$  ( $\Omega_m = 1.0$ ,  $\Gamma = 0.21$ ,  $\sigma_8 = 0.5$ ) for comparison. Voit (2005) found that: (1) The evolution of the mass function is more pronounced in  $\tau\text{CDM}$  than in  $\Lambda\text{CDM}$  because it is sensitive to the current matter density; (2) At higher-redshifts, the evolution of the mass function is weaker as a function of the ICM temperature because clusters of a given mass have higher temperatures at higher redshifts; (3) The strong  $L$ – $T$  evolution (e.g.  $L \propto T^3(1+z)^{1.5}$  as found in Kotov & Vikhlinin 2005) shifts the cluster number density distributions in the  $\Lambda\text{CDM}$  case nearly on top of one another at  $L_X \approx 10^{44} h_{70}^{-1} \text{ erg s}^{-1}$ , roughly compensating for all of the evolution in the underlying mass function. Therefore, Voit (2005) concluded that the evolution in the  $M$ – $T$  relation weakens the observed amount of cluster evolution when the cluster number density is plotted as a function of temperature.

The uncertainty in the value of the normalization of the  $M$ – $T$  relation is the most important issue to obtain a precise cosmological constraint, especially for  $\sigma_8$ , using the cluster mass function and its evolution. Pierpaoli et al. (2001) found the uncertainty in  $\sigma_8$  is dominated by the normalization of the  $M$ – $T$  relation. Pierpaoli et al. (2001, 2003) investigated the dependence of the determined  $\sigma_8$  on the normalization ( $T_*$  in Pierpaoli et al 2003) of the  $M$ – $T$  relation. They concluded that a better estimate of the  $M$ – $T$  relation, especially its normalization, would greatly reduce the errors on  $\sigma_8$  as shown in Fig. 3.3. Therefore, a more precise  $M$ – $T$  relation for X-ray clusters contributes the major improvement in the application of galaxy clusters to constrain cosmological parameters. Henry (2004) found that the systematic errors are larger than the statistical errors for  $\sigma_8$  with his sample. Henry (2004) thus concluded that the errors of the measured value for  $\sigma_8$  depend on the details of the marginalization over the normalization of the  $M$ – $T$  relation.

As demonstrated in the above examples (e.g. Pierpaoli et al. 2001, 2003; Henry 2004; Voit 2005), it is very important to constrain the mass–observable relations and their evolution based on precisely measured observables.

#### 3.1.3 Cluster number density

The gravitational growth of fluctuations, which can be precisely measured through the cluster number density, is a sensitive test of the values of the density parameter (Press & Schechter 1974, PS; Peebles 1980).  $N$ -body simulations (e.g. Governate et al. 1999) found non-negligible deviations from the PS mass function. Sheth & Tormen (1999) obtained a better fit to the mass function in  $N$ -body simulations, which is called the ST mass function. Jenkins et al. (2001) confirmed that the ST mass function is indeed a good fit providing that halos are defined at the same density contrast relative to the mean in all cosmological models. Jenkins et al. (2001) found that the ST mass function overestimates the number density of extremely rare objects, and gave a more accurate fitting formula, which is called the J01 mass function. The detailed statistical basis is described in Chapter 2. Pierpaoli et al. (2001) found that the uncertainty of the  $\sigma_8$  estimate is reduced by 4–8% (depending on  $\Omega_m$ ) using the ST mass function or the J01 mass function, rather than the PS mass function.

---

<sup>2</sup>It is an alternative cosmological model for comparison which is composed of photons, baryons, CDM and massless neutrinos.  $\Gamma$  is the shape parameter of the power spectrum considering an adiabatic CDM model with a mixture of baryons.



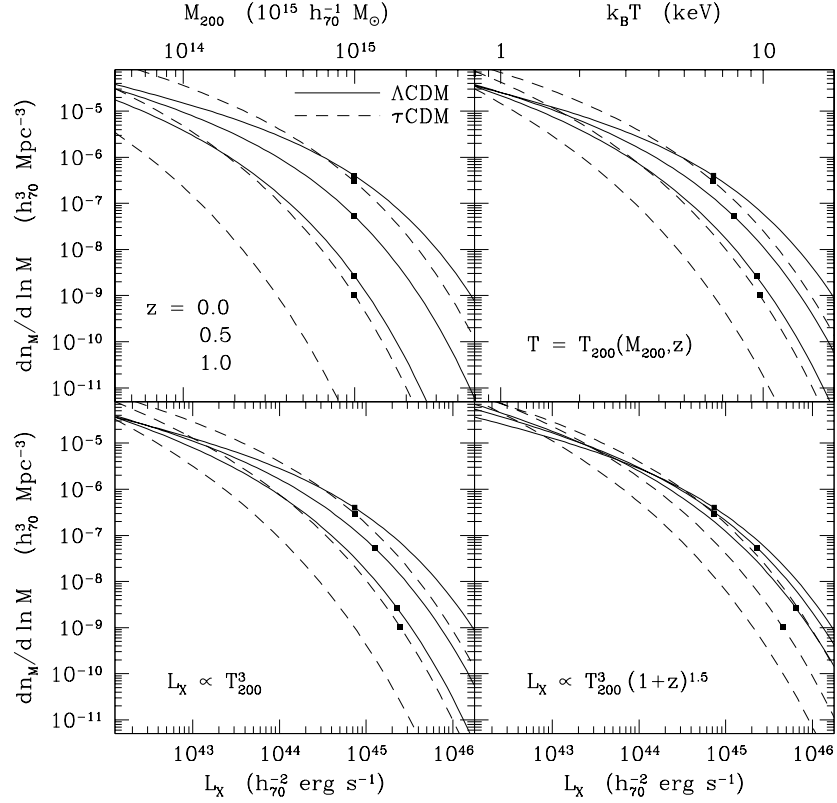


**Figure 3.2:** Evolution of the cluster mass function displayed as a function of mass and alternatively as a function of temperature and luminosity (Voit 2005). Evolution of the mass function, shown at the upper left, is far more pronounced in  $\tau$ CDM (dashed lines) than in  $\Lambda$ CDM (solid lines) because it is so sensitive to the current matter density. Each set of three lines shows the differential mass function  $dn_M/d \ln M$  at  $z = 0, 0.5,$  and  $1.0,$  from top to bottom, and black squares show the value of the mass function at a fiducial mass of  $10^{15} h_{70}^{-1} M_{\odot}$ . The upper right panel shows the same mass functions plotted against temperature, assuming  $T = T_{200}(M_{200}, z)$ . Notice that the higher-redshift curves have shifted to the right, weakening the evolution in temperature space, because clusters of a given mass have higher temperatures at higher redshifts. In order to convert these curves to temperature functions, one would need to convolve them with the scatter in the  $M$ - $T$  relation and to multiply by  $d \ln M / d \ln T \approx 1.5$ . The lower two panels show these same curves as a function of luminosity, assuming  $L_X = (6 \times 10^{44} h_{70}^{-2} \text{ erg s}^{-1}) T_{200}^3$  at  $z = 0$  and two different redshift dependences of the  $L$ - $T$  relation. In the case without  $L$ - $T$  evolution on the left-hand side, the curves are just re-labeled versions of the ones in the upper-right panel. However, the strong  $L$ - $T$  evolution in the right-hand panel ( $L \propto T^3(1+z)^{1.5}$ ) shifts the three curves in the  $\Lambda$ CDM case nearly on top of one another at  $L_X \approx 10^{44} h_{70}^{-1} \text{ erg s}^{-1}$ . Convoluting these curves with the dispersion in the  $M$ - $L$  relation and multiplying by  $d \ln M / d \ln L \approx 0.5$  converts them to luminosity functions.

### 3 Scientific motivation

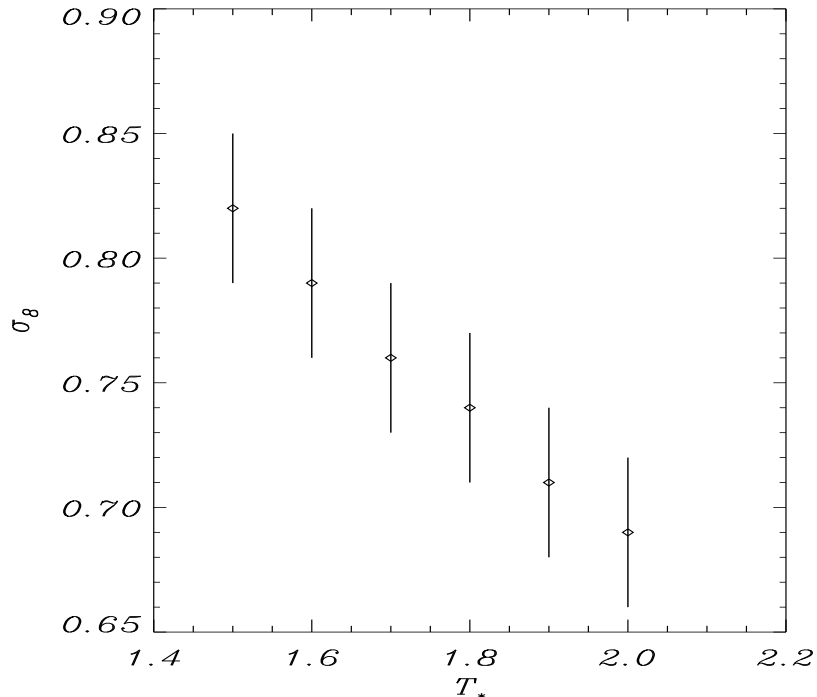


**Figure 3.3:** The dependence of the derived  $\sigma_8$  on the value of the  $M$ - $T$  normalization  $T_*$  assumed (Pierpaoli et al. 2003). Here the matter density is fixed to  $\Omega_m = 0.3$  and Hubble constant  $H_0 = 70 \text{ km s}^{-1} \text{ Mpc}^{-1}$ . Error bars are  $1\sigma$  assuming an intrinsic scatter of 10% in  $T_*$ . The choice of  $T_*$  probably causes the most important differences between discrepant values of  $\sigma_8$  in the literature.

Galaxy clusters are good tracers of LSS. One can measure the amplitude of the matter density fluctuations on scales of 5–10 Mpc, where the growth of density fluctuations is almost linear and can thus be predicted from the normalized cosmic matter density ( $\Omega_m$ ). Therefore, the evolution of the temperature function (also mass function or luminosity function) can be used to constrain  $\Omega_m$  as shown in Ikebe et al. (2002) and Henry (1997, 2004). To perform a precise constraint on  $\Omega_m$ , one has to: (i) probe the strong evolutionary effect along a broad redshift baseline, and (ii) take the hottest end of the temperature function which shows the most dramatic evolutionary effect. As the largest virialized systems, massive galaxy clusters therefore provide one of the most efficient ways to study the evolution of the growth of LSS. Evaluated at  $\Omega_m = 0.3$ , the low value of the parameter  $\sigma_8$  can be measured consistently (e.g. Pierpaoli et al. 2001).

If the baryon fractions were completely independent of cluster mass and radius, the baryon mass inside a radius containing a mean baryon density of 200 times of the critical density would directly give  $M_{200}$  (e.g. Voit 2005). The cluster mass function could then be determined by measuring the baryon mass function within a given scale radius (e.g. Vikhlinin et al. 2003). Voit (2005) reviewed the previous studies (e.g. Mohr et al. 1999) and found that the baryon fraction is not quite constant in low mass clusters due to the same galaxy formation effects that shift the  $M$ - $T$  and  $L$ - $T$  relations. The baryon fraction

measured in clusters above 6 keV is statistically consistent with a constant value (e.g. Mohr et al. 1999; Reiprich 2001). Therefore, the baryon mass function can also be used to constrain the cosmological parameters (e.g. Vikhlinin et al. 2003)

Haiman et al. (2005) pointed out that the amount and nature of dark energy can be tightly constrained with the uncertainties of  $\Omega_{\text{DE}}^3$  and  $w$  of 0.0067 and 0.49, respectively, by measuring the spatial correlations and evolution of a galaxy cluster survey, consisting of  $\sim 100,000$  clusters in the redshift range of  $0 < z \lesssim 1.5$ .

### 3.1.4 Complexity in galaxy clusters

Since galaxy clusters are dynamically young objects, some of them show quite complex morphology. Based on the Einstein X-ray observations of around 200 clusters, Forman & Jones (1991) classified galaxy clusters into several broad groups by morphology, such as “single”, “double”, “complex”, “off-center” etc. Schuecker et al. (2001) found that  $\sim 50\%$  galaxy clusters show significant deviation from perfect symmetry based on more than 450 nearby galaxy clusters in the ROSAT X-ray All-Sky Survey (RASS, Voges et al. 1999). The systematic errors in estimating cluster mass and gas mass fraction caused by mergers are as important as possible selection effects in cluster survey studies (e.g. Böhringer et al. 2004a).

Significant amounts of mass infalling in the outskirts makes the slope of the electron density and thus the surface brightness ( $S_X \propto n_e^2$ ) steeper than the generally adopted  $\beta$ -model ( $\beta \sim 2/3$ ). This might distort hydrostatic equilibrium and introduce a systematic error in the virial mass measurements (e.g. Horner 2001).

An accurate mass determination of a galaxy cluster is one of the most important observational task. In general, X-ray mass measurements are more reliable than optical estimates, which is a complementary study of the mass distribution measured by gravitational lensing (e.g. Soucail et al. 2000; Böhringer et al. 2000). The results of some very relaxed clusters show a good agreement between the X-ray and lensing masses. However, several lensing clusters show a significant discrepancy, e.g. CL0024+17, A1689 and A2218. A hint of the explanation for this interesting mass discrepancy came from the detailed analysis of the galaxy dynamics of these clusters. Based on  $\sim 300$  redshifts of galaxy members of CL0024+17, Czoske et al. (2001, 2002) found that the line-of-sight velocity distribution is not that of a relaxed cluster and is at least bimodal. They also demonstrated that the redshifts can approximately be explained by a line-of-sight merger of two systems with a mass ratio of the order of 1:2. In addition, the weak lensing analysis shows a mass distribution with substructure, modeled as a bimodal distribution of two systems with slightly different central positions in the plane of the sky (Kneib et al. 2003). Coia et al. (2003) found that the infrared observations imply significant star forming activities with star formation rates (SFRs) one to two orders of magnitude higher than those computed from the optical. The underestimation of the SFRs in the optical is due to absorption by dust (Coia et al. 2003). Therefore, a deeper X-ray observation of the cluster center with a high spatial resolution would shed new light on such enigmatic systems to understand the complex structure and most probably solve the mass discrepancy problem.

---

<sup>3</sup>Normalized dark energy density

### 3 Scientific motivation

---

#### 3.1.5 Summary

To approach the first three tasks, one has to perform a systematic study of cluster structure, scaling relations and correlations on the basis of high spatial resolution and spectral resolution X-ray observations of a statistically well selected cluster sample. To approach the fourth task, one has to make use of as many independent methods as possible to investigate those known merger clusters which show a quite complicated structure.

### 3.2 Current status

With the recent improvements in the spatial resolution and spectral resolution of X-ray observations, a lot of progress has been made for the X-ray studies of galaxy clusters.

#### 3.2.1 Cluster total mass and gas mass fraction

The recent WMAP measurements, the normalized Hubble constant  $h = 0.71_{-0.03}^{+0.04}$ , the normalized baryon density  $\Omega_b = 0.022 \pm 0.001 h^{-2}$  and the normalized cosmic matter density  $\Omega_m = 0.132_{-0.009}^{+0.008} h^{-2}$  (e.g. Spergel et al. 2003) give a universal baryon fraction of  $f_b = \Omega_b/\Omega_m = 0.167 \pm 0.014$ . An average gas mass fraction of  $\sim 0.11$  has been found for many massive clusters showing temperatures greater than 5 keV (e.g. Mohr et al. 1999). Allen et al. (2002) analyzed Chandra observations of 7 clusters yielding  $f_{\text{gas}}$  in a range of 0.105–0.138  $h_{70}^{-3/2}$ . Sanderson et al. (2003) obtained an average gas mass fraction of  $f_{\text{gas}} = 0.13 \pm 0.01 h_{70}^{-3/2}$  based on ASCA/GIS, ASCA/SIS and ROSAT/PSPC observations of 66 clusters. Ettori et al. (2002a) obtained a similar result based on BeppoSAX observations of 22 nearby clusters. Pratt & Arnaud (2002) measured the gas mass fraction for A1413 at redshift  $z = 0.143$  based on XMM-Newton observations yielding  $f_{\text{gas}} \sim 0.12 h_{70}^{-3/2}$ .

Chandra observations indicate that the gas mass fraction within a given radius asymptotically approaches  $(0.113 \pm 0.005)h_{70}^{-3/2}$  at a radius with overdensity of 2500 in relaxed, massive clusters (Allen et al. 2002). The correction for the baryons in stars is approximately  $0.16h_{70}^{1/2}$  times that of the gas mass fraction, and yields an overall baryon fraction in clusters of  $f_b = 0.13$  for  $h_{70} = 1$ . The baryon fraction in galaxy clusters is expected to be similar to the global cosmic baryon fraction in the Universe (e.g. White et al. 1993). The normalized cosmic baryon density is thus  $\Omega_b = 0.045 h_{70}^{-2}$  which is consistent with the abundances of light elements (e.g. Burles et al. 2001). Allen et al. (2002) found  $\Omega_m = 0.30_{-0.03}^{+0.04}$  considering the uncertainties in  $\Omega_b$  and  $H_0$ , which agrees with the WMAP results giving  $\Omega_m \approx 0.3$  (Spergel et al. 2003). Ettori et al. (2003) analyzed 8 distant galaxy clusters based on the Chandra data, and obtained: (i)  $w < -0.49$ , and (ii)  $\Omega_m = 0.34_{-0.05}^{+0.07}$  and  $\Omega_\Lambda = 1.30_{-1.09}^{+0.44}$  for  $w = -1$ .

#### 3.2.2 Scaling relations and correlations

A self-similar scaling of the distribution of the ICM properties such as temperature, density, entropy, pressure and total mass of massive clusters ( $> 5$  keV) is indicated by ROSAT, ASCA, Chandra and XMM-Newton observations (e.g. Markevitch 1998; Markevitch et al. 1998; Vikhlinin et al. 1999, 2005a; Arnaud et al. 2002a; Reiprich & Böhringer 2002; Ota

**Table 3.1:** Power law,  $Y = Y_0 X^\alpha$  in units of  $\text{erg s}^{-1}$  or  $M_\odot$ , parameterized correlations in literature.

$Y-X$	$Y_0$	$\alpha$	Reference	Method
$L_X^{\text{bol}}-T$	$10^{43.05 \pm 0.08} h_{50}^{-2}$	$2.62 \pm 0.10$	Edge & Stewart 91	OLS <sup>c</sup>
$L_X^{\text{bol}}-T$	$10^{43.01 \pm 0.29} h_{50}^{-2}$	$2.7 \pm 0.4$	Henry & Arnaud 91	OLS
$L_X^{\text{bol}}-T$	$10^{42.68 \pm 0.08} h_{50}^{-2}$	$2.98 \pm 0.11$	White et al. 97	ORD
$L_X^{\text{bol}}-T$	$10^{42.43 \pm 0.04} h_{100}^{-2}$	$2.64 \pm 0.27$	Markevitch 98 <sup>a</sup>	BCES <sup>d</sup>
$L_X^{\text{bol}}-T$	$10^{42.82 \pm 0.03} h_{50}^{-2}$	$2.88 \pm 0.15$	Arnaud & Evrard 99	OLS
$L_X^{\text{bol}}-T$	$10^{43.08 \pm 0.05} h_{50}^{-2}$	$2.72 \pm 0.05$	Wu et al. 99	ORD
$L_X^{\text{bol}}-T$	$10^{42.97 \pm 0.07} h_{50}^{-2}$	$2.79 \pm 0.08$	Xue & Wu 00a	ORD
$L_X^{\text{bol}}-T$	$10^{42.73 \pm 0.10} h_{50}^{-2}$	$2.84 \pm 0.13$	Horner 01	BCES
$L_X^{\text{bol}}-T$	$10^{42.85 \pm 0.09} h_{50}^{-2}$	$2.98 \pm 0.12$	Reiprich & Böhringer 02	BCES
$L_{X,500}^{\text{bol}}-T$	$10^{43.00 \pm 0.11} h_{70}^{-2}$	$2.5 \pm 0.1$	Borgani et al. 2004 <sup>b</sup>	OLS
$L_X^{0.1-2.4}-T$	$10^{42.19 \pm 0.27} h_{100}^{-2}$	$2.44 \pm 0.39$	Ikebe et al. 02	OLS
$L_X^{0.1-2.4}-T$	$10^{42.52 \pm 0.04} h_{100}^{-2}$	$2.10 \pm 0.24$	Markevitch 98	BCES
$L_X^{0.1-2.4}-T$	$10^{42.79 \pm 0.09} h_{50}^{-2}$	$2.60 \pm 0.13$	Reiprich & Böhringer 02	BCES
$L_X^{\text{bol}}-M_{200}$	$10^{17.95 \pm 1.25} h_{50}^{-2}$	$1.81 \pm 0.08$	Reiprich & Böhringer 02	BCES
$L_X^{\text{bol}}-M_{200}$	$10^{14.51 \pm 0.22} h_{70}^{-2}$	$2.01 \pm 0.20$	Popesso et al. 05	ORD
$L_X^{0.1-2.4}-M_{500}$	$10^{25.19 \pm 0.10} h_{70}^{-2}$	$1.30 \pm 0.12$	Popesso et al. 05	ORD
$L_X^{0.1-2.4}-M_{200}$	$10^{20.73 \pm 0.24} h_{70}^{-2}$	$1.58 \pm 0.23$	Popesso et al. 05	ORD
$M_{1000}-T$	$10^{13.30 \pm 0.02} h_{50}^{-1}$	$1.79 \pm 0.05$	Nevalainen et al. 00	—
$M_{500}-T$	$10^{13.63 \pm 0.08} h_{50}^{-1}$	$1.48 \pm 0.10$	Finoguenov et al. 01b	BCES
$M_{500}-T$	$10^{13.40 \pm 0.02} h_{70}^{-1}$	$1.59 \pm 0.05$	Borgani et al. 04	OLS
$M_{200}-T$	$10^{13.59 \pm 0.07} h_{50}^{-1}$	$1.48 \pm 0.12$	Horner 01	BCES
$M_{200}^\beta-T$	$10^{13.760 \pm 0.003} h_{50}^{-1}$	$1.60 \pm 0.04$	Xu et al. 01	ODR
$M_{200}^{\text{NFW}}-T$	$10^{13.535 \pm 0.003} h_{50}^{-1}$	$1.81 \pm 0.04$	Xu et al. 01	ODR
$M_{200}-T$	$10^{13.77 \pm 0.03} h_{50}^{-1}$	$1.65 \pm 0.05$	Reiprich & Böhringer 02	BCES
$M_{200}-T$	$10^{13.37 \pm 0.03} h_{70}^{-1}$	$1.84 \pm 0.06$	Sanderson et al. 03	ODR
$M_{\text{gas},500}-T$	$10^{12.26 \pm 0.05} h_{70}^{-1}$	$1.80 \pm 0.08$	Borgani et al. 04	OLS

<sup>a</sup> Cooling cores excluded; <sup>b</sup> Simulations; <sup>c</sup> Ordinary Least Squares method (Akritas & Bershadsky 1996, OLS); <sup>d</sup> Bivariate Correlated Errors and intrinsic Scatter method (Isobe et al. 1990, BCES).

& Mitsuda 2005; Pratt & Arnaud 2005) and simulations (e.g. Borgani 2004; Borgani et al. 2004; Kay 2004; Kay et al. 2004).

As indicated by the hierarchical structure formation model, observations show tight correlations between the characteristic density contrast and virial mass ( $\delta_c-M_{\text{vir}}$ ) and between the concentration parameter and virial mass ( $c_{\text{vir}}-M_{\text{vir}}$ ). Cheng & Wu (2001) derived the best fits of  $\delta_c = 10^{19.44 \pm 2.65} (M_{\text{vir}}/M_\odot)^{-1.06 \pm 0.07}$  and  $c_{\text{vir}} = 10^{7.34 \pm 1.10} (M_{\text{vir}}/M_\odot)^{-0.45 \pm 0.07}$ .

Some of the main correlations, such as  $L-T$  (e.g. Isobe et al. 1990; Markevitch 1998; Arnaud & Evrard 1999; Ikebe et al. 2002; Reiprich & Böhringer 2002),  $L-M$  (e.g. Reiprich & Böhringer 2002; Popesso et al. 2005),  $M-T$  (e.g. Nevalainen et al. 2000; Finoguenov et al. 2001b; Neumann & Arnaud 2001; Xu et al. 2001; Horner 2001; Reiprich & Böhringer 2002; Sanderson et al. 2003; Pierpaoli et al. 2001, 2003), and luminosity–metallicity ( $L-Z$ , e.g. Garnett 2002), have been intensively studied for comparison of observations with theory and simulations. Most of the published correlations have been collected in Table 3.1.

The logarithmic uncertainty of the  $L-T$  relation is in the range of 0.03–0.29, in which

### 3 Scientific motivation

---

the exclusion of cooling cores can efficiently reduce the uncertainty to 0.03–0.05. However, Horner (2001) pointed out that more luminous clusters for a given temperature have higher central gas densities and smaller core radii, which may indicate a deeper gravitational potential in clusters. Horner (2001) concluded that any interpretation of the scatter in the  $L$ – $T$  relation in terms of cooling flows should be done with caution. The logarithmic uncertainty of the  $L$ – $M$  relation is in the range of 0.10–1.25, which is relatively large compared to the  $L$ – $T$  relation. The logarithmic uncertainty of the  $M$ – $T$  relation is in the range of 0.003–0.080. The  $M$ – $T$  relation shows the least scatter among the correlations.

#### 3.2.3 Cluster number density

Henry (1997) was the first to find an indication for evolution of the X-ray temperature function. The evolution of the temperature/mass/luminosity function has been intensively studied but with a pronounced dispersion in the indicated values of  $\Omega_m$  (e.g. Rosati et al. 1998, 2002; Vikhlinin et al. 1999; Borgani et al. 2001; Reiprich & Böhringer 2002). Schuecker et al. (2003) obtained  $0.28 \leq \Omega_m \leq 0.37$  and  $0.56 \leq \sigma_8 \leq 0.80$  using the REFLEX galaxy cluster survey. Schuecker (2005) found that the overlap of the results of Borgani et al. (2001), Schuecker et al. (2003) and Allen et al. (2003) gives  $\Omega_m = 0.31 \pm 0.03$ .

Shimizu et al. (2003) derived the  $M$ – $T$  relation from the observed  $L$ – $T$  relation and X-ray temperature function, and suggested  $\sigma_8$  in the range of 0.7–0.8. Henry (2004) reviewed the previous studies (e.g. Henry 1997; Pierpaoli et al. 2001, 2003; Ikebe et al. 2002; Reiprich & Böhringer 2002; Rosati et al. 2002; Bahcall et al. 2003; Allen et al. 2003; Schuecker et al. 2003) regarding the determination of  $\sigma_8$  using cluster number density, which give the derived values of  $\sigma_8$  in a range of 0.5–1.0. Schuecker (2005) derived a comparatively low normalization of  $\sigma_8 = 0.76 \pm 0.10$  by summarizing many observations. Vikhlinin et al. (2003) inferred a cluster mass function from the baryon mass function and derived  $\sigma_8 = 0.72 \pm 0.04$  assuming  $\Omega_m = 0.3$ ,  $\Omega_\Lambda = 0.7$  and  $H_0 = 71 \text{ km s}^{-1} \text{ Mpc}^{-1}$ . Voit (2005) pointed out that this value of  $\sigma_8$  agrees with those derived from the observationally calibrated  $M$ – $T$  and  $M$ – $L$  relations although it does not explicitly rely on those calibrations. Based on the X-ray temperatures for the Extended Medium-Sensitivity Survey (EMSS) high-redshift cluster sample, Henry (2004) measured the normalization of the mass fluctuation power spectrum and derived  $\sigma_8 = 0.66 \pm 0.16$  (68% confidence).

#### 3.2.4 Complexity in galaxy clusters

Mohr et al. (1995) presented a detailed study of obvious substructures of 7 clusters based on the X-ray and optical observations. Systematic studies (e.g. Schuecker et al. 2001; Feretti & Venturi 2002) show a high substructure occurrence rate which ranges from 20% to 80%, making it difficult to precisely determine the total mass. With the high spatial resolution (Fig. 4.1) of XMM-Newton ( $\sim 15''$ ) and Chandra (down to arcsecond scales), the substructure can be better defined by 2-dimensional map studies (e.g. Briel et al. 2004; Finoguenov et al. 2005). The cluster mass can thus be measured more precisely if one understands how to correct for the effects of the substructure. Forman et al. (2003) gave a detailed review of the high angular resolution Chandra view of mergers, mixing and bubbling in galaxy clusters. New phenomena observed with XMM-Newton and Chandra provide a unique

opportunity to understand the cluster morphology and its evolution. Jeltema et al. (2005) made use of Chandra archival data to quantify the evolution of the cluster morphology and confirmed the previous work (e.g. Randall et al. 2002) regarding the large deviations in cluster luminosity, temperature, velocity dispersion caused by mergers.

Vikhlinin et al. (1999) found a mild trend for  $\beta$  increasing as a function of the cluster temperature, which gives  $\beta \sim 0.80$  for clusters around 10 keV. As an indication of mass infalling, Bahcall (1999) found that the electron number density scales as  $n_e \propto r^{-2.4}$  at large radii.

Many studies have been performed to investigate the complex structure of individual clusters. RXCJ0658.5–5556 (also called 1E0657–56) is a classic supersonic merger cluster and was found by Tucker et al. (1995). Markevitch et al. (2002, 2004) analyzed this cluster in detail and found a dense core moving to the west of the cluster center. Vikhlinin et al. (2001a, 2001b) performed a study of A3667 and derived the pressure of the ICM on the moving cold front from the gas density and temperature.

For a few known clusters, mergers happened along the line-of-sight, which make the situation even more complicated. A1689 has been observed by ASCA (Benitez et al. 2002), Chandra (Xue & Wu 2002) and XMM-Newton (Andersson et al. 2004), which shows a pronounced discrepancy between the X-ray mass and lensing mass. Oguri et al. (2005) suggested that A1689 has a triaxial DM halo. Pratt et al. (2005) analyzed the XMM-Newton observations of A2218, and confirmed the observed substructure in the optical, suggesting a line-of-sight merger. Similar to A1689 (Oguri et al. 2005) and A2218 (Girardi et al. 1997; Pratt et al. 2005), the apparent discrepancy between the X-ray and gravitational lensing determined masses of CL0024+17 (Soucail et al. 2000; Böhringer et al. 2000; Ota et al. 2004) is most probably due to a line-of-sight merger of two almost comparable subsystems (Czoske 2001, 2002). The line-of-sight orientation makes it difficult to reveal the merger structure in the X-ray data, but on the other hand it enhances the probability of finding strong lensing features. As demonstrated in the following work, the deviation of the X-ray properties, such as temperature and luminosity, and their correlations can also be used to indicate the complex structure.

### 3.3 Major goals

To use clusters of galaxies as sensitive probes to test cosmological models, one needs a better knowledge of the cluster structure, total mass, gas mass fraction, and scaling relations for most clusters, and a better understanding of the complex structure for some individual clusters.

#### 3.3.1 Cluster total mass and gas mass fraction

The first major goal is to precisely measure the gravitational mass and gas mass fraction of a galaxy cluster within a well-defined radius.

An average uncertainty within 25% up to  $r_{500}$  is expected for the total mass determination of the REFLEX-DXL project. The mass measure is expected to be pushed almost to the boundary of the hydrostatic equilibrium ( $\sim r_{500}$ ) through a careful modeling of the ICM observables. The cluster structure and dynamical state has to be characterized by the

### 3 Scientific motivation

---

combination of X-ray images, temperature profiles, density profiles, entropy profiles and lensing results. A systematic approach was developed in this work to measure the total mass of the merger clusters by characterizing the undisturbed part of the cluster.

Around 30% of the galaxy clusters in the REFLEX-DXL sample appear quite regular, and show high central X-ray surface brightness and dense cool gas in the center. Their masses are relatively well defined. Those clusters are considered to be quite relaxed and can be used as one type of the “standard cosmic candles” (White et al. 1993). Those clusters will also be used to study the DM distribution to constrain the cuspy center of the DM halo.

A narrow gas mass fraction range at  $r_{200}$  is expected for the REFLEX-DXL sample based on the precise mass determination. As a medium distant ( $z \sim 0.3$ ) sample of massive galaxy clusters, the gas mass fractions of the REFLEX-DXL sample can be used for comparison with nearby samples (e.g. Allen et al. 2004) and distant samples (e.g. Vikhlinin et al. 2002; Ettori et al. 2003) to test evolutionary effects. The average value of the gas mass fractions of the REFLEX-DXL sample can be used as a test of the cosmic matter density of the Universe.

#### 3.3.2 Scaling relations and correlations

The second major goal is to investigate the cluster structure and thermodynamics and its evolution using the scaling relations and correlations of the X-ray properties in galaxy clusters.

The REFLEX-DXL sample can be exploited to study the scaling relations statistically. A systematic analysis of the sample provides spatially resolved temperature profiles. The temperature measurements are expected to approach an accuracy better than 15% (50%) in the  $r < 2'$  ( $r > 2'$ ) region assuming a flat  $\Lambda$ CDM cosmology with the normalized cosmic matter density parameter  $\Omega_m = 0.3$  and a Hubble constant of  $H_0 = 70 \text{ km s}^{-1} \text{ Mpc}^{-1}$ . The temperature and mass analyses as well as the 2-d analysis can be pushed out to  $r_{500}$ . An average accuracy of the cluster mass determination of  $\sim 25\%$  provides tight scaling relations. The similarity of the ICM distributions, such as temperature, gas density, entropy and total mass can be investigated and quantified. The typical temperature profile, gas-to-total mass ratio of the sample can be characterized. The REFLEX-DXL sample will provide some high precision points to the cluster mass–observable relations. The evolutionary effect of the mass–observable relations can be investigated by comparing the REFLEX-DXL sample with nearby samples. The accuracy of the normalization of those correlations at medium redshift can be improved based on the XMM-Newton observations.

#### 3.3.3 Cluster number density

The third major goal is to provide the cluster number density through the cluster temperature function at  $z \sim 0.3$  based on the precisely measured observables.

As a flux-limited and almost volume-complete sample, the temperature function of the sample will be used to study the evolutionary effect by comparing this sample to nearby and more distant samples. The cosmic matter density will then be determined with a better accuracy combining the REFLEX-DXL sample with other samples at different redshift



bins, especially the “XMM-Newton Legacy-Type Program for the Study of Galaxy Cluster Structure” program (XMM-LP; PI: Böhringer).

### 3.3.4 Complexity in galaxy clusters

The fourth major goal is to exploit the complex structure in medium distant galaxy clusters.

The REFLEX-DXL clusters can be used to check the slope of the matter density profile in the outskirts. The substructure of these clusters, not only in the X-ray surface brightness distribution, but also in the temperature, entropy and pressure distributions can be investigated in detail to develop a rigorous diagnostics to characterize unrelaxed and merging clusters. Based on these results, a systematic method can be developed to exclude the substructure to derive a precise mass estimate. Additionally, the merger clusters in the sample have been observed with Chandra. A detailed study of the complex merger features in these clusters is postponed to be deduced as an extension of this work.

The medium distant lensing cluster, CL0024+17, which shows a large discrepancy between X-ray and strong lensing gravitational masses, is an interesting object for such a study. It has been observed by XMM-Newton ( $\sim 40$  ks) and can be investigated by combining the XMM-Newton observations with the Chandra and HST observations. A global temperature measure with an accuracy within 10% is expected. A detailed investigation, including a 2-dimensional analysis, can be performed to study the gas density and temperature distributions. Both the XMM-Newton and Chandra data will be analyzed to make a cross calibration for a reliable determination of the ICM X-ray properties in CL0024+17. The gravitational potential can then be deduced with an uncertainty of 20–30%. This will provide a good basis to resolve/confirm the discrepancy between the X-ray and lensing measured masses. Since XMM-Newton has a large field of view (FOV), the large-scale morphology around CL0024+17 can also be investigated to check the possible filament systems which could give rise to infalling matter and merger events. Hopefully, the detailed studies of the structures in this cluster would shed light on possible solutions of the discrepancy between X-ray and strong lensing measurements.

### 3 Scientific motivation

---

## 4 XMM-Newton observatory

### Abstract

In this chapter, I will provide a simple description of the XMM-Newton X-ray observatory and data reduction.

### 4.1 X-ray observations and XMM-Newton

An X-ray survey is one of the most efficient ways to detect medium distant galaxy clusters since they are easily identified as extended sources in X-rays in comparison to the point-like sources (e.g. Forman 2003).

In the past, progress in cosmological applications and astrophysical studies using galaxy clusters was limited by the large observational uncertainties in the cluster mass estimates and by the rough knowledge about the scaling relations of cluster mass and observables. It is promising to improve the situation fundamentally by making use of data taken by the advanced X-ray telescopes, XMM-Newton<sup>1</sup> (the X-ray Multi-Mirror Satellite Observatory of ESA) and Chandra (NASA).

Current X-ray observations with their high spatial resolution (see Fig. 4.1) and energy resolution provide a unique approach to understand deviations from dynamical equilibrium and the non-gravitational processes in galaxy clusters which explains the scatter in the scaling relations and correlations. Detailed analytic studies and simulations together with the observations can be used to quantify the non-gravitational effects which become important, e.g. in the cluster center (e.g. Ponman et al. 2003). New insight into the ICM structure in the cluster center (Böhringer et al. 2001b) and outskirts (Finoguenov et al. 2003) has been gained using the X-ray data observed by XMM-Newton and Chandra. The reduced difference between the gravitational lensing measure and X-ray results is encouraging (e.g. Zhang et al. 2005a). The temperature structure as a function of radius has been mapped (Zhang et al. 2004a). These results illustrate how the advanced X-ray instruments provide a unique means to study galaxy clusters.

Since XMM-Newton is the most important instrument to perform the observations in this work, a brief description is provided. A reliable pipeline procedure of data reduction, which is described in detail in later chapters, was developed for this work.

XMM-Newton is a high throughput X-ray spectroscopy Multi-Mirror mission. The XMM-Newton mission is the second of four cornerstone projects in the ESA long-term program HORIZON 2000 for space science. It was launched from French Guyana on 1999, December 10.

---

<sup>1</sup><http://www.mpe.mpg.de/projects.html#xmm>

## 4 XMM-Newton observatory

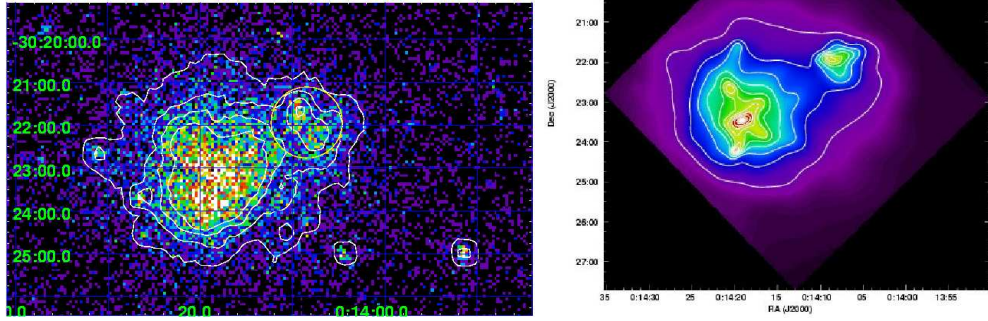


**Figure 4.1:** XMM-Newton (left, this work) and Chandra (right, Kempner & David 2004) images of A2744.

The primary scientific objective of XMM-Newton is to perform high throughput spectroscopy of cosmic X-ray sources over a broad band of energies ranging from 0.1 keV to 10 keV (Fig. 4.2). The XMM-Newton spacecraft payload includes three highly-nested grazing-incidence mirror modules of type Wolter I coupled to two reflection grating spectrometers (RGSs, with resolving powers up to 1000) and one small optical/UV telescope. The three Wolter I telescopes have an effective area of 1550 cm<sup>2</sup> at 1.5 keV. Each consists of 58 nested mirrors with diameters up to 70 cm. They focus the in-coming X-ray photons into the detectors of the European Photon Imaging Camera (EPIC), X-ray charge-coupled device (CCD) cameras. The EPIC cameras have resolving powers ranging from 20 to 50. Two Wolter I telescopes are identical. Each can collect  $\sim 44\%$  of its incoming light onto a linear strip of 9 CCDs, where there is a Metal-Oxide Semi-conductor camera (MOS1 or MOS2). The remaining light goes to the RGSs. The third Wolter I telescope unaffectedly collects all the X-ray incoming light in its light path to the EPIC p-n-junction (pn) camera. The pn array has 12 integrated back-illuminated CCD chips. The four individual quadrants have three pn-CCD subunits each with  $200 \times 64$  pixels, operating in parallel. The pixel size is 4.1''.

For all cameras the sensitive area of the detector is about 30' across. More than 90% of the flux of an on-axis point source is collected on one pn CCD chip

The first critical parameter determining the quality of an X-ray mirror module is its ability to focus photons. One of XMM-Newton's major advantages is that the core of its on-axis point-spread function (PSF) is narrow and varies little over a wide energy range (0.1-4 keV). Above 4 keV, the PSF becomes only slightly more energy dependent. Better than the earlier instruments, XMM-Newton provides a large effective area and broad, sensitive energy range. The effective area reflects the ability of the mirrors to collect radiation at different photon energies. For our analysis, the effective area information has been extracted from the ready-made EPIC response matrices (extended full-frame mode or full-frame mode, thin filter) and from response matrices created with the SAS task `rmfgen` in case of the EPIC's. One can see that the XMM-Newton mirrors are most efficient in the energy range from 0.1 to 10 keV, with a maximum at about 1.5 keV and a pronounced edge near 2 keV (the Au M edge). The effective areas of the two MOS cameras are lower than that of the pn, because only part of the incoming radiation falls onto these detectors,

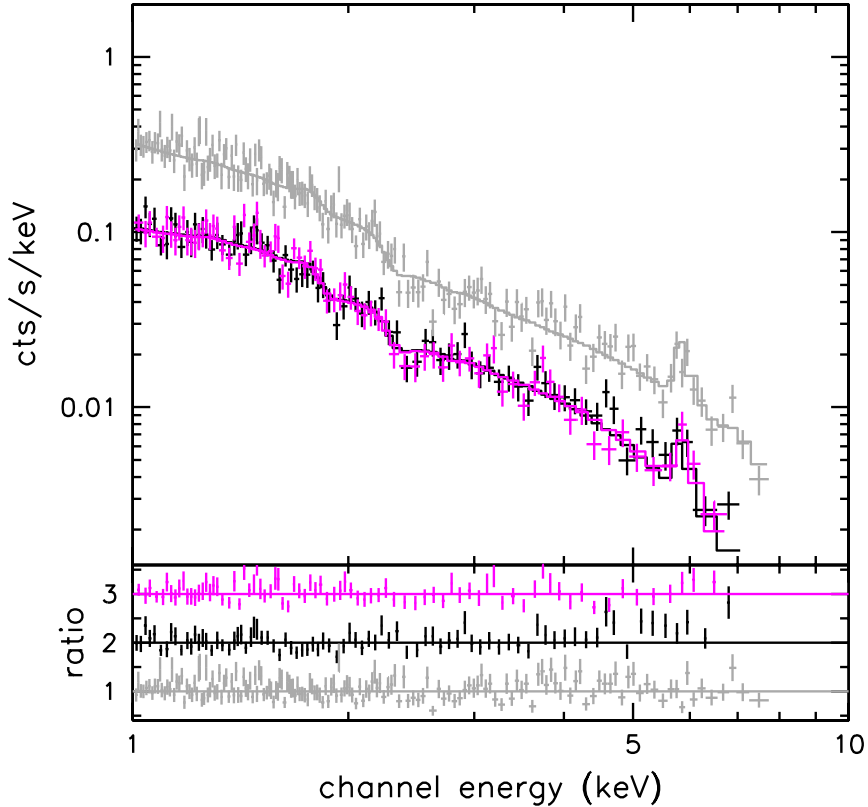


**Figure 4.2:** XMM-Newton spectra (pn in grey, MOS1 in black, and MOS2 in magenta) of RXCJ0547.6-3152 of the  $r < 40''$  region fitted by mekal model. The ratios of the observational data to the models are in the lower parts of the panels (offset zero for pn, +1 for MOS1, +2 for MOS2). The pronounced spectral line at  $\sim 6$  keV is Fe Ly $\alpha$ .

which is partially obscured by the RGSs (see Fig. 4.3).

The pixel size of XMM-Newton corresponds to  $1.1''$  ( $4.1''$ ) on the sky for MOS (pn). Given the FWHM of the PSF, the angular resolution can be  $6''$ . XMM-Newton has a broad energy band (0.15–15 keV) and a moderately high spectral resolution ( $\sim 80$  eV at 1 keV). The energy resolution of EPIC pn is  $\sim 150$  eV around the iron line at around 6.8 keV. The 2–7 keV energy band is most important for the temperature determination of massive clusters. There is a degradation of approximately 13% in the energy resolution of the MOS compared to its performance after launch. The degradation is due to an increase in the Charge Transfer Inefficiency (CTI) of the CCDs with time in orbit.

Compared to the recent mission Chandra, XMM-Newton provides a crucial advantage for extended object studies, a large FOV ( $\sim 30'$ ). It provides for the first time the capability for a detailed study of the mass distribution and dynamical state of the massive, medium distant (e.g.  $z \sim 0.3$ ) X-ray clusters of galaxies up to  $r_{500}$ . The large FOV also leaves enough field in the outskirts to compare the background of the blank sky pointings and target pointings to monitor and to subtract the residuals.

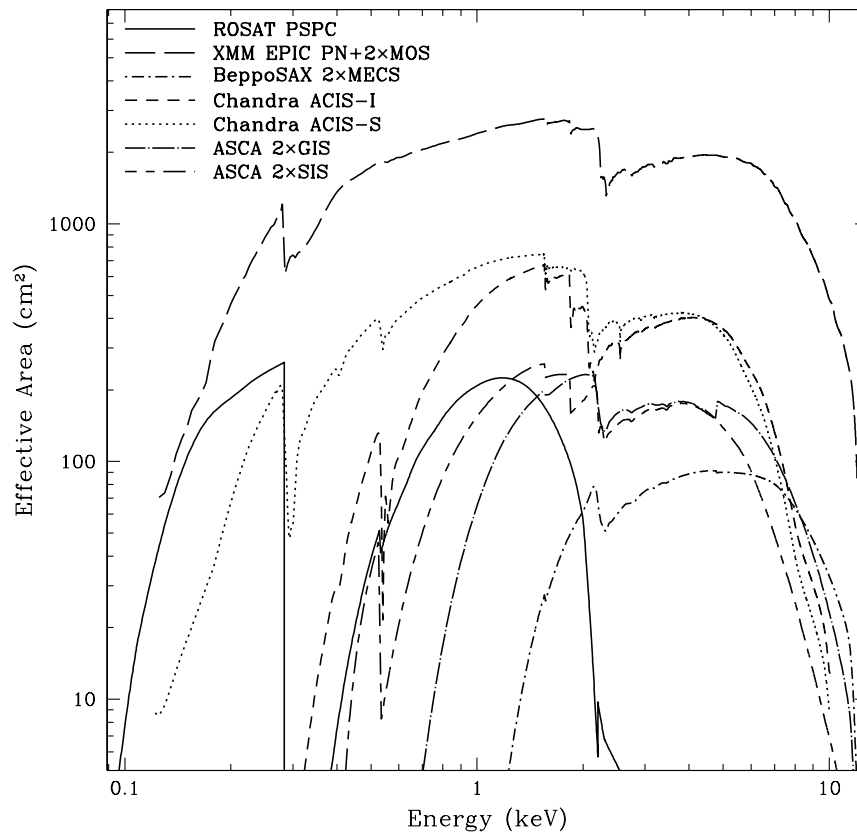


**Figure 4.3:** A comparison of the effective area of some important X-ray telescopes (Reiprich 2001, the figure provided by V. Burwitz).

This work is based on the observations taken by XMM-Newton for all the clusters, and by Chandra and HST for some of the clusters.

## 4.2 Data reduction technique

A standard data analysis for all the observations has been developed. The key requirement for XMM-Newton imaging spectroscopy analyses is a good background subtraction. The REFLEX-DXL clusters at  $z \sim 0.3$  provide optimal coverage of the FOV to optimize the collection of photons and to allow us to perform a residual background subtraction using the outskirts of the FOV of the target pointings and blank sky pointings. A precise two-step background removal has been developed, e.g. in Zhang et al. (2004a, 2005a, 2005c). The recipes are well tested to provide reliable results by, e.g. (i) the good agreement between the measurements of CL0024+17 obtained from the XMM-Newton observations using the recipes developed in this work and the results obtained from the Chandra data by the CfA experts using their recipes (see Zhang et al. 2005a), and (ii) the consistency of the radial profiles and 2-d results (see Finoguenov et al. 2005). A combination of the radial profile

analysis and 2-dimensional analysis can be used to provide sufficient information of the cluster structure. A precise determination of the total mass and gas mass fraction can thus be obtained. A detailed description of the approach is given in the later chapters.





# 5 Temperature gradients in the REFLEX-DXL galaxy clusters

## Abstract

We present XMM-Newton results on the temperature profiles of a volume-limited sample of galaxy clusters at redshifts  $z \sim 0.3$ , selected from the REFLEX survey (REFLEX-DXL sample). In the spectral analysis, where only the energies above 1 keV were considered, we obtained consistent results on the temperature derived from the pn, MOS1 and MOS2 data. Useful temperature measurements could be performed out to radii with overdensity 500 ( $r_{500}$ ) for all nine clusters. We discovered a diversity in the temperature gradients at the outer cluster radii with examples of both flat and strongly decreasing profiles. Using the total mass and the gas mass profiles for the cluster RXCJ0307.0–2840 we demonstrate that the errors on the mass estimates for the REFLEX-DXL clusters are within 25% up to  $r_{500}$ .

## 5.1 Introduction

The number density of galaxy clusters probes the cosmic evolution of large-scale structure (LSS) and thus provides an effective test of cosmological models. It is sensitive to the matter density ( $\Omega_m$ ) and the amplitude of the cosmic power spectra on cluster scale ( $\sigma_8$ ) (e.g. Schuecker et al. 2003). Its evolution is sensitive to the dark energy ( $\Omega_\Lambda$ ) (e.g. Vikhlinin et al. 2002). The most massive clusters are especially important in tracing LSS evolution since they are expected to show the largest evolutionary effects. In addition, the X-ray properties of the most massive clusters should be easier to describe in hierarchical modeling since the structure of the X-ray emitting intracluster plasma is essentially determined by gravitational effects and shock heating. With decreasing cluster mass and intracluster medium (ICM) temperature, non-gravitational effects play an important role before and after the shock heating (Voit & Bryan 2001; Voit et al. 2002; Zhang & Wu 2003; Ponman et al. 2003). Therefore, the most massive clusters provide the cleanest results in comparing theory with observations.

In this project we are analyzing an almost volume-complete sample of thirteen X-ray luminous ( $L_X \geq 10^{45}$  erg s $^{-1}$  for 0.1 – 2.4 keV) clusters selected from the ROSAT-ESO Flux-Limited X-ray (REFLEX) galaxy cluster survey (Böhringer et al. 2001a) in the redshift interval  $z = 0.27$  to 0.31. There is only a very small correction to the volume completeness with a well known selection function for  $L_X \geq 10^{45}$  erg s $^{-1}$  at the higher redshift as described in Böhringer et al. (2005; Paper I). With this REFLEX-DXL (Distant X-ray Luminous) sample we want to obtain a robust measure of the cluster abundance of this epoch, in particular to perform studies of the evolution of the cluster population by

## 5 Temperature gradients in the REFLEX-DXL galaxy clusters

**Table 5.1:** Compilation of some observational information on the nine REFLEX-DXL clusters. Column (1): cluster name. Columns (2–3): sky coordinates. Columns (4–6): net exposure time of MOS1, MOS2 and pn after cleaning for the flaring episodes. Columns (7–9): light curve cleaning upper limit. Column (10): hydrogen column density in units of  $10^{20}\text{cm}^{-2}$  (Dickey & Lockman 1990). Column (11): revolution of XMM-Newton. Footnotes give the alternative names.

Cluster (RXCJ)	$\alpha$ ( $^{\circ}$ )	$\delta$ ( $^{\circ}$ )	Exposure Time (s)			Criteria (cts/100s)			$n_{\text{H}}$	orbit
	Eq. J2000.0		MOS1	MOS2	pn	MOS1	MOS2	pn		
0014.3 – 3022 <sup>1</sup>	3.5837	–30.3757	15085	15510	10057	23.4	23.7	61.2	1.60	270
0043.4 – 2037 <sup>2</sup>	10.8508	–20.6225	11253	11248	6318	23.5	25.0	69.8	1.54	380
0232.2 – 4420	38.0717	–44.3453	11979	11508	7741	22.2	22.4	63.4	2.49	474
0307.0 – 2840 <sup>3</sup>	46.7667	–28.6708	12309	12610	8126	21.9	22.5	56.8	1.36	218
0528.9 – 3927	82.2342	–39.4636	7097	6806	3297	23.3	23.2	57.4	2.13	324
0532.9 – 3701	83.2350	–37.0260	10374	11191	6527	23.3	25.3	63.0	2.90	518
0658.5 – 5556 <sup>4</sup>	104.5700	–55.9600	25339	23365	18307	24.7	23.6	57.7	6.53	159
1131.9 – 1955 <sup>5</sup>	172.9858	–19.9258	11660	11164	8511	22.3	22.3	57.8	4.50	286
2337.6 + 0016 <sup>6</sup>	354.4204	0.2760	12216	11915	7412	22.4	23.3	69.1	3.82	365

<sup>1</sup>A2744 (AC118), <sup>2</sup>A2813, <sup>3</sup>A3088, <sup>4</sup>1ES0657-558, <sup>5</sup>A1300, <sup>6</sup>A2631.

comparing these observations with more nearby and more distant clusters. A prime goal is to obtain reliable ICM temperatures of these clusters as a measure of the cluster masses (e.g. Evrard 1997). Since peculiarities in the cluster structure introduce a scatter in the mass–temperature relation and since in particular on-going cluster mergers can lead to a temporary increase in the cluster temperature and X-ray luminosity (Randall et al. 2002), we aim for a detailed study of the deep XMM-Newton observations described here. The clusters are also scheduled for a detailed spectroscopic study of the cluster dynamics with the ESO-VLT-VIMOS instrument.

The selection of the REFLEX-DXL sample and its properties are described in detail in Paper I. For all clusters in this sample the XMM-Newton observations have confirmed that the X-ray luminosity is dominated by diffuse thermal emission from the ICM of these systems. Therefore, the REFLEX-DXL sample contributes a unique sample of X-ray luminous and consequently very massive clusters from roughly the same epoch, which are not only interesting as cosmological probes, but also for astrophysical studies like the statistics of cluster substructure, galaxy evolution, Sunyaev-Zeldovich observations and many other applications (e.g. Böhringer et al. 2001c).

The estimate or derivation of the cluster mass is an essential step in almost all these studies. The mass can be either approximately estimated from the temperature (Evrard 1997), or determined from the temperature and density distributions of the ICM under the assumption of hydrostatic equilibrium of the intracluster gas (e.g. Cavaliere & Fusco-Femiano 1976; Serio et al. 1981), or otherwise determined from the mass of the intracluster gas and the assumption of the universality of the cluster baryon fraction (e.g. White et al. 1993; Vikhlinin et al. 2002). The first two methods require a robust determination of the ICM temperature and a good understanding of the cluster structure for a reliable interpretation of the results.

Therefore, it is the aim of this paper to establish a reliable method of spatially resolved

**Table 5.2:** Parameters of the residual background models fitted in the 0.4–15 keV band. Column (1): cluster name. Columns (2–4): index of the “powerlaw/b” residual background model for MOS1, MOS2 and pn. Columns (5–7): normalization at 1 keV of the “powerlaw/b” residual background model scaled to 1 arcmin<sup>2</sup> area for MOS1, MOS2 and pn in units of  $10^{-4}$  cts s<sup>-1</sup> keV<sup>-1</sup> arcmin<sup>-2</sup>.

Cluster (RXCJ)	Index			Normalization		
	MOS1	MOS2	pn	MOS1	MOS2	pn
0014.3–3022	1.47	1.48	1.95	1.21	1.73	6.49
0043.4–2037	1.71	1.43	1.61	1.57	1.28	8.50
0232.2–4420	1.26	1.52	1.54	1.26	1.73	6.60
0307.0–2840	1.28	1.43	1.82	0.89	1.21	2.80
0528.9–3927	0.80	0.96	1.56	0.93	1.12	3.36
0532.9–3701	1.60	1.67	2.08	0.32	1.51	3.89
0658.5–5556	1.52	1.64	1.95	7.66	3.99	15.26
1131.9–1955	1.98	2.34	3.19	1.73	1.89	5.96
2337.6+0016	1.24	1.47	1.43	1.71	1.58	8.74

temperature determination for the clusters in the REFLEX-DXL sample and to derive temperature profiles for all the clusters. XMM-Newton with its superior sensitivity combined with its good spatial resolution provides the best means for such studies (Arnaud et al. 2002b). Previously, large data sets on cluster temperature profiles have been compiled from ASCA (e.g. Markevitch et al. 1998; White 2000; Finoguenov et al. 2001a; Finoguenov et al. 2002; Sanderson et al. 2003) and BeppoSAX observations (Molendi & De Grandi 1999; Ettori et al. 2002a).

This paper is structured as follows. In Sect. 7.2, we describe the background components, which are important to this study. Then we present a double background subtraction method, which is developed to provide a precise background removal. In Sect. 7.3, we analyse the properties of the hot gas in the galaxy clusters, and show our analytic temperature model. Then we determine the total mass and gas mass fraction in the cluster RXCJ0307.0–2840 based on the precise temperature and gas density profiles. In Sect. 7.5, we draw our conclusions. We adopt a flat  $\Lambda$ CDM cosmology with the density parameter  $\Omega_m = 0.3$  and the Hubble constant  $H_0 = 70$  km s<sup>-1</sup> Mpc<sup>-1</sup>. Error bars correspond to the 68% confidence level, unless explicitly stated otherwise.

## 5.2 Method

### 5.2.1 Data preparation

Of the thirteen XMM-Newton observations of REFLEX-DXL clusters conducted so far, eight have sufficient quality for the detailed studies described here. The remaining five clusters are heavily affected by soft proton flares. Some properties of these observations are described in Paper I. Re-observations of these targets have been allocated. An additional X-ray luminous REFLEX cluster RXCJ0307.0–2840 at  $z = 0.2578$  was observed in this project and is also analyzed here. It has very good observational data and appears to be a very regular and symmetric cluster. We have therefore selected this object as an example

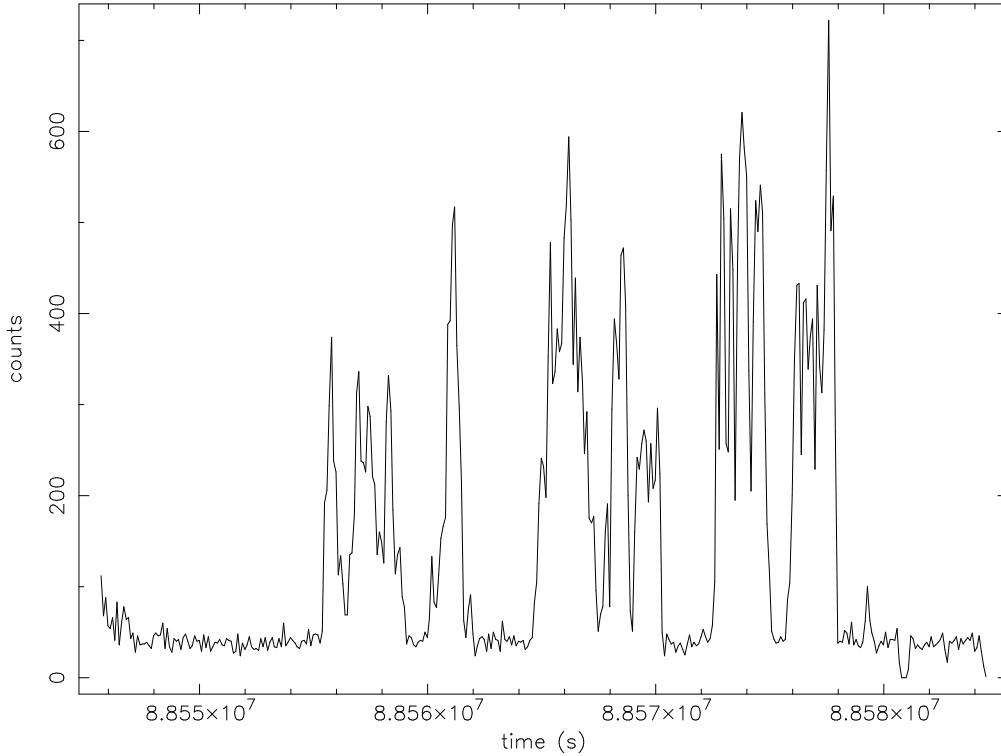


**Figure 5.1:** Light curve of RXCJ0658.5–5556 for pn in the 10–15 keV energy band. Time is measured in second relative to the XMM-Newton internal clock.

to demonstrate our method of analysis.

An overview on the observational data of the complete sample of thirteen plus one clusters is given in Paper I. In this paper we compiled further observational information on the sample targets in Table 5.1, which includes the observational parameters of the data and the alternative names of these targets.

We use the XMMSAS v5.4 software for data reduction. The MOS and pn data were taken in standard Full Frame mode and Extended Full Frame mode, respectively. For all detectors, the thin filter has been used.

Above 10 keV, there is little X-ray emission from the clusters due to the low telescope efficiency at these energies; the particle background therefore completely dominates. The cluster emission is not variable, so any spectral range can be used for temporal variability studies of the background. Therefore, the 10–15 keV energy band (binned in 100 s intervals) was used to monitor the particle background and to excise periods of high particle flux. In this screening process we use the settings  $FLAG = 0$  and  $PATTERN < 5$  for pn, and  $PATTERN < 13$  for MOS. As an example, Fig. 5.1 shows the 10–15 keV pn light curve of RXCJ0658.5–5556.

We reject those time intervals affected by flares in which the detector countrate (ctr) exceeds a threshold of  $2\sigma$  above the average ctr, where the average and the variance have been interactively determined from the ctr histogram below the rejection threshold. A similar cleaning criterion is applied to the screening of the background observation. We

note, however, that the thresholds will be different for the source and background accumulations. Formal freezing of the cleaning criterion does not overcome the difference in the mean background ctr. In our analysis we searched through a number of background observations to find the one matching our target observations. The selection criterion is therefore to find the one with a similar cleaning threshold.

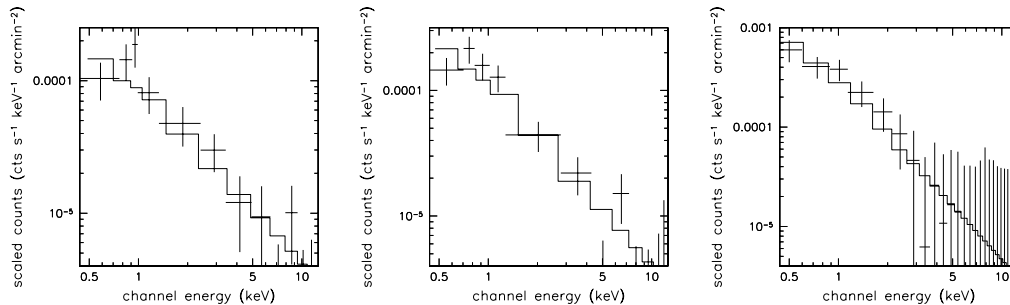


**Figure 5.2:** Residual background (after subtraction of the background obtained from the XMM-Newton observations of CDFS) of RXCJ0307.0–2840 for the 9.2–11.5′ region from the pointing centers of the MOS1 (top), MOS2 (middle) and pn (bottom) scaled to 1 arcmin<sup>2</sup> area. The data are fitted by a power law model (solid lines).

As shown in Table 5.1, the pn and MOS detectors all have their own similar cleaning thresholds for all observations. In Sect. 7.2.2 we consider in detail how this background behavior affects the temperature determination.

In the analysis of the pn data, we statistically remove the out-of-time effect by creating an out-of-time (OOT) event list file and using the XMMSAS products such as images and spectra to subtract it. The present observations have been taken in the Extended Full Frame mode (frame time=199 ms). At this mode, the fraction of OOT effect amounts 2.32%, which we used to normalize the XMMSAS OOT product before we subtract it from the XMMSAS normal product.

## 5.2.2 Background analysis

The purpose of the background analysis described in the following is to find a suitable “blank field” observation to be used for the background subtraction and to further analyze the difference between the target and background to take this residual background into account.

The background has several components which exhibit different spectral and temporal characteristics. In the low energy band (< 0.3 keV), the instrumental background is dominated by electronic noise consisting of a large number of small amplitude events added up during each frame accumulation (Read 2002). This noise depends on the read-out frequency of the cameras and is sensitive to the energy offset of each individual pixel. Energetic particles produce several line and continuum components in the background, which can be further subdivided into time variable and constant components. The constant component has been intensively studied by Lumb et al. (2002) and Read & Ponman (2003). This component can be removed using the so called blank field observations. De Luca &

Molendi (2001) report some evidence for a secular evolution of the background level on a half year time scale. Therefore, background accumulations close to the date of the target observation are more suitable. In addition, variations in the instrumental background on a much shorter time scale have been seen (e.g. De Luca & Molendi 2001). Part of such periods with an increased background are rejected through the analysis of the light curve (e.g. Read & Ponman 2003). However, we sometimes still observe a residual enhancement of the background associated with an increase in the quiet flux of soft protons. The typical time-scale for the variation of this ‘quiet’ component is comparable to or exceeds the typical observational time-scale. Therefore, it is in general not possible to remove observational intervals affected by this enhancement. Chen et al. (2003) describe an example of such an observation where quite different ‘quiet’ background levels are observed before and after a flare, respectively.

The photon background consists of foreground emission from the Galaxy as well as the Cosmic X-ray Background (CXB). Observations of the blank field also contain both components, provided the accumulations are done with the same instrumental set-up (e.g. with a particular filter) and the spectra of the X-ray background are the same for both the target and the blank field. This is only guaranteed for the CXB and the emission from the Galaxy halo. Since the Galaxy also plays a role as absorber and foreground emitter, it is important to have a similar absorbing column density for both the target and background accumulations. Additionally, there are some extra Galactic components, that display spatial variations. To constrain them, one has to look into the ROSAT All-Sky Survey data around both the background accumulations and the target. Observations with normal conditions of the Galactic emission are referred to the quiet Galactic zones. So are most of the X-ray background accumulations (Lumb et al. 2002; Read & Ponman 2003). Some source removal is performed on the existing background accumulations. This changes the shape and intensity of the residual CXB. Therefore, a similar source removal has to be performed in the analysis of the target.

Several available XMM-Newton pointings have been investigated. We conclude that the XMM-Newton pointings in the Chandra Deep Field South (CDFS) have similar background conditions as most targets and sufficient exposure time. Therefore, the CDFS is a good candidate for the background for our study. However, there is still a small difference between the background of our sources and the CDFS, e.g. the background ctr in the target observations is slightly higher (10–20%) than in the CDFS, which we ascribe mostly to the contamination by soft protons.

We have carefully planned this cluster study such that the radii in which the cluster emission can be observed extent up to spherical overdensities of 500, i.e., the ratio of the mean density of the dark halo with respect to the redshift-dependent critical density  $\rho_{\text{crit}}(z)$ . This is the region to which the cluster X-ray emission is expected to be essentially confined, covering about half of the field of view (FOV) of the XMM-Newton telescope. This enables us to extract a source spectrum from the background region of the target field for comparison with a background spectrum from the background field extracted with the same detector coordinates. Our residual background modeling procedure consists of analyzing such regions not affected by cluster emission. We assume little or no vignetting of the soft proton induced background, as suggested by recent studies (Lumb et al. 2002). Spectra are extracted from the 9.2–11.5’ region from the pointing center for our source observations

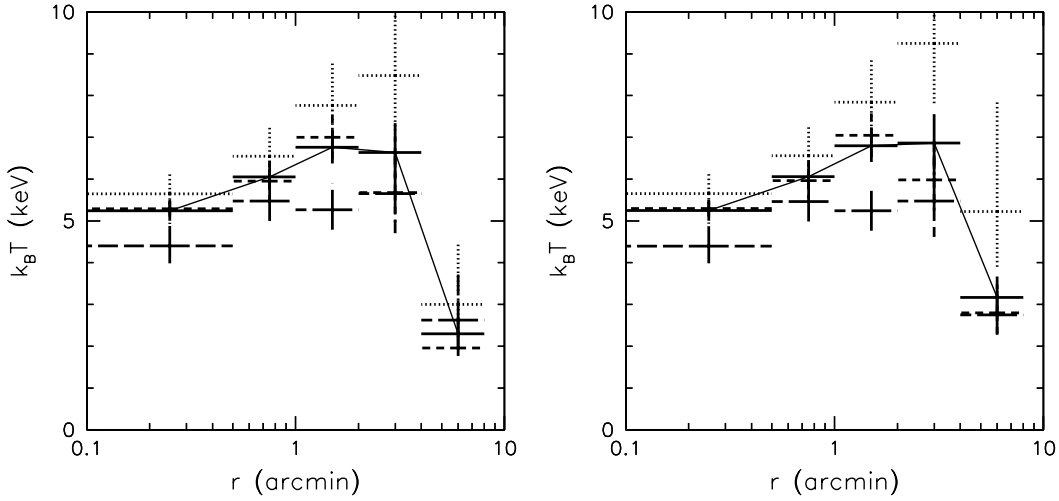


**Figure 5.3:** Temperature profiles for RXCJ0307.0–2840 with residual background subtraction (upper panel) and without residual background subtraction (lower panel) fitted in the 0.4–10 keV band for MOS1 data (dotted lines), MOS2 data (dashed lines), pn data (dash-dotted lines) and combined data (solid lines). Additional solid lines connect the temperature measurements for the combined data.

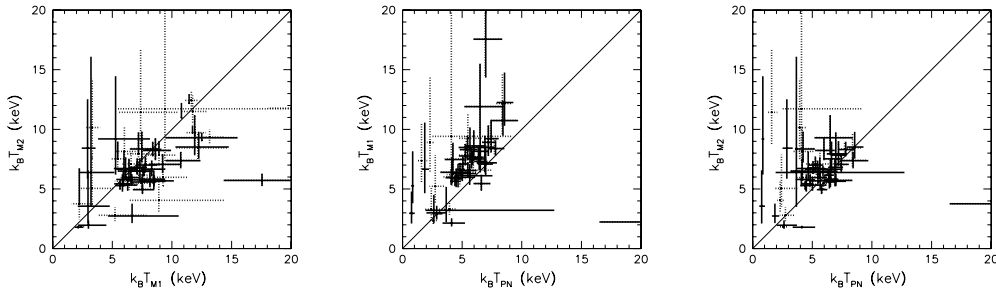


**Figure 5.4:** Comparison of the temperature estimates for RXCJ0014.3–3022, RXCJ0043.4–2037, RXCJ0232.2–4420, RXCJ0307.0–2840, RXCJ0528.9–3927, RXCJ0532.9–3701, RXCJ0658.5–5556, RXCJ1131.9–1955 and RXCJ2337.6+0016 from MOS1, MOS2 and pn fitted in the 0.4–10 keV band with residual background subtraction (solid lines) and without residual background subtraction (dotted lines).

and background candidate observations. In a first step, we compare the spectra extracted from the outer regions in the 0.4–15 keV band between the sources and the background pointings. The residual background signal found after the subtraction of the background field from the target field in this outer area is then modeled by a power law spectrum (model “powerlaw/b” in XSPEC, a power law background model which is convolved with the instrumental redistribution matrix but not with the effective area). We use this model to account for the excess soft proton background in our observations as compared to the background field. This residual power law background model is introduced over the whole energy range (“wabs\*mekal+powerlaw/b”, an emission spectrum from hot diffuse gas, e.g. Mewe et al. 1985, considering the Galactic absorption and modeling the residual back-

ground by a power law), which yields the correct shape of the background component after the combination with the blank field background (double background subtraction method). During this procedure, the normalization of the residual background component is always scaled to the area of the source extraction region.

In Fig. 5.2 we present examples of the residual background. The parameters of the residual background models fitted in the 0.4–15 keV band for the clusters are given in Table 7.1. The residual background in pn is higher than in MOS because the larger thickness of the pn-pixels leads to a higher sensitivity to the particle flux. Since the subtraction of the residual background is only a second order correction to the data and because of the large noise in the residual background data, we are not attempting a perfect model fitting, but approximating the data by a simple power law model. The uncertainty in the normalization is, anyway, within 5% and 10% for MOS and pn, respectively. The correction due to the residual background makes only a 1–4% effect in the cluster signals and an up to 10% effect to the temperature determinations for cluster radii  $r \leq 4'$ . At larger radii the effect of the correct background effect is large as shown in Fig. 5.3, but the uncertainty in the approximation of the residual background – a third order effect – is still small.

To recover the correct spectral shape and normalization of the cluster component, we need both the response matrix file (rmf) and auxiliary response file (arf). The following need to be taken into account in either rmf or arf: (i) Pure redistribution matrix giving the probability that a photon of energy  $E$ , once detected, will be measured in data channel  $PI$ . (ii) Quantum efficiency (with closed filter position) of the CCD detector. (iii) Filter transmission. (iv) Geometric factors such as bad pixel corrections and gap corrections (around 4%). (v) Telescope effective area as a function of photon energy. (vi) Vignetting correction to effective area for off-axis pointings. We choose the rmf which corresponds to (i) and (ii) (with closed filter position). The pn rmf that corresponds to this choice has a ‘\_closed’ keyword in their naming conventions. For the MOS detectors we use software to generate such files, kindly provided by S. Sembay. The arf corresponds to (iii), (iv) and (v) and is made according to the average flux detected in the different extraction annuli, which takes (vi) into account. It is created using the XMMSAS based program ‘clarf’ by A. Finoguenov. Furthermore, in our analysis we apply the logarithmically spaced radial bins, which provide nearly the same flux per bin. The importance of the scattering due to the point-spread-function (PSF) is therefore suppressed. Using the XMM-Newton PSF calibrations by Ghizzardi (2001) we have estimated the loss fraction of the flux: 20% for the central bins ( $0.5'$ ) and less than 10% for the other bins ( $\geq 1'$ ) with energy dependent effects being negligible.

In summary the spectral analysis is performed in two steps. (i) A model for the residual background (background difference) is obtained in XSPEC from a comparison of the outer region of the target and background fields (see Fig. 5.2 and Table 7.1). (ii) The spectral modeling is performed in XSPEC with the cluster region as source data, the CDFS as background and the residual background as a second model component with model parameters fixed to the values found in step (i) (see Fig. 5.5).

In Fig. 5.3 we present the temperature profiles resulting from this background subtraction method fitted in the 0.4–10 keV band for the example object, RXCJ0307.0–2840. We actually compare the results of the two step background subtraction considering the residual background with the simple one step background subtraction. In Fig. 6.2 we provide



the comparisons of the results from MOS1, MOS2 and pn fitted in the 0.4–10 keV band. One notes that the residual background subtraction provides results in which all three instruments tend to show a slightly better consistency. The upper limit of the uncertainties between the instruments goes down from 90% to 15% after the residual background subtraction. A detailed treatment of the background does not completely remove the differences between the instruments. We found systematically lower temperatures obtained with pn compared to MOS1 and MOS2 (partially). Because the pn detector is sensitive to the soft component, the pn measurements are easily affected by the soft band, which results in the lower temperatures given by pn compared to MOS. Since the temperature estimates of the pn are more strongly dependent on the soft energy band compared to MOS, we have carried out a spectral analysis in the 1–10 keV band. Despite the larger error bars, all temperature determinations in the central three bins of the cluster become higher, once the 0.4–1 keV band is excluded. In the following we will systematically investigate the effect of an energy band selection in the temperature and mass estimate.

## 5.3 Results

### 5.3.1 Redshift, mean temperature, and metallicity

In a first step of the data analysis we derive global properties of all nine galaxy clusters with good XMM-Newton data. Since a fraction of the clusters have cooling cores, dense central regions with lower temperature and so-called cooling flows, while the others do not display this phenomenon, we derive global temperatures including and excluding these regions. In addition the signal-to-noise decreases fast in the outer regions of the clusters. Therefore, the global temperature was determined in the  $r < 8'$  region and alternatively in the  $0.5 < r < 4'$  region (see Fig. 5.5). The global temperatures determined in both regions show some differences. The explanation is partially revealed by the temperature profiles. The metallicities in both zones are very similar.

We fit the spectra in XSPEC using the one and two step correction models (“mekal\*wabs” and “mekal\*wabs+powerlaw/b”) after subtracting the background and applying the rmf and arf. The fit using the latter model is better. For the regions covering radii of  $0.5 < r < 4'$  and  $r < 8'$ , respectively, we use the 0.4–10 keV and 1–10 keV energy bands. Furthermore, we exclude the regions of substructure and/or some very bright point sources for several clusters throughout the procedure (cf. Table 5.3). The temperature of the small and large substructures in the well-known post merger cluster RXCJ0658.5–5556 are  $8.3^{+2.1}_{-1.4}$  keV and  $15.0^{+2.3}_{-1.9}$  keV from the double background subtraction method in the 2–12 keV band. We exclude the small substructure to measure the global temperature. The flux within the region we excluded contributes 60% (10'') to 85% (30'') to the total flux of the point source. The temperature measurements vary within 10% after the subtraction.

The redshifts obtained from the X-ray data (see Table 5.4) which are ascribed to the ICM, are consistent with the redshifts obtained from optical spectra of individual cluster galaxies (see Böhringer et al. 2005) except for RXCJ2337.6+0016. The optical redshifts contain a heliocentric correction, while the uncertainty in the X-ray determined redshifts is one to two magnitude larger than this correction and thus no correction was made. We believe that the optical redshift of RXCJ2337.6+0016 with 5 coincident cluster galaxy

## 5 Temperature gradients in the REFLEX-DXL galaxy clusters

---

redshifts is more reliable and accurate than the X-ray result at this stage. We plan to obtain further information on this object to resolve this discrepancy.

The measurements of the global temperatures are summarized in Table 5.4. Similar to the measurements for the  $0.5 < r < 4'$  region, the measurements for the  $r < 8'$  region in the 0.4–10 keV band are lower than in the 1–10 keV band. Therefore, we only provide the comparison of the measurements for the  $0.5 < r < 4'$  region fitted in two bands. The results obtained for the full and restricted spatial zones are consistent within  $1-2\sigma$  (formal errors) within 15% uncertainties.

The global temperatures obtained from model fits to the larger spectral range 0.4–10 keV are always lower compared to the temperatures obtained from 1–10 keV. To check if the discrepancy is partially due to residual Galactic emission, we undertake the following test. We extract the spectra from the inner (hereafter “A”) and outer (hereafter “B”) parts of the background region in both the background (hereafter “bkg”) and target (hereafter “src”) observations. If there is some difference in the Galactic emission between the background and target observations, there must be some residual Galactic emission after we subtract the spectrum “ $B(src) - B(bkg)$ ”, scaled by the area of the region A, from the spectrum “ $A(src) - A(bkg)$ ” because of the vignetting effect of the Galactic emission. We apply a thermal emission spectral model (“apec”) with all parameters free in XSPEC to fit this residual emission. We found that the temperature of this component is around 0.2 keV and the redshift is close to zero. In the following analysis, we fix the temperature to 0.2 keV, the abundance to solar abundance and the redshift to zero, and obtain the normalization of this component. We re-analyze the global properties of the clusters introducing the residual Galactic emission normalized by the area and vignetting effect. Since the difference in the temperatures determined in the 0.4–10 keV and 1–10 keV bands still remains, we report the temperature measurements setting the normalization of the residual Galactic emission to its upper limit (cf. Table 5.4). However, this component only makes a  $< 1\%$  effect in the cluster signals. It is thus clear that the discrepancy is not or not mainly due to the residual Galactic emission. This discrepancy will again be discussed below.

### 5.3.1.1 Comparison with previous results

Mushotzky & Scharf (1997) have measured a temperature of  $12.08_{-0.88}^{+1.42}$  keV ( $2\sigma$  errors) for RXCJ0014.3–3022 with ASCA data. Horner (2001) presents the temperature for the same cluster of  $9.61_{-0.56}^{+0.64}$  keV, for RXCJ0232.2–4420 of  $7.19_{-0.38}^{+0.42}$  keV, for RXCJ0307.0–2840 of  $6.71_{-0.53}^{+0.60}$  keV, and for RXCJ1131.9–1955 of  $8.26_{-0.58}^{+0.63}$  keV, all with  $2\sigma$  errors based on ASCA data. Lemonon et al. (1997) measured a temperature for the post-merger cluster RXCJ1131.9–1955 of  $5 \pm 3$  keV using ROSAT PSPC data. They also found some evidence for a temperature gradient.

For the cluster RXCJ0658.5–5556 the published temperature measurements are less consistent. Tucker et al. (1998) measured a temperature of  $17.4 \pm 2.5$  keV ( $2\sigma$  error) with ASCA. Andreani et al. (1999) obtained  $14.5_{-1.7}^{+2.0}$  keV using both ASCA and ROSAT data. Yaqoob (1999) measured  $11 \sim 12$  keV with ASCA data. He found that a temperature of  $\sim 17$  keV can be artificially obtained if the true spectrum has a stronger low-energy cut-off than that for Galactic absorption only.

We notice that the ASCA spectra of RXCJ0658.5–5556 have in the 0.5–1 keV band only

**Table 5.3:** Regions with substructures and point sources excluded from the analysis. Column (1): cluster name. Columns (2–3): center of the circle in sky coordinates for J2000.0. Column (4): radii. Column (5): “Yes” if there is an optical point-like counterpart in a digitized optical survey (e.g. DSS2).

Cluster (RXCJ)	$\alpha$ ( $^{\circ}$ )	$\delta$ ( $^{\circ}$ )	r ( $''$ )	opt
0014.3–3022	3.6306	−30.3754	15	Yes
	3.5198	−30.4154	15	Yes
	3.5172	−30.4176	10	Yes
	3.5353	−30.3654	30	
0232.2–4420	38.1566	−44.3634	20	Yes
0528.9–3927	82.2427	−39.4647	15	Yes
	82.3071	−39.4809	15	Yes
	82.1450	−39.3867	15	Yes
	82.1435	−39.3724	10	Yes
	82.1134	−39.3713	10	Yes
0532.9–3701	83.1957	−36.9415	15	
	83.1506	−37.0285	10	
0658.5–5556	104.5884	−55.9413	20	

a few data points with large error bars. The differences in the temperature measurements described above come therefore clearly from the inclusion or exclusion of this soft part of the spectrum. Studies of nearby clusters suggest that putative non-thermal and warm thermal components are important at softer energies, while for rich clusters like Coma, the ICM dominates the X-ray emission up to 25 keV (Fusco-Femiano et al. 1999). Non-thermal emission dominates the emission at energies above 3 keV only in some of the groups of galaxies (Fukazawa et al. 2000). Since the expected temperatures of rich clusters are higher than 4 keV, we consider the temperature determination in the hard energy band as a more robust measure of the dominant gas mass component of a cluster, which traces the total mass. For RXCJ0658.5–5556 we decided to restrict our temperature determinations to the energy range 2–12 keV (see Tables 5.4 and 5.5).

Our results on RXCJ0658.5–5556 are consistent with Chandra measurements obtained by Markevitch et al. (2002) yielding a temperature of  $14.8_{-1.2}^{+1.7}$  keV from a fit of a spectrum extracted from the central  $r < 3'$  region. Although the authors show that  $k_B T > 15$  keV in some parts of this cluster, the temperatures have quite large error bars of 7 keV so that we regard this finding as not very significant.

Additionally, Markevitch et al. (2002) fixed the value of the galactic hydrogen column density to  $n_H = 4.6 \times 10^{20} \text{ cm}^{-2}$  which is significantly lower than  $n_H = 6.5 \times 10^{20} \text{ cm}^{-2}$  obtained from Dickey & Lockman (1999). To check this result with our XMM-Newton data we set all parameters to be free to fit the spectrum extracted from the annulus region covering radii of  $0.5 < r < 4'$  in the 0.4–12 keV band. In this case a high temperature of  $k_B T = 18.8 \pm 2.1$  keV was obtained while the  $n_H$  went down to an unrealistically small value of  $1.8 \pm 0.5 \times 10^{20} \text{ cm}^{-2}$ , although the remaining parameters were still relatively reasonable. Therefore, we decide to fix  $n_H = 6.5 \times 10^{20} \text{ cm}^{-2}$ , but exclude the soft band (0.4–2 keV). In this case we obtained stable results for the temperature, metallicity, and redshift (see Table 5.4). No significant metallicity gradients were found in our analysis.

## 5 Temperature gradients in the REFLEX-DXL galaxy clusters

**Table 5.4:** Global temperatures, metallicities and redshifts of 9 REFLEX-DXL clusters. Column (1): Cluster name. Column (2): Radius of annulus in arcmin. Column (3): Energy band for fit. Column (4): X-ray temperature measurements. Column (5): Metallicity in solar abundance. Column (6): Redshift obtained from the X-ray spectrum. Column (7):  $\chi^2$  per degree of freedom (d.o.f.). Column (8): Redshift obtained from optical spectra as given in the REFLEX catalogue (see Böhringer et al. 2005). All X-ray spectra are fitted by the XSPEC model “mekal\*wabs+powerlaw/b”.

RXCJ	Region	Band (keV)	$k_B T$ (keV)	Z ( $Z_\odot$ )	$z_{X-ray}$	$\chi^2/d.o.f.$	$z_{opt}$
0014.3-3022	$0 < r < 8'$	1 – 10	$8.65^{+0.43}_{-0.29}$	$0.24 \pm 0.05$	$0.294 \pm 0.008$	392.9/397	0.3066
	$0.5 < r < 4'$	0.4 – 10	$7.51^{+0.20}_{-0.20}$	$0.22 \pm 0.04$	$0.276 \pm 0.009$	383.2/371	
*			$7.63^{+0.21}_{-0.20}$	$0.22 \pm 0.04$	$0.274 \pm 0.007$	377.2/379	
		1 – 10	$8.29^{+0.43}_{-0.32}$	$0.22 \pm 0.05$	$0.276 \pm 0.011$	269.4/258	
0043.4-2037	$0 < r < 8'$	1 – 10	$7.50^{+0.47}_{-0.40}$	$0.23 \pm 0.06$	$0.309 \pm 0.015$	198.0/238	0.2924
	$0.5 < r < 4'$	0.4 – 10	$5.88^{+0.22}_{-0.21}$	$0.24 \pm 0.06$	$0.303 \pm 0.006$	197.8/197	
*			$5.96^{+0.23}_{-0.21}$	$0.25 \pm 0.06$	$0.302 \pm 0.011$	191.1/197	
		1 – 10	$6.81^{+0.43}_{-0.39}$	$0.23 \pm 0.07$	$0.300 \pm 0.012$	124.4/129	
0232.2-4420	$0 < r < 8'$	1 – 10	$6.70^{+0.24}_{-0.25}$	$0.32 \pm 0.05$	$0.275 \pm 0.002$	292.0/332	0.2836
	$0.5 < r < 4'$	0.4 – 10	$6.33^{+0.22}_{-0.17}$	$0.22 \pm 0.05$	$0.295 \pm 0.008$	384.2/287	
*			$6.27^{+0.20}_{-0.17}$	$0.23 \pm 0.05$	$0.296 \pm 0.010$	372.6/287	
		1 – 10	$7.62^{+0.40}_{-0.33}$	$0.24 \pm 0.05$	$0.296 \pm 0.009$	195.4/195	
0307.0-2840	$0 < r < 8'$	1 – 10	$6.17^{+0.24}_{-0.27}$	$0.28 \pm 0.06$	$0.241 \pm 0.002$	270.8/281	0.2578
	$0.5 < r < 4'$	0.4 – 10	$6.10^{+0.20}_{-0.22}$	$0.28 \pm 0.06$	$0.244 \pm 0.003$	275.0/251	
*			$6.17^{+0.21}_{-0.21}$	$0.28 \pm 0.06$	$0.244 \pm 0.004$	265.1/251	
		1 – 10	$6.63^{+0.34}_{-0.31}$	$0.29 \pm 0.07$	$0.243 \pm 0.004$	176.5/167	
0528.9-3927	$0 < r < 8'$	1 – 10	$8.07^{+0.59}_{-0.52}$	$0.31 \pm 0.08$	$0.262 \pm 0.012$	163.2/159	0.2839
	$0.5 < r < 4'$	0.4 – 10	$6.49^{+0.29}_{-0.27}$	$0.30 \pm 0.08$	$0.281 \pm 0.011$	162.8/148	
*			$6.42^{+0.28}_{-0.27}$	$0.31 \pm 0.08$	$0.281 \pm 0.010$	154.8/148	
		1 – 10	$7.66^{+0.63}_{-0.52}$	$0.28 \pm 0.10$	$0.282 \pm 0.016$	91.5/97	
0532.9-3701	$0 < r < 8'$	1 – 10	$7.46^{+0.38}_{-0.36}$	$0.34 \pm 0.07$	$0.274 \pm 0.003$	286.1/239	0.2747
	$0.5 < r < 4'$	0.4 – 10	$7.09^{+0.31}_{-0.44}$	$0.29 \pm 0.08$	$0.262 \pm 0.009$	226.5/202	
*			$6.98^{+0.35}_{-0.28}$	$0.30 \pm 0.09$	$0.262 \pm 0.011$	224.3/202	
		1 – 10	$7.76^{+0.72}_{-0.48}$	$0.28 \pm 0.10$	$0.259 \pm 0.016$	143.7/137	
0658.5-5556	$0 < r < 8'$	2 – 12	$13.59^{+0.71}_{-0.58}$	$0.24 \pm 0.03$	$0.287 \pm 0.002$	621.3/608	0.2965
	$0.5 < r < 4'$	2 – 12	$14.56^{+0.91}_{-0.69}$	$0.21 \pm 0.04$	$0.290 \pm 0.005$	378.1/400	
*			$14.61^{+0.57}_{-0.74}$	$0.21 \pm 0.04$	$0.291 \pm 0.004$	377.1/400	
		0.4-10	$9.63^{+0.22}_{-0.17}$	$0.23 \pm 0.02$	$0.288 \pm 0.002$	1214.5/892	
1131.9-1955	$0 < r < 8'$	1 – 10	$6.42^{+0.26}_{-0.25}$	$0.26 \pm 0.05$	$0.299 \pm 0.003$	322.5/283	0.3075
	$0.5 < r < 4'$	0.4 – 10	$6.71^{+0.08}_{-0.40}$	$0.23 \pm 0.09$	$0.285 \pm 0.009$	263.1/255	
*			$6.62^{+0.38}_{-0.21}$	$0.26 \pm 0.07$	$0.287 \pm 0.012$	248.4/255	
		1 – 10	$7.44^{+0.67}_{-0.22}$	$0.26 \pm 0.07$	$0.295 \pm 0.024$	163.4/174	
2337.6+0016	$0 < r < 8'$	1 – 10	$8.02^{+0.59}_{-0.57}$	$0.22 \pm 0.07$	$0.328 \pm 0.009$	211.1/255	0.2779
	$0.5 < r < 4'$	0.4 – 10	$6.77^{+0.29}_{-0.24}$	$0.24 \pm 0.06$	$0.315 \pm 0.011$	176.5/234	
*			$6.83^{+0.22}_{-0.28}$	$0.25 \pm 0.06$	$0.318 \pm 0.009$	172.7/234	
		1 – 10	$7.50^{+0.44}_{-0.37}$	$0.22 \pm 0.06$	$0.317 \pm 0.011$	116.2/161	

\*Introduce the upper limit of the residual Galactic emission described by an “apec” model in the double background subtraction method.

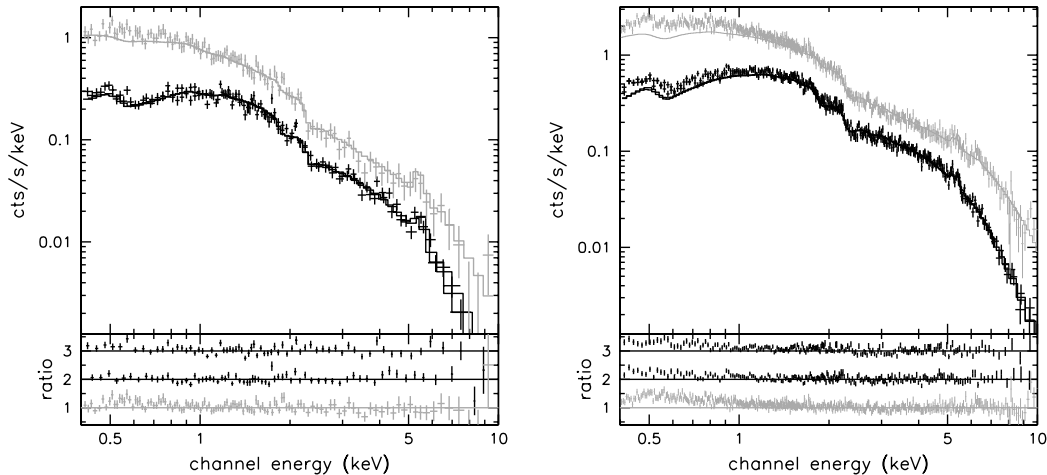


**Figure 5.5:** XMM-Newton spectra of RXCJ0307.0–2840 (top panel, fitted in the 1–10 keV band) and RXCJ0658.5–5556 (bottom panel, fitted in the 2–12 keV band) extracted from the  $0.5 < r < 4'$  region (pn in grey and MOS in black) with mekal model, considering the Galactic absorption and modeling the residual background by a power law. The ratios of the observational data to the models are in the lower parts of the panels (offset zero for pn, +1 for MOS1, +2 for MOS2).

We notice that the temperature of RXCJ0528.9–3927 (also in other clusters) changes significantly with the low cut-off of the energy band used in the fit. In Fig. 5.7, we thus used the X-ray spectra to test the energy band dependence and possible method dependencies by comparing the temperature measurements versus low energy band (low-E) cut-off from two different methods (the double background subtraction method and the method applied in Arnaud et al. 2002b, i.e. we use the standard XMMSAS command ‘evigweight’ to correct vignetting, use ‘arfgen’ and ‘rmfgen’ to create on-axis arf and rmf, and apply the blank sky provided by Lumb 2002). For comparison, we applied the following models to fit the spectra in the 0.4–10 keV band after double background subtraction. We obtain  $k_{\text{B}}T = 7.69^{+0.28}_{-0.46}$  keV and  $n_{\text{H}} \sim 0 - 0.1 \times 10^{20} \text{ cm}^{-2}$  using a single-phase temperature model (“wabs\*mekal+powerlaw/b”) with free  $n_{\text{H}}$ . We obtain  $k_{\text{B}}T = 10.12 \pm 3.13$  keV using two component thermal model (“wabs\*(mekal+powerlaw)+powerlaw/b”) with fixed  $n_{\text{H}}$ . We also obtain  $k_{\text{B}}T_1 = 9.34^{+5.93}_{-1.04}$  keV and  $k_{\text{B}}T_2 \sim 0.49 - 1.34$  keV using two thermal component model (“wabs\*(mekal+apec)+powerlaw/b”), in which we fix the redshift of the soft component to the redshift of the cluster. The metallicity and redshift measurements among the different modelings and different low-E cut-off vary within 5%. The results presented in Fig. 5.7 suggest some influence of the low energy band on the temperature measurements. As we discussed above, the results obtained in the harder energy band should recover the correct cluster temperature. Similar phenomena are also found for A1413 (Pratt & Arnaud 2002) using XMM-Newton data, and Coma, A1795 and A3112 (Nevalainen et al. 2003) based on the comparison of XMM-Newton and ROSAT PSPC observations. Nevalainen et al. interpret this as a soft excess, possibly due to a ‘warm-hot’ intergalactic medium. We will analyze this feature of our sample in more detail in a forthcoming paper.

## 5 Temperature gradients in the REFLEX-DXL galaxy clusters

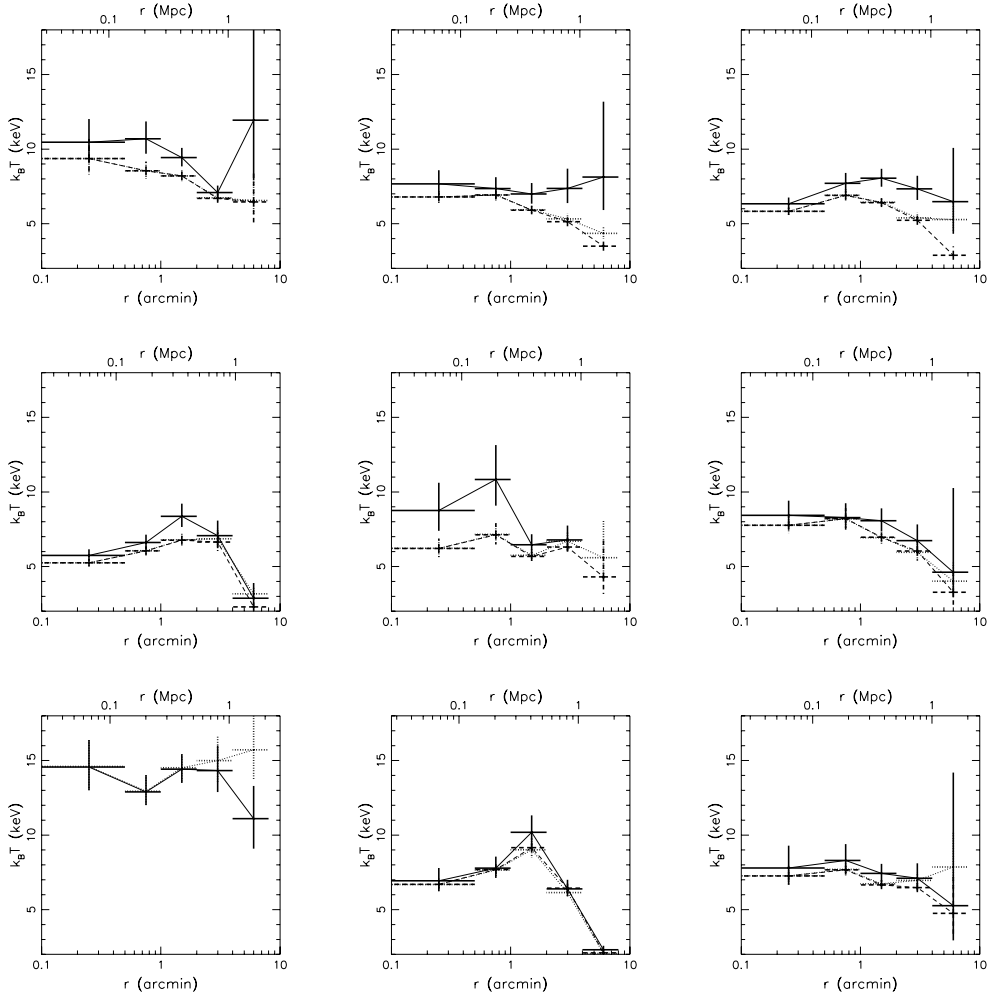


**Figure 5.6:** From left to right and from top to bottom, temperature profiles of RXCJ0014.3–3022, RXCJ0043.4–2037, RXCJ0232.2–4420, RXCJ0307.0–2840, RXCJ0528.9–3927, RXCJ0532.9–3701, RXCJ0658.5–5556, RXCJ1131.9–1955 and RXCJ2337.6+0016. All the clusters except RXCJ0658.5–5556 are fitted in the 0.4–10 keV band with (dashed lines) and without (dotted lines) the residual background subtraction. And the solid lines present the case with the residual background subtraction but fitted in the 1–10 keV band. The corresponding lines show the temperature profiles. Temperature profiles of RXCJ0658.5–5556 are fitted in 2–12 keV with (solid lines) and without (dotted lines) the residual background subtraction.

### 5.3.2 Temperature profiles

We have already noted that the differences between the global temperatures of the regions covering radii of  $0.5 < r < 4'$  and  $r < 8'$ , respectively, in Table 5.4 are possibly caused by

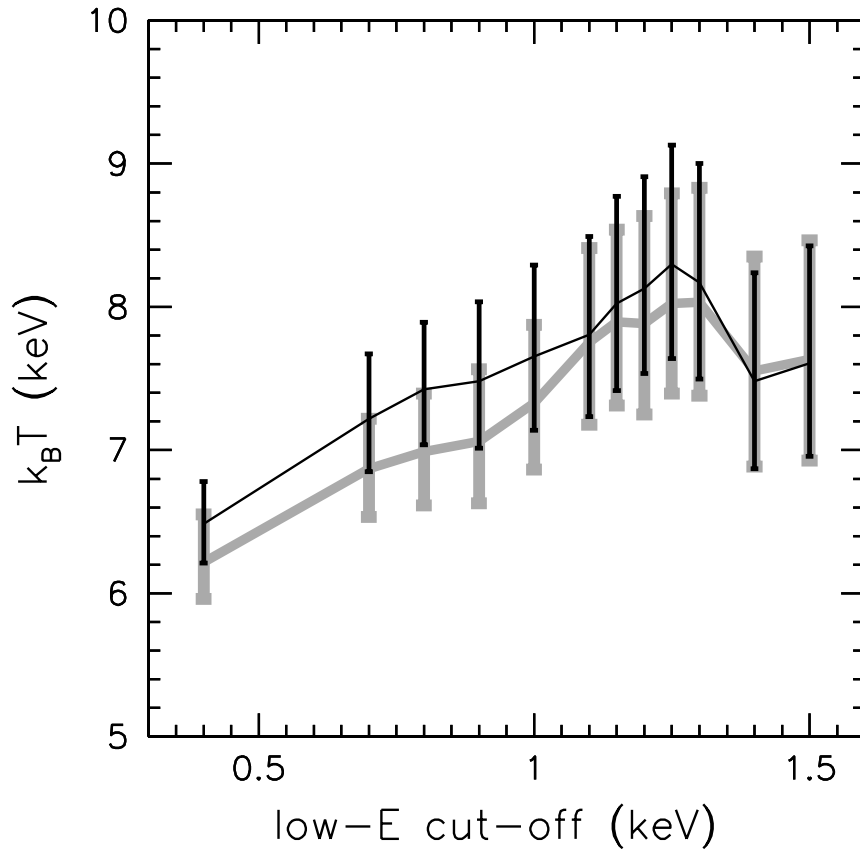


**Figure 5.7:** The temperature measurements versus low-E cut-off from two different methods, the double background subtraction method (black) and the method applied in Arnaud et al. 2002b (grey).

systematic temperature gradients. For a more detailed study of the temperature profiles we divide the cluster regions into the five annuli 0–0.5′, 0.5–1′, 1–2′, 2–4′, and 4–8′ (cf. Fig. 5.3). Note that in the spectra extracted from the outermost rings of RXCJ0014.3–3022 and RXCJ0528.9–3927 we ignore a narrow energy band containing the residual background around the 1.49 keV Al line (Freyberg et al. 2002).

Table 5.5 shows the temperature profile catalogue of the 9 REFLEX-DXL clusters from the spectral analysis fitted by one or two step background subtraction, “mekal\*wabs” or “mekal\*wabs+powerlaw/b”. We use both the > 0.4 keV and > 1 keV energy bands except for RXCJ0658.5–5556. We apply the 2–12 keV band for this high temperature cluster. The temperature profiles of the clusters are also shown in Fig. 5.6.

For most of the objects, the temperature can be measured out to  $r_{500}$ . The overall temperature profile is characterized by a rather moderate decrease towards the center, and a decrease towards the outer regions, yet on different levels, including no decrease at all for some of the clusters. This confirms a suggestion of Finoguenov et al. (2001b) that the differences in the behavior of the temperature profiles in the outskirts of clusters have a statistical origin, rather than simple reflections of measurement errors.

## 5 Temperature gradients in the REFLEX-DXL galaxy clusters

**Table 5.5:** Temperature profiles of 9 REFLEX-DXL clusters obtained from the spectral analysis with residual background subtraction (double background subtraction) and without residual background subtraction. Column (1): Cluster name. Column (2): Energy band for spectral fit. Column (3): Model used in XSPEC. Columns (4-8): Temperature measurements. We do not obtain a consistent temperature measurement for RXCJ0528.9–3927 in 4–8' region from the combined data because of the high background.

RXCJ	Band (keV)	Model	$k_B T$ (keV)				
			$0 < r < 0.5'$	$0.5 < r < 1'$	$1 < r < 2'$	$2 < r < 4'$	$4 < r < 8'$
0014.3–3022	0.4–10	model1 <sup>a</sup>	$9.37^{+1.30}_{-1.07}$	$8.54^{+0.62}_{-0.54}$	$8.20^{+0.38}_{-0.35}$	$6.74^{+0.32}_{-0.29}$	$6.56^{+1.30}_{-1.02}$
		model2 <sup>b</sup>	$9.37^{+1.31}_{-1.07}$	$8.55^{+0.62}_{-0.55}$	$8.20^{+0.39}_{-0.35}$	$6.70^{+0.32}_{-0.30}$	$6.46^{+2.14}_{-1.49}$
0043.4–2037	0.4–10	model2	$10.46^{+1.56}_{-1.33}$	$10.69^{+1.17}_{-1.00}$	$9.43^{+0.65}_{-0.59}$	$7.09^{+0.47}_{-0.43}$	$11.94^{+11.69}_{-4.03}$
		model1	$6.79^{+0.47}_{-0.41}$	$6.93^{+0.42}_{-0.37}$	$5.93^{+0.31}_{-0.28}$	$5.33^{+0.36}_{-0.34}$	$4.35^{+0.43}_{-0.37}$
0232.2–4420	0.4–10	model2	$6.79^{+0.42}_{-0.42}$	$6.93^{+0.37}_{-0.37}$	$5.91^{+0.31}_{-0.28}$	$5.13^{+0.34}_{-0.34}$	$3.49^{+0.46}_{-0.35}$
		model2	$7.67^{+0.92}_{-0.76}$	$7.36^{+0.76}_{-0.66}$	$6.99^{+0.74}_{-0.65}$	$7.37^{+1.32}_{-0.99}$	$8.13^{+5.05}_{-2.21}$
0307.0–2840	0.4–10	model1	$5.83^{+0.27}_{-0.25}$	$6.91^{+0.42}_{-0.37}$	$6.44^{+0.32}_{-0.29}$	$5.39^{+0.35}_{-0.34}$	$5.28^{+1.19}_{-0.86}$
		model2	$5.83^{+0.27}_{-0.25}$	$6.90^{+0.42}_{-0.37}$	$6.41^{+0.32}_{-0.30}$	$5.23^{+0.36}_{-0.33}$	$2.88^{+0.61}_{-0.37}$
0307.0–2840	1.0–10	model2	$6.34^{+0.42}_{-0.37}$	$7.71^{+0.69}_{-0.60}$	$8.05^{+0.63}_{-0.57}$	$7.34^{+0.87}_{-0.74}$	$6.48^{+3.61}_{-2.16}$
		model1	$5.25^{+0.26}_{-0.24}$	$6.06^{+0.34}_{-0.31}$	$6.80^{+0.42}_{-0.39}$	$6.86^{+0.69}_{-0.61}$	$3.17^{+0.50}_{-0.40}$
0528.9–3927	0.4–10	model2	$5.24^{+0.26}_{-0.24}$	$6.05^{+0.34}_{-0.31}$	$6.76^{+0.42}_{-0.39}$	$6.64^{+0.70}_{-0.60}$	$2.30^{+0.40}_{-0.30}$
		model2	$5.74^{+0.40}_{-0.36}$	$6.61^{+0.53}_{-0.46}$	$8.37^{+0.84}_{-0.72}$	$7.07^{+1.01}_{-0.84}$	$2.87^{+1.02}_{-0.63}$
0528.9–3927	1.0–10	model1	$6.22^{+0.67}_{-0.58}$	$7.16^{+0.77}_{-0.65}$	$5.75^{+0.43}_{-0.38}$	$6.70^{+0.68}_{-0.58}$	$5.59^{+2.66}_{-1.58}$
		model2	$6.21^{+0.67}_{-0.58}$	$7.12^{+0.76}_{-0.64}$	$5.68^{+0.42}_{-0.37}$	$6.30^{+0.62}_{-0.53}$	$4.30^{+2.67}_{-1.14}$
0532.9–3701	0.4–10	model1	$8.75^{+1.86}_{-1.36}$	$10.84^{+2.31}_{-1.76}$	$6.46^{+0.70}_{-0.59}$	$6.79^{+0.96}_{-0.77}$	—
		model2	$7.77^{+0.61}_{-0.53}$	$8.19^{+0.70}_{-0.61}$	$6.93^{+0.48}_{-0.43}$	$5.96^{+0.64}_{-0.56}$	$4.02^{+1.24}_{-0.81}$
0658.5–5556	2.0–12	model2	$7.77^{+0.61}_{-0.53}$	$8.21^{+0.61}_{-0.61}$	$6.96^{+0.49}_{-0.43}$	$6.04^{+0.59}_{-0.59}$	$3.28^{+1.34}_{-0.89}$
		model2	$8.44^{+0.98}_{-0.81}$	$8.28^{+0.97}_{-0.80}$	$8.07^{+0.83}_{-0.71}$	$6.73^{+1.09}_{-0.85}$	$4.61^{+5.65}_{-1.69}$
1131.9–1955	0.4–10	model1	$14.60^{+1.81}_{-1.57}$	$12.94^{+1.13}_{-0.90}$	$14.52^{+0.98}_{-0.91}$	$14.99^{+1.62}_{-1.46}$	$15.72^{+2.40}_{-2.01}$
		model2	$14.57^{+1.57}_{-1.80}$	$12.90^{+1.11}_{-0.89}$	$14.42^{+0.98}_{-0.92}$	$14.33^{+1.68}_{-1.44}$	$11.1^{+2.20}_{-2.00}$
2337.6+0016	0.4–10	model1	$6.69^{+0.46}_{-0.41}$	$7.66^{+0.47}_{-0.42}$	$9.02^{+0.61}_{-0.54}$	$6.15^{+0.36}_{-0.33}$	$2.06^{+0.11}_{-0.10}$
		model2	$6.70^{+0.47}_{-0.41}$	$7.69^{+0.47}_{-0.42}$	$9.15^{+0.63}_{-0.56}$	$6.44^{+0.41}_{-0.36}$	$2.10^{+0.14}_{-0.12}$
2337.6+0016	1.0–10	model2	$6.93^{+0.86}_{-0.70}$	$7.79^{+0.77}_{-0.66}$	$10.19^{+1.14}_{-0.94}$	$6.39^{+0.51}_{-0.51}$	$2.31^{+0.37}_{-0.32}$
		model1	$7.27^{+0.67}_{-0.58}$	$7.70^{+0.48}_{-0.43}$	$6.73^{+0.31}_{-0.29}$	$6.96^{+0.53}_{-0.46}$	$7.86^{+2.34}_{-1.56}$
2337.6+0016	0.4–10	model2	$7.26^{+0.68}_{-0.58}$	$7.67^{+0.48}_{-0.43}$	$6.66^{+0.31}_{-0.29}$	$6.48^{+0.49}_{-0.44}$	$4.75^{+2.52}_{-1.37}$
		model2	$7.80^{+1.49}_{-1.11}$	$8.30^{+1.09}_{-0.86}$	$7.43^{+0.64}_{-0.55}$	$7.11^{+1.00}_{-0.82}$	$5.26^{+8.93}_{-2.33}$

<sup>a</sup> mekal\*wabs.

<sup>b</sup> mekal\*wabs+powerlaw/b.

To test the validity of the results without a geometrical deprojection in our analysis, we apply the deprojection model provided in XSPEC (“project”) to study the deprojection effect for RXCJ0307.0–2840. This model performs a three dimension to two dimension projection of shells onto annuli. It is assumed that the inner boundary is specified by the outer boundary of the next annulus in. In the “project” model, for each shell in a combined fit to all annuli spectra simultaneously, the contribution of each ellipsoidal shell to each annulus is determined and the spectral fitting results are then determined. In this fitting the outer shells are not affected by the emission from the inner shells. Similar work has been described by Pizzolato et al. (2003). Figure 5.8 presents the temperature profiles from the spectral fit with and without projected modeling in the 0.4–10 keV energy band. The



temperature gradient becomes slightly more significant when the geometrical deprojection effect is taken into account. The differences are, however, within the error bars and can thus be neglected. The relatively small effect of the deprojection is due to the steep surface brightness profiles of clusters which strongly reduce the influence of the emission from the outer shells on the observed spectra of the central regions. Therefore, the application of deprojection gives really significant improvement only if the count statistics is very high (e.g. Matsushita et al. 2002).

Systematic differences in the temperature profiles caused by the inclusion of the 0.4–1 keV band in the spectral analysis are not the same among the clusters. For example, RXCJ1131.9–1955 is not affected at all, RXCJ0043.4–2037 and RXCJ0232.2–4420 are affected in the outskirts, while RXCJ0014.3–3022, RXCJ0307.0–2840 and RXCJ0528.9–3927 are affected in the center. Since the instrumental setup used to observe this sample is the same, it hardly is an instrumental artifact. However, more detailed analyses are needed in order to distinguish between the Galactic and extragalactic origin of this component in the outskirts of some of the clusters in our sample (e.g. Finoguenov et al. 2003).

### 5.3.3 Modeling RXCJ0307.0–2840

We use RXCJ0307.0–2840 as an illustrative example to demonstrate the accuracy of measurements of the total gravitating cluster mass and the gas mass fraction attainable with the XMM-Newton observations of the REFLEX-DXL-like clusters. Similar analyses of the REFLEX-DXL clusters are in progress. RXCJ0307.0–2840 is also very bright, but at a slightly lower redshift than the selection range for the REFLEX-DXL clusters.

#### 5.3.3.1 Gas distribution

The regularity of the photon distribution shown in Fig. 5.9 suggests that there are no large substructures in RXCJ0307.0–2840. We thus assume a radially symmetric gas distribution. In order to get the actual gas distribution we directly deproject the data from the spectroscopic analysis to get the gas mass profile (cf. Fabian et al 1981; Kriss et al. 1983). We divide the rings used for the temperature determinations into small subrings and fit the normalization for each subring separately, fixing the temperature profile to the values obtained from the above spectral analysis, the metallicities to  $Z = 0.2Z_{\odot}$ , the redshifts to  $z_{\text{opt}}$  as given in Table 5.4, and the Galactic absorption to  $n_{\text{H}}$  as given in Table 5.1. We use a constant metallicity here since we did not detect a significant variation of metallicity with radius within the error limits of our analysis. In the soft band, the X-ray emission is almost independent of the temperature (Fabricant et al. 1980). The gas mass in each spherical shell is proportional to the square root of the integral emission, which can be calculated from the normalization of the spectroscopic analysis (e.g. Vikhlinin et al. 1999).

In Fig. 5.10 we show the electron number density profiles for RXCJ0307.0–2840. Here,  $l' = 0.240$  Mpc at  $z = 0.2578$ . For the fits we use the standard  $\beta$  model

$$n_e(r) = n_{e0} \left[ 1 + \left( \frac{r}{r_c} \right)^2 \right]^{-\frac{3\beta}{2}}, \quad (5.1)$$

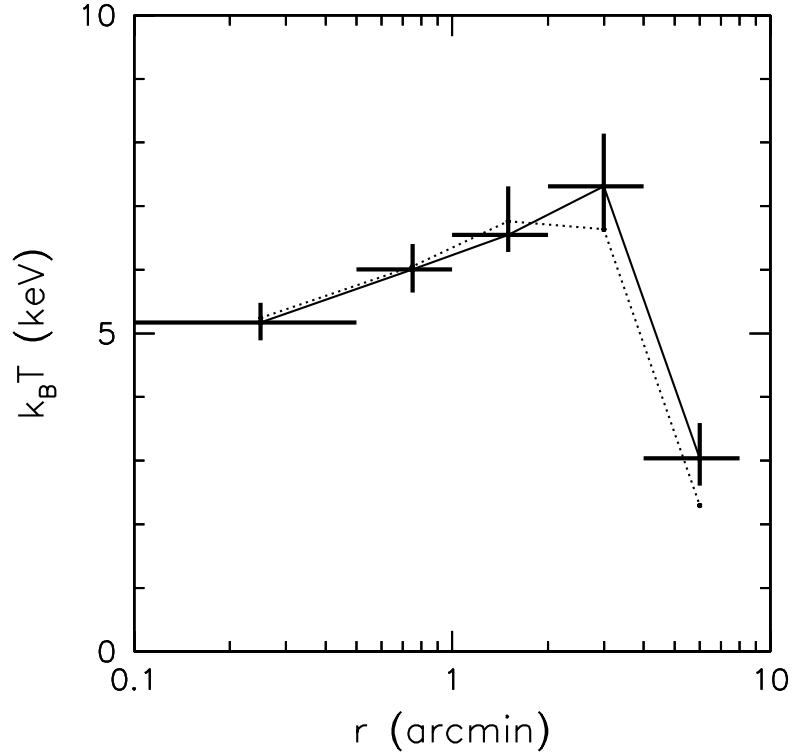


**Figure 5.8:** Temperature profiles for RXCJ0307.0–2840 from spectral fits with (solid lines) and without (dotted lines) a geometrical deprojection.

with the core radius  $r_c$  and the shape parameter  $\beta$ . The parameters from the best  $\chi^2$  fits are listed in Table 7.5. The energy band used for the spectral fits does not affect the normalization, which corresponds to the electron number density profile (cf. Fig. 5.10).

### 5.3.3.2 Temperature distribution

The precise estimate of the temperature structure greatly contributes to a reliable mass distribution. The temperature profile of RXCJ0307.0–2840 drops towards the center due to cooling. We found that the parameterization

$$k_B T(r) = \frac{1}{Ar^2 + Br + C} \quad (5.2)$$

fits the measured temperature profiles quite well. Fig. 5.11 presents the best  $\chi^2$  fit for RXCJ0307.0–2840 with the parameters given in Table 7.5. The temperature profile in the outermost regions can be fitted by a polytropic model,  $k_B T(r) = k_B T_0 (n_e/n_{e0})^{\gamma-1}$  (e.g. Finoguenov et al. 2001b). In order for the system to be convectionally stable, the value of  $\gamma$  should not exceed 5/3. Using the results of the spectral analysis in the 0.4–10 keV (1–10 keV) band we obtain  $\gamma = 1.59$  ( $\gamma = 1.46$ ), which fulfills the stability criteria.

### 5.3.3.3 Mass distribution

We assume the intracluster gas to be in hydrostatic equilibrium with the underlying gravitational potential dominated by the dark matter component. For the cosmological constant  $\Lambda = 0$  we have

$$\frac{1}{\mu m_p n_e} \frac{d(n_e k_B T)}{dr} = - \frac{GM_{\text{DM}}(r)}{r^2}, \quad (5.3)$$

where  $n_e$  and  $k_B T$  are the electron number density and temperature distributions, respectively, and  $\mu = 0.62$  is the mean molecular weight per hydrogen atom (e.g. Zakamska & Narayan 2003).

Analytic models of the gas density and temperature profiles can be easily combined with Eq.(7.4) to obtain the mass profile:

$$M(< r) = \frac{r^2}{\mu m_p G} k_B T(r) \left[ \frac{3\beta r}{r_c^2 + r^2} + (2Ar + B)k_B T(r) \right]. \quad (5.4)$$

We determine the mass distribution by using our temperature model and the  $\beta$  gas density model. We use a Mont-Carlo simulation to calculate the error bars.

Masses measured by the strong gravitational lensing are sometimes found to be larger compared to the measured masses based on X-rays (Böhlinger et al. 2000; Wu 2000; Wu et al. 1998). High spatially resolved temperature profiles could help to resolve this discrepancy. In order to test the effects of temperature gradients we compare the mass estimates obtained under the assumptions of isothermality using the global temperature as measured in the  $0.5 < r < 4'$  region fitted in the 1–10 keV band, and of non-isothermality. The mass and gas mass profiles are plotted in Fig. 5.12. Under the assumption of hydrostatic equilibrium and isothermality, the virial radius and the total gravitational cluster mass are 2.14 Mpc and  $8.8 \times 10^{14} M_\odot$ , respectively.

### 5.3.3.4 Modeling a NFW mass distribution

Navarro et al. (1997; NFW) described a universal density profile from numerical simulations in hierarchical clustering scenarios,

$$\rho_{\text{DM}}(r) = \frac{\delta_{\text{crit}} \rho_{\text{crit}}}{(r/r_s)(1 + r/r_s)^2}, \quad (5.5)$$

where  $\delta_{\text{crit}}$  and  $r_s$  are the characteristic density and scale of the halo, respectively, and  $\rho_{\text{crit}}$ , the critical density of the Universe at the cosmic epoch  $z$ .  $\delta_{\text{crit}}$  is related to the concentration parameter of a dark halo  $c = r_{\text{vir}}/r_s$  by

$$\delta_{\text{crit}} = \frac{200}{3} \frac{c^3}{\ln(1+c) - c/(1+c)}. \quad (5.6)$$

We fit the observational temperature profile to obtain the parameters  $\rho_s = \delta_{\text{crit}} \rho_{\text{crit}}$  and  $r_s$  if we assume that the hot gas is in hydrostatic equilibrium with the dark matter. The

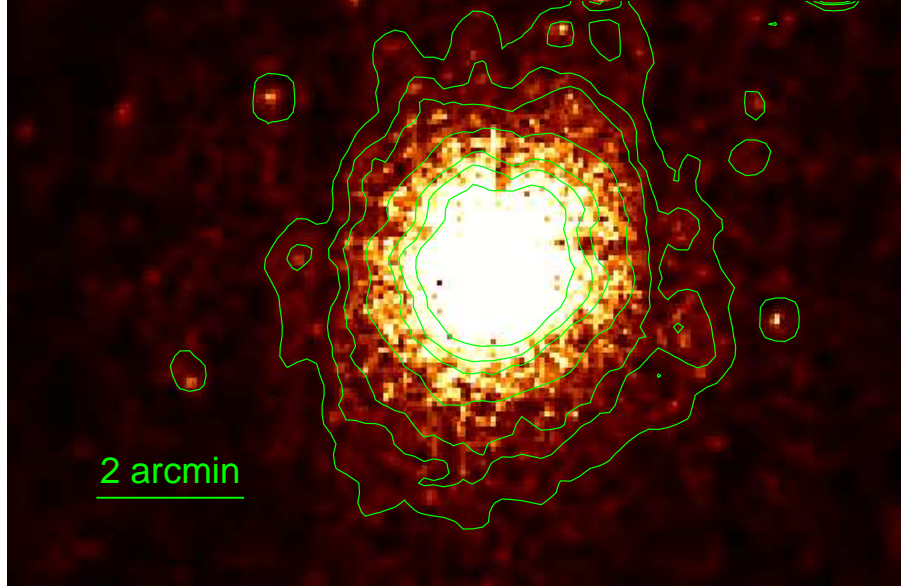


**Figure 5.9:** Merged image from the three instruments for RXCJ0307.0–2840 in the 0.5–2 keV band. Superposed contours suggest a quite regular morphology.

former is well fitted by a standard  $\beta$  profile. The parameters of the best fit of the NFW profile are presented in Table 7.5. The virial radius and virial mass estimates are smaller than the estimates under the assumption of isothermality.

The NFW model describes the mass and gas mass fraction in the outer region well. Due to the cuspy NFW profile in the cluster center, the temperature fit based on the NFW model is higher than the observations. As a result, the gas mass fraction becomes lower in the center. But for this small central region we can not resolve the temperature structure well enough to perfectly recover the dark matter mass profile at the small radii.

### 5.3.3.5 Modified hydrostatic equilibrium with $\Lambda$

To be consistent with our background cosmological model with  $\Lambda \neq 0$  we should expect a second-order modification of the equation of hydrostatic equilibrium in the form

$$\frac{1}{\mu m_p n_e} \frac{d(n_e k_B T)}{dr} = -\frac{GM_{\text{DM}}(r)}{r^2} + \frac{\Lambda c^2}{3} r. \quad (5.7)$$

The effect of a non-zero  $\Lambda$  is smaller than one percent and can thus be neglected compared to the relative error in our mass estimations. Sussman & Hernandez (2003) also point out a small effect of  $\Lambda$  on virialized structures, and that it could be significant only in the linear regime on large scales of  $r \sim 30$  Mpc.

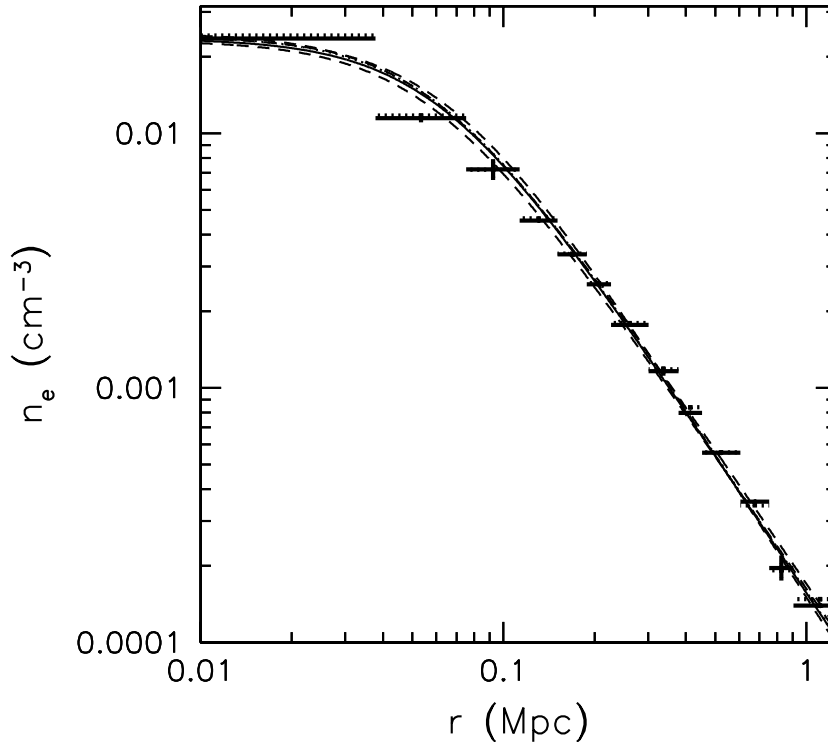


**Figure 5.10:** Measured electron number density profiles of RXCJ0307.0–2840 fitted in the 0.4–10 keV band (dotted lines) and 1–10 keV band (solid lines), respectively. The corresponding curves present the best fits using the standard  $\beta$  model with the confidence intervals (dashed curves).

### 5.3.3.6 Gas mass fraction distribution

The distribution of the gas mass fraction is obtained according to the definition  $f_{\text{gas}}(r) = M_{\text{gas}}(r)/M_{\text{DM}}(r)$ . Since the derived gas mass is not completely unrelated to the derived total mass, we calculate the error bars of the gas fraction,

$$\Delta f_{\text{gas}} = \sqrt{(\Delta M_{\text{gas}} M_{\text{DM}})^2 + (M_{\text{gas}} \Delta M_{\text{DM}})^2} / M_{\text{DM}}^2. \quad (5.8)$$

The profile of the gas mass fraction based on the NFW modeling is steeper in the central region as seen in Fig. 5.13. In both mass modelings the gas fractions increase with radius, and range from  $f_{\text{gas}} = 0.035 \pm 0.012$  to  $0.138 \pm 0.026$  in the outermost regions ( $r_{\text{out}} = 1.441$  Mpc) (see Table 7.5).

These results are in good agreement with the measurements of Allen et al. (2002) based on Chandra observations of seven clusters yielding  $f_{\text{gas}} \sim 0.105\text{--}0.138$ , and with the measurements of Sanderson et al. (2003) based on ASCA GIS & SIS and ROSAT/PSPC observations of 66 clusters yielding  $f_{\text{gas}} = 0.13 \pm 0.01 h_{70}^{-3/2}$ . Our value is below the universal baryon fraction obtained with the recent WMAP measurement  $f_b = \Omega_b/\Omega_m = 0.166$ , where

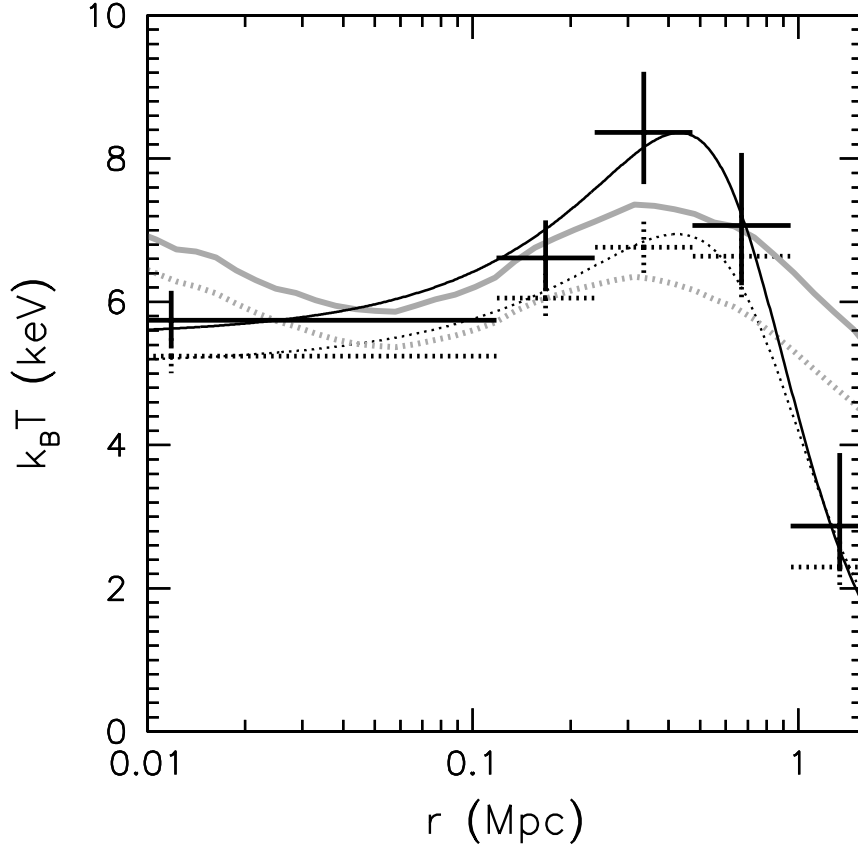


**Figure 5.11:** Measured temperatures of RXCJ0307.0–2840 fitted in the 0.4–10 keV band (dotted lines) and 1–10 keV band (solid lines). The corresponding curves show the best fits using the NFW profile (grey) and Eq.(6.6) (black).

$\Omega_b h^2 = 0.0224$  and  $\Omega_m h^2 = 0.135$  (Spergel et al. 2003). This reassures the estimate of the mass distribution.

We also make use of the  $8 < r < 10'$  region to obtain an upper limit of the gas mass in this shell applying the model “mekal+wabs” without residual background subtraction. The upper limit of the total gas mass within 10 arcmin (2.37 Mpc) is  $2.49 \times 10^{14} M_\odot$ . Based on the above mass modeling described by Eq.(5.4), the upper limit of the gas fraction within 10 arcmin is 0.49. This unreasonably high value confirms that the background dominates in this region.

## 5.4 Summary and Conclusions

We studied eight clusters of the REFLEX-DXL sample, selected from the REFLEX cluster survey at redshifts around  $z \sim 0.3$ , and one supplementary cluster at redshift  $z = 0.2578$ . The data are from the MOS1, MOS2 and pn detectors of XMM-Newton. The consistent results from the three detectors, obtained by excluding the energies below 1 keV, give a good confidence in the applied method and provide tight constraints on the ICM parameters

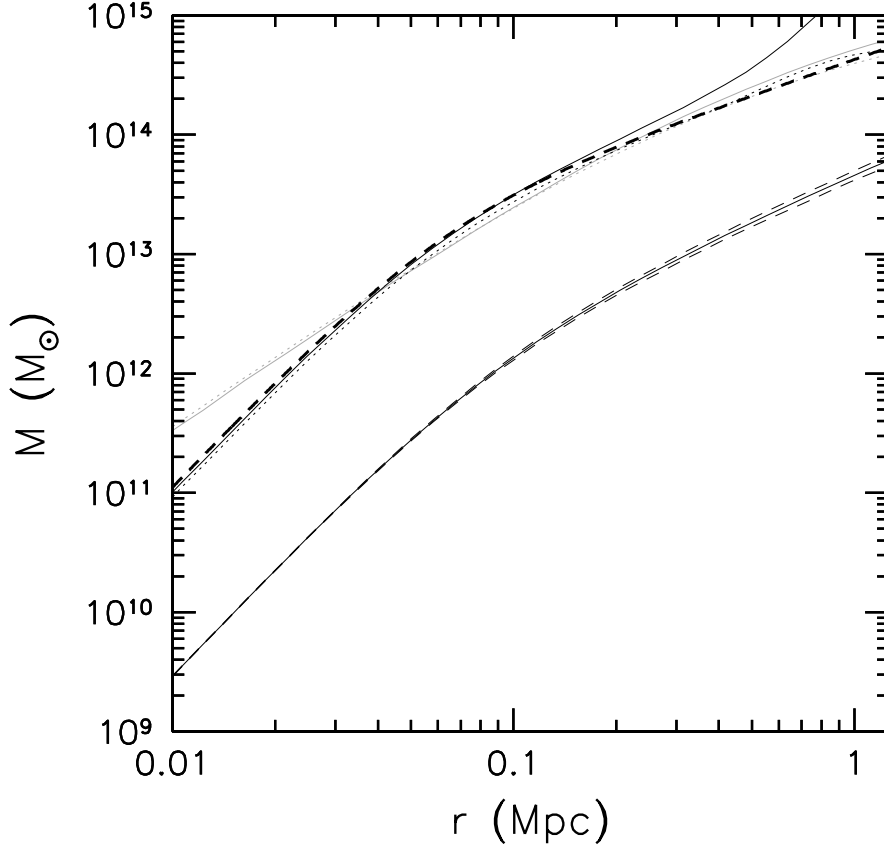


**Figure 5.12:** Mass profiles (top) of RXCJ0307.0–2840 based on the temperature measurements fitted in the 0.4–10 keV band (dotted curves) and 1–10 keV band (solid curves) using the NFW model (grey) and Eq.(5.4) (black). An additional dashed curve presents the mass profile under the assumption of isothermality. The solid curve (bottom) with the confidence intervals (dashed curves) presents the gas mass distribution.

like the temperature, metallicity, and redshift.

Some of the clusters have been previously studied with ASCA, ROSAT and Chandra. The Chandra measurement of the temperature of RXCJ0658.5–5556 includes mainly the central  $r < 3'$  region, where the temperature is high. We measure the global temperatures over a larger radial range  $0.5 < r < 4'$  and  $r < 8'$ , respectively.

The parameter which best characterizes cluster mass, and which is most relevant for studies of the LSS and cosmology, is the hot temperature of the bulk of the ICM. To avoid contamination by a possible central cooling core and by a possible soft excess or residual calibration uncertainties, we excluded the central  $r < 0.5'$  region and the softest part of the X-ray spectrum ( $< 1$  keV) yielding reliable temperatures. These are the global temperatures that will be used in Paper I to derive the X-ray temperature function for this sample.

We obtained the spatially resolved X-ray temperature profiles for each cluster. For the determination of temperature profiles, the good statistics of the data allowed us to derive

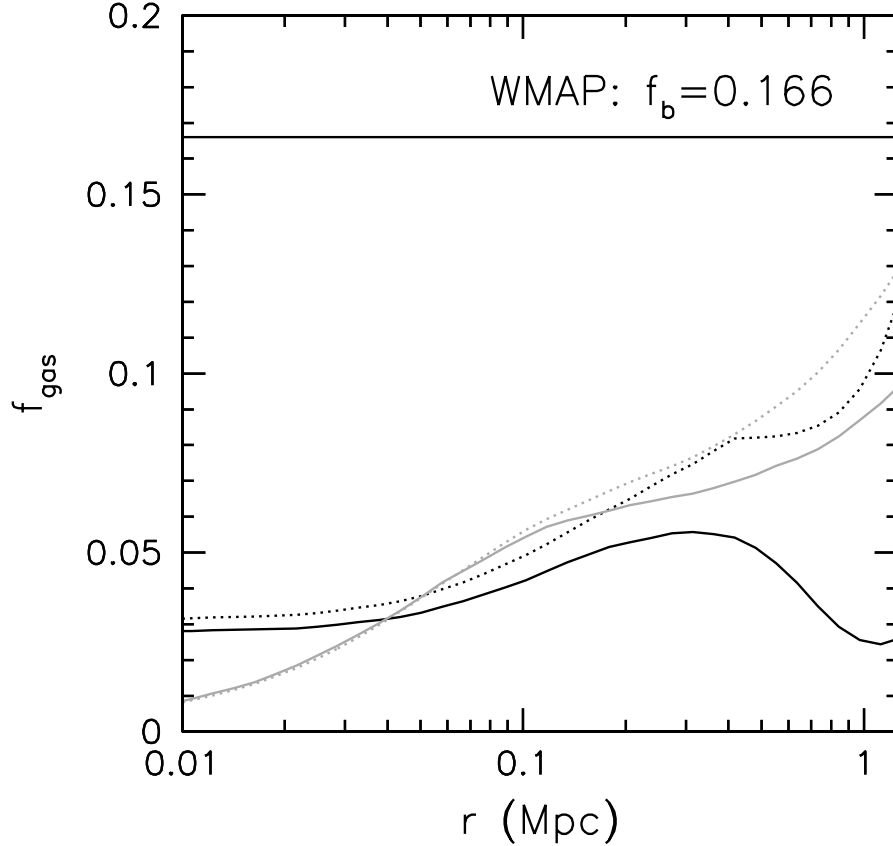


**Figure 5.13:** Gas mass fraction distributions of RXCJ0307.0–2840 based on the temperature measurements fitted in the 0.4–10 keV band (dotted curves) and 1–10 keV band (solid curves) using the NFW model (grey) and Eq.(5.4) (black).

temperature values in five radial bins. In the inner regions an accuracy of better than 10–20 % can still be reached while the errors increase in the outer or outermost two bins. The temperature varies as a function of radius by factors of 1.5–2. The intracluster gas is cool in the center of RXCJ0232.2–4420, RXCJ0307.0–2840, RXCJ0528.9–3927, and RXCJ1131.9–1955. No significant cooling gas is found with temperatures below 2 keV. In the outer region, the temperature drops at different levels. The differences of the temperature profiles in the cluster center may reveal that some clusters have relaxed cooling cores (but not all) and to some degree that we see the effect of non-gravitational processes. In this respect, it is remarkable that cooling cores are not only found in clusters with symmetric and regular X-ray images which might suggest a relaxed dynamical state, but also in the elongated, very disturbed cluster RXCJ1131.9–1955.

To study RXCJ0307.0–2840 in detail, we find a model which fits the complex temperature profile of this cluster quite well.

The mass distribution of this cluster, based on the precise measurements of the distributions of the temperature and gas density, is similar to the mass distribution obtained under the assumption of isothermality within the region we can measure. We investigated



**Table 5.6:** Parameters of each model from the best  $\chi^2$  fits.  $r_{\text{out}} = 1.441$  Mpc is the outermost region where we can measure these parameters.  $r_{500}$  and  $r_{\text{vir}}$  are measured from the data.

Model	parameter	0.4–10 keV	1–10 keV
$\beta$	$r_c$ (Mpc)	$0.061 \pm 0.004$	$0.062 \pm 0.004$
	$n_{e0}$ ( $10^{-2} \text{cm}^{-3}$ )	$2.43 \pm 0.03$	$2.37 \pm 0.04$
	$\beta$	$0.60 \pm 0.02$	$0.60 \pm 0.02$
Eq.(6.6)	$A$ ( $\text{Mpc}^{-2} \text{keV}^{-1}$ )	$0.283 \pm 0.046$	$0.331 \pm 0.082$
	$B$ ( $\text{Mpc}^{-1} \text{keV}^{-1}$ )	$-0.240 \pm 0.028$	$-0.285 \pm 0.052$
	$C$ ( $\text{keV}^{-1}$ )	$0.195 \pm 0.004$	$0.181 \pm 0.007$
NFW	$r_s$ (Mpc)	$0.267 \pm 0.028$	$0.306 \pm 0.034$
	$\rho_s$ ( $10^{15} \text{M}_\odot \text{Mpc}^{-3}$ )	$2.2 \pm 0.3$	$1.9 \pm 0.5$
	$c$	$5.81 \pm 0.59$	$5.56 \pm 0.68$
	$M_{500}$ ( $10^{14} \text{M}_\odot$ )	$4.10 \pm 0.37$	$5.13 \pm 0.85$
	$r_{500}$ (Mpc)	1.038	1.116
	$M_{\text{vir}}$ ( $10^{14} \text{M}_\odot$ )	$5.52 \pm 0.49$	$7.13 \pm 1.18$
	$r_{\text{vir}}$ (Mpc)	1.550	1.701
	$f_{\text{gas}}(r < r_{\text{vir}})$	$0.144 \pm 0.028$	$0.124 \pm 0.036$
	$M_{r_{\text{out}}}$ ( $10^{14} \text{M}_\odot$ )	$5.17 \pm 0.46$	$6.30 \pm 1.04$
	$f_{\text{gas}}(r < r_{\text{out}})$	$0.138 \pm 0.026$	$0.112 \pm 0.032$
	Eq.(5.4)	$M_{500}$ ( $10^{14} \text{M}_\odot$ )	$6.86 \pm 0.01$
$r_{500}$ (Mpc)		1.231	1.118
$M_{r_{\text{out}}}$ ( $10^{14} \text{M}_\odot$ )		$6.91 \pm 0.01$	$16.46 \pm 4.69$
$f_{\text{gas}}(r < r_{\text{out}})$		$0.103 \pm 0.010$	$0.035 \pm 0.012$

the gas mass fraction of RXCJ0307.0–2840 and found an increasing gas mass fraction as a function of radius, which is typical for most clusters. In the outermost region of the cluster, it is below the value of the universal baryon fraction. The uncertainty of the gas fraction is mainly caused by the temperature measurement. Therefore, a reliable determination of the temperature profile is a key point to obtain the precise estimates of both the mass and the gas mass fraction. It plays an important role in the M-T scaling relation.

## Acknowledgements

The XMM-Newton project is supported by the Bundesministerium für Bildung und Forschung, Deutschen Zentrum für Luft und Raumfahrt (BMBF/DLR), the Max-Planck Society and the Haidenhaim-Stiftung. We acknowledge Jacqueline Bergeron, PI of the XMM-Newton observation of the CDFS, and Martin Turner, PI of the XMM-Newton observation of RXJ0658.5-5556. We acknowledge Steve Sembay who kindly provides us the software to generate the rmf for MOS and Wolfgang Pietsch, Michael Freyberg, Frank Haberl and Ulrich G. Briel providing useful suggestions. YYZ acknowledges receiving the International Max-Planck Research School Fellowship. AF acknowledges receiving the Max-Planck-Gesellschaft Fellowship. PS acknowledges support under the DLR grant No. 50 OR 9708 35. YYZ thanks Linda Pittroff for careful reading the manuscript and useful suggestions.



# 6 X-ray properties in massive galaxy clusters

## Abstract

We selected an almost volume complete sample of 13 distant, X-ray luminous (DXL,  $z \sim 0.3$ ) clusters and one supplementary cluster at  $z = 0.2578$  from the REFLEX Survey (the REFLEX-DXL sample) to perform a detailed study of their X-ray properties using XMM-Newton observations. Based on precise gas density and temperature distributions, we obtain robust cluster masses. We derived gas mass fractions in the narrow range of 0.06–0.15. This agrees with previous cluster studies and the WMAP baryon fraction measurement. The cluster mass measurements with improved accuracy tighten scaling relations. The profiles of the surface brightness, temperature, entropy, and mass are well characterized by a self-similar behavior at  $r > 0.1r_{\text{vir}}$ . This is the origin of the small scatter of the correlations of various cluster properties. We confirmed previous studies with a higher precision on the normalization of the correlations such as  $L$ – $T$ ,  $L$ – $M$ ,  $M$ – $T$  and  $M_{\text{gas}}$ – $T$  relations. We found that the evolution of the correlations can be accounted for by the redshift evolution correction. We investigated the intrinsic scatter of the correlations, which, for example, gives  $(0.30 | 0.17)$  for  $(M | T)$  of the  $M$ – $T$  relation.

## 6.1 Introduction

The number density of galaxy clusters probes the cosmic evolution of large-scale structure (LSS) and thus provides an effective test of cosmological models. It is sensitive to the matter density,  $\Omega_{\text{m}}$ , and the amplitude of the cosmic power spectra on cluster scales,  $\sigma_8$  (e.g. Schuecker et al. 2003). Its evolution is sensitive to the dark energy whose density is characterized by the parameter  $\Omega_{\Lambda}$  (e.g. Vikhlinin et al. 2002; Allen et al. 2004; Chen & Ratra 2004). The most massive clusters show the strongest evolutionary effects. They are therefore especially important in tracing LSS evolution. In addition, the X-ray properties of the most massive clusters are well described in hierarchical modeling since they are less affected by non-gravitational processes than low mass clusters. The structure of the X-ray emitting intracluster plasma is thus predominantly determined by gravitational effects and shock heating. Only with decreasing cluster mass and intracluster medium (ICM) temperature, non-gravitational effects play an important role before and after the shock heating (Voit & Bryan 2001; Voit et al. 2002; Zhang & Wu 2003; Ponman et al. 2003). Therefore, the most massive clusters provide the cleanest results in comparing theory with observations.

Excluding the cooling cores (Fabian & Nulsen 1977), a self-similar scaling of the ICM properties such as the temperature, density and entropy of massive clusters ( $> 4$  keV) is indicated in the ROSAT and ASCA observations (e.g. Markevitch 1998; Markevitch et al. 1998; Vikhlinin et al. 1999, 2005a; Arnaud et al. 2002a; Reiprich & Böhringer 2002; Zhang

et al. 2004a, 2004b, 2005b; Ota & Mitsuda 2005; Pratt & Arnaud 2005) and simulations (e.g. Borgani 2004; Borgani et al. 2004; Kay 2004; Kay et al. 2004). Precise measurements of the ICM structure allow accurate cluster mass and gas mass fraction determinations. This is important for the study of the X-ray scaling relations and correlations, and to understand their intrinsic scatter. On-going mergers, partially account for the scatter in the scaling relations. On-going cluster mergers may not only lead to a temporary increase in the cluster temperature and X-ray luminosity (Randall et al. 2002), but also increase the slope of the surface brightness profile. The luminosity–temperature ( $L$ – $T$ , e.g. Isobe et al. 1990; Markevitch 1998; Arnaud & Evrard 1999; Ikebe et al. 2002; Reiprich & Böhringer 2002), luminosity–mass ( $L$ – $M$ , e.g. Reiprich & Böhringer 2002; Popesso et al. 2005), mass–temperature ( $M$ – $T$ , e.g. Nevalainen et al. 2000; Finoguenov et al. 2001b; Neumann & Arnaud 2001; Xu et al. 2001; Horner 2001; Reiprich & Böhringer 2002; Sanderson et al. 2003; Pierpaoli et al. 2001, 2003), and luminosity–metallicity ( $L$ – $Z$ , e.g. Garnett 2002) relations have been intensively studied for comparison of theory with simulations and observations.

The ROSAT-ESO Flux-Limited X-ray (REFLEX, Böhringer et al. 2001a, 2004a) galaxy cluster survey provides the largest homogeneously selected catalog of X-ray clusters of galaxies so far. It provides the basis to construct an unbiased subsample of clusters with specific selection criteria. We exploit it to compose a sample of distant, X-ray luminous (DXL) clusters in the redshift range,  $z = 0.27$  to  $0.31$ , with  $L_X \geq 10^{45}$  erg s $^{-1}$  for the 0.1–2.4 keV band and one supplementary cluster at  $z = 0.2578$  (the REFLEX-DXL sample)<sup>1</sup>. The volume completeness correction can be done using the well known selection function of the REFLEX survey (Böhringer et al. 2004a).

A prime goal for the study of the REFLEX-DXL sample is to obtain reliable ICM properties such as temperature structure (Zhang et al. 2004a, Paper II). It can be used to test the evolution of the temperature function (e.g. Henry 2004) comparing to nearby cluster samples. The ICM properties have been used to determine accurate cluster mass and gas mass fraction. The scaling relations and their intrinsic scatter can then be investigated in detail. The normalization of the correlations can be constrained with improved accuracy. The evolution of the correlations can thus be investigated by comparing the REFLEX-DXL sample (at  $z \sim 0.3$ ) to the nearby samples.

This paper is organized as follows. In Sect. 7.2, we describe the data reduction. In Sect. 7.3, we study the X-ray properties of the ICM and determine the total masses and gas mass fractions based on precise gas density and temperature profiles. In Sect. 6.4, we investigate the scaling relations and in Sect. 6.5, we show the correlations of the X-ray properties of the REFLEX-DXL clusters. Sect. 6.6 provides a discussion of the peculiarities of the individual clusters accounting for the scatter around the self-similar model. In Sect. 7.5, we draw our conclusions. We adopt a flat  $\Lambda$ CDM cosmology with the density parameter  $\Omega_m = 0.3$  and the Hubble constant  $H_0 = 70$  km s $^{-1}$  Mpc $^{-1}$ . All coordinates are given in epoch J2000. We adopt the solar abundance values of Anders & Grevesse (1989). Confidence intervals correspond to the 68% confidence level, unless explicitly stated

---

<sup>1</sup>A flat cosmological model with the Hubble constant  $H_0 = 50$  km s $^{-1}$  Mpc $^{-1}$  was used for the  $L_X$  threshold in the sample construction. This luminosity threshold corresponds to  $L_X \geq 5.9 \times 10^{44}$  erg s $^{-1}$  for a flat  $\Lambda$  cold dark matter ( $\Lambda$ CDM) cosmology with the density parameter  $\Omega_m = 0.3$  and the Hubble constant  $H_0 = 70$  km s $^{-1}$  Mpc $^{-1}$

otherwise.

## 6.2 Data reduction

### 6.2.1 Data preparation

All 14 REFLEX-DXL clusters were observed by XMM-Newton. Some properties of these observations and an overview of the sample are described in Böhringer et al. (2005a, Paper I). The observations of 5 clusters in AO-1 were heavily contaminated by flares. They have been re-observed in AO-3 in which four have sufficient quality for a detailed study. Zhang et al. (2004a) investigated the temperature structure of 9 REFLEX-DXL clusters observed in AO-1. Finoguenov et al. (2005) applied the 2-dimensional approach to study the structure such as pressure for those 9 REFLEX-DXL clusters. We use the XMMSAS v6.0 software for the data reduction. For all detectors, the thin filter has been used. The MOS data have been taken in Full Frame (FF) mode. The pn data have been taken either in Extended Full Frame (EFF) mode or in FF mode. For pn, the fractions of the out-of-time (OOT) effect are 2.32% and 6.30% for the EFF mode and FF mode, respectively. An OOT event list file is created and used to statistically remove the OOT effect.

Above 10 keV (12 keV), there is little X-ray emission from clusters for MOS (pn) due to the low telescope efficiency at these energies. The particle background therefore dominates. The light curve in the range 10–12 keV (12–14 keV) for MOS (pn), binned in 100 s intervals, is used to monitor the particle background and to excise periods of high particle flux. Furthermore, episodes of “soft proton flares” (De Luca & Molendi 2004) were detected in the light curve for the 0.3–10 keV band, binned in 10 s intervals. The 10 s interval bin size is chosen for the soft band to provide a similar good photon statistics as for the hard band. The average and variance of the count rate (ctr) have been interactively determined for each light curve from the ctr histogram. Good time intervals (GTIs) are those intervals with ctrs below the threshold, which is  $3\sigma$  above the average. The GTIs of both the hard band and the soft band have been used to screen the data. The background observations have also been individually screened for each cluster using the GTIs obtained in both the hard band and the soft band. Since the REFLEX-DXL clusters are luminous and hot, a low energy cut-off of 1 keV has been chosen for the cluster spectral analysis to avoid possible soft excess. Settings of  $FLAG = 0$  and  $PATTERN < 13$  ( $PATTERN < 5$ ) for MOS (pn) have been used in the screening process.

### 6.2.2 Source detection

Over half of the clusters show clear substructures or/and elongations. An “edetect\_chain” command has been used to detect point-like sources. The point sources outside the cluster center are easily detected and subtracted correctly. The substructures have also been subtracted before spectral analysis and surface brightness profile determination. Only the main component has been used for the further studies.

However, the substructure, which shows a low surface brightness extension, is difficult to subtract correctly because it shows a less significant boundary relative to the surroundings. Point-like sources in the cluster center are hard to identify because their emission is blended

## 6 X-ray properties in massive galaxy clusters

**Table 6.1:** Properties of the point-like sources in the cluster center covering  $r < 25''$ . Col. (1): Cluster name. Cols. (2–3): Sky coordinates of the point-like source. Col. (4): Index of the best power law fit. Col. (5): X-ray luminosity of the point-like source.

RXCJ	X-ray centroid		Power law	$L_X$ (0.1–2.4 keV) ( $10^{44}$ erg s $^{-1}$ )
	R.A.	decl.		
0232.2–4420	02 32 18.6	–44 20 48.2	$1.77 \pm 0.03$	$5.22 \pm 0.27$
0437.1+0043	04 37 09.8	+00 43 48.9	$1.82 \pm 0.03$	$3.56 \pm 0.18$
0528.9–3927	05 28 52.6	–39 28 16.8	$1.70 \pm 0.05$	$3.20 \pm 0.27$
1131.9–1955	11 31 54.2	–19 55 39.8	$1.75 \pm 0.04$	$1.97 \pm 0.08$
2308.3+0211	23 08 21.6	–02 11 29.1	$1.67 \pm 0.05$	$2.24 \pm 0.12$
2337.6+0016	23 37 35.3	+00 15 52.1	$1.80 \pm 0.06$	$1.02 \pm 0.10$

with the strongly peaked cluster emission, in particular in cooling core clusters (CCCs, defined in Sect. 7.3.6). It can thus be difficult to subtract those point sources. Cluster emission is thermal and point source emission is expected to be non-thermal. The spectral shape can thus be used to identify point sources. A spectrum well fitted by a power law is usually a sign of contamination by point sources. We studied the peculiarities in the individual clusters and checked the possible presence of point sources in the cluster center. At the angular resolution of the observations, it is in some cases difficult to distinguish between a steep cooling core cusp and a central point source (an AGN in central dominant galaxy). We therefore also checked the spectral signature of the photons from this region. We found that both “mekal” and “powerlaw” models provide acceptable fits to the spectra extracted from the cluster center of those clusters. It can be either an evidence of point source contamination or a result due to poor statistics. We only checked the properties of these central regions, but we are not confident enough to subtract those suspicious regions before the further data reduction. The central photon statistics does not allow for a clear discrimination and we can not rule out a point source contribution to the cooling core cusp for the clusters listed in Table 6.1.

### 6.2.3 Background subtraction

The background consists of several components. They exhibit different spectral and temporal characteristics (e.g. De Luca & Molendi 2001; Lumb et al. 2002; Read & Ponman 2003). The background components can be approximately divided into two groups (cf. Zhang et al. 2004a). Group I contains the background components showing significant vignetting (here after BVIGs), e.g. the cosmic X-ray background (CXB). Group II contains the components showing little or no vignetting (here after BNVIGs), e.g. particle-induced background.

It is safe to use a local background only if the vignetting effect for the source and the background regions is similar. It becomes less reliable if large vignetting corrections are needed. The REFLEX-DXL cluster emission has covered most of the FOV ( $r \sim 8'$ ), the only available local background is the outskirts of the FOV, which need large vignetting corrections. Also the background component caused by the instrumental lines is different from position to position which cannot be accounted by a local background. Additionally,

the vignetting effect is significant at energies above 5 keV. Therefore clusters with temperatures above 5 keV, e.g. the REFLEX-DXL clusters, tend to show a soft excess when the local background has been used. Therefore, a local background is not the best choice for the REFLEX-DXL clusters.

Suitable background observations for such hot clusters are XMM-Newton pointings of almost blank fields using the same instrumental set-up (e.g. a particular filter). The blank sky accumulations in the Chandra Deep Field South (CDFS) have been chosen as background. For the CDFS observations, also the thin filter has been used for all detectors and the FF (EFF) mode has been used for MOS (pn). In Zhang et al. (2005a), we have investigated the blank sky accumulations in Lumb et al. (2002) as an alternative background comparing to the CDFS pointings. We found that the measurements vary within  $1\sigma$  in both the spectral and surface brightness analyses.

Suitable background pointings guarantee similar BVIGs as for the targets in the same detector coordinates. One can subtract such a background extracted in the same detector coordinates as for the targets. However, the difference between the target and background should be also taken into account as a residual background in the background subtraction. This can be done for the REFLEX-DXL clusters because the cluster X-ray emission covers less than half of the whole field of view (FOV). The outer parts (e.g.  $9.2' < r < 11.5'$ ) of the FOV have been used to analyze the residual background.

### 6.2.3.1 Spectral analysis

We use the XSPEC v11.3.0 software for the spectral analysis. A double background subtraction procedure can be applied in two ways in the spectral analysis. One approach was firstly described in Zhang et al. (2004a, 2005a, here after DBS I). The other method was well illustrated in Pratt & Arnaud (2002, here after DBS II). We developed both pipelines to perform the data reduction and obtained similar results using these two approaches, which indirectly tested the two approaches. For a given region of interest covering cluster emission, the spectrum has been extracted from the background pointings in the same detect coordinates as for the target.

Both, the response matrix file (rmf) and auxiliary response file (arf), have to be used to recover the correct spectral shape and normalization of the cluster emission component. The following has to be taken into account for the rmf and arf. (i) Pure redistribution matrix giving the probability that a photon of energy  $E$ , once detected, will be measured in data channel  $PI$ . (ii) Quantum efficiency (without any filter, which, in XMM-Newton calibration, is called closed filter position) of the CCD detector. (iii) Filter transmission. (iv) Geometric factors such as bad pixel corrections and gap corrections (e.g. around 4% for MOS). (v) Telescope effective area as a function of photon energy. (vi) Vignetting correction to effective area for off-axis pointings.

In DBS I, the rmf corresponding to (i) and (ii) has been chosen. The arf corresponds to (iii), (iv), (v) and (vi). (vi) has been approximately accounted for by creating the arfs according to the average flux detected in the individual annuli.

A source spectrum has then been extracted from the outer region of the target pointings. A background spectrum has been extracted from the background pointings in the same detector coordinates. Using only the rmf, the residual background spectrum has been

found after subtracting the background spectrum from the source spectrum in the outer region. This residual background mainly consists of the BNVIGs, e.g. soft protons. The vignetting effect can thus be ignored for the residual spectrum. It has been modeled by a “powerlaw/b” model in XSPEC <sup>2</sup> limited to 0.4–15 keV. This model can be used to account for the residual background in the spectral analysis. It is used over the whole energy range using a combined model of “wabs\*mekal+powerlaw/b” in XSPEC <sup>3</sup> in the fitting procedure. This yields a correct shape of the background component in the fit. We note that the normalization of the “powerlaw/b” model is scaled to the area of the interesting region. We did not consider the uncertainties of the fitting parameters of the “powerlaw/b” model when we introduced it as a residual component in the spectral analysis. This may result in an underestimate of the temperature uncertainty in the spectral analysis using DBS I. The advantage of DBS I is that the shape of the residual spectra is conserved during the procedure.

In DBS II, all spectra have been extracted considering (vi) by a weighted column in the event list produced by “evigweight”. The on-axis rmf and arf have been co-created to account for (i) to (v). The target spectrum has been extracted from the interesting region. The first-order background spectrum has been derived by extracting a spectrum from the background pointings in the same detector coordinates as for the source spectrum, and scaling it using the ctr ratio of the targets and background limited to 10–12 keV (12–14 keV) for MOS (pn).

The second-order background spectrum, the residual background spectrum, is prepared as follows. We extracted a source spectrum from the outer region of the target pointings and its background spectrum from the same outer region of the background pointings. We subtracted its scaled background spectrum also using the ctr ratio of the targets and background limited to 10–12 keV (12–14 keV) for MOS (pn) from the source spectrum and obtained a residual background spectrum. It is normalized to the area of the interesting region. We then subtracted the first-order background spectrum and the second-order background spectrum, the normalized residual background spectrum, from the target spectrum. A combined model of “wabs\*mekal” is then used with the on-axis arf and rmf in XSPEC for the fitting (Fig. 6.1). Since the residual spectra have large error bars and some negative data points, the temperature uncertainty is probably overestimated in the spectral analysis using DBS II.

In Fig. 6.2 we show the temperature profiles measured using both DBS I and DBS II. The two approaches provide consistent results within  $1\text{-}\sigma$  errors. A small discrepancy found mostly in the last bin shows no trend of being higher for one particular approach. Since there is no preferred indication of one of the two approaches, we chose the measurements using DBS II for further computations<sup>4</sup>.

---

<sup>2</sup> “powerlaw/b”, a power law background model which is convolved with the instrumental redistribution matrix but not with the effective area

<sup>3</sup> “mekal”, an emission model for hot diffuse gas, cf. Mewe et al. 1985, 1986; Arnaud & Rothenflug 1985; Arnaud & Raymond 1992; Kaastra 1992; Liedahl et al. 1995; “wabs”, a model considering the Galactic absorption

<sup>4</sup> The DBS II approach is simple in, (i) modeling the residual background, by applying the residual spectrum, instead of looking for an acceptable ( $\chi^2 < 2$ ) power law model fit; and (ii) generating the arfs, in which one on-axis arf works for all the spectra.



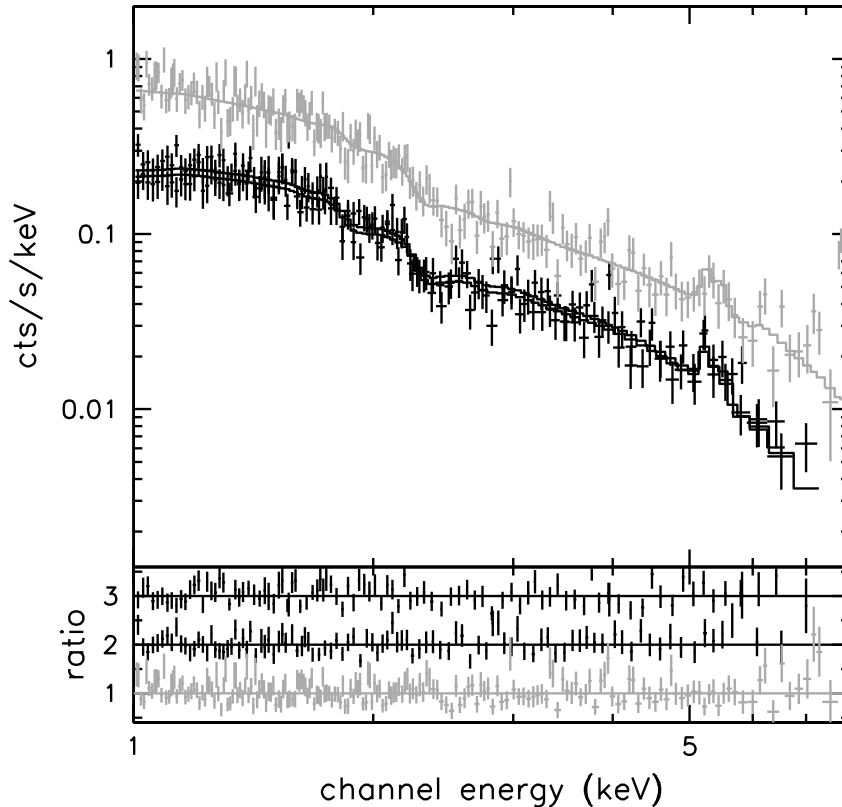


**Figure 6.1:** XMM-Newton spectra (pn in grey and MOS in black) of RXCJ0303.8–7752 of the  $0.5 < r < 4'$  region fitted by mekal model using DBS II. The ratios of the observational data to the models are in the lower parts of the panels (offset zero for pn, +1 for MOS1, +2 for MOS2).

This detailed treatment of the background does not completely remove the differences between the instruments. In general, lower temperature measurements have been derived from the pn data than for the MOS1 data and MOS2 data (partially). This is because pn is sensitive to the soft component so that the pn measurements depend strongly on the soft band compared to the MOS results. In Zhang et al. (2004a), we have systematically investigated the effect of an energy band selection. We have carried out the spectral analysis in the energy ranges of 0.4–10 keV and 1–10 keV, respectively (Zhang et al. 2004a, 2005a). Despite the larger error bars, all the pn measured temperatures in the central three bins of the clusters become higher, once the 0.4–1 keV band is excluded. The temperatures of all instruments are then in good agreement for the higher low-energy cut-off. Therefore, the spectral analysis has been performed in the 1–10 keV energy band unless explicitly stated otherwise such as 2–12 keV for the hottest cluster RXCJ0658.5–5556.

## 6 X-ray properties in massive galaxy clusters

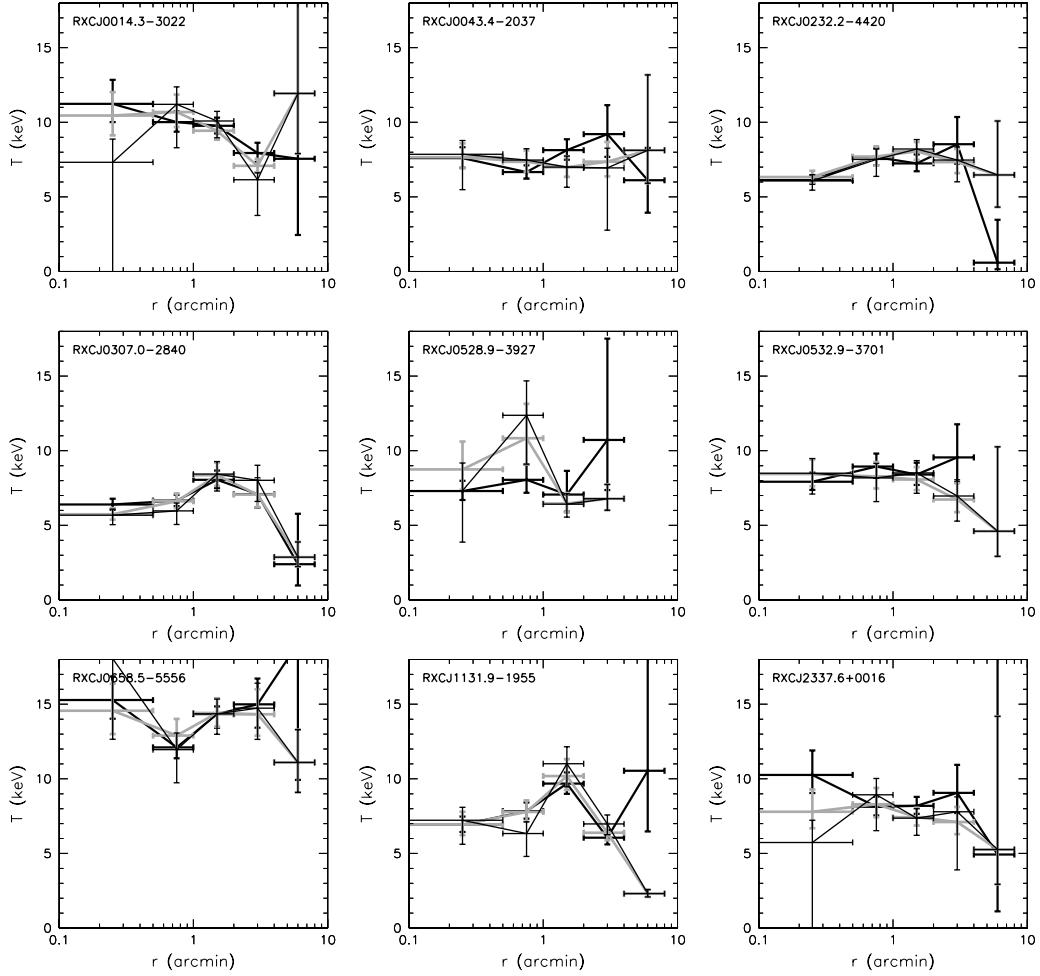


**Figure 6.2:** Projected (grey, thick) and deprojected (black, thin) temperature profiles using DBS I and projected (black, thick) temperature profiles using DBS II for 9 clusters observed in AO-1.

### 6.2.3.2 Image analysis

Geometric factors and vignetting correction have been accounted for in the exposure maps. An azimuthally averaged surface brightness profile of CDFS has been derived in the same detector coordinates and bin size as for the targets. The ctr ratios of the targets and CDFS in the 10–12 keV band and 12–14 keV band for MOS and pn, respectively, have been used to scale the CDFS surface brightness. The data are rebinned to ensure (1) at least 50 counts (30 counts for limited photon statistics cases) per bin, and (2) a signal-to-noise ratio (S/N) higher than  $2\sigma$ . We have subtracted the scaled CDFS surface brightness profile and obtained the surface brightness profile including the cluster surface brightness profile and a residual soft X-ray background. The residual background is almost flat over the whole FOV. It is estimated in the outer region (e.g.  $11' < r < 15'$ ). We have taken account of this residual background in the fitting as described in Sect. 7.3.6.

### 6.2.4 PSF and deprojection

In the spectral analysis, we have used equal logarithmic width for radial bins to extract spectra. This provides almost equal flux per bin. A large radial binning, greater than  $0.5'$ , has been used to reduce the PSF effect. Using the XMM-Newton point spread function (PSF) calibrations by Ghizzardi (2001) we have estimated the loss fraction of the flux. We found 20% for the central two bins ( $0.5'$ ) and less than 10% for the other bins ( $\geq 1'$ ) neglecting energy dependent effects. The PSF blurring can not be completely considered for the spectral analysis as it is done for the image analysis because of the limited photon statistics. For such distant clusters, the PSF effect is important within  $0.3r_{\text{vir}}$  which introduces an added uncertainty to the final results of the temperature profiles. This can only be investigated using deep exposures with better photon statistics.

In the imaging analysis, we have taken into account the PSF effect by fitting<sup>5</sup> the cluster surface brightness profile by a surface brightness model convolved with the PSF. An empirical PSF matrix (Ghizzardi 2001) has been determined according to the mean energy and the off-axis radii in the image analysis.

The projected temperature is the observed temperature from a particular annulus, containing in projection the foreground and background temperature measurements. Under the assumption of spherical symmetry, the gas temperature measure in each spherical shell can be derived by deprojecting the projected temperature profile. In this procedure, the inner shells contribute nothing to the outer annuli. The temperature in the outermost annulus is thus equal to the temperature in the outermost shell. The temperature in the neighboring inner annulus is determined by all the temperature measurements in the shell at the equal radius to the annulus and in the outer shells by Eq.(6.1) as shown in Suto et al. (1998). A combined fit to the temperature measurements in all annuli simultaneously, the contribution of each spherical shell to each annulus is determined. The deprojected measurements  $T^{\text{deproj}}(r)$  are then determined based on the projected temperature profile  $T^{\text{proj}}(r)$ .

$$T^{\text{proj}}(r) = \frac{\int_r^\infty T^{\text{deproj}}(R)\xi(R)RdR/\sqrt{R^2 - r^2}}{\int_r^\infty \xi(R)RdR/\sqrt{R^2 - r^2}}, \quad (6.1)$$

where  $\xi(r)$  is the emission per volume element (also see Sect. 7.3.6). This deprojection procedure increases the uncertainties in the temperature profile.

## 6.3 X-ray properties

The primary parameters in the spectral analysis are given in Table 7.6.

### 6.3.1 Metallicity and temperature

A “mekal” model has been used to fit the spectra of each cluster with fixed Galactic absorption (Dickey & Lockman 1990) and redshift (Böhringer et al. 2004a). In general, the  $r < 8'$  region has been chosen to extract the spectra to measure the global spectral

<sup>5</sup>We apply the Orthogonal Distance Regression method (Feigelson & Babu 1992, ODR) for the parameter fitting.

## 6 X-ray properties in massive galaxy clusters

**Table 6.2:** Primary parameters. Col. (1): Cluster name. Col. (2): Optical redshift (Böhringer et al. 2004a). Cols. (3–4): Sky coordinates of the cluster center. Col. (5): Hydrogen column density in units of  $10^{20}\text{cm}^{-2}$  (Dickey & Lockman 1990).

RXCJ	$z_{\text{opt}}$	X-ray centroid		$N_{\text{H}}$
		R.A.	decl.	
0014.3–3022	0.3066	00 14 18.6	–30 23 15.4	1.60
0043.4–2037	0.2924	00 43 24.5	–20 37 31.2	1.54
0232.2–4420	0.2836	02 32 18.8	–44 20 51.9	2.49
0303.7–7752	0.2742	03 03 47.2	–77 52 39.0	8.73
0307.0–2840	0.2578	03 07 02.2	–28 39 55.2	1.36
0437.1+0043	0.2842	04 37 09.5	+00 43 54.5	8.68
0516.7–5430	0.2943	05 16 35.2	–54 30 36.8	6.86
0528.9–3927	0.2839	05 28 52.5	–39 28 16.7	2.12
0532.9–3701	0.2747	05 32 55.9	–37 01 34.5	2.90
0658.5–5556	0.2965	06 58 30.2	–55 56 33.7	6.53
1131.9–1955	0.3075	11 31 54.7	–19 55 40.5	4.50
2011.3–5725	0.2785	20 11 27.2	–57 25 10.2	3.90
2308.3–0211	0.2966	23 08 22.3	–02 11 32.1	4.45
2337.6+0016	0.2753	23 37 37.8	+00 16 15.5	3.82

**Table 6.3:** Results of the XMM-Newton spectral analysis. Col. (1): Cluster name. Col. (2): Region. Cols. (3–4): Temperature and metallicity. Col. (5): Reduced  $\chi^2$ .

RXCJ	Region	$T_{\text{spec}}$ (keV)	$Z$ ( $Z_{\odot}$ )	$\chi^2/\text{d.o.f.}$
0014.3–3022	$r < 8'$	$8.65 \pm 0.43$	$0.22 \pm 0.04$	392.9/397
0043.4–2037	$r < 8'$	$6.81 \pm 0.43$	$0.23 \pm 0.07$	124.4/129
0232.2–4420	$0.5' < r < 4'$	$7.62 \pm 0.40$	$0.24 \pm 0.05$	195.4/195
0303.7–7752	$0.5' < r < 4'$	$9.15 \pm 0.56$	$0.28 \pm 0.06$	450.8/394
0307.0–2840	$0.5' < r < 4'$	$6.63 \pm 0.34$	$0.28 \pm 0.05$	176.5/167
0437.1+0043	$0.5' < r < 4'$	$5.67 \pm 0.52$	$0.30 \pm 0.00$	95.4/ 76
0516.7–5430	$0.5' < r < 4'$	$7.76 \pm 0.76$	$0.13 \pm 0.12$	201.2/124
0528.9–3927	$r < 8'$	$8.07 \pm 0.59$	$0.28 \pm 0.10$	91.5/ 97
0532.9–3701	$0.5' < r < 4'$	$7.76 \pm 0.72$	$0.28 \pm 0.10$	143.7/137
0658.5–5556	$0.5' < r < 4'$	$14.56 \pm 0.91$	$0.21 \pm 0.04$	1214.5/892
1131.9–1955	$0.5' < r < 4'$	$7.44 \pm 0.67$	$0.26 \pm 0.05$	163.4/174
2308.3–0211	$0.5' < r < 4'$	$8.71 \pm 0.87$	$0.17 \pm 0.10$	216.3/199
2337.6+0016	$r < 8'$	$8.02 \pm 0.59$	$0.22 \pm 0.06$	116.2/161

temperature ( $T_{\text{spec}}$ ) and metallicity. The  $0.5'–4'$  region has been adopted instead for the clusters showing cooler gas in the cluster center. The results of the global spectral analysis are shown in Table 6.3. We have investigated that the X-ray determined redshifts agree with the optical measured redshifts (also see Zhang et al. 2004a). We therefore fixed the values to the optical redshifts. The observations of RXCJ2011.3–5725 were contaminated by flares. We thus obtained only a global temperature ( $\sim 3.77$  keV) with a fixed metallicity of  $0.3 Z_{\odot}$ .

We performed a detailed spectral analysis in five annuli:  $0–0.5'$ ,  $0.5'–1'$ ,  $1'–2'$ ,  $2'–4'$ , and  $4'–8'$  (see Table 6.4). RXCJ0437.1+0043 has limited photon statistics. We thus fixed

**Table 6.4:** Temperature (in keV) and metallicity (in  $Z_{\odot}$ ) profiles of the REFLEX-DXL clusters using DBS II. Col. (1): Cluster name. Col. (2): Observable. Cols. (3–7): Temperature or metallicity measurements in 5 annuli.

RXCJ		$r < 0.5'$	$0.5' < r < 1'$	$1' < r < 2'$	$2' < r < 4'$	$4' < r < 8'$
0014.3–3022	$T$	$11.2^{+1.6}_{-1.2}$	$10.1^{+0.7}_{-0.7}$	$9.8^{+0.6}_{-0.5}$	$8.1^{+0.7}_{-0.6}$	$7.6^{+2.3}_{-5.1}$
	$Z$	0.30*	$0.24^{+0.08}_{-0.08}$	$0.22^{+0.06}_{-0.06}$	$0.05^{+0.07}_{-0.05}$	0.30*
0043.4–2037	$T$	$7.5^{+0.8}_{-0.7}$	$6.9^{+0.5}_{-0.5}$	$8.2^{+0.8}_{-0.7}$	$9.3^{+1.9}_{-1.6}$	$6.1^{+2.2}_{-2.2}$
	$Z$	$0.35^{+0.13}_{-0.12}$	$0.15^{+0.08}_{-0.08}$	$0.23^{+0.10}_{-0.10}$	$0.29^{+0.23}_{-0.24}$	0.30*
0232.2–4420	$T$	$6.0^{+0.3}_{-0.3}$	$7.7^{+0.6}_{-0.5}$	$7.2^{+0.6}_{-0.5}$	$8.5^{+1.8}_{-1.3}$	$0.6^{+2.9}_{-0.4}$
	$Z$	$0.41^{+0.07}_{-0.06}$	$0.24^{+0.09}_{-0.09}$	$0.31^{+0.10}_{-0.10}$	0.30*	0.30*
0303.7–7752	$T$	$8.1^{+1.1}_{-0.9}$	$9.1^{+0.8}_{-0.7}$	$8.5^{+0.7}_{-0.6}$	$9.9^{+1.7}_{-1.3}$	$4.5^{+5.6}_{-1.8}$
	$Z$	$0.19^{+0.13}_{-0.13}$	$0.21^{+0.08}_{-0.08}$	$0.33^{+0.09}_{-0.09}$	$0.32^{+0.18}_{-0.18}$	0.30*
0307.0–2840	$T$	$6.4^{+0.4}_{-0.4}$	$6.7^{+0.4}_{-0.4}$	$8.1^{+0.6}_{-0.6}$	$7.1^{+1.1}_{-0.9}$	$2.5^{+3.6}_{-1.2}$
	$Z$	$0.27^{+0.06}_{-0.06}$	$0.29^{+0.08}_{-0.08}$	$0.28^{+0.08}_{-0.08}$	$0.44^{+0.21}_{-0.20}$	0.30*
0437.1+0043	$T$	$5.3^{+0.3}_{-0.3}$	$5.7^{+0.5}_{-0.4}$	$6.2^{+0.9}_{-0.7}$	$8.4^{+4.5}_{-2.5}$	$0.0^{+0.0}_{-0.0}$
	$Z$	$0.40^{+0.08}_{-0.08}$	$0.28^{+0.10}_{-0.10}$	$0.33^{+0.23}_{-0.21}$	0.30*	0.30*
0516.7–5430	$T$	$8.5^{+2.3}_{-1.4}$	$5.7^{+0.5}_{-0.4}$	$6.8^{+0.5}_{-0.5}$	$6.2^{+0.6}_{-0.5}$	$12.7^{+24.7}_{-5.6}$
	$Z$	0.30*	0.30*	$0.24^{+0.12}_{-0.12}$	$0.25^{+0.15}_{-0.14}$	0.30*
0528.9–3927	$T$	$7.3^{+0.7}_{-0.6}$	$8.0^{+1.0}_{-0.9}$	$7.1^{+1.6}_{-1.1}$	$10.7^{+6.8}_{-3.4}$	$79.9^{+0.0}_{-65.8}$
	$Z$	0.30*	0.30*	0.30*	0.30*	0.30*
0532.9–3701	$T$	$7.9^{+0.6}_{-0.5}$	$8.5^{+0.9}_{-0.8}$	$8.4^{+0.8}_{-0.7}$	$9.6^{+2.2}_{-1.6}$	$79.9^{+0.0}_{-18.6}$
	$Z$	$0.40^{+0.09}_{-0.09}$	$0.15^{+0.11}_{-0.11}$	$0.18^{+0.11}_{-0.11}$	$0.44^{+0.28}_{-0.28}$	0.30*
0658.5–5556	$T$	$15.3^{+1.6}_{-1.3}$	$12.1^{+0.8}_{-0.7}$	$14.3^{+0.5}_{-0.9}$	$15.0^{+1.7}_{-1.6}$	$19.1^{+60.8}_{-9.1}$
	$Z$	$0.23^{+0.08}_{-0.08}$	$0.26^{+0.06}_{-0.05}$	$0.12^{+0.05}_{-0.05}$	$0.21^{+0.07}_{-0.08}$	0.30*
1131.9–1955	$T$	$6.9^{+0.5}_{-0.5}$	$7.8^{+0.6}_{-0.5}$	$9.7^{+0.8}_{-0.7}$	$6.1^{+0.5}_{-0.5}$	$10.5^{+13.3}_{-4.1}$
	$Z$	$0.33^{+0.09}_{-0.08}$	$0.18^{+0.07}_{-0.07}$	$0.32^{+0.09}_{-0.09}$	$0.28^{+0.09}_{-0.08}$	0.30*
2308.3–0211	$T$	$6.9^{+0.7}_{-0.6}$	$8.3^{+1.0}_{-0.8}$	$8.1^{+1.2}_{-1.0}$	$12.1^{+7.3}_{-3.8}$	$0.0^{+0.0}_{-0.0}$
	$Z$	$0.48^{+0.12}_{-0.11}$	$0.53^{+0.16}_{-0.15}$	$0.44^{+0.18}_{-0.17}$	0.30*	0.30*
2337.6+0016	$T$	$10.3^{+1.6}_{-1.2}$	$8.1^{+0.6}_{-0.6}$	$8.2^{+0.6}_{-0.5}$	$9.1^{+1.9}_{-1.4}$	$4.9^{+75.0}_{-3.8}$
	$Z$	$0.15^{+0.18}_{-0.15}$	$0.14^{+0.08}_{-0.08}$	$0.19^{+0.08}_{-0.08}$	$0.31^{+0.26}_{-0.26}$	0.30*

\* Fixed value.

the metallicity distribution to  $0.3 Z_{\odot}$  for the spectral study. For the other clusters, we fixed the metallicity to  $0.3 Z_{\odot}$  for the outer annuli with limited photon statistics. All the REFLEX-DXL clusters have been combined to obtain the average metallicity distribution of the REFLEX-DXL sample.

We obtained an average with error,  $0.23 \pm 0.07 Z_{\odot}$ , of the global spectral metallicities for the REFLEX-DXL clusters. This is consistent with the averaged metallicity  $\bar{Z} = 0.21^{+0.10}_{-0.05} Z_{\odot}$  for 18 distant ( $0.3 < z < 1.3$ ) clusters in Tozzi et al. (2003). We obtained the average metallicity values of  $0.27 \pm 0.07 Z_{\odot}$  and  $0.22 \pm 0.08 Z_{\odot}$  for the CCCs and non-CCCs (NCCCs), respectively. This agrees with the values of  $0.34 Z_{\odot}$  and  $0.21 Z_{\odot}$  in Allen & Fabian (1998) and the results in De Grandi et al. (2004).

In Table 6.4, we list the data of the metallicity profiles. The metallicity distributions of the CCCs (see Fig. 6.11) show high central concentrations (e.g. Tamura et al. 2001; Ettori et al. 2002b; Chen et al. 2003; Ikebe et al. 2004; Pointecouteau et al. 2004). They become flat in the outskirts which is expected from the simulations (e.g. Kobayashi 2004). The NCCCs show a flat metallicity distribution as also found by De Grandi et al. (2004).

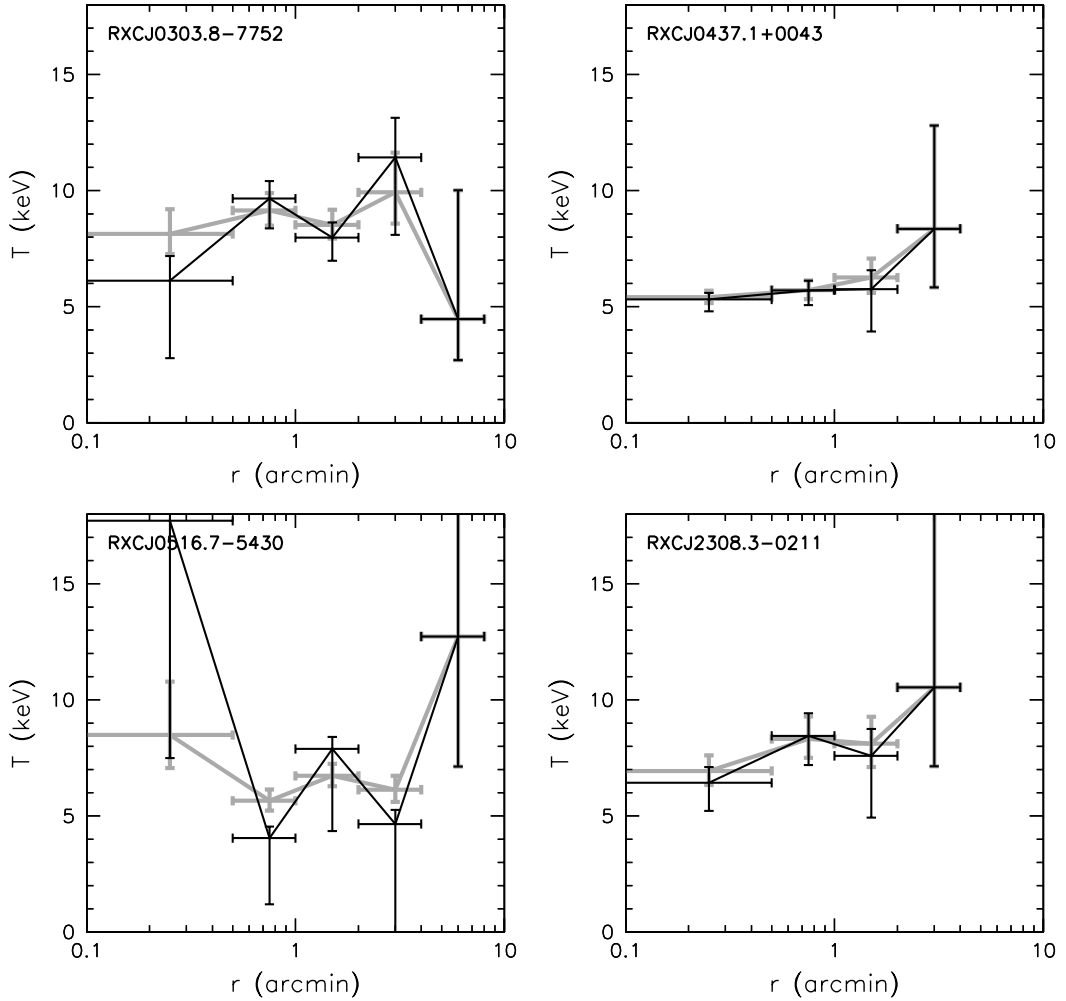


**Figure 6.3:** Projected (grey) and deprojected (black) temperature profiles using DBS II for 4 clusters observed in AO-3.

Temperature profiles (see Table 6.4) provide a useful means to study the thermodynamical history of galaxy clusters. XMM-Newton (also Chandra), in contrast to earlier instruments, provides a less energy-dependent and smaller PSF. It is thus more reliable to study cluster temperature profiles. We have included the temperature profiles of 9 REFLEX-DXL clusters in Paper II. We have obtained consistent results within  $1\sigma$  using DBS I and DBS II except for the last annulus for RXCJ0232.2–4420 and RXCJ1131.9–1955. This disagreement (see Fig. 6.2) is caused by the limited photon statistics.

In Fig. 6.3 we show the temperature profiles of the data obtained in XMM-Newton AO-3 using DBS II. The deprojected temperature profiles (see Sect. 6.2.4) keep a good agreement in the outer parts with the projected profiles. The projection effect matters only in the central parts as an accumulated geometric deprojection from the outer annuli.

**Table 6.5:** Parameters of Model I. Col. (1): Cluster name. Cols. (2–3):  $\beta$ -model parameters for the electron number density profile, which  $n_{e0}$  is included in Table 6.7). Cols. (4–6):  $\beta$ -model parameters for the pressure profile. Col. (7): Reduced  $\chi^2$ .

RXCJ	$r_c$ (Mpc)	$n_e$	$\beta$	$r_c^P$ (Mpc)	$\beta^P$	$P_e$	$P_0$ (cm $^{-3}$ keV)	$\chi^2/\text{d.o.f.}$
0014.3–3022	0.431 $\pm$ 0.005	0.880 $\pm$ 0.009	0.37 $\pm$ 0.01	0.943 $\pm$ 0.016	0.037 $\pm$ 0.001	466.6/ 367		
0043.4–2037	0.197 $\pm$ 0.002	0.692 $\pm$ 0.004	0.17 $\pm$ 0.01	0.653 $\pm$ 0.027	0.050 $\pm$ 0.002	158.0/ 103		
0303.7–7752	0.246 $\pm$ 0.004	0.742 $\pm$ 0.008	0.24 $\pm$ 0.01	0.741 $\pm$ 0.023	0.038 $\pm$ 0.001	254.7/ 173		
0516.7–5430	0.502 $\pm$ 0.012	0.744 $\pm$ 0.014	0.69 $\pm$ 0.09	0.931 $\pm$ 0.118	0.010 $\pm$ 0.000	421.6/ 124		
0532.9–3701	0.125 $\pm$ 0.002	0.639 $\pm$ 0.006	0.12 $\pm$ 0.00	0.627 $\pm$ 0.008	0.087 $\pm$ 0.000	387.2/ 229		
0658.5–5556	0.391 $\pm$ 0.003	0.877 $\pm$ 0.005	0.46 $\pm$ 0.02	1.029 $\pm$ 0.039	0.074 $\pm$ 0.003	618.5/ 346		
1131.9–1955	0.187 $\pm$ 0.002	0.677 $\pm$ 0.003	0.25 $\pm$ 0.03	0.808 $\pm$ 0.046	0.043 $\pm$ 0.004	311.1/ 188		
2308.3–0211	0.111 $\pm$ 0.002	0.631 $\pm$ 0.006	0.11 $\pm$ 0.01	0.624 $\pm$ 0.014	0.073 $\pm$ 0.004	210.5/ 115		
2337.6+0016	0.344 $\pm$ 0.003	0.878 $\pm$ 0.005	0.40 $\pm$ 0.02	1.098 $\pm$ 0.031	0.028 $\pm$ 0.001	247.1/ 156		

#### 6.3.2 Surface brightness

The 0.5–2 keV band has been selected to derive the surface brightness profiles (also see Zhang et al. 2005a). This ensures an almost temperature-independent X-ray emission coefficient over the expected temperature range.

The NCCCs (9 clusters) show slightly flat cores in the surface brightness profiles. A  $\beta$ -model (e.g. Cavaliere & Fusco-Femiano 1976; Jones & Forman 1984)

$$S_x(r) = S_0 \left(1 + \frac{r^2}{r_c^2}\right)^{-3\beta+1/2} \quad (6.2)$$

provides an acceptable  $\chi^2$  fit ( $\chi^2 \lesssim 2$ ) of the surface brightness profiles for the NCCCs (Fig. 6.4). In Zhang et al. (2005a), we have studied the influence of the central emission of the  $\beta$ -model fit and found that the parameters like  $\beta$  and  $r_c$  change within 2% when the central bins have been masked. The surface brightness profile approximated by a  $\beta$ -model can be analytically deprojected to yield the emission per volume element,  $\xi(r) = \tilde{\Lambda}(r)n_e^2(r)$ . With the given emissivity,  $\tilde{\Lambda}(r)$ , from the applied plasma model, one can derive the electron density profile  $n_e(r) = n_{e0} \left(1 + \frac{r^2}{r_c^2}\right)^{-3\beta/2}$  with the parameters given in Table 7.3 combining the three instruments. The X-ray bolometric luminosity (here we use the 0.01–100 keV band) is an integral of the density and temperature distributions as  $L_X^{\text{bol}} \propto \int \tilde{\Lambda}(r)n_e^2(r)dV$ .

The CCCs are those (i.e. RXCJ0232.2–4420, RXCJ0307.0–2840, RXCJ0437.1+0043 and RXCJ0528.9–3927) in REFLEX-DXL which show cooling times less than 0.5 Gyr and central entropies (by extrapolations) less than 100 keV cm $^2$  as shown in Table 6.7. For the CCCs, the central parts of the surface brightness profile are not well fitted by a single  $\beta$ -model. Therefore, we explored three alternative fits of the surface brightness profiles for those clusters: a model based on an ext-NFW DM profile (Navarro et al. 2004, ext-NFW, defined by Eq.(7.8)) combining with Eq.(6.6) and Eq.(7.4) (see Sect. 6.3.6.2 and Fig. 7.7), a double  $\beta$ -model (Fig. 6.6), and a simple power law fit of the outer slope.

The ext-NFW model is suggested from many simulations as an approximate description

## 6 X-ray properties in massive galaxy clusters

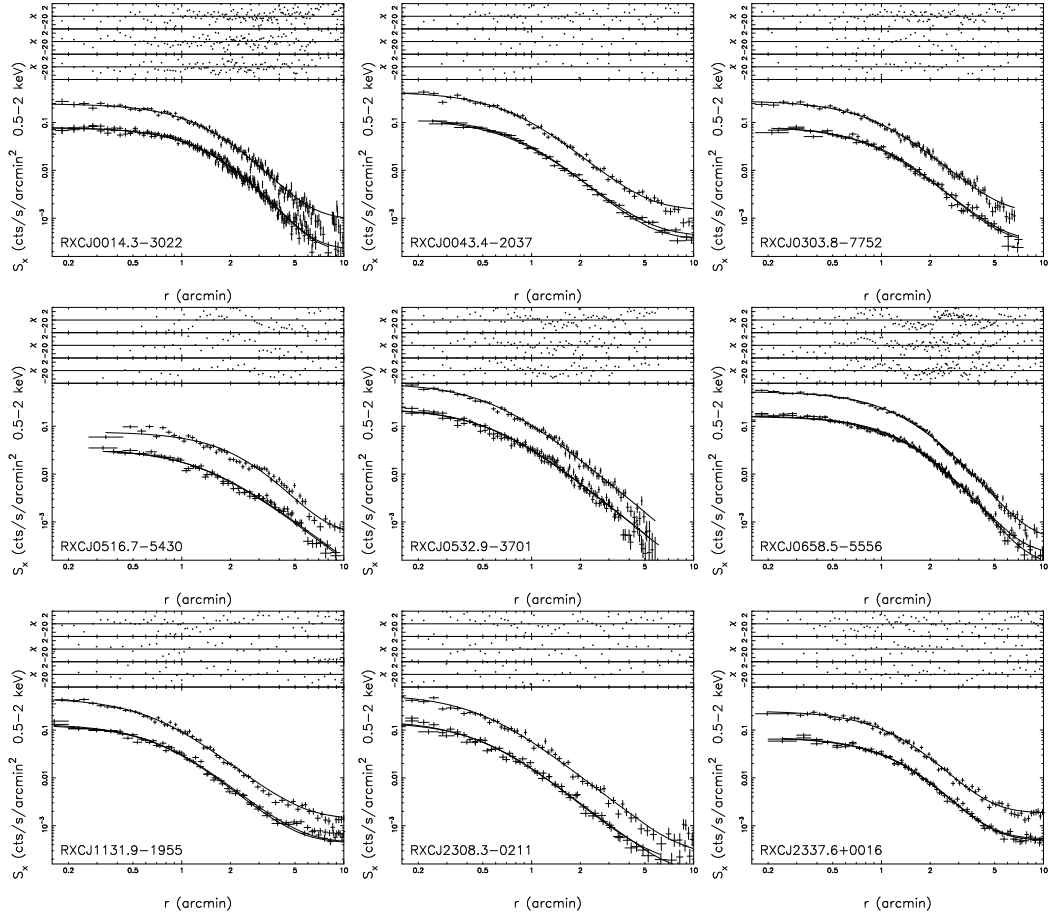


**Figure 6.4:** Observational data (PSF convolved, including the cluster surface brightness profile and a residual soft X-ray background) and their best fits for pn (top curve) and MOS (bottom curves). Residuals scaled by the data uncertainties appear above for pn, MOS1 and MOS2 from top to bottom.

of the matter distribution in dark halo, such as clusters (e.g. Hernquist 1990; Zhao 1996; Suto et al. 1998; Moore et al. 1999) given by

$$\rho_{\text{DM}}(r) = \delta_c \rho_c \left( \frac{r}{r_s} \right)^{-\alpha} \left( 1 + \frac{r}{r_s} \right)^{\alpha-3}. \quad (6.3)$$

$\delta_c$  and  $r_s$  are the characteristic density and scale of the halo, respectively.  $\rho_c$  is the critical density of the Universe at the cosmic epoch  $z$  and  $\rho_s = \delta_c \rho_c$ . This mass density profile has a steeper central slope compared to the  $\beta$ -model. Combining the assumption of hydrostatic equilibrium with the observed temperature profile and spherical symmetry, we constructed the gas density and surface brightness profiles for a given ext-NFW DM model and searched for the best fitting ext-NFW parameters (see Sect. 6.3.6.2). In Fig. 7.7 and Table 6.6, we summarize the best fitting results. Apart from deviation due to cluster substructure, the ext-NFW modeling produces acceptable ( $\chi^2 \lesssim 2$ ) fits. We found that the fitting of the double  $\beta$ -model produced a similar satisfactory results for the CCCs (Fig. 6.6).



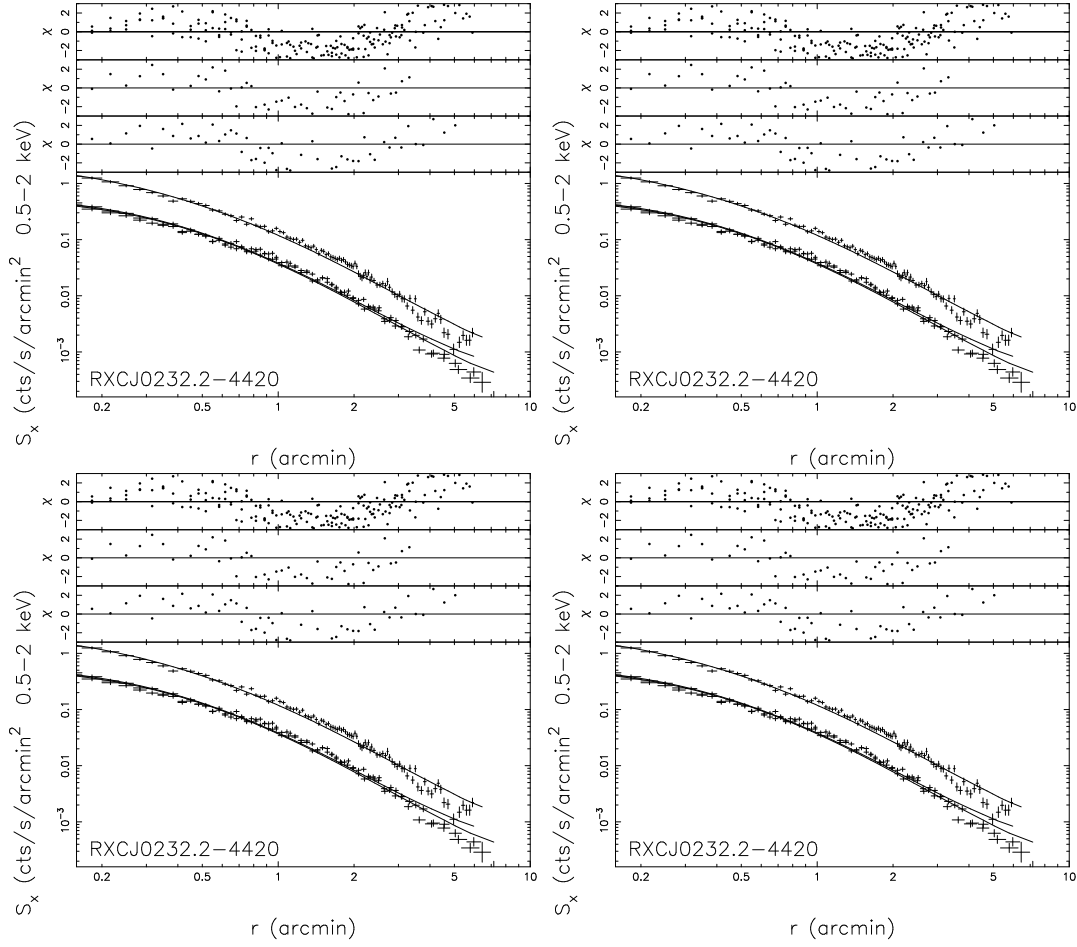


**Figure 6.5:** The same as in Fig. 6.4 but for the 4 CCCs.

**Table 6.6:** Parameters of Model II. Col. (1): Cluster name. Cols. (2–4): Ext-NFW model parameters. Col. (5–6): Parameters of Eq. (6.6). Col. (7): Reduced  $\chi^2$ .

RXCJ	$r_s^{\text{ext-NFW}}$ (Mpc)	$\rho_s^{\text{ext-NFW}}$ ( $10^9 M_\odot$ )	$\alpha$	$\gamma$	$T_0$ (keV)	$\chi^2/\text{d.o.f.}$
0232.2-4420	398.	1.087	$1.785 \pm 0.003$	$1.00 \pm 0.03$	$7.12 \pm 0.45$	724.8/ 201
0307.0-2840	351.	0.481	$1.884 \pm 0.004$	$1.10 \pm 0.03$	$6.43 \pm 1.53$	468.2/ 318
0437.1+0043	444.	2.297	$1.657 \pm 0.004$	$0.91 \pm 0.04$	$6.21 \pm 0.38$	285.6/ 121
0528.9-3927	358.	0.624	$1.885 \pm 0.003$	$1.08 \pm 0.08$	$7.89 \pm 1.03$	260.5/ 135

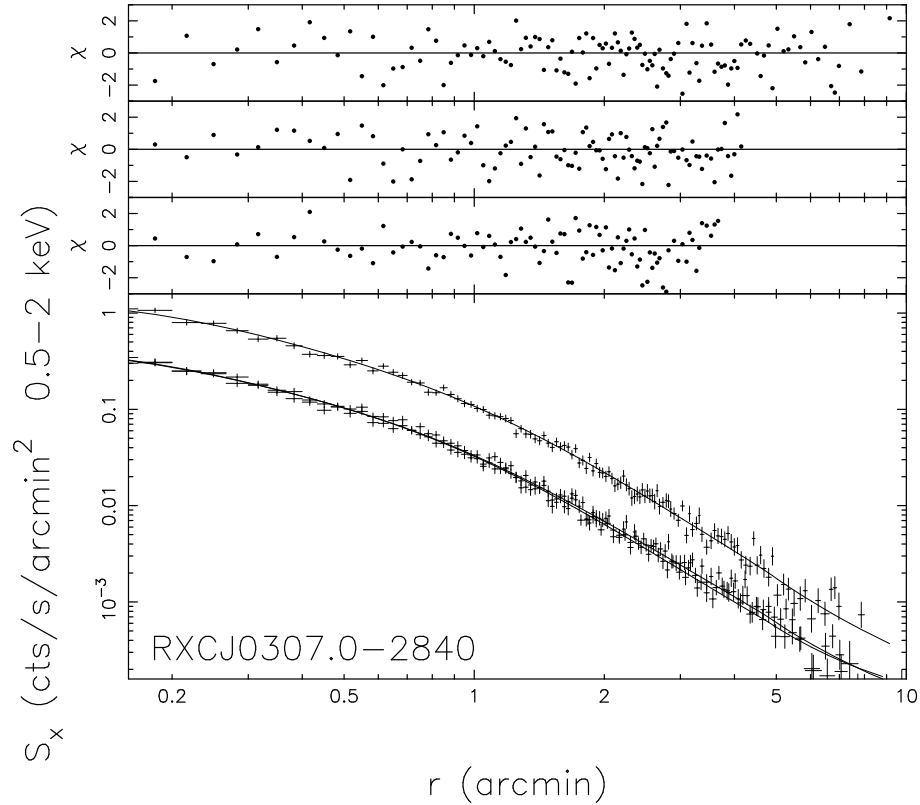


**Figure 6.6:** The same as in Fig. 7.7 to illustrate a satisfactory fit by a double  $\beta$ -model.

A dense gaseous cluster core, as observed in the CCCs, does not necessarily require a cusp of the DM distribution as provided by the ext-NFW model. Alternatively, a sufficiently cooler central temperature also results in a dense core without a cuspy DM profile which is demonstrated as follows. Restricting the analysis to  $r < 0.5'$ , we used the pronounced CCC RXCJ0307.0–2840 to illustrate the total mass distribution in the dense and cool gaseous region in the cluster. In general, no cool gas has been observed showing a central temperature lower than half of the mean temperature. We thus assume an extreme temperature drop to 1/3 of the observed temperature of the inner most bin towards the center. Assuming a steep central gas density distribution and hydrostatic equilibrium, we derived a relatively low mass concentration in the cluster center (see Fig. 6.7). There are two possibilities for the existence of the dense and cool gas in the cluster center: (1) a cuspy dark matter halo distribution and a relatively flat temperature profile; and (2) a relatively flat DM halo distribution and cool gas showing a decreasing temperature profile towards the center. We can not easily distinguish which of the above two cases co-exists with the dense gaseous cluster core using the current observations.

We have applied a power law to fit the surface brightness in the outskirts (e.g.  $2'–8'$ ). We found the slope of the NCCCs in the outskirts is less steep than the slope of the CCCs. The slope in the cluster outer part is often steeper than the model prediction for

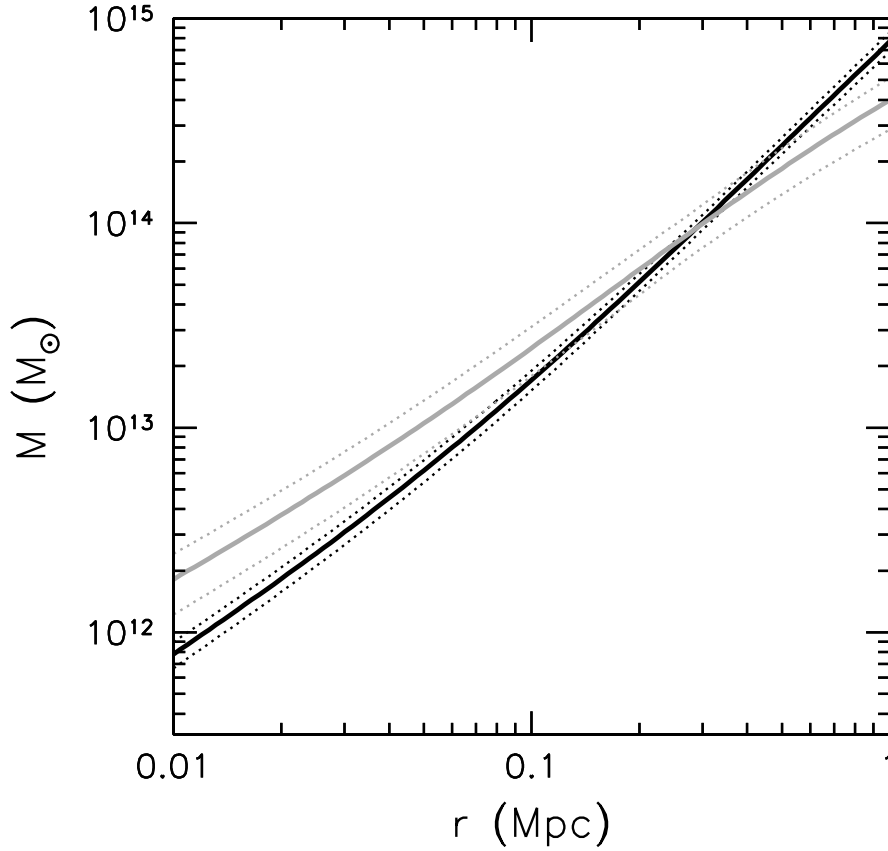


**Figure 6.7:** The central mass (thick) distributions of RXCJ0307.0–2840 derived using the observed temperature profile (grey) and assumed temperature profile showing a fast drop towards the center (black), respectively. The confidence intervals are shown as dotted curves.

the  $\beta$ -model and also for the NFW model (more details see Sect. 6.6.1).

### 6.3.3 Cooling time

The cooling time can be derived by the total energy of the gas divided by the energy loss rate

$$t_c \propto n_g k_B T / n_e^2 \tilde{\Lambda} \quad (6.4)$$

where  $\tilde{\Lambda}$ ,  $n_g$ ,  $n_e$  and  $T$  are the radiative cooling function, gas number density, electron number density and temperature, respectively. We list the central cooling time in Table 6.7. We assume that clusters formed at  $z \sim 3$ , the age of the cluster is thus 7.94 Gyr at  $z \sim 0.3$ . Cooling regions are those regions showing cooling time less than the age of the cluster at the epoch of observations. The boundary radius of such a region is called the cooling radius. It is zero if the cooling time is larger than the cluster age at all regions. The central cooling times and cooling radii are given in Table 6.7. The CCCs show shorter cooling times.

## 6 X-ray properties in massive galaxy clusters

**Table 6.7:** Cluster catalogue part I. Col. (1): Cluster name. Col. (2): Central electron number density. Col. (3): Central entropy. Cols. (4–5): Cooling time and cooling radius. Col. (6):  $r_{500}$ . Cols. (7–9): Gas mass, total mass and gas mass fraction at  $r_{500}$ .

RXCJ	$n_{e0}$ ( $10^{-3} \text{ cm}^{-3}$ )	$S_0$ ( $\text{keV cm}^2$ )	$t_c$ (Gyr)	$r_{\text{cool}}$ (Mpc)	$r_{500}$ (Mpc)	$M_{\text{gas},500}$ ( $10^{14} M_{\odot}$ )	$M_{500}$ ( $10^{14} M_{\odot}$ )	$f_{\text{gas},500}$
0014.3–3022	$3.29 \pm 0.02$	$473 \pm 73$	$4.5 \pm 0.1$	0.354	1.216	$0.96 \pm 0.01$	$7.04 \pm 0.74$	$0.14 \pm 0.01$
0043.4–2037	$6.00 \pm 0.06$	$233 \pm 30$	$2.1 \pm 0.1$	0.335	1.156	$0.66 \pm 0.01$	$5.91 \pm 1.46$	$0.11 \pm 0.03$
0232.2–4420	$35.53 \pm 1.00$	$46 \pm 9$	$0.1 \pm 0.0$	0.119	1.205	$0.93 \pm 0.13$	$6.67 \pm 0.64$	$0.14 \pm 0.02$
0303.7–7752	$4.35 \pm 0.04$	$306 \pm 42$	$3.1 \pm 0.1$	0.294	1.309	$0.70 \pm 0.01$	$8.41 \pm 1.50$	$0.08 \pm 0.02$
0307.0–2840	$19.63 \pm 0.40$	$55 \pm 11$	$0.4 \pm 0.0$	0.091	1.040	$0.55 \pm 0.07$	$4.15 \pm 1.19$	$0.13 \pm 0.05$
0437.1+0043	$17.13 \pm 0.40$	$59 \pm 17$	$0.2 \pm 0.0$	0.090	1.268	$0.65 \pm 0.14$	$7.72 \pm 0.97$	$0.08 \pm 0.02$
0516.7–5430	$1.65 \pm 0.02$	$608 \pm 171$	$7.4 \pm 0.5$	0.118	1.352	$0.93 \pm 0.01$	$9.49 \pm 2.99$	$0.10 \pm 0.04$
0528.9–3927	$32.62 \pm 2.00$	$81 \pm 26$	$0.3 \pm 0.0$	0.075	1.156	$0.78 \pm 0.08$	$5.90 \pm 1.21$	$0.13 \pm 0.03$
0532.9–3701	$10.35 \pm 0.12$	$178 \pm 22$	$1.3 \pm 0.1$	0.310	1.211	$0.67 \pm 0.01$	$6.68 \pm 0.58$	$0.10 \pm 0.01$
0658.5–5556	$5.13 \pm 0.02$	$490 \pm 62$	$3.8 \pm 0.1$	0.341	2.018	$2.10 \pm 0.01$	$31.56 \pm 6.75$	$0.07 \pm 0.01$
1131.9–1955	$6.36 \pm 0.06$	$202 \pm 27$	$1.7 \pm 0.1$	0.317	1.178	$0.69 \pm 0.01$	$6.36 \pm 2.56$	$0.11 \pm 0.05$
2308.3–0211	$9.27 \pm 0.15$	$158 \pm 17$	$1.3 \pm 0.1$	0.266	1.151	$0.48 \pm 0.01$	$5.88 \pm 1.13$	$0.08 \pm 0.01$
2337.6+0016	$3.54 \pm 0.03$	$336 \pm 66$	$3.6 \pm 0.2$	0.320	1.216	$0.68 \pm 0.01$	$6.78 \pm 1.39$	$0.10 \pm 0.02$
Mean	—	—	—	—	—	—	—	$0.11 \pm 0.07$

### 6.3.4 Overdensity

The mean cluster overdensity is the average density with respect to  $\rho_c(z) = \rho_{c0} E^2(z)$ , where  $E^2(z) = \Omega_m(1+z)^3 + \Omega_\Lambda + (1 - \Omega_m - \Omega_\Lambda)(1+z)^2$ . The average overdensity at redshift  $z$ ,  $\Delta_{c,z}$ , at the virial radius,  $r_{\text{vir}}$ , can be completely determined by the cosmological model and cluster redshift. For example,  $\Delta_{c,z} = 18\pi^2 + 82[\Omega_m(z) - 1] - 39[\Omega_m(z) - 1]^2$  for a flat Universe.  $\Omega_m(z)$  is the cosmic density parameter at redshift  $z$ . In the mass modeling, the virial radius,  $r_{\text{vir}}$ , is generally defined to be the radius where the overdensity is  $\Delta_{c,z}$ .

To check the dependence on the evolution of the cosmological parameters, we adopted the redshift evolution corrections of Ettori et al. (2004),

$$\begin{aligned}
 S \cdot E(z)^{4/3} (\Delta_{c,z}/\Delta_{c,0})^{2/3} &\propto f(T) \\
 L \cdot E(z)^{-1} (\Delta_{c,z}/\Delta_{c,0})^{-0.5} &\propto f(T) \\
 M \cdot E(z) (\Delta_{c,z}/\Delta_{c,0})^{0.5} &\propto f(T) \\
 M_{\text{gas}} \cdot E(z) (\Delta_{c,z}/\Delta_{c,0})^{0.5} &\propto f(T).
 \end{aligned}$$

### 6.3.5 Gas entropy

The entropy is the key to an understanding of the thermodynamical history. The observed entropy is generally defined as  $S = T n_e^{-2/3}$  for galaxy cluster studies (e.g. Ponman et al. 1999). It results from shock heating of the gas during cluster formation. It scales with the cluster temperature. An excess above this scaling law indicates the effect of an additional, non-gravitational heating source or feedback from supernovae (SN) and AGNs (e.g. Lloyd-Davies et al. 2000), while a low central entropy indicates radiative cooling. The clusters with non-flat surface brightness profiles are identical to those with low central entropy values. For some REFLEX-DXL clusters, the central entropy ( $r < 0.1r_{\text{vir}}$ ) is below the

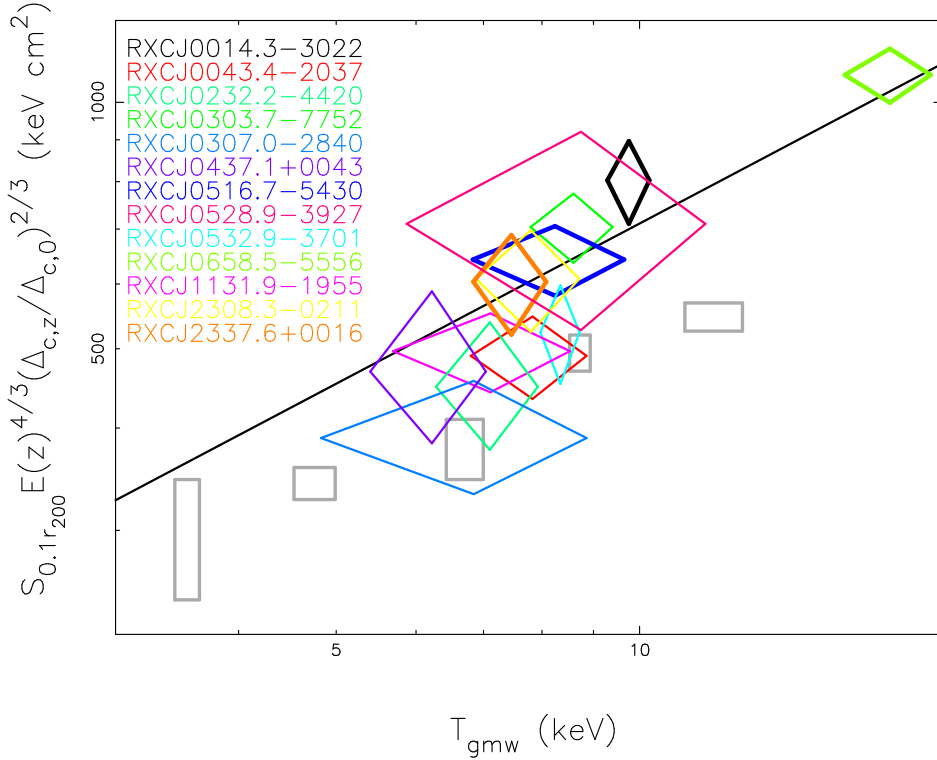


**Figure 6.8:** Redshift corrected entropy (diamond) at  $0.1r_{200}$  vs.  $T_{\text{gmw}}$  for the REFLEX-DXL clusters. The merger clusters are shown as thick lines. Nearby clusters in Ponman et al. (2003, box) are shown for comparison. The solid line denotes  $S \sim T^{0.65}$ .

entropy floor,  $S \sim 124h_{70}^{-1/3}$  keV cm<sup>2</sup>, derived by Lloyd-Davies et al. (2000). Neglecting the resolution problem, this indicates some effect from radiative cooling. As shown in Fig. 6.8 ( $T_{\text{gmw}}$  defined in Sect. 6.4), the central entropies for the REFLEX-DXL clusters at  $0.1r_{200}$  are lower than for the nearby clusters in Ponman et al. (2003), but keep an overall agreement after the redshift evolution correction despite of the merger clusters which show relatively higher central entropies. The central entropies of the REFLEX-DXL clusters agree with the scaling,  $T^{0.65}$ . As shown later in Fig. 6.14 in Sect. 6.4.4, the entropy profiles above  $0.1r_{\text{vir}}$  show the same power law,  $S \propto r^{0.97}$ , as found by Ettori et al. (2002b). The cluster showing the most significant merger feature has the highest central entropy in the REFLEX-DXL sample. RXCJ0516.7–5430, RXCJ0014.3–3022, RXCJ0658.5–5556 and RXCJ2337.6+0016 are 4 typical examples as shown in Fig. 6.8. The central entropy can thus be used not only as a mechanical educt of the non-gravitational process, but also as an indicator of the merger stage.

### 6.3.6 Mass distribution

We assume that the intracluster gas is in hydrostatic equilibrium within the gravitational potential dominated by DM. The ICM can thus be used to trace the cluster potential. Under the assumption of spherical symmetry, the cluster mass can be obtained from the

X-ray measured ICM density and temperature distributions.

$$\frac{1}{\mu m_p n_e} \frac{d(n_e k_B T)}{dr} = -\frac{GM(r)}{r^2}, \quad (6.5)$$

where  $\mu = 0.62$  is the mean molecular weight per hydrogen atom. We note that the ICM density is derived from the X-ray surface brightness as described in Sect. 7.3.6.

The total mass can be underestimated due to the assumption of spherical symmetry for the clusters showing elongation (Castillo-Morales & Schindler 2003). RXCJ0516.7–5430 is such an example in the REFLEX-DXL sample. The observations of Zhang et al. (2004a) show a less than 1% contribution to the cluster mass density by a cosmological constant,  $\Omega_\Lambda$  (or dark energy). The simulations (e.g. Bartelmann et al. 2005) also show that core halo densities are imprinted early during their formation by the mean cosmological density independent of the cosmological constant. The contribution to mass by a cosmological constant is thus negligible at these high overdensities on the cluster scale.

### 6.3.6.1 Model I: $\beta$ model

For the NCCCs, the projection effect on the temperature profiles is negligible. A smooth approximation to the projected temperature profile (e.g.  $T(r) = 1/(ar^2 + br + c)$ ) and the electron density profile have been used to derive the pressure distribution,  $P(r)$ . The pressure profile shows a peak in the center. It declines as a function of radius appearing as a power law slope in roughly  $\beta$ -model manner. We derived the mass profile (Fig. 6.15) from the  $\beta$ -model described gas density and pressure profiles under the assumption of hydrostatic equilibrium.

### 6.3.6.2 Model II: ext-NFW model

For typical CCCs, the projection effect becomes significant. However, for the pronounced CCCs, e.g. the CCCs in the REFLEX-DXL sample, the projection effect is significant only in the central bin of the temperature profile. The projection effect on such a temperature structure is still negligible (see Zhang et al. 2004a). To avoid increase of the temperature uncertainties by the deprojection procedure, we used the projected temperature profile as the radial temperature profile.

It is difficult to determine the mass profile with a binned temperature profile. Therefore we used the smooth approximation, based on a polytropic gas model which gives

$$T(r)/T_0 = (n_e(r)/n_{e0})^{\gamma-1}, \quad (6.6)$$

where  $\gamma$  is the polytropic index.

For the mass profile, we used the ext-NFW model (e.g. Navarro et al. 2004). We note that Eq.(7.8) gives the NFW (Navarro et al. 1997, NFW) model when  $\alpha = 1$ . The total mass profile is thus given by the integral of Eq.(7.8),

$$M(r) = 4\pi\delta_c\rho_c r_s^3 \int_0^r r'^2 r'^{-\alpha} (r+r_s)^{\alpha-3} dr'. \quad (6.7)$$

Combining Eq.(6.6), Eq.(6.7) and Eq.(7.4), we computed the predictions of the surface brightness and temperature profiles for the fitting to the observed surface brightness and temperature profiles. The best fitting parameters for the ext-NFW model and the polytropic index were given by searching for the values that best reproduce the observed surface brightness and temperature profiles.

### 6.3.7 Gas mass fraction distribution

The gas mass fraction is an important parameter for cluster physics, e.g. heating and cooling processes, and cosmological applications using galaxy clusters (e.g. Vikhlinin et al. 2002; Allen et al. 2004). The gas mass fraction distribution is defined to be  $f_{\text{gas}}(< r) = M_{\text{gas}}(r)/M(r)$ .

We show the gas mass fraction profiles in Fig. 7.14. In the central regions, the CCCs show lower gas mass fractions. The gas mass fractions slightly increase as a function of the radius in the inner parts. This indicates that the DM shows a higher mass concentration in the center. The gas mass fraction becomes constant above  $r_{500}$  according to the modeling. We derived an average gas mass fraction of  $0.11 \pm 0.07$  at  $r_{500}$ . This is found for many massive clusters showing temperatures greater than 5 keV (e.g. Mohr et al. 1999). The gas mass fractions around  $r_{2500}$  show the smallest scatter,  $0.090 \pm 0.005$ , and the values are similar to the measurements of Allen et al. (2002) based on Chandra observations of seven clusters yielding  $f_{\text{gas}} \sim 0.105\text{--}0.138h_{70}^{-3/2}$ . At  $r_{200}$ , the gas mass fractions (Table 6.8) show consistency with the measurements of Sanderson et al. (2003) based on ASCA/GIS, ASCA/SIS and ROSAT/PSPC observations of 66 clusters yielding  $f_{\text{gas}} = 0.13 \pm 0.01h_{70}^{-3/2}$ , the measurements of Ettori et al. (2002a) based on BeppoSAX observations of 22 nearby clusters, and the gas mass fraction for A1413 (Pratt & Arnaud 2002) at  $z = 0.143$  based on XMM-Newton observations yielding  $f_{\text{gas}} \sim 0.12h_{70}^{-3/2}$ . The gas mass fraction distributions of the REFLEX-DXL clusters are slightly lower than the universal baryon fraction,  $f_b = \Omega_b/\Omega_m = 0.167 \pm 0.014$ , based on the recent WMAP measurements,  $h = 0.71_{-0.03}^{+0.04}$ ,  $\Omega_b h^2 = 0.022 \pm 0.001$  and  $\Omega_m h^2 = 0.132_{-0.009}^{+0.008}$  (e.g. Spergel et al. 2003; Hansen et al. 2004). This is expected because the baryons in galaxy clusters reside mostly in hot gas together with a fraction (15%  $f_{\text{gas}}$ ) in stars as implied from simulations (e.g. Eke et al. 1998; Kravtsov et al. 2005). In principle,  $\Omega_m$  can be determined from the baryon fraction,  $f_b = f_{\text{gas}} + f_{\text{gal}}$ , in which a contribution from stars in galaxies is given by  $f_{\text{gal}} = 0.02 \pm 0.01h_{50}^{-1}$  (White et al. 1993). The gas mass fractions,  $\sim 0.11$ , of the REFLEX-DXL clusters (Table 6.7, Table 6.8, and Table 6.9) support a low matter density Universe as shown in recent studies (e.g. Allen et al. 2002; Ettori et al. 2003; Vikhlinin et al. 2003).

RXCJ0516.7–5430 displays a significantly elongated and distorted morphology. The cluster central position is not clear due to the twist of the isophotes. The center shows a compression of the isophote distribution north of the cluster center. A clear substructure is the low surface brightness extension to  $r_{200}$  south of the cluster center. All these phenomena indicate that the cluster is still dynamically young. This can invalidate the hypothesis of spherical symmetry and hydrostatic equilibrium. Therefore, RXCJ0516.7–5430 shows the largest deviation in the gas mass fraction from those of the other REFLEX-DXL clusters.

## 6 X-ray properties in massive galaxy clusters

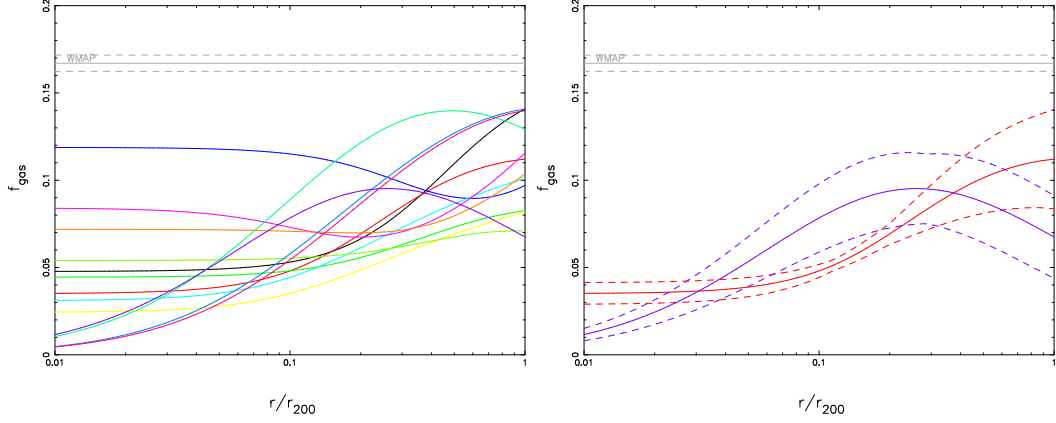


**Figure 6.9:** Gas mass fraction profiles for the REFLEX-DXL sample (left), with 1-sigma error corridor (dashed) displayed for two clusters only (right). The horizontal line represents the WMAP inferred baryon fraction with confidence intervals (dashed). The colors have an identical meaning as those in Fig. 6.8.

**Table 6.8:** Cluster catalogue part II. Cluster catalogue part I. Col. (1): Cluster name. Col. (2):  $r_{200}$ . Cols. (3–5): Gas mass, total mass and gas mass fraction at  $r_{200}$ .

RXCJ	$r_{200}$ (Mpc)	$M_{\text{gas},200}$ ( $10^{14} M_{\odot}$ )	$M_{200}$ ( $10^{14} M_{\odot}$ )	$f_{\text{gas},200}$
0014.3–3022	1.884	$1.53 \pm 0.01$	$10.41 \pm 1.31$	$0.15 \pm 0.02$
0043.4–2037	1.884	$1.16 \pm 0.01$	$10.28 \pm 2.94$	$0.11 \pm 0.03$
0232.2–4420	2.018	$1.61 \pm 0.23$	$12.48 \pm 1.49$	$0.13 \pm 0.02$
0303.7–7752	2.084	$1.15 \pm 0.01$	$13.68 \pm 2.85$	$0.08 \pm 0.02$
0307.0–2840	1.640	$0.92 \pm 0.12$	$6.52 \pm 2.02$	$0.14 \pm 0.05$
0437.1+0043	2.244	$1.16 \pm 0.26$	$17.21 \pm 2.91$	$0.07 \pm 0.02$
0516.7–5430	2.113	$1.69 \pm 0.02$	$14.47 \pm 7.30$	$0.12 \pm 0.08$
0528.9–3927	1.866	$1.38 \pm 0.14$	$9.87 \pm 2.74$	$0.14 \pm 0.04$
0532.9–3701	1.936	$1.17 \pm 0.01$	$10.93 \pm 1.13$	$0.11 \pm 0.01$
0658.5–5556	3.243	$3.10 \pm 0.01$	$52.37 \pm 13.35$	$0.06 \pm 0.02$
1131.9–1955	1.758	$1.11 \pm 0.01$	$8.45 \pm 3.97$	$0.13 \pm 0.07$
2308.3–0211	1.832	$0.84 \pm 0.01$	$9.50 \pm 1.98$	$0.09 \pm 0.02$
2337.6+0016	1.774	$0.99 \pm 0.01$	$8.42 \pm 2.07$	$0.12 \pm 0.03$
Mean	—	—	—	$0.11 \pm 0.08$



**Table 6.9:** Cluster catalogue part III. Cluster catalogue part I. Col. (1): Cluster name. Col. (2):  $r_{\text{vir}}$ . Cols. (3–5): Gas mass, total mass and gas mass fraction at  $r_{\text{vir}}$ .

RXCJ	$r_{\text{vir}}$ (Mpc)	$M_{\text{gas, vir}}$ ( $10^{14} M_{\odot}$ )	$M_{\text{vir}}$ ( $10^{14} M_{\odot}$ )	$f_{\text{gas, vir}}$
0014.3–3022	2.339	$1.87 \pm 0.01$	$12.52 \pm 1.69$	$0.15 \pm 0.02$
0043.4–2037	2.426	$1.53 \pm 0.02$	$13.66 \pm 4.19$	$0.11 \pm 0.03$
0232.2–4420	2.624	$2.05 \pm 0.29$	$16.96 \pm 2.25$	$0.12 \pm 0.03$
0303.7–7752	2.673	$1.48 \pm 0.02$	$17.64 \pm 3.95$	$0.08 \pm 0.02$
0307.0–2840	2.084	$1.15 \pm 0.15$	$8.14 \pm 2.64$	$0.14 \pm 0.05$
0437.1+0043	3.013	$1.49 \pm 0.34$	$25.77 \pm 5.01$	$0.06 \pm 0.02$
0516.7–5430	2.600	$2.17 \pm 0.03$	$16.80 \pm 9.93$	$0.13 \pm 0.10$
0528.9–3927	2.371	$1.77 \pm 0.18$	$12.57 \pm 4.02$	$0.14 \pm 0.05$
0532.9–3701	2.483	$1.57 \pm 0.02$	$14.15 \pm 1.58$	$0.11 \pm 0.01$
0658.5–5556	4.121	$3.68 \pm 0.02$	$67.28 \pm 18.50$	$0.05 \pm 0.02$
1131.9–1955	2.143	$1.39 \pm 0.01$	$9.64 \pm 4.83$	$0.14 \pm 0.08$
2308.3–0211	2.328	$1.11 \pm 0.02$	$12.14 \pm 2.63$	$0.09 \pm 0.02$
2337.6+0016	2.153	$1.17 \pm 0.01$	$9.22 \pm 2.45$	$0.13 \pm 0.03$
Mean	—	—	—	$0.11 \pm 0.09$

## 6.4 Scaling relations

Simulations (e.g. Navarro et al. 1997) suggested a self-similar structure for galaxy clusters in hierarchical structure formation scenarios. The scaled profiles of the X-ray properties and their scatter can be used to quantify the structural variations. This provides a probe to test the regularity in galaxy clusters and to understand their formation and evolution. The accuracy of the determination of the correlations, limited by how precise the cluster mass and other global observables can be estimated, is of prime importance for the cosmological applications of clusters of galaxies.

As a representation of cluster mass, the global temperature is most important for scaling relations. The global temperature can be determined by the temperature profile weighted by, e.g.  $M_{\text{gas}}$  over the annuli truncated at, e.g.  $r_{200}$ . We have determined five different global temperatures defined as (a) spectral measured global temperatures,  $T_{\text{spec}}$  (defined in Sect. 6.3.1), (b) emission weighted temperatures,  $T_{\text{esw}}$ , (c) emission measure weighted temperatures,  $T_{\text{emw}}$ , (d) total mass weighted temperatures,  $T_{\text{mw}}$ , and (e) gas mass weighted temperatures,  $T_{\text{gmw}}$ , respectively. (a) slightly depends on the region selection. (b), (c), (d) and (e) are almost independent on the truncation radii for integration.  $T_{\text{esw}}$  and  $T_{\text{emw}}$  are tightly correlated with each other. So are  $T_{\text{mw}}$  and  $T_{\text{gmw}}$ . We found that  $T_{\text{spec}}$  and  $T_{\text{gmw}}$  reduce the scatter of the scaling relations at most (see Fig. 6.10). This is expected because  $T_{\text{spec}}$  and  $T_{\text{gmw}}$  are less weighted by the gas density and are thus less affected by cooling flows. Therefore, we only show the scaling relations and correlations using  $T_{\text{gmw}}$ .

We used  $r_{\text{vir}}$ ,  $r_{200}$  and  $r_{500}$ , respectively, for radial scaling. The presence of a cooling flow in some clusters increases the scatter because of the weight of the central region.

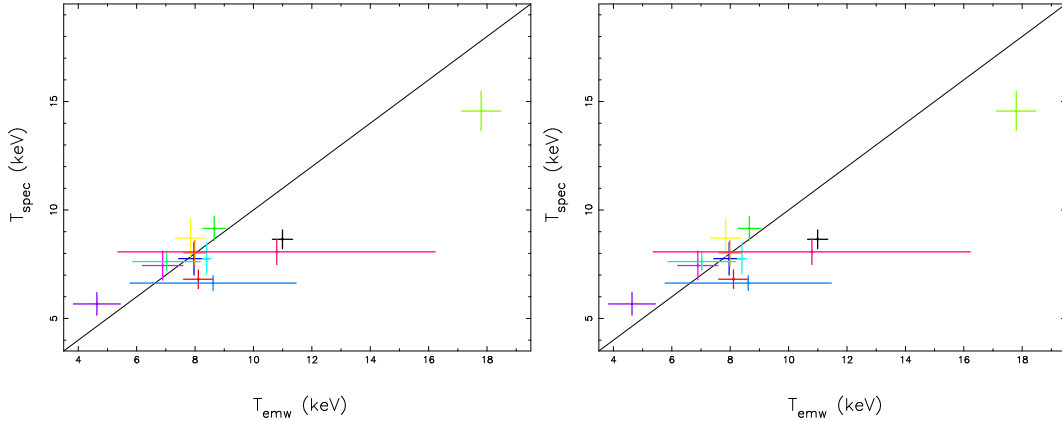


**Figure 6.10:** A comparison of  $T_{\text{spec}}$  to  $T_{\text{emw}}$  (left) and  $T_{\text{gmw}}$  (right), respectively, integrated up to the  $r_{200}$ . The colors have an identical meaning as those in Fig. 6.8.

### 6.4.1 Scaled metallicity profiles

The metallicity gradients in clusters can be used to study the star formation history and chemical enrichment history (e.g. Mushotzky & Loewenstein 1997). A uniform metallicity profile is expected if clusters virialized without subsequent metal injections. Enrichment after the virialization produces a higher metal concentration by the injections in the cluster center (e.g. Mushotzky & Loewenstein 1997). This happens significantly in the CCCs.

We have compared the scaled metallicity profiles of the REFLEX-DXL clusters (see Fig. 6.11) to the profiles of the nearby clusters (e.g. De Grandi et al. 2004) and more distant clusters (e.g. Tozzi et al. 2003). We found that the metallicity profiles of massive clusters are relatively universal. Mergers can disperse cooling flows and thus destroy the central metallicity concentration. Since the REFLEX-DXL CCCs only show moderate cooling flows, the difference between the metallicity profiles of the REFLEX-DXL CCCs and NCCCs is not as significant as for the other cluster samples in e.g. Tozzi et al. (2003) and De Grandi et al. (2004). On the other hand, the resolution of the REFLEX-DXL sample may not be good enough to observe the metallicity peaks.

### 6.4.2 Scaled temperature profiles

Studies of the cluster temperature distributions (e.g. Markevitch et al. 1998; De Grandi & Molendi 2002) indicate a steep decline beyond an isothermal center. We scaled the projected and deprojected temperature profiles. The deprojected temperature profiles show higher uncertainties as described in Sect. 6.2.4.

Excluding individual data points with error bars  $\geq 1.5$  of the mean value, we derived an average temperature profile using the scaled projected temperature profiles of the REFLEX-DXL clusters. As shown in Fig. 6.12, we found a closely self-similar behavior. Up to  $0.3r_{\text{vir}}$ , we observed a constant temperature for the NCCCs, but an increasing temperature with radius for the CCCs with a temperature peak at around  $0.2-0.3 r_{\text{vir}}$ . A decreasing temperature profile down to 50% has been observed outside  $0.3r_{\text{vir}}$  for most of the REFLEX-

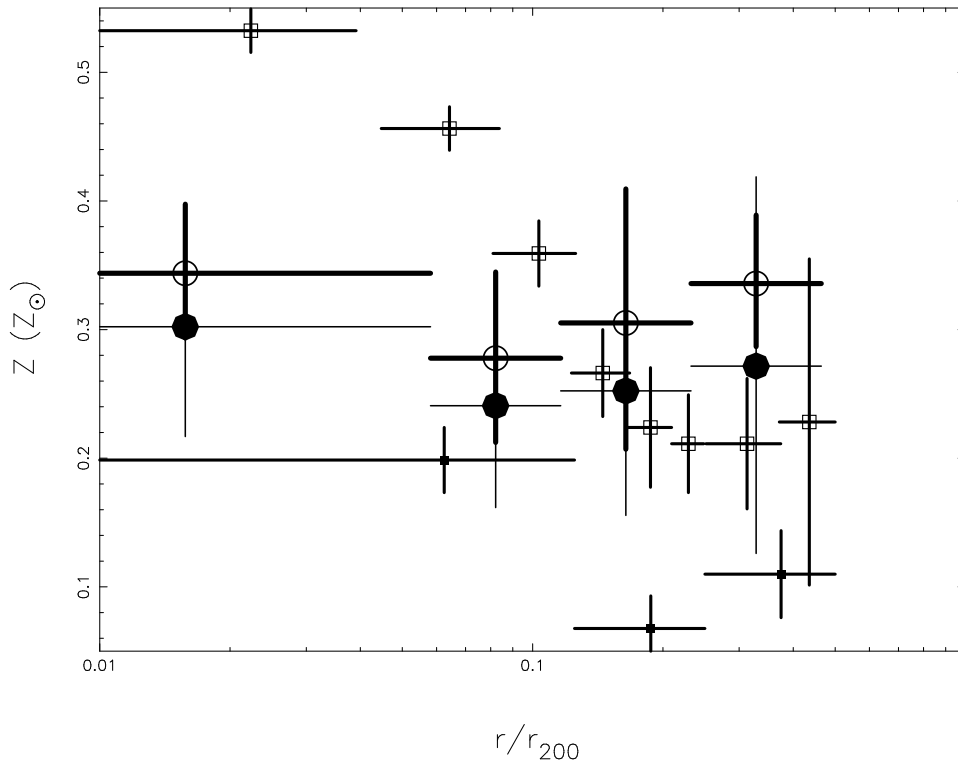


**Figure 6.11:** Metallicity profiles for the CCCs (open) and NCCCs (filled) in De Grandi et al. (2004, box) and in this work (circle).

DXL clusters. This average temperature profile is consistent with the average profiles from ASCA in Markevitch et al. (1998), BeppoSAX in De Grandi & Molendi (2002) and Chandra in Vikhlinin et al. (2005a) within the observational dispersion. We note that we assume an uncertainty of 20% of the central temperature for the averaged temperature profile in Vikhlinin et al. (2005a). A similarly universal temperature profile is indicated by simulations (Borgani et al. 2004; Borgani 2004).

### 6.4.3 Scaled surface brightness profiles

The surface brightness profiles can be scaled according to the standard self-similar model,  $S_X \propto T^{0.5}$  (e.g. Arnaud et al. 2002a). We found good self-similarity at  $r > 0.1 r_{\text{vir}}$  (see Fig. 6.13). The empirically determined relation,  $S_X \propto T^{1.38}$  including additional physical processes, does not improve the scatter significantly. This is expected since the sample covers a narrow temperature range. The NCCCs show flat cores. The core radii span a broad range of  $0.1\text{--}0.5 h_{70}^{-1}$  Mpc (around  $0.04\text{--}0.1 r_{\text{vir}}$ ). A surface brightness excess has been found in the central parts for the CCCs.

RXCJ0516.7–5430 shows an elongation with an ellipticity of 0.94. RXCJ0658.5–5556 shows a significant subclump with a mass ratio of 1:6 (Markevitch et al. 2002) although the subclump can approximately be removed. These two clusters introduce a significant observational scatter in the scaled surface brightness profiles.

## 6 X-ray properties in massive galaxy clusters

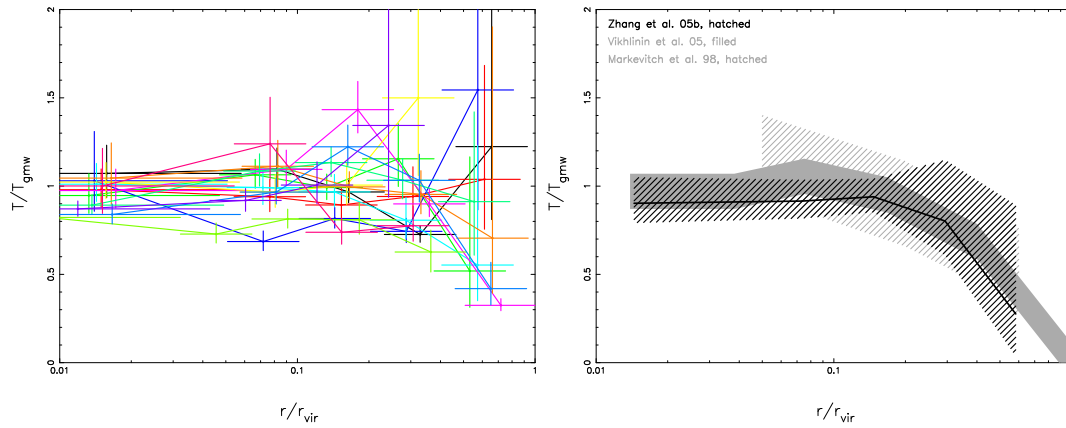


**Figure 6.12: Left:** Scaled projected temperature profiles. The colors have an identical meaning as those in Fig. 6.8. **Right:** An average temperature profile of the REFLEX-DXL clusters in Zhang et al. (2005b, black, hatched, the mean shown in a thick line) and the temperature profile ranges in Markevitch et al. (1998, grey, hatched) and Vikhlinin et al. (2005a, grey, filled).

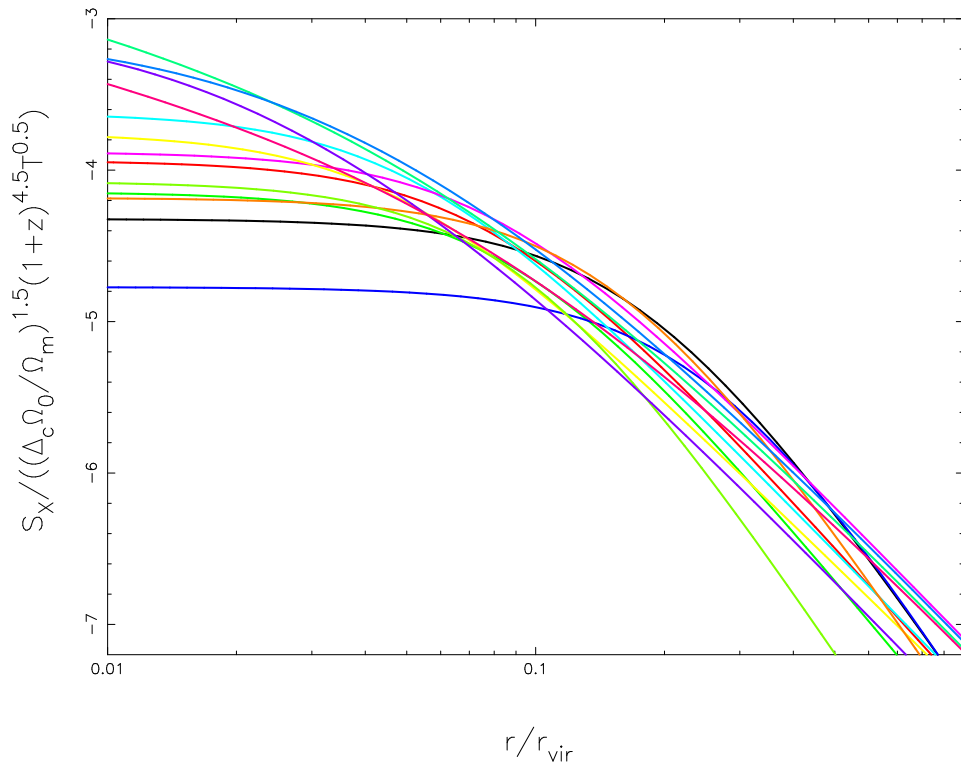


**Figure 6.13:** Surface brightness profile fits scaled according to the self-similar model,  $S_X \propto T^{0.5}$ . The colors have an identical meaning as those in Fig. 6.8.

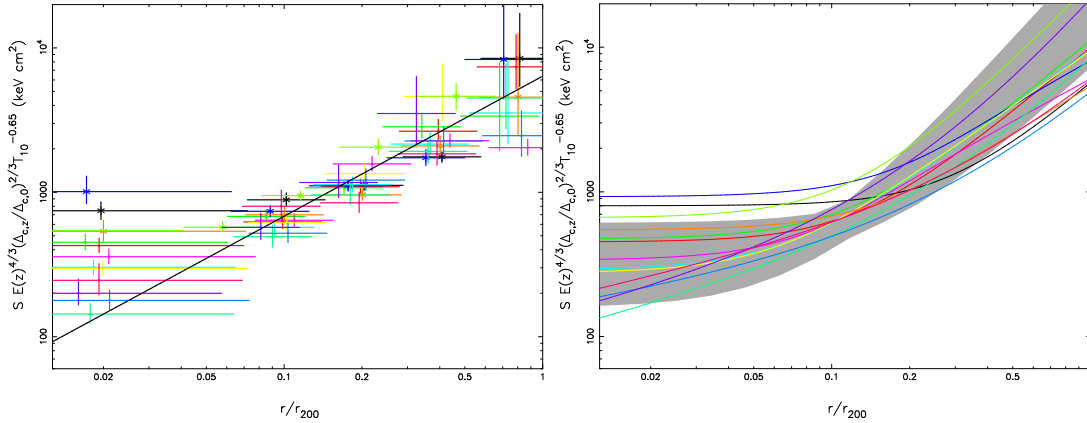


**Figure 6.14:** **Left:** Scaled entropy profiles. The line denotes the best fit scaling with a radial dependence of  $r^{0.97}$ . The merger clusters are shown with asterisk symbols. **Right:** Scaled entropy profile fits of the REFLEX-DXL sample comparing to the Birmingham-CfA clusters (grey shadow) in a temperature range of 6–20 keV. The colors have an identical meaning as those in Fig. 6.8.

#### 6.4.4 Scaled entropy profiles

According to the standard self-similar model the entropy scales as  $S \propto T$  (e.g. Pratt & Arnaud 2005). Ponman et al. (2003) suggested to scale the entropy as  $S \propto T^{0.65}$ . In the preheating scenario, the entropy can be scaled by  $1 + \frac{T(r)}{T_{\text{pre}}}$ , in which  $T_{\text{pre}} \sim 2$  keV is a constant related to the degree of preheating (Ponman et al. 2003). In Fig. 6.14, we show the scaled entropy profiles of the REFLEX-DXL clusters. The REFLEX-DXL sample agrees with the Birmingham-CfA clusters (Ponman et al. 2003) in the same temperature range (6–20 keV) within the observational dispersions. Similar to the scaled temperature profiles, the empirically determined relation (Ponman et al. 2003),  $S \propto T^{0.65}$ , does not reduce the scatter significantly (Fig. 6.14) due to the narrow temperature range of the sample. For example, the scatter around  $0.1\text{--}0.2r_{200}$  is 57% and 60% in the entropy profile scaled as  $S \propto T^{0.65}$  and  $S \propto T$ , respectively. The entropy profiles above  $0.1r_{\text{vir}}$  agree with the results in Ettori et al. (2002b) showing  $S \propto r^{0.97}$ , but is shallower than the predicted slope from a spherical accretion shock model of  $S \propto r^{1.1}$  (e.g. Kay 2004).

#### 6.4.5 Scaled total mass profiles

The mass profiles have been scaled using the  $M_{\text{vir}}$  and  $r_{\text{vir}}$  (Fig. 6.15). We found similarity at  $r > 0.1r_{\text{vir}}$ . In the inner parts with  $r < 0.1r_{\text{vir}}$ , the CCCs show a higher mass concentration than the NCCCs. The NFW model provides the best fit at  $r > 0.1$  Mpc (Fig. 6.15).

## 6 X-ray properties in massive galaxy clusters

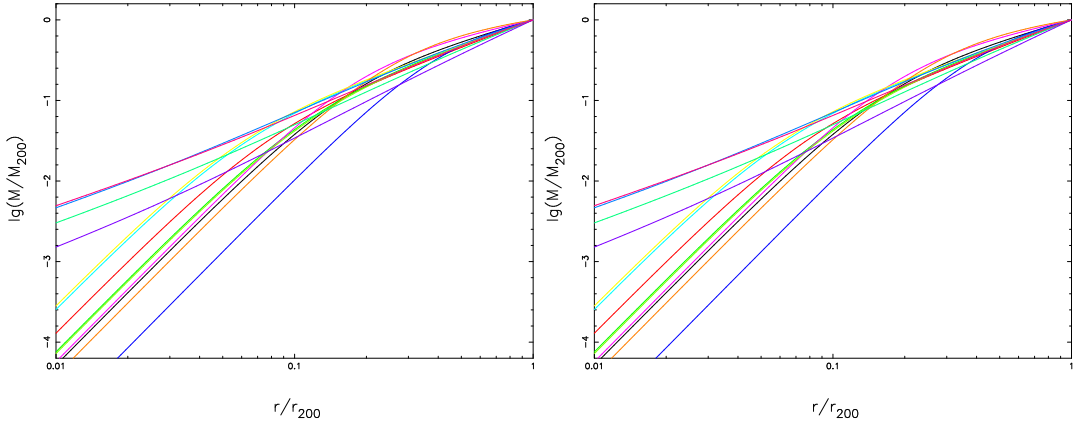


**Figure 6.15:** Scaled total mass profiles for the REFLEX-DXL sample (left), with  $1\text{-}\sigma$  error corridor (dashed) and the best NFW model fits (dash-dotted) displayed for two clusters (right). The colors have an identical meaning as those in Fig. 6.8.

### 6.5 Correlations

We have investigated some relations between different X-ray properties of the REFLEX-DXL clusters. The strength of the correlation of two properties can be indicated<sup>6</sup> by the Pearson's correlation coefficient  $R_{xy} = \frac{\Sigma_i(x_i - \bar{x})\Sigma_i(y_i - \bar{y})}{\sqrt{\Sigma_i(x_i - \bar{x})^2 \Sigma_i(y_i - \bar{y})^2}}$ . The tightly correlated relations have then been fitted using a power law model.

#### 6.5.1 Core radius

The core radius and slope in the  $\beta$ -model are correlated showing a bimodal behavior (see Table 7.3). This results in that merging clusters show both large core radius and steep slope.

The total mass shows no significant correlation with the core radius. The core radius is anti-correlated with the cooling time which can be explained physically. For example, mergers flatten the surface brightness which increases the core radius. Mergers heat the ICM which increases the cooling time.

#### 6.5.2 Gas mass fraction

Since we only consider massive clusters in this work, the influence on the ICM of non-gravitational effects of energy input is expected to be less important. This is also indicated by simulations (Rowley et al. 2004). The gas mass fractions at  $r_{500}$  and  $r_{200}$  are thus not correlated with the cluster temperatures and masses. The ratio of the gas mass fractions at larger and smaller radii (e.g.  $r_{200}$  and  $r_{500}$ ) can be used to characterize the extent of gas relative to DM. The gas is more extended than DM if  $f_{\text{gas},200}/f_{\text{gas},500} > 1$  (Reiprich 2002). For the REFLEX-DXL clusters, the ratio is around 1 (Fig. 6.16). This indicates that gas follows DM in the outer region.

<sup>6</sup>We only use the coefficient as an initial indication for the further correlation studies

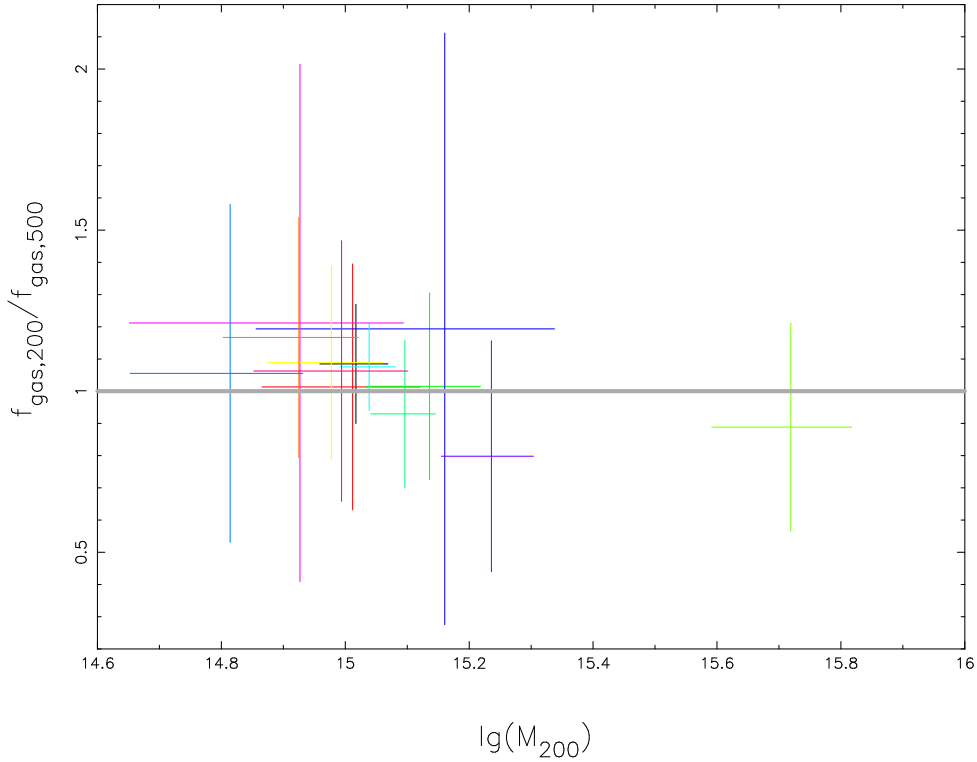


**Figure 6.16:** Gas mass fraction ratio,  $f_{\text{gas},200}/f_{\text{gas},500}$ , for the REFLEX-DXL clusters. The thick horizontal line represents  $f_{\text{gas},200}/f_{\text{gas},500} = 1$ . The colors have an identical meaning as those in Fig. 6.8.

### 6.5.3 $\delta_c$ - $M_{\text{vir}}$ and $c_{\text{vir}}$ - $M_{\text{vir}}$ relations

In the hierarchical scenario, low mass halos formed at earlier epoch and are thus denser than high mass halos. The low mass halos subsequently merge to form the larger mass ones. As indicated by simulations, the density profiles of DM have a universal form, e.g. the NFW model. Therefore, the characteristic density and scale of the halo should be correlated with the  $M_{\text{vir}}$  of the dark halos (e.g. Navarro et al. 1997).

The NFW model fits the X-ray mass profile of the NCCCs and CCCs at  $r > 0.1r_{200}$ . Therefore we also provide the best NFW model fits for the REFLEX-DXL clusters excluding the  $r < 0.1$  Mpc region (see Table 6.10). The concentration parameter is defined by  $c_{\Delta} = r_{\Delta}/r_s$ .

Observational relations of  $\delta_c$ - $M_{\text{vir}}$  and  $c_{\text{vir}}$ - $M_{\text{vir}}$  are therefore critical tests of hierarchical structure formation models. Cheng & Wu (2001) derived the best fits of  $\delta_c = 10^{19.44 \pm 2.65} (M_{\text{vir}}/M_{\odot})^{-1.06 \pm 0.07}$  and  $c_{\text{vir}} = 10^{7.34 \pm 1.10} (M_{\text{vir}}/M_{\odot})^{-0.45 \pm 0.07}$ . The  $\delta_c$ - $M_{\text{vir}}$  and  $c_{\text{vir}}$ - $M_{\text{vir}}$  (Fig 6.17) relations of the REFLEX-DXL clusters agree with the best fits in Cheng & Wu (2001). Three CCCs show a slightly larger deviation<sup>7</sup>.

<sup>7</sup>Note: these deviations are not related to cluster mergers.

## 6 X-ray properties in massive galaxy clusters

**Table 6.10:** Cluster catalogue part IV. Col. (1): Cluster name. Col. (2): Power law index of the surface brightness profile fit in the outskirts ( $2' < r < 8'$ ). Cols. (3–6): NFW parameters of the mass profile fit and the concentration parameters. Cols. (7–8): Bolometric X-ray luminosity within  $r_{200}$  including and excluding  $r < 0.1r_{200}$  in units of  $10^{45} \text{ erg s}^{-1}$ .

RXCJ	Index	$\delta_c^{\text{NFW}}$	$r_s^{\text{NFW}}$ (Mpc)	$c_{200}^{\text{NFW}}$	$c_{\text{vir}}^{\text{NFW}}$	$L_X^{\text{bol},200}$	$L_X^{\text{bol},200,*}$
0014.3–3022	2.57	$2857.1 \pm 223.8$	$0.63 \pm 0.02$	$2.98 \pm 0.12$	$3.69 \pm 0.15$	$3.89 \pm 0.13$	$3.68 \pm 0.12$
0043.4–2037	1.81	$2205.6 \pm 192.4$	$0.74 \pm 0.03$	$2.55 \pm 0.12$	$3.29 \pm 0.16$	$2.93 \pm 0.04$	$2.58 \pm 0.03$
0232.2–4420	2.39	$1053.4 \pm 72.0$	$1.15 \pm 0.04$	$1.75 \pm 0.07$	$2.27 \pm 0.09$	$4.03 \pm 0.10$	$2.91 \pm 0.04$
0303.7–7752	2.30	$2354.5 \pm 129.4$	$0.78 \pm 0.02$	$2.67 \pm 0.08$	$3.43 \pm 0.10$	$2.35 \pm 0.05$	$2.07 \pm 0.05$
0307.0–2840	2.29	$2247.8 \pm 142.0$	$0.64 \pm 0.02$	$2.58 \pm 0.08$	$3.28 \pm 0.10$	$2.80 \pm 0.01$	$2.15 \pm 0.04$
0437.1+0043	1.82	$504.0 \pm 19.0$	$1.90 \pm 0.04$	$1.18 \pm 0.03$	$1.58 \pm 0.04$	$2.17 \pm 0.09$	$1.46 \pm 0.01$
0516.7–5430	2.17	$174.7 \pm 31.4$	$2.91 \pm 0.37$	$0.73 \pm 0.10$	$0.89 \pm 0.13$	$2.22 \pm 0.06$	$2.14 \pm 0.05$
0528.9–3927	3.16	$1698.2 \pm 113.8$	$0.83 \pm 0.03$	$2.25 \pm 0.08$	$2.86 \pm 0.10$	$3.51 \pm 0.22$	$2.77 \pm 0.24$
0532.9–3701	2.13	$4066.2 \pm 418.3$	$0.56 \pm 0.03$	$3.43 \pm 0.18$	$4.39 \pm 0.23$	$3.25 \pm 0.04$	$2.61 \pm 0.05$
0658.5–5556	2.99	$2097.7 \pm 147.8$	$1.22 \pm 0.05$	$2.65 \pm 0.11$	$3.37 \pm 0.15$	$8.81 \pm 0.22$	$7.37 \pm 0.17$
1131.9–1955	2.97	$7221.5 \pm 792.2$	$0.38 \pm 0.02$	$4.61 \pm 0.24$	$5.61 \pm 0.30$	$2.85 \pm 0.12$	$2.54 \pm 0.12$
2308.3–0211	2.61	$4106.3 \pm 445.4$	$0.53 \pm 0.03$	$3.43 \pm 0.19$	$4.35 \pm 0.24$	$1.80 \pm 0.16$	$1.43 \pm 0.12$
2337.6+0016	2.26	$6220.2 \pm 1314.1$	$0.39 \pm 0.04$	$4.57 \pm 0.49$	$5.55 \pm 0.60$	$2.13 \pm 0.03$	$1.98 \pm 0.02$
Mean	2.42	—	—	—	—	—	—

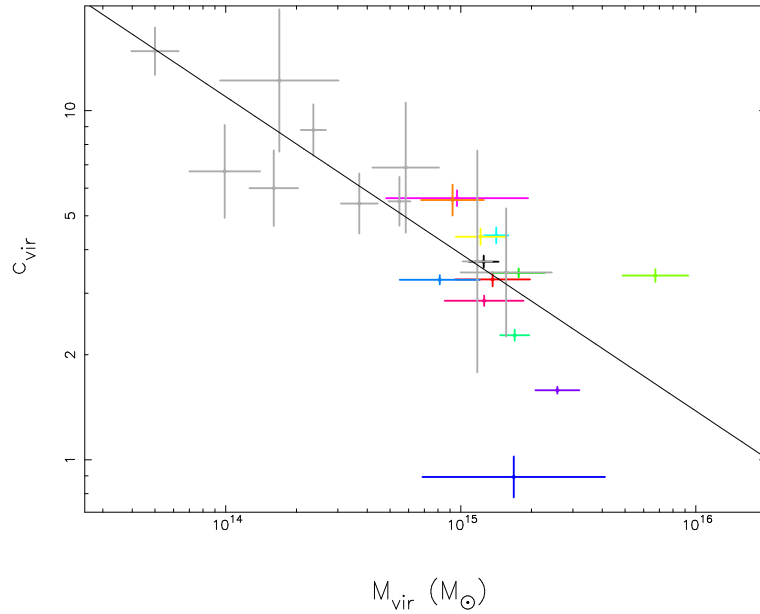


**Figure 6.17:**  $c_{\text{vir}}$  vs.  $M_{\text{vir}}$  for the REFLEX-DXL clusters and the clusters in Cheng & Wu (2001, grey). The best fit is from Cheng & Wu (2001). The colors have an identical meaning as those in Fig. 6.8.



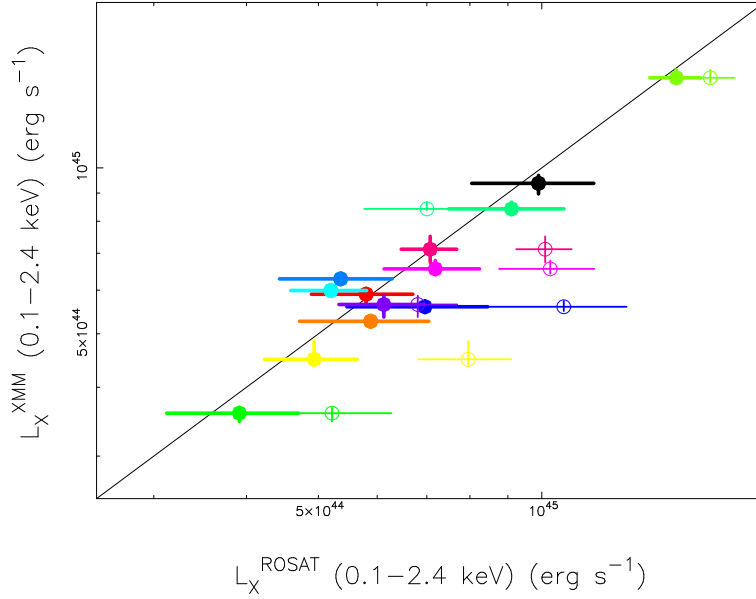


**Figure 6.18:** A comparison of the XMM-Newton luminosities and ROSAT luminosities taken from Böhringer et al. (2004a). Filled and open circles correspond to the substructure and point-like source subtracted and unsubtracted ROSAT luminosities considering the point-like sources and substructures according to the XMM-Newton observations. The colors have an identical meaning as those in Fig. 6.8.

#### 6.5.4 $L-T$ , $L-M$ , $M-T$ , $M_{\text{gas}}-T$ and $L-Z$ relations

To construct a temperature function and mass function of this flux-limited and almost volume-limited sample, it is important to calibrate the correlations between the X-ray luminosity, temperature and gravitational mass. These correlations are usually parameterized by a power law. The intrinsic dispersion between the observed relationship and theory is caused by various processes.

##### 6.5.4.1 ROSAT and XMM-Newton luminosities

We compared the ROSAT and XMM-Newton luminosity measurements. We used the ROSAT truncation radii and the ROSAT band (0.1–2.4 keV) to compute the XMM-Newton luminosities. The XMM-Newton results agree with the ROSAT measurements with reduced error bars (Fig. 6.18) for 8 REFLEX-DXL clusters. For the remaining clusters, the ROSAT luminosity is different from the XMM-Newton results since the substructure contribution is included in the ROSAT cluster luminosity but not in the XMM-Newton cluster luminosity.

The frequency of substructure occurrence is around  $52 \pm 7\%$  (Schuecker et al. 2001) in galaxy clusters. Although the substructure is part of the cluster, we subtract the substructure and leave the main, largely relaxed component which better complies with the hypothesis of spherical symmetry. The high resolution of the XMM-Newton data allows us to identify the substructure and point-like sources better than what was possible with the

## 6 X-ray properties in massive galaxy clusters

**Table 6.11:** Approximate luminosities of the substructure and point-like sources in units of the ROSAT measured cluster luminosities.

RXCJ	Substructure	Point-like sources	Remark
0232.2–4420	$\sim -0.30$	—	a
0303.7–7752	$\sim 0.20-0.25$	$\sim 0.05$	—
0516.7–5430	$\sim 0.35$	—	b
0528.9–3927	$\sim 0.20$	$\sim 0.03-0.10$	—
0658.5–5556	$\sim 0.10$	—	—
1131.9–1955	$\sim 0.15-0.20$	$\sim 0.03-0.10$	—
2308.3–0211	—	$\sim 0.30-0.40$	c

a, the substructure contribution was overestimated in the ROSAT count rate analysis. b, the low surface brightness extension was included in the ROSAT analysis. c, the central point-like source contributes 0.23.

earlier X-ray telescopes. In Table 6.11, we show the contribution to the cluster luminosity from the substructure which was included in the ROSAT measured cluster luminosity but not in the XMM-Newton measured cluster luminosity. Excluding the substructure contribution to the ROSAT measured cluster luminosities, we found a good agreement between the ROSAT and XMM-Newton measured luminosities for the REFLEX-DXL clusters. The XMM-Newton data provide a reliable detection of the substructures and point-like sources. Therefore we make use of this capability to obtain a better approximation to spherical symmetry and dynamical equilibrium of the main cluster component by excluding the substructures and point-like sources. This is more representative for investigating various correlations of the global properties of the galaxy clusters, such as the  $L$ - $T$  relation.

### 6.5.4.2 $L$ - $T$ and $L$ - $M$ relations

The X-ray luminosity is a key parameter among the fundamental cluster properties including also mass, temperature and velocity dispersion. Excluding the cooling core ( $\sim 0.1h_{50}^{-1}$  Mpc), Markevitch (1998) reduced the scatter in the  $L_X^{\text{bol}}-T$  relation. However, the normalization of the  $L$ - $T$  relation was also reduced by excluding cooling cores. In Table 6.10, we list the bolometric X-ray luminosities of the REFLEX-DXL clusters including and excluding the cluster cores,  $r < 0.05r_{200}$  as used in many studies (e.g. Markevitch 1998; Zhang 2001). We found that 4–33% of the luminosity is contributed by the cluster cores, 11–33% and 4–13% for the CCCs and NCCCs, respectively, for the REFLEX-DXL clusters. In Table 6.12, we have collected the published  $L$ - $T$  relations and compared them to the  $L$ - $T$  relation of the REFLEX-DXL sample. We note that we used the same truncation radius for the integral to derive  $L$  as for  $T_{\text{gmw}}$  and  $M$ . Comparing the REFLEX-DXL sample to the nearby samples, we found a positive evolution of the  $L$ - $T$  and  $L$ - $M$  relations. This can be accounted for by the redshift evolution corrections. As shown in Table 6.12, Fig. 6.19, and Fig. 6.20, we obtained an overall agreement with the previous studies of the  $L$ - $T$  relation for galaxy clusters by the redshift evolution correction. This redshift evolution in the  $L$ - $T$  relation was also described in Kotov & Vikhlinin (2005) as  $L \propto T^{2.64}(1+z)^{1.8}$ . Their result agrees with that of the REFLEX-DXL sample within the observational dispersion. The isothermal mass modeling provides a higher mass estimate by a factor of 30% (Maughan et al. 2003) compared to the non-isothermal mass modeling. Therefore, we also modify

**Table 6.12:** Power law,  $Y = L_0 X^\alpha$  erg s $^{-1}$ , parameterized  $L$ - $T$  relations in this work and in literature.

Relation	$L_0$	$\alpha$	Reference	Method
$L_X^{\text{bol}}-T$	$10^{43.05 \pm 0.08} h_{50}^{-2}$	$2.62 \pm 0.10$	Edge & Stewart 91	OLS <sup>c</sup>
$L_X^{\text{bol}}-T$	$10^{43.01 \pm 0.29} h_{50}^{-2}$	$2.7 \pm 0.4$	Henry & Arnaud 91	OLS
$L_X^{\text{bol}}-T$	$10^{42.68 \pm 0.08} h_{50}^{-2}$	$2.98 \pm 0.11$	White et al. 97	ODR
$L_X^{\text{bol}}-T$	$10^{42.43 \pm 0.04} h_{100}^{-2}$	$2.64 \pm 0.27$	Markevitch 98 <sup>a</sup>	BCES <sup>d</sup>
$L_X^{\text{bol}}-T$	$10^{42.82 \pm 0.03} h_{50}^{-2}$	$2.88 \pm 0.15$	Arnaud & Evrard 99	OLS
$L_X^{\text{bol}}-T$	$10^{43.08 \pm 0.05} h_{50}^{-2}$	$2.72 \pm 0.05$	Wu et al. 99	ODR
$L_X^{\text{bol}}-T$	$10^{42.97 \pm 0.07} h_{50}^{-2}$	$2.79 \pm 0.08$	Xue & Wu 00	ODR
$L_X^{\text{bol}}-T$	$10^{42.73 \pm 0.10} h_{50}^{-2}$	$2.84 \pm 0.13$	Horner 01	BCES
$L_X^{\text{bol}}-T$	$10^{42.85 \pm 0.09} h_{50}^{-2}$	$2.98 \pm 0.12$	Reiprich & Böhringer 02	BCES
$L_{X,500}^{\text{bol}}-T$	$10^{43.00^{+0.11}_{-0.15}} h_{70}^{-2}$	$2.5 \pm 0.1$	Borgani et al. 2004 <sup>b</sup>	OLS
$L_{X,500}^{\text{bol}}-T$	$10^{42.99 \pm 0.04} h_{70}^{-2}$	$2.64^*$	This work	ODR
$L_{X,500}^{\text{bol}} E(z)^{-1} \left(\frac{\Delta_{c,z}}{\Delta_{c,0}}\right)^{-0.5} -T$	$10^{42.88 \pm 0.04} h_{70}^{-2}$	$2.64^*$	This work	ODR
$L_{X,500}^{\text{bol}} (1+z)^{1.8} -T$	$10^{42.79 \pm 0.04} h_{70}^{-2}$	$2.64^*$	This work	ODR
$L_{X,200}^{\text{bol}}-T$	$10^{43.02 \pm 0.05} h_{70}^{-2}$	$2.64^*$	This work	ODR
$L_{X,200}^{\text{bol}} E(z)^{-1} \left(\frac{\Delta_{c,z}}{\Delta_{c,0}}\right)^{-0.5} -T$	$10^{42.91 \pm 0.05} h_{70}^{-2}$	$2.64^*$	This work	ODR
$L_{X,200}^{\text{bol}} (1+z)^{1.8} -T$	$10^{42.82 \pm 0.04} h_{70}^{-2}$	$2.64^*$	This work	ODR
$L_{X,\text{vir}}^{\text{bol}}-T$	$10^{43.03 \pm 0.04} h_{70}^{-2}$	$2.64^*$	This work	ODR
$L_{X,\text{vir}}^{\text{bol}} E(z)^{-1} \left(\frac{\Delta_{c,z}}{\Delta_{c,0}}\right)^{-0.5} -T$	$10^{42.92 \pm 0.04} h_{70}^{-2}$	$2.64^*$	This work	ODR
$L_{X,\text{vir}}^{\text{bol}} (1+z)^{1.8} -T$	$10^{42.83 \pm 0.04} h_{70}^{-2}$	$2.64^*$	This work	ODR
$L_X^{0.1-2.4} -T$	$10^{42.19^{+0.27}_{-0.29}} h_{100}^{-2}$	$2.44^{+0.39}_{-0.38}$	Ikebe et al. 02	OLS
$L_X^{0.1-2.4} -T$	$10^{42.52 \pm 0.04} h_{100}^{-2}$	$2.10 \pm 0.24$	Markevitch 98	BCES
$L_X^{0.1-2.4} -T$	$10^{42.79 \pm 0.09} h_{50}^{-2}$	$2.60 \pm 0.13$	Reiprich & Böhringer 02	BCES
$L_{X,500}^{0.1-2.4} -T$	$10^{42.41 \pm 0.05} h_{70}^{-2}$	$2.64^*$	This work	ODR
$L_{X,500}^{0.1-2.4} E(z)^{-1} \left(\frac{\Delta_{c,z}}{\Delta_{c,0}}\right)^{-0.5} -T$	$10^{42.30 \pm 0.05} h_{70}^{-2}$	$2.64^*$	This work	ODR
$L_{X,500}^{0.1-2.4} (1+z)^{1.8} -T$	$10^{42.21 \pm 0.05} h_{70}^{-2}$	$2.64^*$	This work	ODR
$L_{X,200}^{0.1-2.4} -T$	$10^{42.43 \pm 0.05} h_{70}^{-2}$	$2.64^*$	This work	ODR
$L_{X,200}^{0.1-2.4} E(z)^{-1} \left(\frac{\Delta_{c,z}}{\Delta_{c,0}}\right)^{-0.5} -T$	$10^{42.32 \pm 0.05} h_{70}^{-2}$	$2.64^*$	This work	ODR
$L_{X,200}^{0.1-2.4} (1+z)^{1.8} -T$	$10^{42.23 \pm 0.05} h_{70}^{-2}$	$2.64^*$	This work	ODR
$L_{X,\text{vir}}^{0.1-2.4} -T$	$10^{42.45 \pm 0.05} h_{70}^{-2}$	$2.64^*$	This work	ODR
$L_{X,\text{vir}}^{0.1-2.4} E(z)^{-1} \left(\frac{\Delta_{c,z}}{\Delta_{c,0}}\right)^{-0.5} -T$	$10^{42.34 \pm 0.05} h_{70}^{-2}$	$2.64^*$	This work	ODR
$L_{X,\text{vir}}^{0.1-2.4} (1+z)^{1.8} -T$	$10^{42.25 \pm 0.05} h_{70}^{-2}$	$2.64^*$	This work	ODR

<sup>a</sup> Cooling cores excluded; <sup>b</sup> Simulations; <sup>c</sup> Ordinary Least Squares method (Akritas & Bershadsky 1996, OLS); <sup>d</sup> Bivariate Correlated Errors and intrinsic Scatter method (Isobe et al. 1990, BCES); \* fixed value.

the  $L$ - $M$  relation in Popesso et al. (2003) by decreasing the mass by a factor of 30% as a non-isothermal correction. In Fig. 6.21, we compared the  $L$ - $M$  relation (Table 6.13) of the REFLEX-DXL sample to the sample in Popesso et al. (2005) with and without the non-isothermal correction and obtained a good agreement.

### 6.5.4.3 $M$ - $T$ relation

The scatter in the  $M$ - $T$  relation comes mainly from the temperature measure uncertainty. The massive clusters in a narrow temperature range provide an important means to constrain the normalization of the  $M$ - $T$  relation for clusters at  $z \sim 0.3$ . We have collected the

## 6 X-ray properties in massive galaxy clusters

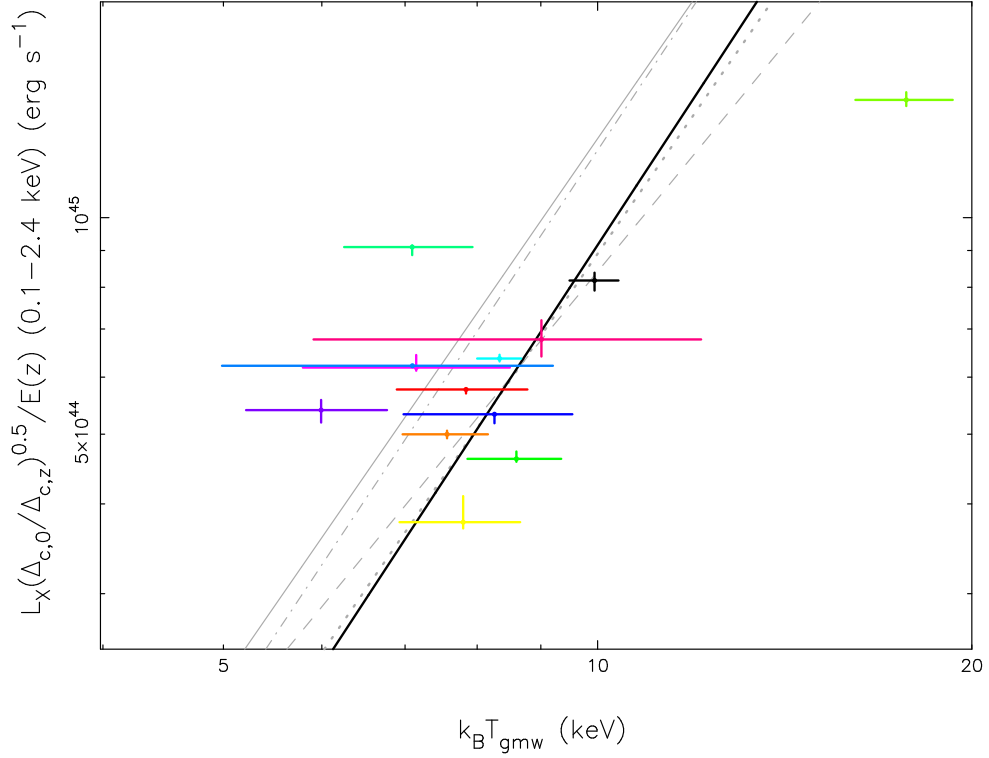


**Figure 6.19:** X-ray luminosity in the ROSAT band (0.1–2.4 keV, upper) vs. gas mass weighted cluster temperature integrated up to  $r_{200}$  and its best fit (black) for the REFLEX-DXL sample. The grey lines denote the best fits in Isobe et al. (1990, solid), Markevitch (1998, dashed), Reiprich & Böhringer (2002, dash-dotted), and Ikebe et al. (2002, dotted). The colors have an identical meaning as those in Fig. 6.8.

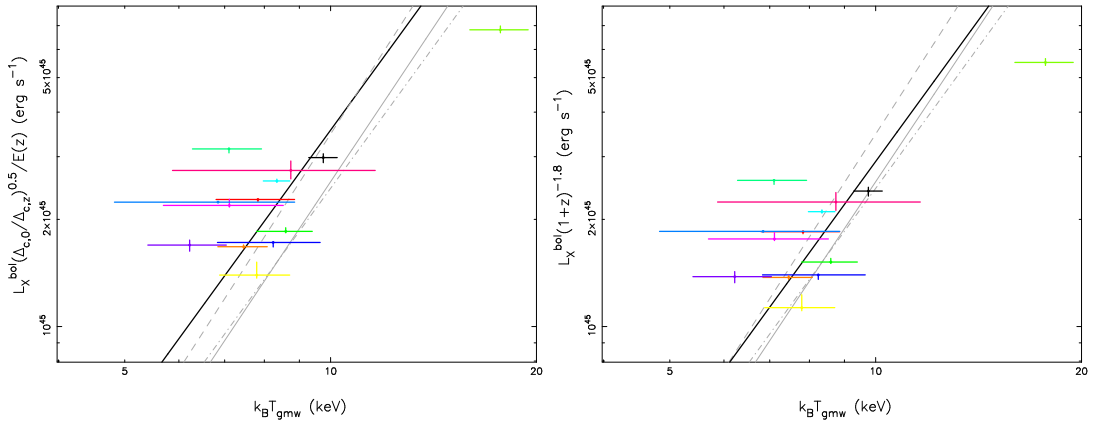


**Figure 6.20:** X-ray bolometric luminosity vs. gas mass weighted cluster temperature integrated up to  $r_{200}$  for the REFLEX-DXL sample and its best fit (black). The grey lines denote the best fits in Markevitch (1998, dash-dotted), Arnaud & Evrard (1999, solid) and Reiprich & Böhringer (2002, dashed). The colors have an identical meaning as those in Fig. 6.8.

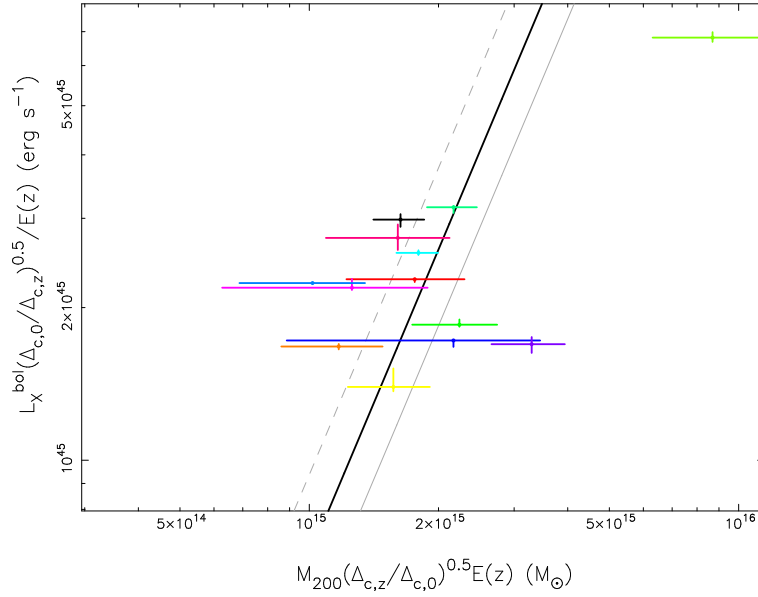


**Figure 6.21:** X-ray bolometric luminosity vs. total mass integrated up to  $r_{200}$ . The lines denote the best fit for the REFLEX-DXL clusters (black) and the clusters in Popesso et al. (2005, grey) with (dashed) and without (solid) non-isothermal corrections. The colors have an identical meaning as those in Fig. 6.8.

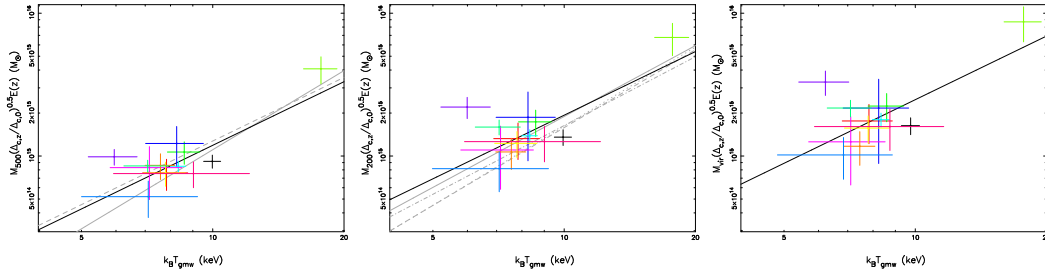


**Figure 6.22:** Mass vs. gas mass weighted temperature, respectively, for the REFLEX-DXL sample and its best fit (black). The grey lines denote the best fits in Nevalainen et al. (2000, solid) and Finoguenov et al. (2001, dashed) in the left panel, Xu et al. (2001,  $\beta$ -model, dash-dotted; NFW model, dashed), Reiprich & Böhringer (2002, solid) and Sanderson et al. (2003, dotted) in the middle panel, and Bryan & Norman (1998, solid) in the right panel. The colors have an identical meaning as those in Fig. 6.8.

published results and compared them to the  $M$ - $T$  relation in this work in Table 6.14 and Fig. 6.22. The scatter in the  $M$ - $T$  relation can partially be explained by the cooling cores.

The  $M_{500}$ - $T$  relation agrees with those in Nevalainen et al. (2000) and Finoguenov et al. (2001b). The  $M_{200}$ - $T$  relation of the REFLEX-DXL clusters agrees with the results for nearby clusters in Xu et al. (2001), Reiprich & Böhringer (2002), and Sanderson et al. (2003). The  $M_{\text{vir}}$ - $T$  relation agrees with the theoretical prediction in Bryan & Norman (1998).

## 6 X-ray properties in massive galaxy clusters

**Table 6.13:** Power law,  $Y = L_0 X^\alpha \text{ erg s}^{-1}$ , parameterized  $L$ - $M$  relations in this work and in literature.

Relation	$L_0$	$\alpha$	Reference	Method
$L_X^{\text{bol}}-M_{200}$	$10^{17.95 \pm 1.25} h_{50}^{-2}$	$1.81 \pm 0.08$	RB02	BCES
$L_X^{\text{bol}}-M_{200}$	$10^{14.51 \pm 0.22} h_{70}^{-2}$	$2.01 \pm 0.20$	P05	ODR
$L_{X,500}^{\text{bol}}-M_{200}$	$10^{15.62 \pm 0.07} h_{70}^{-2}$	2.01*	This work	ODR
$L_{X,500}^{\text{bol}} E(z)^{-1} \left(\frac{\Delta_{c,z}}{\Delta_{c,0}}\right)^{-0.5} - M_{500} E(z) \left(\frac{\Delta_{c,z}}{\Delta_{c,0}}\right)^{0.5}$	$10^{15.30 \pm 0.66} h_{70}^{-2}$	2.01*	This work	ODR
$L_{X,200}^{\text{bol}}-M_{200}$	$10^{14.98 \pm 0.09} h_{70}^{-2}$	2.01*	This work	ODR
$L_{X,200}^{\text{bol}} E(z)^{-1} \left(\frac{\Delta_{c,z}}{\Delta_{c,0}}\right)^{-0.5} - M_{200} E(z) \left(\frac{\Delta_{c,z}}{\Delta_{c,0}}\right)^{0.5}$	$10^{14.66 \pm 0.09} h_{70}^{-2}$	2.01*	This work	ODR
$L_{X,\text{vir}}^{\text{bol}}-M_{200}$	$10^{14.99 \pm 0.09} h_{70}^{-2}$	2.01*	This work	ODR
$L_{X,\text{vir}}^{\text{bol}} E(z)^{-1} \left(\frac{\Delta_{c,z}}{\Delta_{c,0}}\right)^{-0.5} - M_{\text{vir}} E(z) \left(\frac{\Delta_{c,z}}{\Delta_{c,0}}\right)^{0.5}$	$10^{14.67 \pm 0.09} h_{70}^{-2}$	2.01*	This work	ODR
$L_X^{0.1-2.4}-M_{500}$	$10^{25.19 \pm 0.10} h_{70}^{-2}$	$1.30 \pm 0.12$	P05	ODR
$L_X^{0.1-2.4}-M_{200}$	$10^{20.73 \pm 0.24} h_{70}^{-2}$	$1.58 \pm 0.23$	P05	ODR
$L_{X,500}^{0.1-2.4}-M_{500}$	$10^{25.60 \pm 0.05} h_{70}^{-2}$	1.30*	This work	ODR
$L_{X,500}^{0.1-2.4} E(z)^{-1} \left(\frac{\Delta_{c,z}}{\Delta_{c,0}}\right)^{-0.5} - M_{500} E(z) \left(\frac{\Delta_{c,z}}{\Delta_{c,0}}\right)^{0.5}$	$10^{25.36 \pm 0.05} h_{70}^{-2}$	1.30*	This work	ODR
$L_{X,200}^{0.1-2.4}-M_{200}$	$10^{21.12 \pm 0.06} h_{70}^{-2}$	1.58*	This work	ODR
$L_{X,200}^{0.1-2.4} E(z)^{-1} \left(\frac{\Delta_{c,z}}{\Delta_{c,0}}\right)^{-0.5} - M_{200} E(z) \left(\frac{\Delta_{c,z}}{\Delta_{c,0}}\right)^{0.5}$	$10^{20.84 \pm 0.06} h_{70}^{-2}$	1.58*	This work	ODR
$L_{X,\text{vir}}^{0.1-2.4}-M_{\text{vir}}$	$10^{20.95 \pm 0.07} h_{70}^{-2}$	1.58*	This work	ODR
$L_{X,\text{vir}}^{0.1-2.4} E(z)^{-1} \left(\frac{\Delta_{c,z}}{\Delta_{c,0}}\right)^{-0.5} - M_{\text{vir}} E(z) \left(\frac{\Delta_{c,z}}{\Delta_{c,0}}\right)^{0.5}$	$10^{20.67 \pm 0.07} h_{70}^{-2}$	1.58*	This work	ODR

The same as those in Table 6.12. RB02, Reiprich & Böhringer (2002). P05, Popesso et al. (2005).

There is no evolution of the normalization of the  $M$ - $T$  relation after the redshift evolution correction. This was also found for the other distant clusters in Maughan et al. (2003) and Ettori et al. (2002a).

### 6.5.4.4 $M_{\text{gas}}-T$ relation

Alternatively, the gas mass can be used as a measure of the total mass in the cluster. Recent simulations indicate a strong  $M_{\text{gas},500}-T$  relation (e.g. Borgani et al. 2004). We found a similar correlation for the REFLEX-DXL clusters (see Table 6.14 and Fig. 6.23). The  $M_{\text{gas}}-T$  relations derived from the observations and simulations are both steeper than the prediction of the self-similar model. This is consistent with the extra non-gravitational energy input into the ICM inferred from the entropy studies.

### 6.5.4.5 $L-Z$ relation

As shown in Fig. 6.24, no significant correlation has been found for the  $L-Z$  relation of the REFLEX-DXL sample.

### 6.5.5 Intrinsic scatter in the correlations

The key to extracting cosmological parameters from the number density of galaxy clusters is a correct understanding of the correlations between the cluster mass and the observables. The correlation scatter describes how well the observables can be used as an estimator of the total mass. The correlation scatter ( $\sigma_{\text{cor}}$ ) includes the intrinsic scatter ( $\sigma_{\text{int}}$ ) and

**Table 6.14:** Power law,  $Y = M_0 X^\gamma M_\odot$ , parameterized  $M-T$  and  $M_{\text{gas}}-T$  relations in this work and in literature.

Relation	$M_0$	$\gamma$	Reference	Method
$M_{1000}-T$	$10^{13.30 \pm 0.02} h_{50}^{-1}$	$1.79 \pm 0.05$	Nevalainen et al. 00	—
$M_{500}-T$	$10^{13.63^{+0.08}_{-0.07}} h_{50}^{-1}$	$1.48^{+0.10}_{-0.12}$	Finoguenov et al. 01b	BCES
$M_{500}-T$	$10^{13.40 \pm 0.02} h_{70}^{-1}$	$1.59 \pm 0.05$	Borgani et al. 04	OLS
$M_{200}-T$	$10^{13.59 \pm 0.07} h_{50}^{-1}$	$1.48 \pm 0.12$	Horner 01	BCES
$M_{200}^\beta-T$	$10^{13.760 \pm 0.003} h_{50}^{-1}$	$1.60 \pm 0.04$	Xu et al. 01	ODR
$M_{200}^{\text{NFW}}-T$	$10^{13.535 \pm 0.003} h_{50}^{-1}$	$1.81 \pm 0.04$	Xu et al. 01	ODR
$M_{200}-T$	$10^{13.77 \pm 0.03} h_{50}^{-1}$	$1.65 \pm 0.05$	Reiprich & Böhringer 02	BCES
$M_{200}-T$	$10^{13.37 \pm 0.03} h_{70}^{-1}$	$1.84 \pm 0.06$	Sanderson et al. 03	ODR
$M_{500}-T$	$10^{13.49 \pm 0.03} h_{70}^{-1}$	$1.48^*$	This work	ODR
$M_{500} E(z) (\frac{\Delta_{c,z}}{\Delta_{c,0}})^{0.5}-T$	$10^{13.60 \pm 0.03} h_{70}^{-1}$	$1.48^*$	This work	ODR
$M_{200}-T$	$10^{13.70 \pm 0.04} h_{70}^{-1}$	$1.48^*$	This work	ODR
$M_{200} E(z) (\frac{\Delta_{c,z}}{\Delta_{c,0}})^{0.5}-T$	$10^{13.81 \pm 0.04} h_{70}^{-1}$	$1.48^*$	This work	ODR
$M_{\text{vir}}-T$	$10^{13.81 \pm 0.05} h_{70}^{-1}$	$1.48^*$	This work	ODR
$M_{\text{vir}} E(z) (\frac{\Delta_{c,z}}{\Delta_{c,0}})^{0.5}-T$	$10^{13.91 \pm 0.04} h_{70}^{-1}$	$1.48^*$	This work	ODR
$M_{\text{gas},500}-T$	$10^{12.26 \pm 0.05} h_{70}^{-1}$	$1.80 \pm 0.08$	Borgani et al. 04	OLS
$M_{\text{gas},500}-T$	$10^{12.19 \pm 0.02} h_{70}^{-1}$	$1.80^*$	This work	ODR
$M_{\text{gas},500} E(z) (\frac{\Delta_{c,z}}{\Delta_{c,0}})^{0.5}-T$	$10^{12.29 \pm 0.02} h_{70}^{-1}$	$1.80^*$	This work	ODR
$M_{\text{gas},200}-T$	$10^{12.41 \pm 0.02} h_{70}^{-1}$	$1.80^*$	This work	ODR
$M_{\text{gas},200} E(z) (\frac{\Delta_{c,z}}{\Delta_{c,0}})^{0.5}-T$	$10^{12.51 \pm 0.02} h_{70}^{-1}$	$1.80^*$	This work	ODR
$M_{\text{gas,vir}}-T$	$10^{12.51 \pm 0.02} h_{70}^{-1}$	$1.80^*$	This work	ODR
$M_{\text{gas,vir}} E(z) (\frac{\Delta_{c,z}}{\Delta_{c,0}})^{0.5}-T$	$10^{12.62 \pm 0.02} h_{70}^{-1}$	$1.80^*$	This work	ODR

The same as those in Table 6.12.

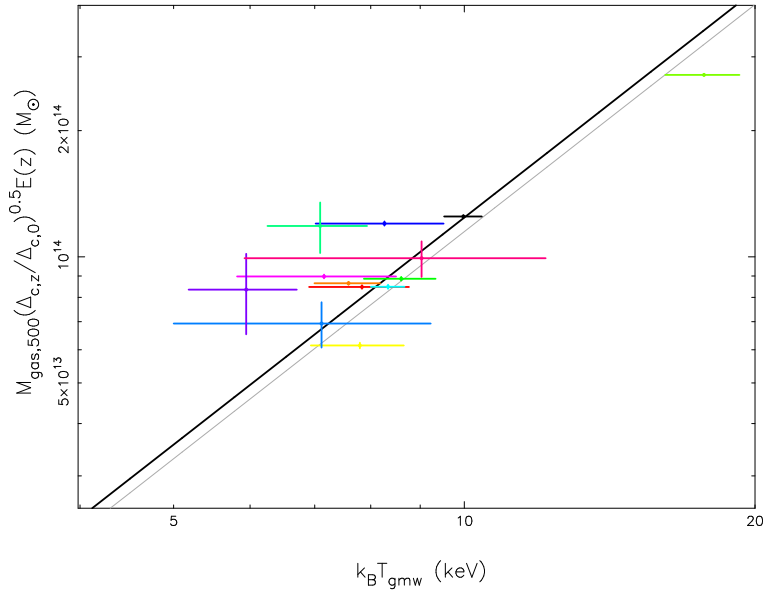


**Figure 6.23:** Gas mass vs. gas mass weighted temperature. The lines denote the best fit for the REFLEX-DXL sample (black) and the prediction in Borgani et al. (2004, grey). The colors have an identical meaning as those in Fig. 6.8.

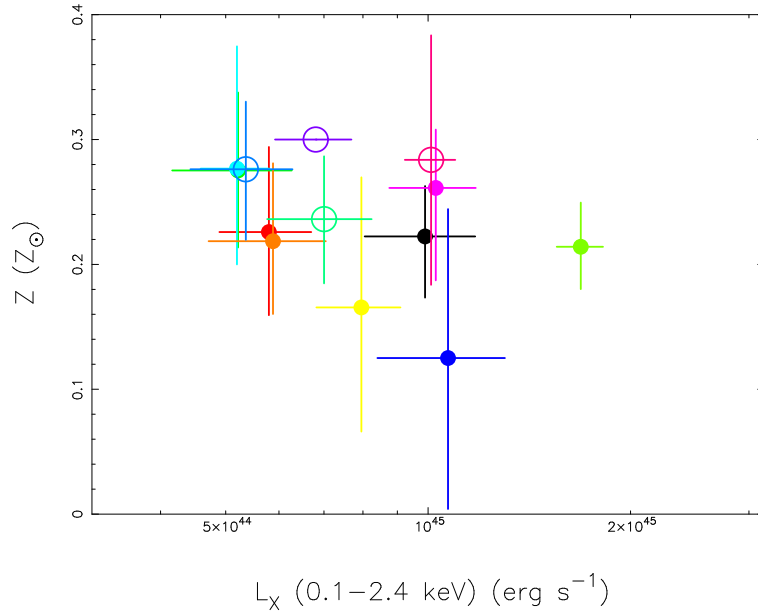


**Figure 6.24:** X-ray luminosity vs. metallicity for the CCCs (open) and NCCCs (filled). We fix metallicity to  $0.3 Z_{\odot}$  for RXCJ0437.1+0043. The colors have an identical meaning as those in Fig. 6.8.

observational scatter ( $\sigma_{\text{obs}}$ ). We investigated the logarithmic intrinsic scatter of 4 main correlations,  $L-T$ ,  $L-M$ ,  $M-T$ , and  $M_{\text{gas}}-T$ , of the REFLEX-DXL sample.

The intrinsic scatter is due to the multi-variate dependencies and random processes. Assuming that  $\sigma_{\text{obs}}$  and  $\sigma_{\text{cor}}$  are not correlated, we apply a Gaussian statistical addition of the two effects to compute the logarithmic intrinsic scatter,  $\sigma_{\text{int}} = \sqrt{\sigma_{\text{cor}}^2 - \sigma_{\text{obs}}^2}$ .

As shown in Fig. 6.25, not for all correlations we found an approximately Gaussian distribution. We observed that the merger clusters (e.g. RXCJ0658.5–5556) are located at the right tail of the histogram distribution as shown in the right panel in Fig. 6.25. The asymmetry of the histogram is most probably due to the variety of cluster morphologies, e.g. mergers, which can produce particular deviation from the mean. It could also be due to the fact that the REFLEX-DXL sample does not contain enough members to give a pronounced Gaussian statistics. We used the average instead of the mean of a Gaussian distributed histogram to derive the logarithmic intrinsic scatter for the whole sample, which is listed in Table 6.15 for 4 main correlations.

Based on a tight correlation which shows the least correlation scatter, the observable gives the best prediction for the total mass or gas mass. For example, the cluster temperature is the best estimator of the gas mass using the  $M_{\text{gas}}-T$  relation for the REFLEX-DXL clusters, which has  $\bar{\sigma}_{\text{cor}} = 0.122$  for  $\lg(M_{\text{gas}})$ .



**Table 6.15:** Logarithmic intrinsic scatter measured for 4 main correlations. Col.(1): Correlation. Col.(2): Variation. Cols.(3–4): Logarithmic intrinsic scatter and observational scatter.

Correlation	Variation	$\bar{\sigma}_{\text{int}}$	$\bar{\sigma}_{\text{obs}}$
$L-T$	$\log(L_{X,200}^{\text{bol}} E(z)^{-1} (\Delta_{c,z}/\Delta_{c,0})^{-0.5})$	0.15	0.01
	$\log(T)$	0.08	0.07
$L-M$	$\log(L_{X,200}^{\text{bol}} E(z)^{-1} (\Delta_{c,z}/\Delta_{c,0})^{-0.5})$	0.29	0.01
	$\log(M_{200} E(z) (\Delta_{c,z}/\Delta_{c,0})^{0.5})$	0.18	0.15
$M-T$	$\log(M_{200} E(z) (\Delta_{c,z}/\Delta_{c,0})^{0.5})$	0.30	0.15
	$\log(T)$	0.17	0.07
$M_{\text{gas}}-T$	$\log(M_{\text{gas},200} E(z) (\Delta_{c,z}/\Delta_{c,0})^{0.5})$	0.12	0.02
	$\log(T)$	0.10	0.07

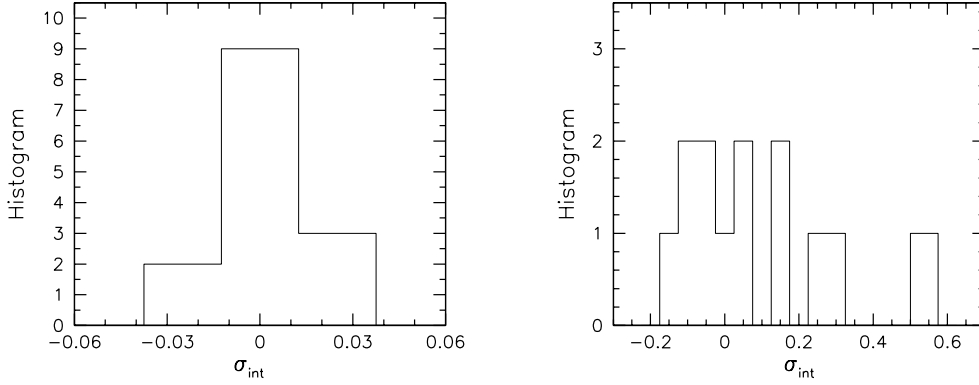


**Figure 6.25:** Histogram of the Gaussian distributed  $\sigma_{\text{int}}$  for  $\log(T)$  of the  $M_{\text{gas}}-T$  relation (left), and the non-Gaussian distributed  $\sigma_{\text{int}}$  for  $\log(M_{200} E(z) (\Delta_{c,z}/\Delta_{c,0})^{0.5})$  of the  $M-T$  relation (right), respectively, for the REFLEX-DXL clusters.

## 6.6 Discussion

### 6.6.1 Mass infalling from the outskirts

Mass infalling becomes significant in the outskirts. This makes the slope of the electron density and the surface brightness ( $S_X \propto n_e^2$ ) steeper than the generally adopted  $\beta$ -model ( $\beta \sim 2/3$ ). Vikhlinin et al. (1999) found a mild trend for  $\beta$  to increase as a function of the cluster temperature, which gives  $\beta \sim 0.80$  for clusters around 10 keV. Bahcall (1999) also found that the electron number density scales as  $n_e \propto r^{-2.4}$  at large radii. As shown in Table 6.10, we confirm their conclusion that  $n_e \propto r^{-2.42}$  at  $r > 2'$  for the REFLEX-DXL clusters. Therefore, the slope is perhaps underestimated and overestimated by the  $\beta$ -model and the NFW model, respectively. This might introduce a systematic error in the virial mass measurements (e.g. Horner 2001).

### 6.6.2 Additional physical processes

The scatter of the X-ray observations around the self-similar model for the REFLEX-DXL clusters is not a simple reflection of measurement errors. It calls for a range of morphologies including mergers as shown in Zhang et al. (2004b). Systematic studies of X-ray mergers have been done in observations using a series of cluster samples (e.g. Schuecker et al. 2001) and simulations (e.g. Schindler & Mueller 1993). Finoguenov et al. (2005) provided such a detailed study of the REFLEX-DXL clusters using a 2-dimensional approach.

## 6.7 Summary and conclusions

X-ray luminous (massive) clusters can be used in a variety of ways to perform both cosmological and astrophysical studies. We selected a flux-limited and almost volume complete sample, the REFLEX-DXL cluster sample, from the REFLEX survey. We performed a systematic analysis to measure the X-ray observables based on the XMM-Newton observations, and investigated the scaling relations and correlations of various X-ray properties of the REFLEX-DXL cluster sample. We summarize two main conclusions as follows.

(i) A self-similar behavior of these X-ray properties, such as metallicity, temperature, surface brightness, entropy, and gravitational mass, has been found in the  $r > 0.1r_{\text{vir}}$  region for the REFLEX-DXL sample.

- We obtained an almost universal metallicity profile for the REFLEX-DXL sample. We found an average metallicity,  $0.23 \pm 0.07 Z_{\odot}$ , for the whole sample, with  $0.27 \pm 0.07 Z_{\odot}$  and  $0.22 \pm 0.08 Z_{\odot}$  for the CCCs and NCCCs, respectively. We confirmed the previous studies that massive clusters show a universal metallicity profile (e.g. De Grandi et al. 2004). This supports the following scenario. The cluster center shows a late enrichment by SN I and stellar winds in the cD galaxy (Böhringer et al. 2002b, 2004b; Fukazawa et al. 2004), while the outer part is mainly enriched by SN II (Finoguenov et al. 2001a). No significant evolution up to  $z \sim 0.3$  was found in the metallicity comparing the REFLEX-DXL sample to the nearby galaxy cluster samples. This agrees with the results in Tozzi et al. (2003) that there is no evolution of the iron abundance up to  $z \sim 1.1$ .

- Based on the XMM-Newton observations, we obtained an average temperature profile of the REFLEX-DXL clusters, which agrees with the previous studies within the observational dispersion. Markevitch et al. (1998) found a steep temperature drop beyond an isothermal center based on the ASCA data. De Grandi & Molendi (2002) derived a universal temperature profile which shows a similar decline using the BeppoSAX observations. Based on the high resolution Chandra observations, Vikhlinin et al. (2005a) and Piffaretti et al. (2005) confirmed the previous studies within the observational dispersion, where they show a less pronounced drop outside of  $0.2\text{--}0.3 r_{\text{vir}}$  in the mean of the universal temperature profile. Additionally, Borgani et al. (2004) reproduced a similar temperature profile in their simulations as found by Vikhlinin et al. (2005a). For the REFLEX-DXL sample, we found a universal temperature profile with a constant value for the NCCCs, but with an increasing distribution for the CCCs up to  $0.3r_{\text{vir}}$ . We observed a mild decrease at  $r > 0.3r_{\text{vir}}$  for most REFLEX-DXL clusters. No cool gas has been observed showing a central temperature lower than half of the mean temperature. Within  $2\sigma$  confidence inter-

vals, the average temperature profile of the REFLEX-DXL sample is also consistent with a constant value and the results from Vikhlinin et al. (2005a) and Piffaretti et al. (2005).

- We determined the XMM-Newton surface brightness profiles of the REFLEX-DXL clusters up to  $r_{500}$ . We observe steeper profiles than what is generally obtained for the  $\beta$ -models with  $\beta \sim 2/3$ . The surface brightness profile of the NCCCs shows a flat core. It can be described by a  $\beta$ -model. The surface brightness profile of the CCCs shows an excess in the cluster center, which accounts for about 11–33% cluster luminosities. It can be fitted either by a double  $\beta$ -model or by a model based on an ext-NFW DM model. There is no well-defined constant central density down to the resolution limit of XMM-Newton for the CCCs. However, the surface brightness profiles are self-similar at  $r > 0.1r_{\text{vir}}$  for the REFLEX-DXL sample.

- We performed the redshift evolution correction on the entropies at  $0.1r_{200}$  for the REFLEX-DXL clusters and obtained consistence with those for the nearby clusters in Ponman et al. (2003) (see Fig. 6.8). The entropies at  $0.1r_{200}$  for the REFLEX-DXL sample agree with the scaling,  $T^{0.65}$ . As shown in Fig. 6.14 in Sect. 6.4.4, the entropy profiles at  $r > 0.1r_{\text{vir}}$  show a similar slope as observed in Ettori et al. (2002b),  $S \propto r^{0.97}$ . However, this is shallower than the predicted slope from a spherical accretion shock model,  $S \propto r^{1.1}$  (e.g. Tozzi & Norman 2001; Kay 2004). We found that mergers increase cluster central entropy. We confirmed that the relatively relaxed clusters show lower central entropies. Therefore we use the central entropy to divide the REFLEX-DXL sample into two subsamples, the CCC and NCCC subsamples. We found that the observational deviation of the ( $S | T$ ) data pair from the  $S$ – $T$  relation for the individual cluster can be used to distinguish the relaxation stage.

- We found a self-similar gravitational mass distribution for the REFLEX-DXL sample. The gas density and temperature profiles provide an excellent diagnostics of the cluster structure and yield precise determinations of the mass and gas mass fraction. In the outskirts, the generally adopted  $\beta$ -model ( $\beta \sim 2/3$ ) gives  $\rho(r) \propto r^{-2}$  and the ext-NFW model gives  $\rho(r) \propto r^{-3}$ . The observational density provides an average of  $\rho(r) \propto r^{-2.42}$  for the REFLEX-DXL sample. The two mass models give systematically different slopes of the mass distributions.

- We observed a deviation around the self-similar model in the central region. This reveals some physical processes rather than simply being statistical fluctuations in the measurements (Zhang et al. 2004b, 2005b; Finoguenov et al. 2005). Many studies (e.g. Markevitch et al. 2002; Randall et al. 2002; Finoguenov et al. 2005) show that the X-ray property estimates in the center can be biased by the phenomena, e.g. ghost cavities, bubbles, shock and cold fronts, that may somehow invalidate the hydrostatic equilibrium hypothesis. Complex dynamical interactions with AGN activities have been indicated by the coincidence of CCCs and radio sources (Clarke et al. 2005). RXCJ0658.5–5556 provides an example to test the effect of merger boosts on the X-ray luminosity and also multi-temperature structure (Matsushita et al. 2002).

(ii) Many X-ray properties are tightly correlated (e.g.  $r_c$ – $\beta$ ,  $L$ – $T$ ,  $L$ – $M$ ,  $M$ – $T$ , and  $M_{\text{gas}}$ – $T$ ) for the REFLEX-DXL sample. After the redshift evolution correction, the correlations of the REFLEX-DXL sample at  $z \sim 0.3$  agree with the correlations of the nearby samples.

- We confirmed the previous studies of those correlations in observations (e.g. Reiprich & Böhringer 2002) and simulations (e.g. Borgani et al. 2004). Since the cluster temperatures of the REFLEX-DXL sample are in a narrow temperature range, the whole sample provides a unique means to constrain the normalizations with a higher accuracy (see Table 6.12 and Table 6.14).

- We found that the CCCs and NCCCs give different normalization in the correlations. For example, for the  $M_{500}-T$  relation, the value from the best power law fit is  $10^{13.61 \pm 0.07} M_{\odot}$  ( $10^{13.46 \pm 0.03} M_{\odot}$ ) for the CCCs (NCCCs), which is 2% higher (28% lower) than the value derived for the whole sample. The correlations are dependent of the variety of the cluster morphologies.

- We investigated the intrinsic scatter of the main correlations which, for example, gives (0.30 | 0.17) for ( $M$  |  $T$ ) in the  $M-T$  relation and confirmed the recent studies in observations (e.g. Reiprich & Böhringer 2002) and simulations (e.g. Stanek et al. 2005).

- We found no deviation in the correlations such as  $L-T$ ,  $L-M$ ,  $M-T$  and  $M_{\text{gas}}-T$  comparing the REFLEX-DXL sample to the nearby samples. Therefore we confirm the general opinion (e.g. Maughan et al. 2003; Vikhlinin et al. 2005a) that the evolution of galaxy clusters up to  $z \sim 1$  is well described by a self-similar model for massive clusters ( $> 2$  keV).

## Acknowledgements

The XMM-Newton project is supported by the Bundesministerium für Bildung und Forschung, Deutsches Zentrum für Luft und Raumfahrt (BMBF/DLR), the Max-Planck Society and the Haidenhaim-Stiftung. We acknowledge Jacqueline Bergeron, PI of the XMM-Newton observation of the CDFS, and Martin Turner, PI of the XMM-Newton observation of RXJ0658.5-5556. We acknowledge Alexey Vikhlinin, Naomi Ota, Michael Freyberg, Ulrich G. Briel, Gabriel Pratt and Takaya Ohashi for providing useful suggestions. Y.Y.Z. acknowledges support under the XMM grant No. NNG 04 GF 68 G. A.F. acknowledges support from BMBF/DLR under grant No. 50 OR 0207 and MPG. P.S. acknowledges support under the DLR grant No. 50 OR 9708 35.

# 7 XMM-Newton study of the lensing cluster of galaxies CL0024+17

## Abstract

We present a detailed gravitational mass measurement based on the XMM-Newton imaging spectroscopy analysis of the lensing cluster of galaxies CL0024+17 at  $z = 0.395$ . The emission appears approximately symmetric. However, on the scale of  $r \sim 3.3'$  some indication of elongation is visible in the northwest-southeast (NW-SE) direction from the hardness ratio map (HRM). Within  $3'$ , we measure a global gas temperature of  $3.52 \pm 0.17$  keV, metallicity of  $0.22 \pm 0.07$ , and bolometric luminosity of  $2.9 \pm 0.1 \times 10^{44} h_{70}^{-2}$  erg s $^{-1}$ . We derive a temperature distribution with an isothermal temperature of 3.9 keV to a radius of  $1.5'$  and a temperature gradient in the outskirts ( $1.3' < r < 3'$ ). Under the assumption of hydrostatic equilibrium, we measure gravitational mass and gas mass fraction to be  $M_{200} = 2.0 \pm 0.3 \times 10^{14} h_{70}^{-1} M_{\odot}$  and  $f_{\text{gas}} = 0.20 \pm 0.03 h_{70}^{-3/2}$  at  $r_{200} = 1.05 h_{70}^{-1}$  Mpc using the observed temperature profile. The complex structure in the core region is the key to explaining the discrepancy in gravitational mass determined from XMM-Newton X-ray observations and HST optical lensing measurements.

## 7.1 Introduction

One of the optically most prominent, but also most puzzling distant lensing galaxy clusters, is CL0024+17 at a redshift of  $z = 0.395$  (Gunn & Oke 1975). Its high galaxy density led to the early discovery by Humason & Sandage (1957), and the cluster has since been the subject of many studies. It was one of the first clusters to display the so-called Butcher-Oemler effect (Butcher & Oemler 1978; Dressler & Gunn 1982; Dressler et al. 1985), and Schneider et al. (1986) described it as a very rich optical cluster.

Koo (1988) discovered gravitational arcs in CL0024+17, and it was subsequently studied extensively (Mellier et al. 1991; Kassiola et al. 1992; Kassiola et al. 1994; Wallington et al. 1995; Colley et al. 1996; Smail et al. 1997; Tyson et al. 1998; Broadhurst et al. 2000; Shapiro & Iliev 2000; Treu et al. 2003; Kneib et al. 2003). A total of eight arc-like lensed images from the same background galaxy were identified (e.g. Tyson et al. 1998). The redshift of the lensed galaxy was determined by Broadhurst et al. (2000) to be  $z = 1.675$ . Bonnet et al. (1994) detected a weak shear signal in this cluster out to a radius of  $2.1 h_{70}^{-1}$  Mpc and inferred a high gravitational mass of about  $1.4\text{--}2.9 \times 10^{15} h_{70}^{-1} M_{\odot}$ . Recently Kneib et al. (2003) revised this lensing mass estimate downward on the basis of a very detailed Hubble Space Telescope (HST) mapping of the cluster which yielded a gravitational mass of  $M_{200} = 5.7_{-1.0}^{+1.1} \times 10^{14} h_{70}^{-1} M_{\odot}$  out to  $r_{200} = 1.7 h_{70}^{-1}$  Mpc. In spite of the massive appearance of CL0024+17 at optical wavelengths, the cluster is relatively faint

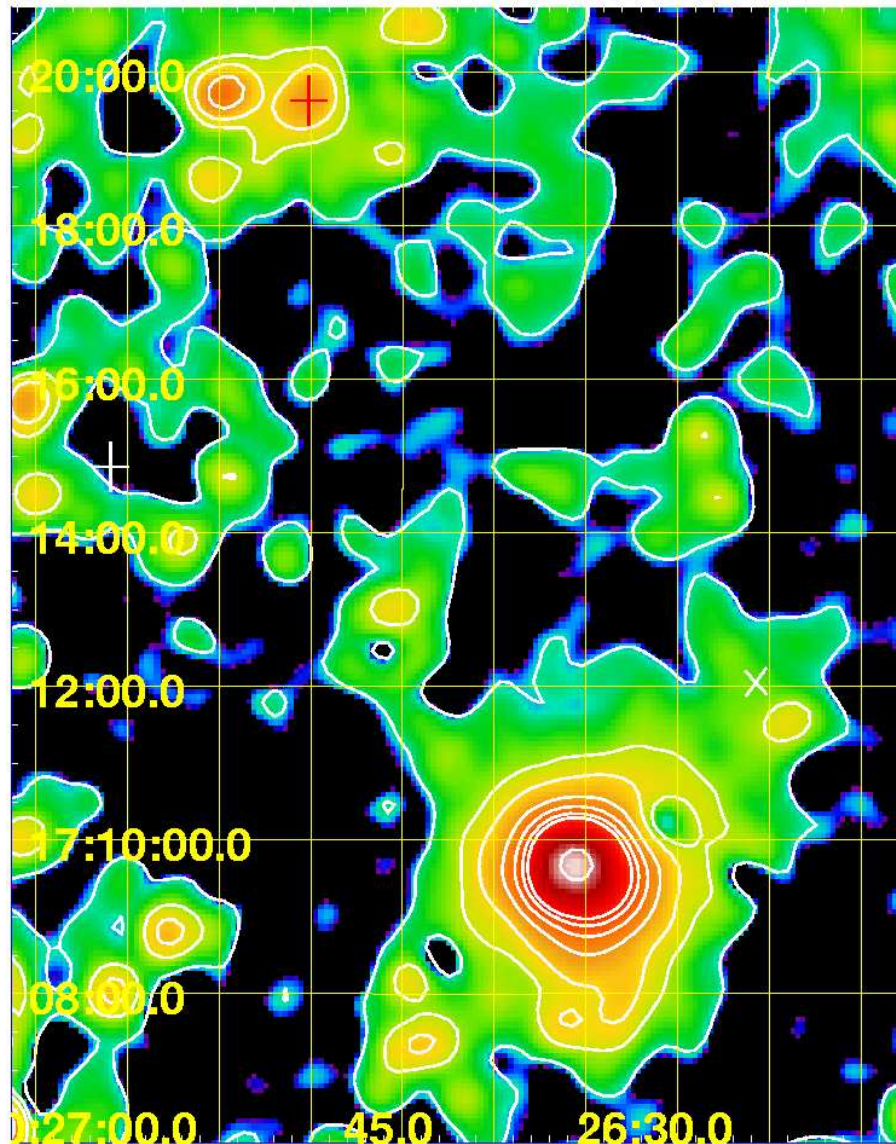


**Figure 7.1:** Flat fielded, point sources masked and adaptively-smoothed XMM-Newton image of CL0024+17 in the 0.5–2 keV band with logarithmically scaled contours. Additionally we show the galaxy pair (cross) in Czoske et al. (2001, 2002) and the substructure (X-point) in Kneib et al. (2003).

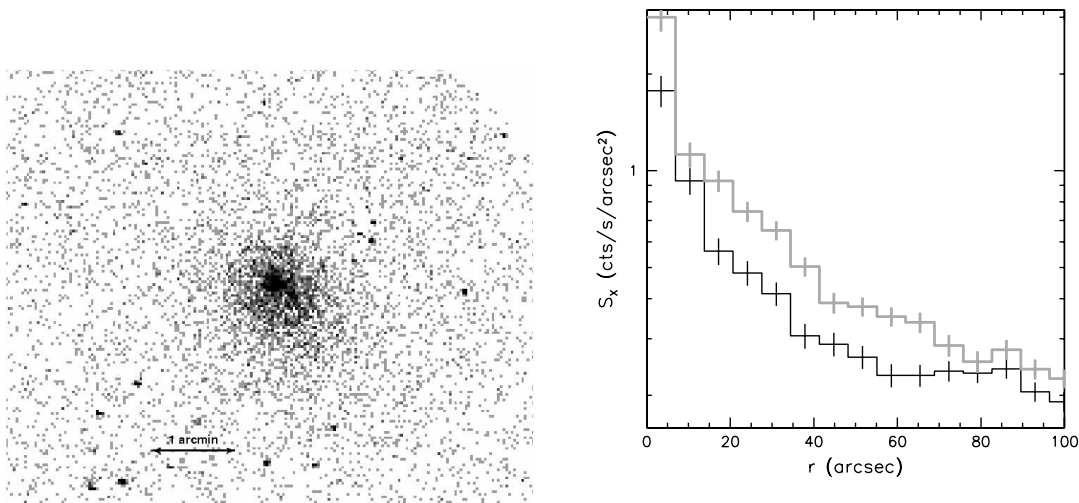


**Figure 7.2:** Chandra image in the 0.5–2.5 keV band (left) and surface brightness profiles (right) in annuli using the 0.5–2.5 keV image with azimuths 30–120° (counter clockwise) from north to east (black) and from south to west (grey), respectively.

in X-rays with a ROSAT determined luminosity of  $L_X = 1.22 \pm 0.08 \times 10^{44} h_{70}^{-2} \text{ erg s}^{-1}$  in the 0.1–2.4 keV band (Böhringer et al. 2000), an ASCA determined temperature of  $5.7_{-2.1}^{+4.2}$  keV (Soucail et al. 2000), and a Chandra temperature of  $4.47_{-0.27}^{+0.42}$  keV (Ota et al. 2004;  $M_{200} = 4.6_{-0.5}^{+0.7} \times 10^{14} h_{70}^{-1} M_{\odot}$  to  $r_{200} = 1.4 h_{70}^{-1}$  Mpc). In addition to the surprisingly low X-ray luminosity in comparison to its optical prominence, the detailed analysis of the X-ray observations yield a total cluster mass in the range  $M_{200} = 2\text{--}4.6 \times 10^{14} h_{70}^{-1} M_{\odot}$  that is 1.3–3 times lower than the weak lensing determined mass (Soucail et al. 2000; Böhringer et al. 2000; Ota et al. 2004). The discrepancy is even larger at the arc radius  $\sim 0.143 h_{70}^{-1}$  Mpc (e.g. Broadhurst et al. 2000).

A hint of the explanation for this mass discrepancy came from the detailed analysis of the galaxy dynamics in CL0024+17 based on  $\sim 300$  redshifts of galaxy members (Czoske et al. 2001, 2002). Czoske et al. (2001, 2002) found that the line-of-sight velocity distribution is not that of a relaxed cluster and is at least bimodal. They also demonstrated that the redshifts can approximately be explained by a line-of-sight merger of two systems with a mass ratio of the order of 1:2. Also the weak lensing analysis shows a mass distribution with substructure, modeled as a bimodal distribution of two systems with slightly different central positions in the plane of the sky (Kneib et al. 2003). The infrared observations imply significant star forming activity with Star Formation Rates (SFRs) one to two orders of magnitude higher than those computed from the optical. The underestimation of the SFRs in the optical is due to absorption by dust (Coia et al. 2003).

Using the capability of XMM-Newton to perform imaging spectroscopy at high angular resolution and thus allowing us to study the density and temperature structure of the intracluster medium (ICM), we performed an XMM-Newton observation of CL0024+17 to shed new light on this enigmatic system.

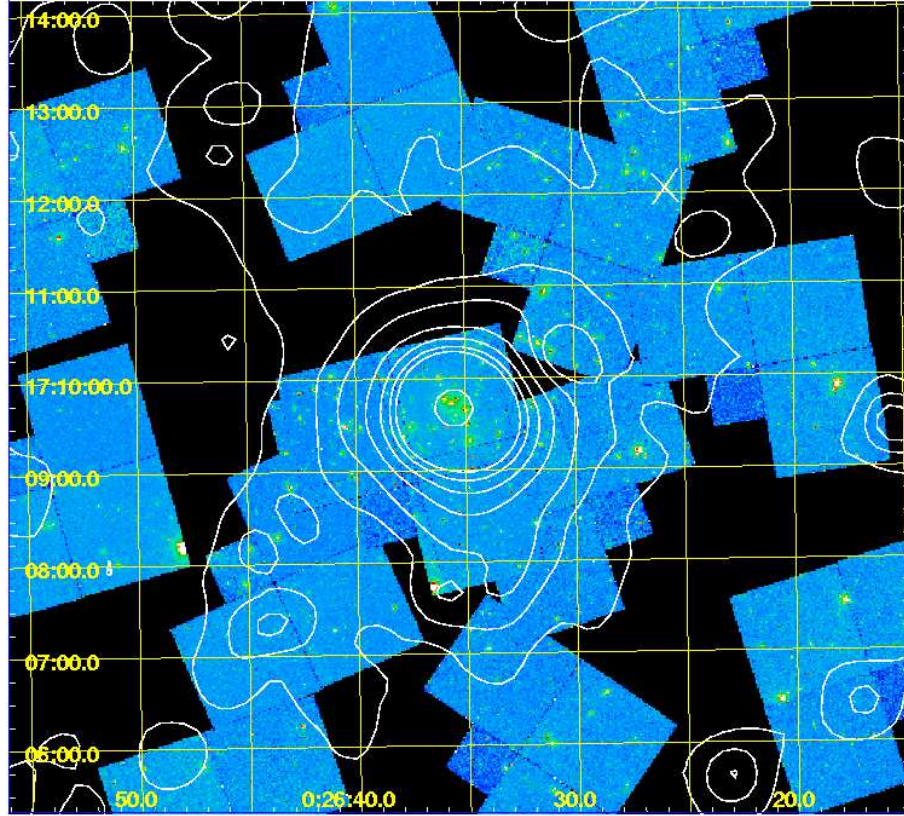


**Figure 7.3:** HST mosaic image of the center of CL0024+17. Superposed X-ray contours of XMM-Newton as shown in Fig. 7.1 indicate the elongation in the NW-SE direction on the scale of  $r \sim 3.3'$  (X-point).

This paper is structured as follows. In Sect. 7.2, we describe a double background subtraction method, which is developed to provide precise spectral background removal. In Sect. 7.3, we analyze the properties of the hot gas in the galaxy cluster CL0024+17, then determine the total mass, projected gravitational mass, and gas mass fraction based on precise temperature and gas density profiles. In Sect. 7.4, we discuss the structures in the cluster and possible solutions for the discrepancy between the X-ray and HST lensing measurements in the gravitational mass. In Sect. 7.5, we present our conclusions. We adopt a flat  $\Lambda$ CDM cosmology with density parameter  $\Omega_m = 0.3$  and Hubble constant  $H_0 = 70 \text{ km s}^{-1} \text{ Mpc}^{-1}$ . Thus  $1' = 0.320h_{70}^{-1} \text{ Mpc}$ . All coordinates are given in epoch J2000. We adopt the solar abundance values of Anders & Grevesse (1989). Error bars correspond to the 68% confidence level, unless explicitly stated otherwise.



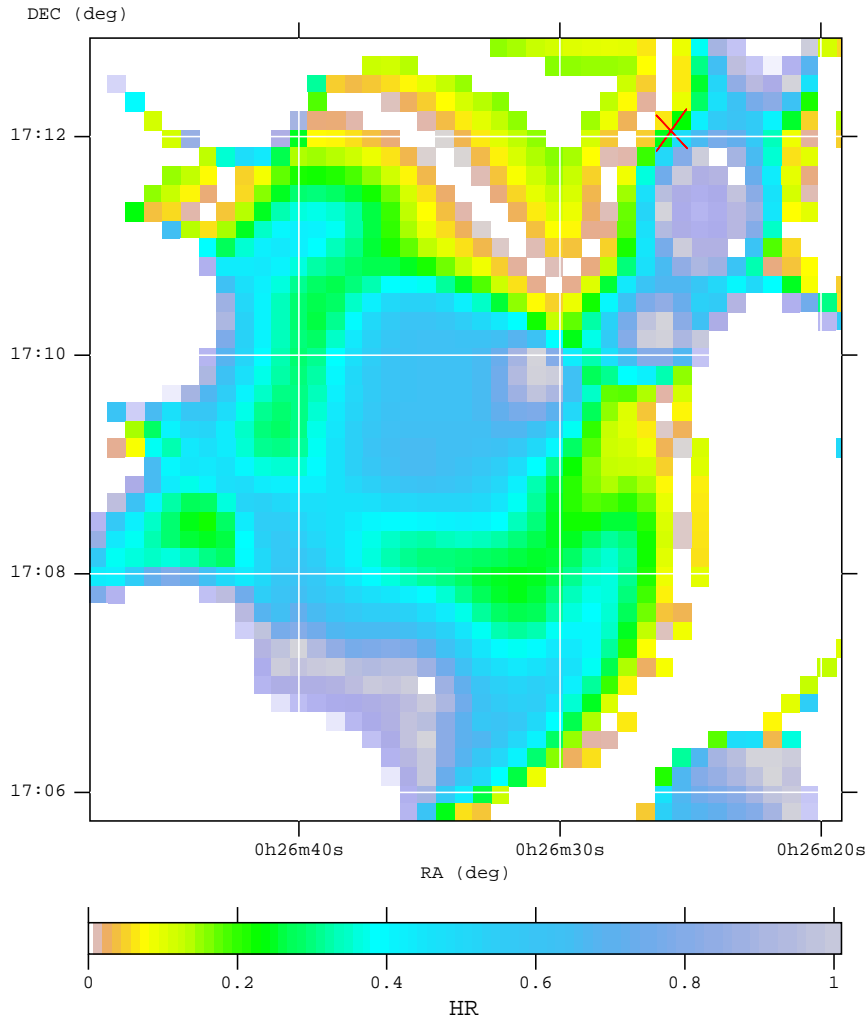


**Figure 7.4:** XMM-Newton HRM ( $\sim 10''$  pixels) of CL0024+17. Additionally we show the position of the substructure (X-point) in kneib et al. (2003).

## 7.2 Method

### 7.2.1 Data preparation

CL0024+17 was observed on Jan 6th, 2001 for a total exposure of 52.1 ks, 52.1 ks and 48.3 ks for MOS1, MOS2 and pn, respectively, by XMM-Newton with the European Photon Imaging Camera (EPIC) in standard Full Frame (FF) mode and Extended Full Frame (EFF) mode for MOS and pn, respectively. For all detectors, the thin filter was used. Data reduction and calibration was carried out using the XMM-Newton Science Analysis System (SAS5.4.1). The central position of the observation is R.A. =  $00^h26^m35^s.7$ , decl. =  $17^\circ09'35''.8$ .

Above 10 keV, there is little X-ray emission from the cluster due to the low telescope efficiency. The particle background therefore completely dominates. The cluster emission

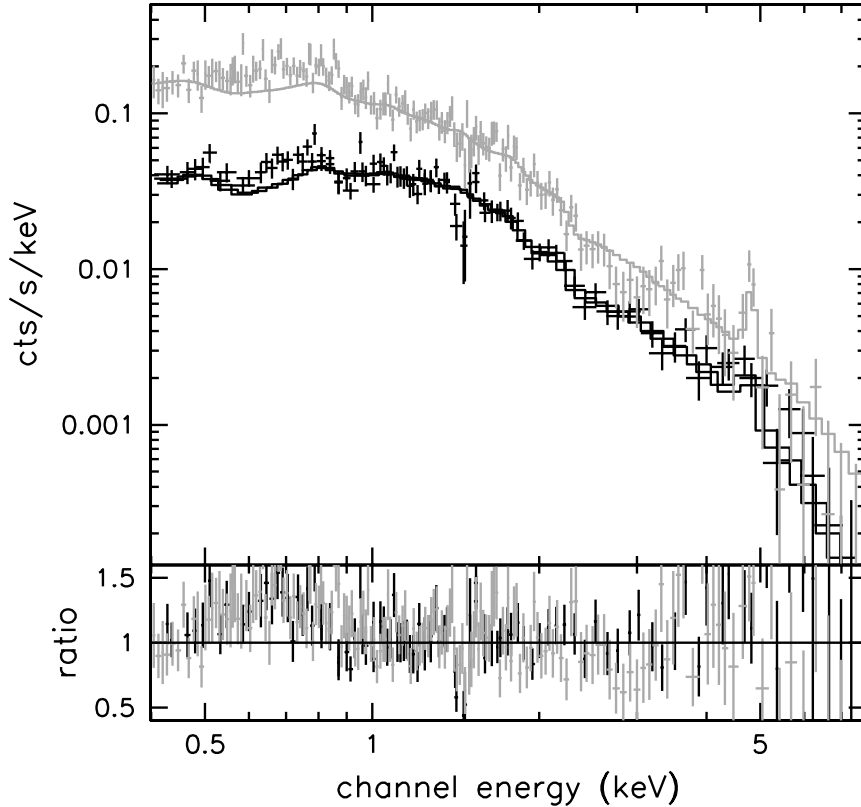


**Figure 7.5:** XMM-Newton spectra (top panel) extracted from the  $< 3'$  region fitted in the 1–10 keV band by an isothermal model and their residuals (bottom panel) for MOS (black) and pn (grey), respectively.

is not variable, so any spectral range can be used for temporal variability studies of the background. The 10–12 keV (12–14 keV) energy band (binned in 100 s intervals) was used to monitor the particle background and to excise periods of high particle flux for MOS (pn). In this screening process we use the settings  $FLAG = 0$  and  $PATTERN \leq 12$  ( $PATTERN \leq 4$ ) for MOS (pn).

We reject those time intervals affected by flares in which the detector countrate (ctr) exceeds a threshold of  $2\sigma$  above the average ctr, where the average and the variance have been iteratively determined from the ctr histogram below the rejection threshold. We screened the data using the thresholds of 21.4, 22.3 and 56.2 for MOS1, MOS2 and pn. The net exposure time is 46.6 ks, 46.0 ks and 42.9 ks for MOS1, MOS2 and pn, respectively.

## 7.2.2 Background analysis

We do not expect any cluster emission outside  $5.4'$ , the virial radius estimated from the redshift ( $z=0.395$ ; Gunn & Oke 1975) and the Chandra average temperature measurement (4.47 keV; Ota et al. 2004). Thus the cluster emission covers less than half of the field of view (FOV) of the XMM-Newton telescope detectors. Actually the significant cluster

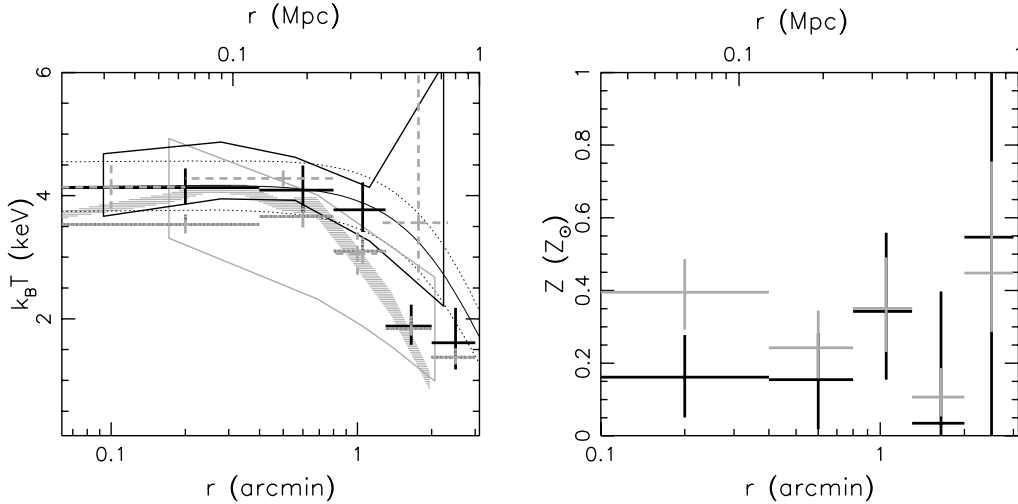


**Figure 7.6:** Projected temperature (left) and metallicity (right) profiles measured from the XMM-Newton data in the 1–7.8 keV band (solid, black) and 0.4–7.8 keV band (solid, grey) with point sources excluded. A solid curve in black indicates the best Gaussian fit of the temperature measurements in the 1–7.8 keV band with confidence intervals as dotted curves. Additionally the similarity temperature profiles in Markevitch et al. (1998; grey) and in Zhang et al. (2004b; black) are indicated by solid outlines. Our Chandra temperature measurements of CL0024+17 (dashed, grey) and the temperature profile of Sersic 159–03 (grey shadow;  $1\sigma$  interval) in Kaastra et al. (2001) scaled to CL0024+17 are presented for comparison.

emission extends only to  $3'$  in the surface brightness of the XMM-Newton observations. Thus we use the  $5 < r < 5.5'$  region in detector coordinates to compare the background conditions of the XMM-Newton pointing of the Chandra Deep Field South (CDFS, which we use as background field for the spectral analysis) with that of CL0024+17. The background of CL0024+17 is higher than that of the background field (CDFS) by  $\sim 30\%$  for MOS and  $\sim 10\%$  for pn on average in the complete energy band, in which the difference is mainly produced in the low energy band below 1 keV.

In the spectral analysis, the regions not affected by cluster emission, enable us to study the residual background in the source observation compared to the background observation. We applied a double background subtraction method as described in Zhang et al. (2004a) using the results of the residual background modeling. In summary the spectral analysis is performed in two steps using the software package XSPEC11.3.0: (i) A power law model for the residual background (background difference) is obtained in XSPEC from a comparison of the outer region ( $5-5.5'$ ) of the target and background fields (cf. Table 7.1). (ii) The spectral modeling is performed in XSPEC with the cluster region of the target field as source data, the region in the same detector coordinates in the background field as background and the residual background as a second model component with model parameters fixed to the values found in step (i). The overall spectra were fitted by a “mekal” model (Mewe et al. 1985, 1986; Kaastra 1992; Liedahl et al. 1995; Arnaud & Rothenflug 1985; Arnaud & Raymond 1992) with Galactic absorption (Dickey & Lockman 1990;  $n_H = 4.23 \times 10^{20} \text{ cm}^{-2}$ ). The results with and without introducing a residual background are consistent within  $1\sigma$ ,

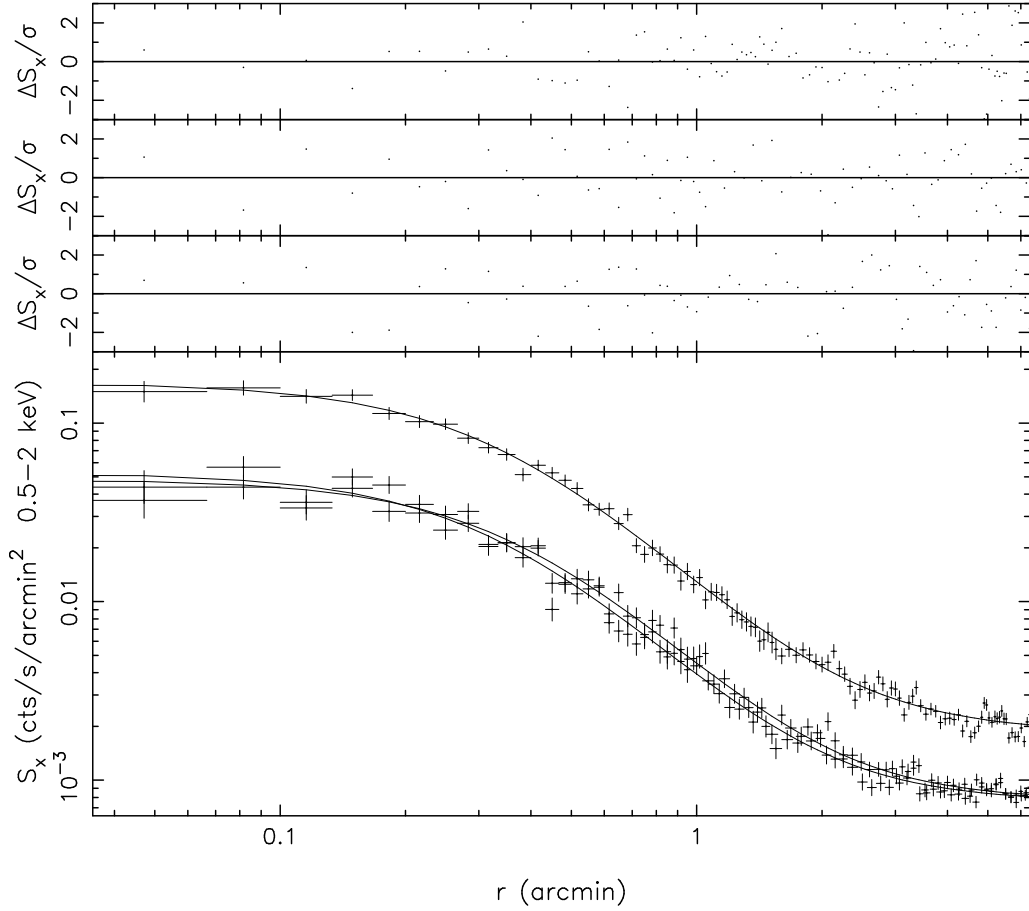


**Figure 7.7:** Flat fielded, point source subtracted and azimuthally averaged radial surface brightness profiles for CL0024+17 in the 0.5–2 keV band for pn (top) and MOS (bottom) and their best  $\chi^2$  fits by a PSF convolved  $\beta$ -model combining a constant residual soft X-ray background. Residuals scaled by the data uncertainties appear in the upper three panels for MOS1, MOS2 and pn, respectively, from top to bottom.

**Table 7.1:** Parameters of the residual background model fitted in the 0.4–15 keV band. Column (1): instrument; Cols. (2–3): index and normalization of the power law residual background in which the normalization was scaled to 1 arcmin<sup>2</sup> in units of  $10^{-4}$  cts s<sup>-1</sup> keV<sup>-1</sup> arcmin<sup>-2</sup>.

Instrument	Index	Normalization
MOS1	1.95	1.00
MOS2	2.21	0.64
pn	1.95	2.25

e.g. the temperature (metallicity) of the  $r < 3'$  region are  $3.52 \pm 0.17$  ( $0.22 \pm 0.07$ ) and  $3.61 \pm 0.28$  ( $0.22 \pm 0.11$ ).

In the image analysis for the surface brightness we carry out a vignetting correction

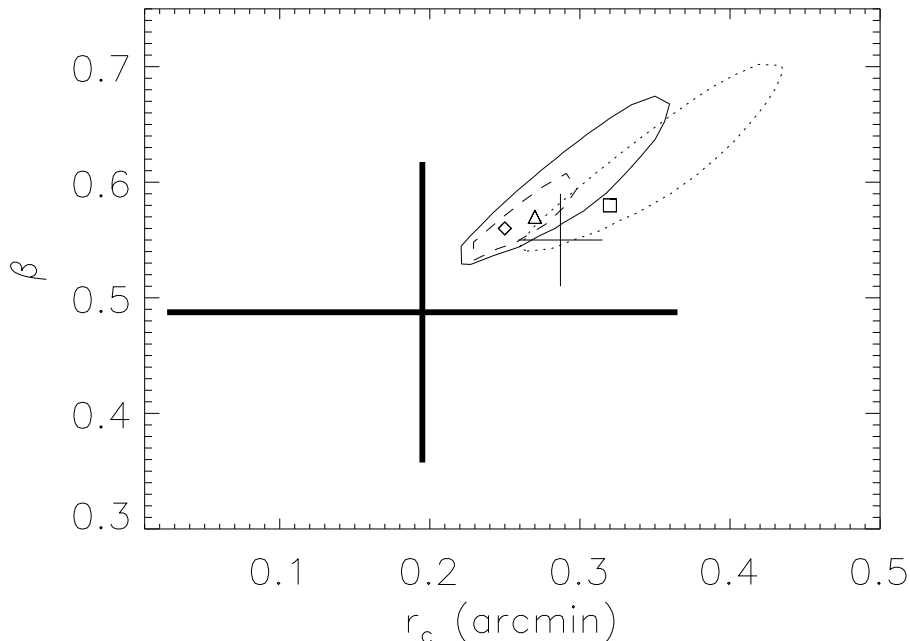


**Figure 7.8:** 90% confidence contours and the best fit values for the core radius  $r_c$  and slope parameter  $\beta$  of the  $\beta$  model for the surface brightness of XMM-Newton for MOS1 (solid; triangle), MOS2 (dotted; square) and pn (dashed; diamond), respectively. Chandra (thin; Ota et al. 2004) and ROSAT (thick; Böhringer et al. 2000) measurements are also shown as crosses.

for CDFS and CL0024+17, respectively. We derive the CDFS surface brightness in the same detector coordinates as CL0024+17 and scale it using the ctr ratio of CL0024+17 and CDFS in the 10–12 keV (12–14 keV) band for MOS (pn). After subtracting the scaled CDFS as a background from CL0024+17, we use a constant model to fit the residual soft X-ray background which is quite flat in the outer region ( $5 < r < 10'$ ).

For comparison, we also used the blank sky background from Lumb et al. (2002) and found that the parameters change less than  $1 \sigma$  for both spectral and surface brightness analyses.

### 7.2.3 Point source subtraction

In a preliminary spectral analysis without subtracting the point sources we found contamination in both the soft and hard bands, especially for pn.

Therefore we generated a list of the bright point sources using SAS task “edetect\_chain” applied to five energy bands: 0.3–0.5 keV, 0.5–2 keV, 2–4.5 keV, 4.5–7.5 keV, 7.5–12 keV. The sources detected include fourteen of sixteen sources which were found in ROSAT HRI observations (Soucail et al. 2000) except that S14 and S15 are out of the FOV of XMM-Newton. Since we carried out analyses only in the  $r < 8'$  region, only the brightest fourteen point sources within this region (including nine ROSAT HRI sources, S1, S2, S3, S4, S5, S6, S8, S9 and S10 in Soucail et al. 2000) were subtracted from the source events using

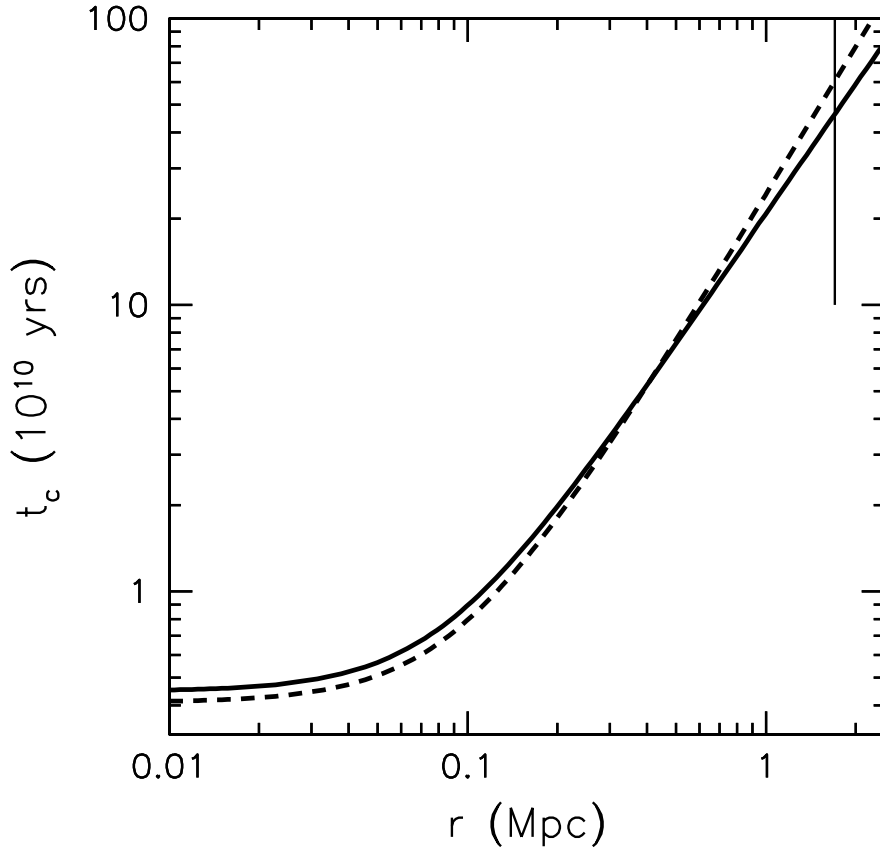


**Figure 7.9:** Cooling time of the gas using the global temperature (dashed) and using the observed temperature profile (solid). The vertical line indicates  $r_{200} = 1.7h_{70}^{-1}$  Mpc, predicted from the lensing data in Kneib et al.(2003).

a radius of  $40''$ , which is comparable to the XMM-Newton Point Spread Function (PSF) cutoff radius of  $\sim 45''$ , for each source that encloses nearly 90% of the flux of the point sources in both the spectroscopic and image analyses (cf. Table 7.2).

## 7.3 Results

### 7.3.1 Image analysis

The images in the 0.5–2 keV band for MOS and pn were corrected for vignetting using their weighted exposure maps and were then combined. We created an adaptively-smoothed image from the combined image with a maximum sigma (the width of the smoothing Gaussian) of  $12'' \times 12''$  and a signal-to-noise of 5.0 (see Fig. 7.1). Superposed XMM-Newton X-ray contours indicate an elongation in the northwest-southeast (NW-SE) direction and substructure in the NW (R.A. =  $00^h26^m25^s.8$ , decl. =  $17^\circ12'03''.7$ ,  $\sim 3.3'$  from the center).

We found no sign of the substructure described in Bonnet et al. (1994) which is  $\sim 6.9'$  from the cluster center (R.A. =  $00^h26^m35^s.7$ , decl. =  $17^\circ09'35''.8$ ) to the northeast (NE).

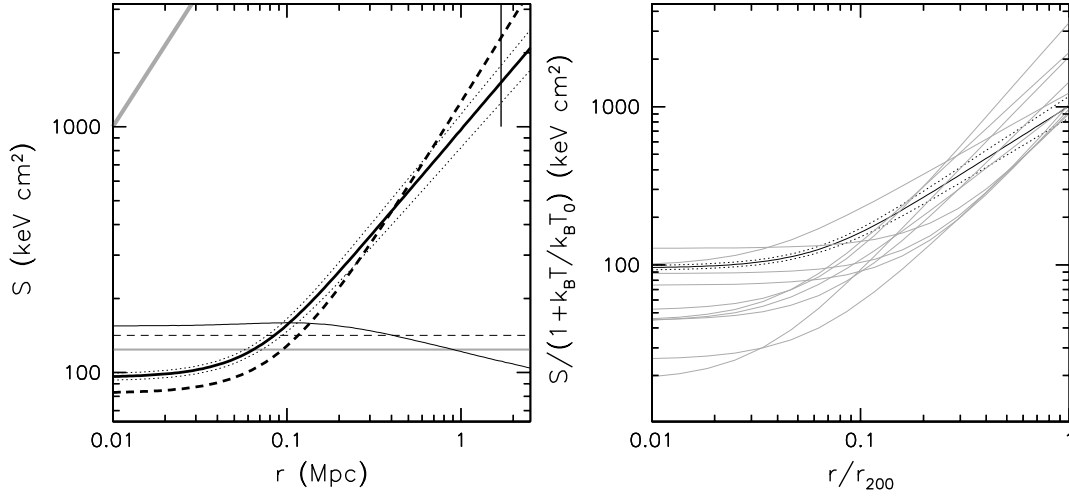


**Figure 7.10:** Left: Entropy (thick, black) and critical entropy floor (thin, black) using the global temperature (dashed) and using the observed temperature profile (solid, confidence intervals as dotted curves). Additional grey lines are the entropy floor (thin),  $S \sim 124h_{70}^{-1/3}$  keV cm<sup>2</sup>, from Lloyd-Davies et al. (2000) and the predicted slope of 1.1 (thick) from the spherical accretion shock model (Kay 2004). The vertical line indicates the radius as defined in Fig. 7.9. Right: Scaled entropy of CL0024+17 vs. scaled radius using the radius of  $r_{200} = 1.05h_{70}^{-1}$  Mpc (black, confidence intervals as dotted curves) and the Birmingham-CfA clusters in a temperature range of 2.9–4.6 keV (grey).

**Table 7.2:** Parameters for the brightest point sources detected in the  $r < 8'$  region. Column (1): No. of the point source; Cols. (2–3): central position; Col. (4): flux determined out to a radius of  $20''$  in the 0.3–12 keV band.

No.	R.A.	decl.	Flux ( $10^{-13}$ cgs)
1	00 26 12.8	17 03 46.8	1.317
2	00 26 30.9	17 10 14.9	0.933
3	00 27 00.0	17 04 22.4	0.890
4	00 26 31.0	17 16 54.2	0.760
5	00 26 20.1	17 17 03.1	0.677
6	00 27 05.3	17 06 40.6	0.671
7	00 26 44.2	17 02 29.4	0.581
8	00 26 26.1	17 09 37.3	0.558
9	00 27 07.5	17 07 48.6	0.542
10	00 26 17.2	17 03 06.1	0.400
11	00 26 45.8	17 12 30.5	0.391
12	00 26 17.9	17 09 45.8	0.259
13	00 27 03.7	17 07 21.5	0.224
14	00 26 42.8	17 08 30.9	0.060

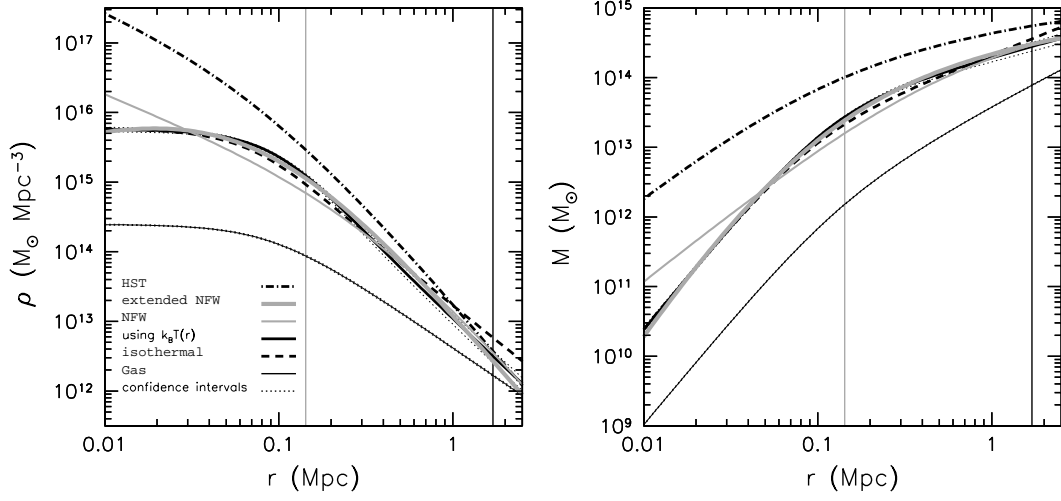


**Figure 7.11:** **Left:** Dark matter density and gas density, **right:** gravitational mass and gas mass. The meaning of the lines is: (i) hydrostatic equilibrium (black) using the global temperature (thick, dashed) and using the observed temperature profile (thick, solid, confidence intervals as dotted curves) and its best fit (grey) of extended NFW model (thick) and NFW model (thin); (ii) HST lensing measurements (Kneib et al. 2003; dash-dotted). Additionally we present the gas density and gas mass (thin, black) with confidence intervals as dotted curves. The black vertical line indicates the radius as defined in Fig. 7.9. The grey vertical line indicates the arc radius of  $0.143h_{70}^{-1}$  Mpc (e.g. Broadhurst et al. 2000).

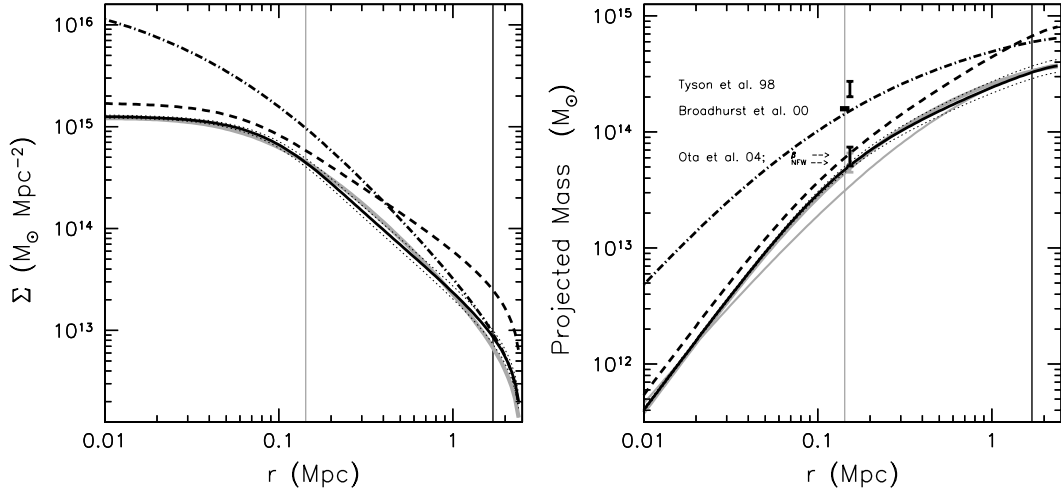


**Figure 7.12:** **Left:** Projected density ( $r_{\text{truncate}} = 2.5h_{70}^{-1}$  Mpc), **right:** projected gravitational mass ( $r_{\text{truncate}} = 2.5h_{70}^{-1}$  Mpc). We label the strong lensing projected gravitational mass of  $1.59 \pm 0.04 \times 10^{14} h_{70}^{-1} M_{\odot}$  (Broadhurst et al. 2000) and  $2.37 \pm 0.36 \times 10^{14} h_{70}^{-1} M_{\odot}$  (Tyson et al. 1998) at the arc radii of  $0.143h_{70}^{-1}$  Mpc and  $0.153h_{70}^{-1}$  Mpc and the Chandra results (Ota et al. 2004) using a  $\beta$ /NFW model at the arc radius of  $0.153h_{70}^{-1}$  Mpc for comparison. The lines have an identical meaning to those in Fig. 7.11.



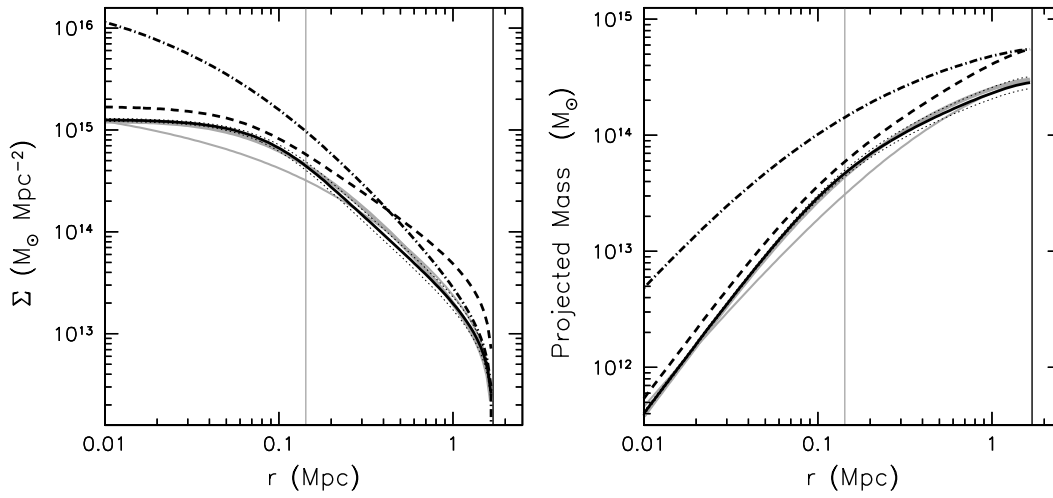


**Figure 7.13:** **Left:** Projected density ( $r_{\text{truncate}} = 1.7h_{70}^{-1}$  Mpc), **right:** projected gravitational mass ( $r_{\text{truncate}} = 1.7h_{70}^{-1}$  Mpc). The lines have an identical meaning to those in Fig. 7.11.

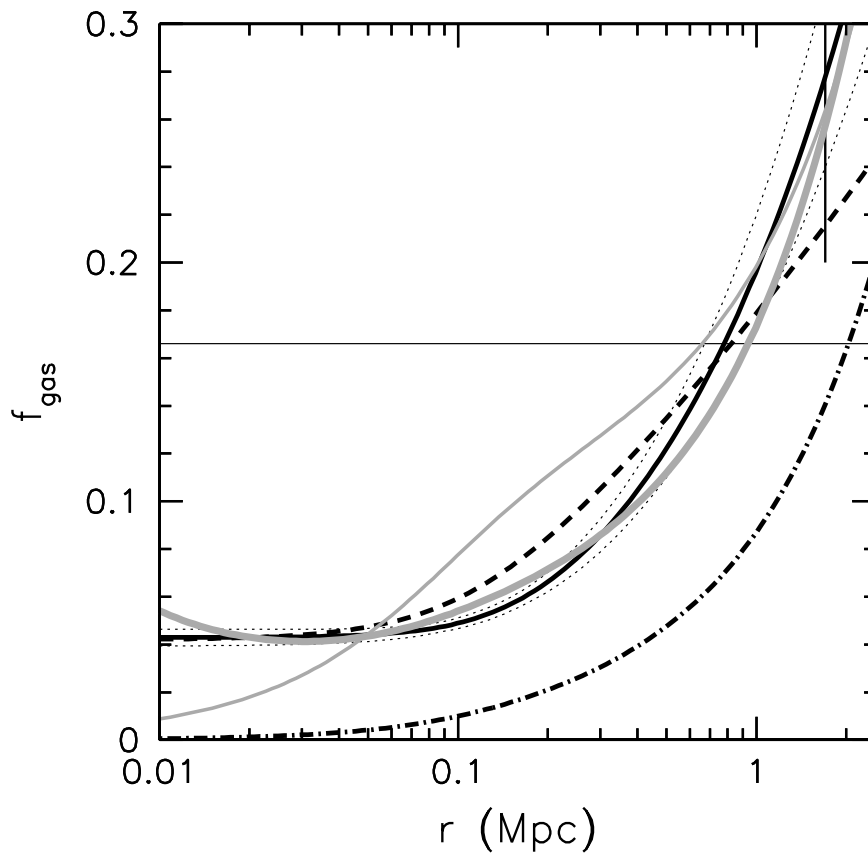


**Figure 7.14:** Gas mass fraction as a function of radius. The lines have an identical meaning to those in Fig. 7.11 except that an additional horizontal line indicates the WMAP measurement  $f_b = \Omega_b/\Omega_m = 0.166$  (Spergel et al. 2003).

However, we observed the substructure, described in Kneib et al. (2003) and Czoske et al. (2001, 2002), located  $\sim 3.3'$  NW from the cluster center covering  $1'$  with a temperature of  $0.87 \pm 0.13$  keV fixing the metallicity to  $Z = 0.3Z_{\odot}$  and a bolometric X-ray luminosity of  $L_X^{\text{bol}} = 0.57 \pm 0.06 \times 10^{43} h_{70}^{-2} \text{ erg s}^{-1}$ , 2% of the total emission of the cluster. We also observed emission from a pair of background groups in the NE which were described in Czoske et al. (2002) at  $z = 0.495$  based on a wide-field spectroscopic survey. The northern group centered at R.A. =  $00^{\text{h}}26^{\text{m}}50^{\text{s}}.1$ , decl. =  $17^{\circ}19'37''.8$  is more compact and X-ray luminous ( $L_X^{\text{bol}} = 0.24 \times 10^{44} h_{70}^{-2} \text{ erg s}^{-1}$ ,  $r < 100''$ ). The southern group centered at R.A. =  $00^{\text{h}}27^{\text{m}}00^{\text{s}}.9$ , decl. =  $17^{\circ}14'51''.7$  is too faint for spectral analysis. If we assume a gas temperature in the range 1–4 keV, then the bolometric luminosity of this group lies in the range  $0.076\text{--}0.079 \times 10^{44} h_{70}^{-2} \text{ erg s}^{-1}$  ( $r < 100''$ ).

### 7.3.2 Chandra observation of the center

CL0024+17 was also observed by Chandra (ID: 929). Ota et al. (2004) showed an adaptively smoothed image of the cluster with a rather symmetric appearance.

A closer inspection reveals asymmetries, however. Fig. 7.2 shows an unsmoothed image (0.5–2.5 keV,  $\sim 2''$  pixels) and surface brightness profiles in annuli using the 0.5–2.5 keV image with azimuths  $30^{\circ}\text{--}120^{\circ}$  (counter clockwise) from north to east and from south to west, respectively. There is a clear asymmetry between the northeast and southwest. To the northeast, we note a sharp decrease at a radius of about  $34''$ . The profile to the southwest displaying a more gradual decline. In Fig. 7.6, we show the azimuthally averaged Chandra temperature profile from a more detailed spectral study (kindly provided by Alexey Vikhlinin) fixing the metallicity to  $Z = 0.3Z_{\odot}$ . We note a corresponding temperature decrease approximately at the same radius as the surface brightness decline. This complex structure including a possible indication of a “shock front” might provide further support to the cluster merger scenario.

### 7.3.3 Optical observations

To compare the X-ray morphology with the optical image in the central region of CL0024+17, we retrieved 15 HST WFPC2 observations including 11 from PI: Ellis (ID: 8559) and 4 from PI: Turner (ID: 5453). They are block 0, 11, 12, 13, 18, 19, 23, 24, 25, 36, 37 and 38 in Treu et al. (2003). All images were taken in the F814W filter (I band). We use the IRAF STSDAS and IMAGES packages to obtain the mosaic image from the calibrated science images.

The X-ray contours of the XMM-Newton observations were plotted on the merged HST image (shown in Fig. 7.3). We note the overlapping cluster centers and galaxy concentrations in the NW ( $\sim 3.3'$ ) of the X-ray and optical images.

### 7.3.4 Hardness ratio maps

To further study the substructure in CL0024+17 we produced hardness ratio map (HRM) of the cluster, which primarily reflects the temperature distribution. The hardness ratio is the photon flux ratio of the hard band of 2–7.5 keV to the soft band of 0.5–2 keV,  $HR = I(2\text{--}7.5 \text{ keV})/I(0.5\text{--}2 \text{ keV})$ . An indication of an elongation in the NW-SE direction

is visible in the HRM (see Fig. 7.4) on a scale of  $r \sim 3.3'$ . The HRM shows a complicated structure with an average  $HR$  of  $0.55 \pm 0.39$  in the central  $r < 3'$  region. The substructure in the NW ( $\sim 3.3'$ ) has an average of  $HR = 0.48 \pm 0.34$  within  $1'$ . We note two peaks: one is at (R.A. =  $00^h26^m24^s.8$ , decl. =  $17^\circ11'13''.2$ ) that is marginally coincident with the NW substructure; the other is close to the center at R.A. =  $00^h26^m30^s.9$ , decl. =  $17^\circ09'50''.3$ .

### 7.3.5 Temperature and metallicity profiles

We first derive global X-ray properties of CL0024+17 from the spectra extracted from the  $r < 3'$  region, covering radii up to a spherical overdensity of  $\sim 250$ , i.e. the ratio of the mean density of the dark halo with respect to the redshift-dependent critical density  $\rho_{\text{crit}}(z)$ . We measure an emission weighted temperature of  $3.52 \pm 0.17$  keV, metallicity of  $0.22 \pm 0.07$  and bolometric luminosity of  $2.9 \pm 0.1 \times 10^{44} h_{70}^{-2} \text{ erg s}^{-1}$  ( $\chi^2/dof = 248.5/228$ ). We confirm the estimates of 3–4.5 keV and  $L_X^{\text{bol}} = 2.40 \times 10^{44} h_{70}^{-2} \text{ erg s}^{-1}$  in Böhringer et al. (2000) from the ROSAT observation and a estimate of  $5.7^{+4.2}_{-2.1}$  keV in Soucail et al. (2000) from the ASCA observations. The Chandra observations yield a comparable temperature of  $4.47^{+0.42}_{-0.27}$  keV and a bolometric luminosity of  $2.60 \times 10^{44} h_{70}^{-2} \text{ erg s}^{-1}$  (Ota et al. 2004). The source spectra for  $r < 3'$  and the fitted model are shown in Fig. 7.5. A lower luminosity of  $1.26 \times 10^{44} h_{70}^{-2} \text{ erg s}^{-1}$  is predicted from the  $L$ – $T$  relation in Arnaud & Evrard (1999) and the XMM-Newton temperature measurement. The high luminosity might indicate the complex cluster center which will be discussed in Sect. 7.4.

For a more detailed spectral study we divide the cluster region into five annuli: 0–0.4', 0.4–0.8', 0.8–1.3', 1.3–2', and 2–3'. We investigate the dependence of the temperature and metallicity measurements on the low energy (low-E) cut-off (0.4 keV or 1 keV) as we did in our earlier study (Zhang et al. 2004a) to test the robustness of the spectral data fitting. We find that in the  $r < 1'$  region the derived temperatures increase by 15% if the low-E cut-off is increased from 0.4 keV to 1 keV. With the decreasing signal-noise-ratio (S/N) in the  $r > 1'$  region the derived temperatures increase by up to 40% if the low-E cut-off is increased from 0.4 keV to 1 keV. As in our earlier work (see also Pratt & Arnaud 2002) we attribute this change in the best fit temperature with energy range to the influence of a contaminating soft spectral component. To minimize its effect, we use the higher energy cut-off at 1 keV above which the results are stable.

The radial metallicity distribution is very flat which is expected from simulations where merging efficiently flattens the metallicity profile (Kobayashi 2004). The deprojection correction does not provide a significant change in the results. In the  $r < 1'$  ( $r > 1'$ ) region the temperature measurements vary by a factor of 5% (50%), which is approximately within the error bars. The temperature and metallicity profiles determined from the spectra in the 5 annuli ( $\chi^2/dof = 68.2/72, 77.0/78, 64.0/60, 50.2/60, 110.1/96$  from the inner to the outer annulus) are shown in Fig. 7.6. A variation of the temperature with radius is found here for the first time for CL0024+17. The inner three bins covering the radial range to a radius of  $1.3'$  ( $416 h_{70}^{-1}$  kpc) are consistent with an isothermal profile. This agrees with the Chandra results by Ota et al. (2004) who found an isothermal temperature profile to an outer radius of  $1.5'$  ( $480 h_{70}^{-1}$  kpc). The form of the temperature profile is very similar to the profile we obtained for the sample of REFLEX-DXL (ROSAT-ESO Flux-Limited X-ray cluster survey, Distant X-ray Luminous) clusters (Zhang et al. 2004b). We scaled the temperature

profile in Markevitch et al. (1998) to CL0024+17 using a radius of  $r_{180} = 1.10h_{70}^{-1}$  Mpc (obtained in Sect. 7.3.9) and an emission weighted global temperature of 3.52 keV. We find good overall agreement as found for the REFLEX-DXL clusters except that the flat part of the temperature profile extends to a larger radius than the average profile of Markevitch et al. (1998). We also scaled the temperature profile for Sersic 159–03 in Kaastra et al. (2001) to CL0024+17, and found a similarly rapid temperature drop as a function of radius as CL0024+17.

We found an isothermal temperature of  $\sim 3.9$  keV to a radius of  $1.5'$  ( $480h_{70}^{-1}$  kpc) and a power law model with an index  $\gamma = 0.98$  outside this radius. We approximate the temperature profile with two analytical models: (a) an isothermal model using the global temperature of  $3.52 \pm 0.17$  keV; (b) a function with the shape of a Gaussian of  $k_B T(r) = k_B T_g \cdot e^{-\frac{1}{2}(\frac{r-r_g}{w})^2}$  (see Table 7.5) which approximately fits the observed temperature profile.

### 7.3.6 Surface brightness

We obtained an azimuthally averaged surface brightness profile for CL0024+17 in the 0.5–2 keV band for each instrument, in which the central position is R.A. =  $00^h 26^m 35^s.7$ , decl. =  $17^\circ 09' 35''.8$ . This energy band is selected because it provides an almost temperature-independent X-ray emission coefficient over the expected temperature range. After the vignetting correction and double-step background subtraction described above, we find that a  $\beta$ -model (e.g. Cavaliere & Fusco-Femiano 1976; Jones & Forman 1984)

$$S_x(r) = S_0 \left(1 + \frac{r^2}{r_c^2}\right)^{-3\beta+1/2} \quad (7.1)$$

convolved with the XMM-Newton PSF provides an adequate  $\chi^2$  fit to the surface brightness profile (Fig. 7.7). A PSF at each position for each instrument is determined from an empirical calibration (Ghizzardi 2001) according to a mean energy  $\sim 1.25$  keV of the 0.5–2 keV band and its off-axis radius.

We compare the PSF convolved and unconvolved  $\beta$ -model parameters in Table 7.3, and find that the core radii are overestimated and the slope parameters are underestimated in the latter case. The combined 90% confidence contours (see Fig. 7.8) of the three instruments provide a narrow range for  $r_c$  and  $\beta$  ( $0.266 < r_c < 0.295'$ ;  $0.551 < \beta < 0.593$ ) at the 90% confidence level. Böhringer et al. (2000) obtained  $r_c = 0.11$ – $0.28'$  and  $\beta = 0.425$ – $0.550$  from the ROSAT HRI data corrected for PSF. Ota et al. (2004) obtained  $r_c = 0.287 \pm 0.014'$  and  $\beta = 0.55 \pm 0.02$  from the Chandra observations. Our result confirms the results from previous X-ray observations with a higher accuracy because of the improvement of the image quality of XMM-Newton compared to previous observations.

The surface brightness profile approximated by a  $\beta$ -model can be analytically deprojected to yield the emission per volume element,  $\xi(r) = \tilde{\Lambda}(r)n_e^2(r)$ . With the given emissivity,  $\tilde{\Lambda}(r)$ , from the applied plasma model, one can derive the electron density profile  $n_e(r) = n_{e0} \left(1 + \frac{r^2}{r_c^2}\right)^{-3\beta/2}$  with the parameters given in Table 7.3 combining the three detectors. We studied the influence of the central emission in the beta model analysis and found that the parameters like  $\beta$  and  $r_c$  change within 2% if the central bins are masked.

**Table 7.3:** Parameters of the  $\beta$ -model. Column (1): instrument; Col. (2): “Y” or “N” means the PSF convolved or unconvolved  $\beta$ -model; Col. (3): central surface brightness (0.5–2 keV) in  $\text{cts s}^{-1} \text{ arcmin}^{-2}$ ; Col. (4): core radius in arcmin; Col. (5): slope parameter; Col. (6):  $\chi^2/dof$ .

	PSF	$S_0$	$r_c$	$\beta$	$\chi^2/dof$
MOS1	Y	$0.106 \pm 0.015$	$0.27 \pm 0.03$	$0.57 \pm 0.02$	99.7/63
	N	$0.047 \pm 0.004$	$0.34 \pm 0.03$	$0.56 \pm 0.01$	204.3/150
MOS2	Y	$0.094 \pm 0.010$	$0.32 \pm 0.03$	$0.58 \pm 0.02$	79.2/65
	N	$0.045 \pm 0.003$	$0.36 \pm 0.03$	$0.54 \pm 0.01$	159.7/150
pn	Y	$0.375 \pm 0.033$	$0.25 \pm 0.02$	$0.56 \pm 0.01$	130.5/88
	N	$0.158 \pm 0.007$	$0.33 \pm 0.02$	$0.54 \pm 0.01$	206.3/150

We obtain the pressure distribution  $P(r)$  as a function of radius directly from the temperature and electron density measurements. Thus a  $\beta$ -model is applied to fit the pressure with results shown in Table 7.5.

Furthermore, we simulated a symmetric, background subtracted and flat fielded image using the parameters of the  $\beta$ -model in Table 7.3. The residual map, which contains the background, is obtained by extracting the simulated image from the adaptively-smoothed image. We confirm the existence of excess emission in the substructure in the NW, while the negative residual surface brightness in the cluster center shows that the elongation flattens the surface brightness compared to a symmetric structure.

To further test if the cluster mass profile can be described by a NFW profile (Navarro et al. 1997; NFW), we fit the observed surface brightness profile by the model computed from the NFW model described dark matter halo (e.g. Makino et al. 1998). A model that fits the data well over a large range of radii shows an inner cusp in the surface brightness. The central surface brightness model at the given resolution is about a factor of two to three higher and thus inconsistent with our observations. Since we detect signatures of a cluster merger in the central region. We are not surprised to find deviations from the NFW model. Also Tyson et al. (1998) found a core in the mass profile in their lensing analysis.

### 7.3.7 Cooling time of the gas

The cooling time is the total energy of the gas divided by the energy loss rate (e.g. Zhang & Wu 2003)

$$t_c = 2.869 \times 10^{10} \text{ yr} \left( \frac{1.2}{g} \right) \left( \frac{k_B T}{\text{keV}} \right)^{\frac{1}{2}} \left( \frac{n_e}{10^{-3} \text{ cm}^{-3}} \right)^{-1}, \quad (7.2)$$

where  $n_e$  and  $k_B T$  are the electron number density and temperature, respectively, and  $g$  is the Gaunt factor (a function of  $k_B T$ ). The resulting cooling time as a function of radius is shown in Fig. 7.9. The central cooling time of 4.5 Gyr is smaller than the age of the Universe and probably smaller than the age of the cluster if we assume that the age of the cluster mass concentration is longer than two crossing time because the merger frequency is expected to be a few Gyr (e.g. Schuecker et al. 2001). An even smaller central cooling time is implied by the Chandra data (Ota et al. 2004) due to the higher angular resolution

of the central region. The data thus correspond, in the classical interpretation, to a small or moderate cooling flow (Fabian & Nulsen 1977).

### 7.3.8 Gas entropy

The main part of the observed entropy, defined as  $S = k_B T n_e^{-2/3}$  (e.g. Ponman et al. 1999), results from shock heating of the gas during cluster formation and it scales with the cluster critical temperature. An excess above this scaling law indicates the effect of an additional, non-gravitational heating source (e.g. Lloyd-Davies et al. 2000). While a low central entropy indicates significant radiative cooling. We show the entropy profile derived for CL0024+17 from the XMM-Newton observations in Fig. 7.10.

The entropy of the  $r > 0.1h_{70}^{-1}$  Mpc region derived from temperature measurements of CL0024+17 has a similar slope as that predicted from a spherical accretion shock model,  $S \propto r^{1.1}$  (Kay 2004; thick grey line in Fig. 7.10). The entropy under the assumption of isothermality becomes steeper than the entropy derived from temperature measurements, especially in the outer region.

The entropy of the gas in the center ( $r < 0.1h_{70}^{-1}$  Mpc) lies below the entropy floor,  $S \sim 124h_{70}^{-1/3}$  keV cm<sup>2</sup>, derived for clusters by Lloyd-Davies et al. (2000). This indicates some effect from radiative cooling.

We scale the entropy of CL0024+17 by  $1 + \frac{k_B T(r)}{k_B T_0}$ , where  $k_B T_0 = 2$  keV is a constant related to the degree of preheating. In Fig. 7.10, we compare it to the entropy of the Birmingham-CfA clusters in the temperature range of 2.9–4.6 keV (Ponman et al. 2003) scaled also by  $1 + \frac{k_B T(r)}{k_B T_0}$ . The entropy of CL0024+17 agrees with the self-similarly scaled entropy described by Ponman et al. (2003) within the observed dispersion of their cluster sample.

Eq.(7.2) can be rewritten as

$$S_c = 100\text{keVcm}^2 \left( \frac{t_c}{2.869 \times 10^{10}\text{yr}} \right)^{\frac{2}{3}} \left( \frac{g}{1.2} \right)^{\frac{2}{3}} \left( \frac{k_B T}{\text{keV}} \right)^{\frac{2}{3}}. \quad (7.3)$$

If the cooling time  $t_c$  is chosen approximately to be the age of the Universe, the above equation would allow us to determine the critical entropy floor  $S_c$  of the gas in the cluster before the onset of significant cooling and possible mass deposition. In the center of CL0024+17 the observed entropy is slightly below this value ( $\sim 154$  keV cm<sup>2</sup>) which implies a insignificant radiative cooling.

### 7.3.9 Mass modeling

We assume the intracluster gas to be in hydrostatic equilibrium within the gravitational potential dominated by dark matter. Neglecting the cosmological constant,  $\Lambda$ , at these high overdensities (a less than 1% effect, see Zhang et al. 2004a), we have

$$\frac{1}{\mu m_p n_e} \frac{d(n_e k_B T)}{dr} = -\frac{GM(r)}{r^2}, \quad (7.4)$$

where  $\mu = 0.62$  is the mean molecular weight per hydrogen atom.

**Table 7.4:** Comparison of the gravitational mass from the X-ray and optical lensing measurements.

Observation		XMM-Newton <sup>a</sup>		Chandra <sup>b</sup>	HST	
$r_{200}$	$(h_{70}^{-1} \text{ Mpc})$	1.11	1.05	1.4	1.7	<sup>c</sup>
$M_{200}$	$(10^{14} h_{70}^{-1} M_{\odot})$	$2.3 \pm 0.1$	$2.0 \pm 0.3$	$4.6_{-0.5}^{+0.7}$	$5.7_{-1.0}^{+1.1}$	<sup>c</sup>
$M_{\text{proj}}(r = 0.143)$	$(10^{14} h_{70}^{-1} M_{\odot})$	$0.61 \pm 0.01$	$0.48 \pm 0.03$	—	$1.59 \pm 0.04$	<sup>d</sup>
$M_{\text{proj}}(r = 0.153)$	$(10^{14} h_{70}^{-1} M_{\odot})$	$0.64 \pm 0.01$	$0.51 \pm 0.03$	$0.60_{-0.09}^{+0.14} (\beta)$ $0.53_{-0.08}^{+0.13} (\text{NFW})$	$2.37 \pm 0.36$	<sup>e</sup>
$M(r = 1.4)$	$(10^{14} h_{70}^{-1} M_{\odot})$	$3.0 \pm 0.2$	$2.4 \pm 0.3$	$4.6_{-0.5}^{+0.7}$	—	
$M(r = 1.7)$	$(10^{14} h_{70}^{-1} M_{\odot})$	$3.6 \pm 0.2$	$2.8 \pm 0.4$	—	$5.7_{-1.0}^{+1.1}$	<sup>c</sup>

<sup>a</sup> XMM-Newton results using the global temperature and using the observed temperature profile in which projected masses use the truncation radius of  $r_{200} = 2.5h_{70}^{-1}$  Mpc; <sup>b</sup> Ota et al. (2004); <sup>c</sup> Kneib et al. (2003); <sup>d</sup> Broadhurst et al. (2000); <sup>e</sup> Tyson et al. (1998).

Analytic models of the gas density and pressure profiles derived above can be easily combined with Eq.(7.4) to obtain the mass profile (Fig. 7.11). The virial radius (not  $r_{200}$ ) is defined to be a radius with overdensity (the average density with respect to  $\rho_{\text{crit}}$  at the cosmic epoch  $z$ ) of  $\Delta_{c,z} = 18\pi^2 + 82[\Omega_{\text{m}}(z) - 1] - 39[\Omega_{\text{m}}(z) - 1]^2$  for a flat universe.  $\Omega_{\text{m}}(z)$  is the cosmic density parameter (e.g. Zhang & Wu 2003). Therefore the mass profiles in Fig. 7.11 combined with the expression for the overdensity yield  $r_{\text{vir}} = 1.37h_{70}^{-1}$  Mpc using the global temperature and  $r_{\text{vir}} = 1.26h_{70}^{-1}$  Mpc using the observed temperature distribution.

We compare the XMM-Newton results with the recent measurements from Chandra and HST in Table 7.4 and Fig. 7.12. The XMM-Newton measurements using the measured temperature profile are slightly lower than Chandra values derived under the assumption of isothermality. As shown in Table 7.4 and Fig. 7.12, the discrepancy between the X-ray measured total mass and strong lensing mass at the radii of  $0.143h_{70}^{-1}$  Mpc (Broadhurst et al. 2000) and  $0.153h_{70}^{-1}$  Mpc (Tyson et al. 1998) remains large, about a factor of 4.

Under the assumption of isothermality, the XMM-Newton measurements are more consistent with the observationally determined  $M_{200}$ - $T$  relation,

$$M_{200} = 4.11 \pm 0.02 \times 10^{13} h_{70}^{-1} \left( \frac{kT_{\text{B}}}{\text{keV}} \right)^{1.60 \pm 0.04} M_{\odot}, \quad (7.5)$$

which is based on the conventional  $\beta$  model for the X-ray surface brightness profile and hydrostatic equilibrium for 22 nearby clusters from Xu et al. (2001). For CL0024+17, Eq.(7.5) provides  $M_{200} = 3.08 \times 10^{14} h_{70}^{-1} M_{\odot}$  using the X-ray temperature. The masses obtained from the X-ray temperature measurement via the  $M$ - $T$  relations in Finoguenov et al. (2001b) and in Bryan & Norman (1998) are  $M_{200} = 5.96 \times 10^{14} h_{70}^{-1} M_{\odot}$  and  $M_{200} = 3.76 \times 10^{14} h_{70}^{-1} M_{\odot}$  in which the former is more consistent with the HST optical lensing estimate.

Navarro et al. (1997; NFW) describe a universal density profile from numerical simulations in hierarchical clustering scenarios

$$\rho_{\text{DM}}(r) = \delta_{\text{crit}} \rho_{\text{crit}} \left( \frac{r}{r_s} \right)^{-1} \left( 1 + \frac{r}{r_s} \right)^{-2}, \quad (7.6)$$

**Table 7.5:** Parameters of each profile model for the best  $\chi^2$  fit.

Model	parameter	
Gaussian	$k_B T_g$ (keV)	$4.2 \pm 0.4$
	$r_g$ ( $h_{70}^{-1}$ Mpc)	$0.08 \pm 0.04$
	$w$	$0.69 \pm 0.04$
$\beta$	$r_c^{ne}$ ( $h_{70}^{-1}$ Mpc)	$0.093 \pm 0.001$
	$n_{e0}$ ( $10^{-3} \text{cm}^{-3}$ )	$8.8 \pm 0.1$
	$\beta^{ne}$	$0.57 \pm 0.01$
	$r_c^P$ ( $h_{70}^{-1}$ Mpc)	$0.11 \pm 0.01$
	$P_0$ ( $10^{-2} \text{keVcm}^{-3}$ )	$3.59 \pm 0.04$
	$\beta^P$	$0.68 \pm 0.01$
NFW	$r_s$ ( $h_{70}^{-1}$ Mpc)	$0.37 \pm 0.03$
	$\rho_s$ ( $10^{14} M_\odot \text{Mpc}^{-3}$ )	$5.3 \pm 0.7$
	$c$	3.5
extended NFW	$r_s$ ( $h_{70}^{-1}$ Mpc)	$0.072 \pm 0.004$
	$\rho_s$ ( $10^{16} M_\odot \text{Mpc}^{-3}$ )	$4.3 \pm 1.7$
	$\alpha$	$-0.8 \pm 0.1$

where  $\delta_{\text{crit}}$  and  $r_s$  are the characteristic density and scale of the halo, respectively,  $\rho_{\text{crit}}$  is the critical density of the Universe at the cosmic epoch  $z$  and  $\rho_s = \delta_{\text{crit}} \rho_{\text{crit}}$ .  $\delta_{\text{crit}}$  is related to the concentration parameter of a dark halo  $c = r_{\text{vir}}/r_s$  by

$$\delta_{\text{crit}} = \frac{200}{3} c^3 \left[ \ln(1+c) - \frac{c}{1+c} \right]^{-1}. \quad (7.7)$$

We fit the X-ray determined mass profile with a NFW model, and found that the NFW model does not provide a good fit to our data in the  $r < 0.1 h_{70}^{-1}$  Mpc region (Fig. 7.11). However the NFW model fit provides a virial radius of  $cr_s = 1.28 h_{70}^{-1}$  Mpc which is consistent with the virial radii of  $r_{\text{vir}} = 1.37 h_{70}^{-1}$  Mpc and  $r_{\text{vir}} = 1.26 h_{70}^{-1}$  Mpc derived from the mass profiles using the global temperature and using the observed temperature distribution, respectively, in Fig. 7.11 combined with the expression for the overdensity. We derive a radius of  $r_{200} = 0.93 h_{70}^{-1}$  Mpc from the empirical relation  $r_{200} = 0.813 (kT_B/\text{keV})^{0.5} (1+z)^{-3/2} h_{70}^{-1}$  Mpc (Navarro et al. 1995), which is slightly lower than  $r_{200} = 1.11 h_{70}^{-1}$  Mpc using the global temperature and  $r_{200} = 1.05 h_{70}^{-1}$  Mpc using the observed temperature distribution.

Furthermore, we apply an extended NFW model (e.g. Hernquist 1990; Zhao 1996; Moore et al. 1999),

$$\rho_{\text{DM}}(r) = \delta_{\text{crit}} \rho_{\text{crit}} \left( \frac{r}{r_s} \right)^{-\alpha} \left( 1 + \frac{r}{r_s} \right)^{\alpha-3} \quad (7.8)$$

to fit the data (Table 7.5) which provides a negative index. This indicates that the dark matter density has a flat core for CL0024+17.

We also present a comparison of the projected mass density and projected mass using the truncation radius of either  $r_{200} = 1.7 h_{70}^{-1}$  Mpc (Fig. 7.13), predicted from the lensing data in Kneib et al. (2003) or a larger radius of  $r = 2.5 h_{70}^{-1}$  Mpc (Fig. 7.12). The discrepancy is larger between the X-ray and strong lensing measurements than between the X-ray and weak lensing measurements.



**Table 7.6:** Measured parameters for CL0024+17. Column (1): parameter; Cols. (2-3): values obtained: (i) in the  $r < 3'$  region for line 2–4; (ii) using the global temperature and observed temperature distribution for line 5–7.

Parameter	Value	
$kT_B$ (keV)	$3.52 \pm 0.17$	
$Z$ ( $Z_\odot$ )	$0.22 \pm 0.07$	
$L_X^{bol}$ ( $10^{44} h_{70}^{-2}$ erg s $^{-1}$ )	$2.9 \pm 0.1$	
$r_{200}$ ( $h_{70}^{-1}$ Mpc)	1.11	1.05
$M_{200}$ ( $10^{14} h_{70}^{-1} M_\odot$ )	$2.3 \pm 0.1$	$2.0 \pm 0.3$
$f_{gas}$ ( $h_{70}^{-3/2}$ )	$0.19 \pm 0.01$	$0.20 \pm 0.03$

### 7.3.10 Gas mass fraction

The gas mass fraction distribution according to the definition  $f_{gas}(r) = M_{gas}(r)/M(r)$  is shown in Fig. 7.14. We found  $f_{gas} = 0.19 \pm 0.01 h_{70}^{-3/2}$  at  $r_{200} = 1.11 h_{70}^{-1}$  Mpc using the global temperature and  $0.20 \pm 0.03 h_{70}^{-3/2}$  at  $r_{200} = 1.05 h_{70}^{-1}$  Mpc using the observed temperature profile, respectively. This result is comparable with the Chandra results  $f_{gas} = 0.14_{-0.02}^{+0.03} h_{70}^{-3/2}$  at  $r_{200} = 1.40 h_{70}^{-1}$  Mpc (Ota et al. 2004), and agrees with the WMAP measured baryon fraction of the Universe  $f_b = \Omega_b/\Omega_m = 0.166$ , where  $\Omega_b h^2 = 0.0224$  and  $\Omega_m h^2 = 0.135$  (Spergel et al. 2003). We obtain a gas mass fraction of  $0.11 \pm 0.01$  using the global temperature at  $r_{2500} = 0.30$  Mpc and  $0.09 \pm 0.01$  using the observed temperature profile at  $r_{2500} = 0.33$  Mpc, which agrees with the measurements of Allen et al. (2002) based on Chandra observations of seven clusters yielding  $f_{gas} \sim 0.105\text{--}0.138 h_{70}^{-3/2}$ . However, this gas mass fraction at  $r_{200}$  is slightly higher than the measurements of Sanderson et al. (2003) based on ASCA/GIS, ASCA/SIS and ROSAT/PSPC observations of 66 clusters yielding  $f_{gas} = 0.13 \pm 0.01 h_{70}^{-3/2}$ , the measurements of Ettori et al. (2002a) based on BeppoSAX observations of 22 nearby clusters, and the gas mass fraction for A1413 (Pratt & Arnaud 2002) at  $z = 0.143$  based on XMM-Newton observations yielding  $f_{gas} \sim 0.12 h_{70}^{-3/2}$ .

The global parameters based on the XMM-Newton observations for CL0024+17 are given in Table 7.6.

## 7.4 Discussion

### 7.4.1 Metallicity

We measure a global metallicity of  $0.22 \pm 0.07 Z_\odot$  which is typical for a cluster with an insignificant cooling flow (Fabian & Nulsen 1977). This metallicity value is in good agreement with the averaged metallicity  $\langle Z \rangle = 0.21_{-0.05}^{+0.10} Z_\odot$  for 18 distant clusters with redshift  $0.3 < z < 1.3$  in Tozzi et al. (2003). However, Ota et al. (2004) obtain a much higher metallicity of  $0.61\text{--}0.95 Z_\odot$ . We use the images in the 5–6 keV and 6–7 keV bands as indicators of the iron K line and continuum emission, respectively, and obtain an iron to continuum map. We extracted the spectra from a suggested high metallicity region in the iron-to-continuum map at R.A. =  $00^h 26^m 32^s .7$ , decl. =  $17^\circ 09' 46'' .3$  covering a radius

**Table 7.7:** Temperature and metallicity measurements in different bin size of the radius.

Region	$k_B T$ (keV)	$Z$ ( $Z_\odot$ )	$\chi^2/dof$
$r < 0.40'$	$4.1 \pm 0.3$	$0.16 \pm 0.10$	68.2/72
$r < 0.50'$	$4.4 \pm 0.3$	$0.10 \pm 0.09$	69.1/69
$r < 1.00'$	$4.1 \pm 0.2$	$0.25 \pm 0.08$	161.3/137
$r < 1.25'$	$4.0 \pm 0.2$	$0.23 \pm 0.07$	159.6/152
$r < 1.50'$	$3.9 \pm 0.2$	$0.23 \pm 0.07$	173.1/170
$r < 1.67'$	$3.8 \pm 0.2$	$0.24 \pm 0.07$	170.9/163
$r < 2.00'$	$3.7 \pm 0.2$	$0.23 \pm 0.07$	185.3/184
$r < 3.00'$	$3.5 \pm 0.2$	$0.22 \pm 0.07$	68.5/71

of  $0.32'$ . No significant high metallicity was obtained by either setting a free temperature ( $5.4 \pm 1.6$  keV) or setting the temperature to the emission weighted temperature (4.09 keV) of the zone covering radii of  $0.4 < r < 0.8'$ . For the same radius of  $1.5'$  as used by Ota et al. (2004), we measure a metallicity of  $0.23 \pm 0.07$  and a temperature of  $3.9 \pm 0.2$  keV (see Table 7.7) using the XMM-Newton data. Therefore the XMM-Newton data with higher significance provide no explanation for the high metallicity value obtained by Ota et al. (2004). The difference between XMM-Newton and Chandra metallicity measurements is an about 2 sigma effect, and may be due to the limited photon statistics in the Chandra data.

#### 7.4.2 Temperature gradient

We derive an isothermal temperature of  $\sim 3.9$  keV to a radius of  $1.5'$  ( $480h_{70}^{-1}$  kpc) and a power law model with an index of  $\gamma = 0.98$  outside this radius. The XMM-Newton temperature in the center is in good agreement with the Chandra measurement which extends to  $1.5'$  in the Chandra observation of CL0024+17, covering the almost isothermal center ( $r < 1.3'$ ) in the XMM-Newton observations. We provide a more extended temperature profile based on the XMM-Newton observations in which the temperature profile decreases in the  $1.3$ – $3'$  region. The strong temperature gradient at large radii makes the gravitational mass lower by a factor of  $\sim 20$ – $25\%$  compared to the isothermal results. We found that the temperature gradient is not a sudden drop at a radius of  $1.3'$  by measuring the temperature in different bin sizes (see Table 7.7). Within a radius of  $3'$  for CL0024+17, we derived a polytropic index of 1.17 for the ICM in the outskirts which is lower than the adiabatic index of  $5/3$ . This implies that the outskirts are still convectively stable. We consider the uncertainty in the mass estimate caused by the temperature gradient by artificially increasing the slope parameter of the temperature distribution by a factor of  $\sim 20\%$ , and find a decrease of the total mass by a factor of  $\sim 10\%$ .

Since the soft band (0.5–2 keV) is not so sensitive to the temperature map as the hard band (2–7.5 keV), the HRM can be used as an indicator of the temperature distribution. Therefore the temperature map can be obtained from the HRM (e.g. Sanders & Fabian 2001; Sanders et al. 2004; Akimoto et al. 2003). The  $HR$  is also a reflection of absorption measure which affects the temperature (e.g. Akimoto et al. 2003). Thus we study the further properties of the features in the HRM by performing a spectral analysis. For the

statistic reason, we extracted the spectra from one of the peaks suggesting high temperature in the HRM at R.A. =  $00^h26^m30^s.9$ , decl. =  $17^\circ09'50''.3$  covering a radius of  $0.33'$ , and obtained a temperature of  $5.8 \pm 1.0$  keV with metallicity fixed to  $0.3 Z_\odot$  and  $5.7 \pm 1.0$  keV with the metallicity free ( $Z = 0.88_{-0.58}^{+0.78} Z_\odot$ ,  $L_X^{\text{bol}} = 0.43 \times 10^{44} h_{70}^{-2}$  erg s $^{-1}$ ). This supports the indication in the HRM of a high temperature region and not an artifact due to metallicity variations. However, the spectra can also be fitted by a power law with an index of  $1.74 \pm 0.14$ , which could then be attributed to some contamination from an AGN. This hot region is located exactly at the position of the substructure described in Czoske et al. (2001, 2002).

### 7.4.3 Complex structure

The Chandra image of the cluster core displays an indication of complex structure. The projection of the counts as a function of radius using the high spatial resolution image from Chandra shows an asymmetric structure and a surface brightness “edge” in the central region. The galaxy alignment in the HST image is perpendicular to the “edge”. Such an asymmetric central structure with an “edge” ( $r < 0.5'$ ) in the XMM-Newton HRM support the idea of a cluster merger.

### 7.4.4 Comparison to lensing measurements

The strongest disagreement between the X-ray mass profiles and the strong lensing results is found in the cluster center. The difference between the X-ray determined mass (Table 7.4) and the strong lensing mass of  $1.59 \pm 0.04 \times 10^{14} h_{70}^{-1} M_\odot$  at the arc radius of  $0.143 h_{70}^{-1}$  Mpc (Broadhurst et al. 2000) and  $2.37 \pm 0.36 \times 10^{14} h_{70}^{-1} M_\odot$  at the arc radius of  $0.153 h_{70}^{-1}$  Mpc (Tyson et al. 1998) is up to a factor of  $\sim 4$ .

This discrepancy is most probably due to the disturbed structure of the cluster center, highlighted by the elongated X-ray iso-surface-brightness contours in the central region. The substructure found in the gravitational lensing mass distribution map by Kneib et al. (2003) is also supported by the X-ray image. The velocity distribution of the galaxies can approximately be explained by a line-of-sight merger of two systems with a mass ratio of the order of 1:2 (Czoske et al. 2001, 2002). Therefore, the application of hydrostatic equilibrium to determine the mass in the central region of the cluster from the gas properties may not be valid.

We observed an elongation in the NW-SE direction in the HRM. The negative residual surface brightness in the cluster center demonstrates that the elongation flattens the surface brightness compared to an azimuthally symmetric structure. The XMM-Newton image analysis shows substructure to the NW of the cluster center which is marked by a galaxy (see Fig. 7.3) in Kneib et al. (2003). This galaxy shows significantly extended X-ray emission compared to the XMM-Newton PSF and has a luminosity of  $L_X^{\text{bol}} = 0.57 \pm 0.06 \times 10^{43} h_{70}^{-2}$  erg s $^{-1}$  and a temperature of  $0.87 \pm 0.13$  keV within  $1'$  at R.A. =  $00^h26^m25^s.8$ , decl. =  $17^\circ12'03''.7$ . Since this high surface brightness region does not have a lower temperature but probably rather has a higher temperature than its surroundings, it does not mark a “cold front” but a high pressure region which coincides with a mass concentration seen in the lensing map. This implies that the second mass peak is included within the

gaseous halo of the cluster and not only seen projected onto the cluster.

### 7.4.5 Comparison to velocity dispersion measurement

The  $M_{200}-\sigma_{\text{DM}}$  relation from simulations in Evrard & Gioia (2002) gives a comparable velocity dispersion of  $848_{-53}^{+51}$  km s<sup>-1</sup> from the HST mass and a relatively low value of the velocity dispersion of  $598_{-31}^{+29}$  km s<sup>-1</sup> using the XMM-Newton mass. Girardi & Mezzetti (2001) obtained a galaxy velocity dispersion of  $911_{-107}^{+81}$  km s<sup>-1</sup> for CL0024+17. The velocity dispersion derived from the XMM-Newton mass is in good agreement with the velocity dispersion measure in Czoske et al. (2002) who found velocity dispersions of  $561_{-83}^{+95}$  and  $554_{-304}^{+175}$  for the central component and foreground component which suggests a line-of-sight merger. If there is a line-of-sight merger, there are almost certainly additional galaxies in the line-of-sight which artificially increase the optical galaxy velocity dispersion if only one component is assumed.

### 7.4.6 X-ray properties

The mass estimates from the  $M-T$  relations in Finoguenov et al. (2001b) and in Bryan & Norman (1998) are  $M_{200} = 5.96 \times 10^{14} h_{70}^{-1} M_{\odot}$  and  $M_{200} = 3.76 \times 10^{14} h_{70}^{-1} M_{\odot}$ , which indicate a higher gravitational mass. We measure a bolometric X-ray luminosity of  $2.9 \pm 0.1 \times 10^{44} h_{70}^{-2}$  erg s<sup>-1</sup>, which is higher than the luminosity of  $1.26 \times 10^{44} h_{70}^{-2}$  erg s<sup>-1</sup> obtained from the  $L-T$  relation in Arnaud & Evrard (1999) which might indicate a merger. The gas mass fraction at  $r_{2500}$  for CL0024+17 agrees with the measurements of Allen et al. (2002) and Pratt & Arnaud (2002). The XMM-Newton measured gas mass fraction of  $0.20 \pm 0.03 h_{70}^{-3/2}$  at  $r_{200}$  for CL0024+17 is higher than the values in Sanderson et al. (2003), Ettori et al. (2002a) and Pratt & Arnaud (2002) for their cluster samples, which is possibly an indication for an underestimated mass beyond  $r_{2500}$  as already noted from the  $M-T$  relation. Thus we suggest that the merger leads to distortions on global scales which reduces the mass for CL0024+17. However, on global scales the effect is smaller than in the cluster center. The relatively small distortion (less than a factor of 2) was found in several simulations (e.g. Evrard et al. 1996; Schindler 1996).

### 7.4.7 Central cooling

CL0024+17 has a bright central galaxy and a compact lensing core. The entropy in the center is a little below the entropy floor value suggested by Lloyd-Davies et al. (2000). However, the cluster almost shows little evidence for a cooling flow or a central temperature decrease which should be found in most cooling flow clusters. This supports the scenario that the cluster center has been disturbed by a recent merger.

## 7.5 Summary and Conclusions

We performed a detailed imaging and spectroscopic study of the XMM-Newton observations of the lensing cluster CL0024+17, and obtained spatially resolved temperature,

metallicity and density distributions. A temperature gradient was observed for the first time in CL0024+17 at large radii ( $1.3' < r < 3'$ ).

The image shows overlapping mass concentrations in the XMM-Newton X-ray data and HST optical data. The substructure which was observed by HST in Kneib et al. (2003) is confirmed in the X-ray data. The HRM shows an elongation in the NW-SE direction on a scale of  $3.3'$ . Further spectroscopy confirms the temperature map suggesting high temperature region with  $k_{\text{B}}T = 5.8 \pm 1.0$  keV. Similar to Sersic 159–03, the observed temperature distribution shows a temperature gradient at  $1.3' < r < 3'$ . The modeling of the temperature distribution yields a polytropic index of 1.17, lower than the adiabatic index of  $\gamma = 5/3$ , which indicates a convectively stable state in the outskirts of CL0024+17.

The cluster does not show a pronounced cooling flow in spite of a dominant central galaxy. Therefore we suggest that a merger in the cluster center ( $< 0.1h_{70}^{-1}$  Mpc) has disrupted any previous cooling flow.

The mass estimate based on the precise measurements of the distributions of the temperature and gas density is lower by a factor of  $\sim 20$ – $25\%$  than the mass obtained under the assumption of isothermality in the outskirts. The NFW model does not fit the X-ray derived mass profile very well in the center ( $r < 0.1h_{70}^{-1}$  Mpc). The extended NFW model fits the data but yields a negative index  $\alpha$ . We attribute this to the disturbance of the core.

The discrepancy remains between the X-ray gravitational mass and optical strong lensing mass at the radii of  $0.143h_{70}^{-1}$  Mpc (Broadhurst et al. 2000) and  $0.153h_{70}^{-1}$  Mpc (Tyson et al. 1998) by a factor of up to 4. The XMM-Newton results are marginally consistent within  $2\sigma$  using the global temperature with the weak lensing measurement in Kneib et al. (2003). CL0024+17 is an example of a cluster for which weak lensing masses and X-ray masses are in acceptable agreement at large radii but for which the strong lensing masses disagree with the X-ray derived values at small radii (also e.g. A1689, Xue & Wu 2002; Dye et al. 2001; Clowe & Schneider 2001).

The XMM-Newton measured parameters for CL0024+17 deviate slightly from the empirical  $M$ – $T$  and  $L$ – $T$  relations. CL0024+17 has a bright central galaxy and a compact lensing core but does not show a significant cooling flow. Similar to A2218 (Girardi et al. 1997; Pratt et al. 2005), the apparent discrepancy between the X-ray and gravitational lensing determined mass of CL0024+17 is most probably due to a line-of-sight merger of two almost comparable subsystems. In addition, filamentary structures could also contribute to the projected mass detected by lensing, but since this mass does not lie within the cluster core, it would not be included in the X-ray mass measurement. The line-of-sight orientation makes it difficult to reveal the merger structure in the X-ray data, but on the other hand it enhances the probability of finding strong lensing features. Thus, the application of hydrostatic equilibrium assumption might break down in the central region. On global scales the agreement becomes better. The galaxy distribution, lensing mass maps, and X-ray data all provide a consistent description of the cluster morphology.

### Acknowledgements

The XMM-Newton project is supported by the Bundesministerium für Bildung und Forschung, Deutsches Zentrum für Luft und Raumfahrt (BMBF/DLR), the Max-Planck Society and the Haidenhaim-Stiftung. We acknowledge Jacqueline Bergeron, PI of the XMM-Newton observation of the CDFS. Y.Y.Z. acknowledges receiving the International Max-Planck Research School Fellowship. W.F. acknowledges support from NASA Grant NAG5-9942 and the Smithsonian Institution. Y.Y.Z. thanks Alexey Vikhlinin, Gabriel Pratt, Kyoko Matsushita, Maxim Markevitch, Keith Arnaud, Xiang-Zhong Zheng, Yas Hashimoto, Takaya Ohashi and Tae Furusho for useful discussions.

## 8 Summary and conclusions

Clusters of galaxies are the largest gravitationally bound systems in the Universe. They are used in a variety of ways to perform both cosmological and astrophysical studies with the aim of a better understanding of cluster structure and mass. The observations taken by XMM-Newton (with high spectral resolution, large effective area, and large field of view) and Chandra (with high spatial resolution) provide for the first time advanced diagnostics to investigate the detailed structure of the intracluster medium (ICM) in galaxy clusters. The new results not only broaden the knowledge of the scaling relations, correlations, and their intrinsic scatter for massive, distant galaxy clusters, but also provide a better understanding of the complexity of galaxy clusters.

### 8.1 Summary of the REFLEX-DXL sample

A flux-limited and almost volume-complete sample of 14 galaxy clusters at redshift  $z \sim 0.3$ , the REFLEX-DXL sample, has been observed by XMM-Newton. Reliable procedures have been developed and tested to conduct this sample. In this work, a systematic analysis has been performed to measure the X-ray observables based on the XMM-Newton observations, and to investigate the scaling relations and correlations of various X-ray properties of the REFLEX-DXL cluster sample. The results are summarized as follows.

#### 8.1.1 Mass and gas mass fraction

- The mass has been precisely measured using the precise ICM density and temperature distributions. The uncertainty is within 25% up to  $r_{500}$ , on average.
- The gas mass fraction can be used as a type of “standard candle” (e.g. White et al. 1993; Pen 1997). The gas mass fractions of the REFLEX-DXL clusters are in the narrow range of 0.06–0.15. The gas mass fractions of the REFLEX-DXL sample show the least scatter at  $r_{2500}$ . The average value of the gas mass fraction at  $r_{200}$  is  $0.11 \pm 0.08$ . The REFLEX-DXL clusters at  $z \sim 0.3$  have similar gas mass fractions as found for the nearby samples (e.g. Allen et al. 2004) and more distant samples (e.g. Vikhlinin et al. 2002; Ettori et al. 2003)

#### 8.1.2 Self-similar behavior of the X-ray properties at $r > 0.1r_{\text{vir}}$

- The average temperature profile of the REFLEX-DXL clusters, which is based on the XMM-Newton observations, agrees with the previous studies (e.g. Markevitch et al. 1998;

## 8 Summary and conclusions

---

De Grandi & Molendi 2002; Vikhlinin et al. 2005a; Piffaretti et al. 2005) within the observational dispersion. Independently, Borgani et al. (2004) reproduced a similar temperature profile in their simulations. The average temperature profile for the REFLEX-DXL sample shows a constant value for the non-cooling core clusters (NCCCs), but with an increasing distribution for the (cooling core clusters) CCCs up to  $0.3r_{\text{vir}}$ . A mild decrease has been observed at  $r > 0.3r_{\text{vir}}$  for most REFLEX-DXL clusters. No cool gas has been observed showing a central temperature lower than half of the mean temperature.

- The XMM-Newton surface brightness profiles of the REFLEX-DXL clusters have been pushed up to  $r_{500}$ . The profiles are steeper than generally obtained for  $\beta$ -models with  $\beta \sim 2/3$ . The surface brightness profiles of a NCCC shows a flat core. It can be described by a  $\beta$ -model. The surface brightness profile of a CCC shows an excess in the cluster center, which accounts for about 11–33% of the cluster luminosities. It can be fitted either by a double  $\beta$ -model or by a model based on an extended Navarro-Frenk-White (NFW) dark matter halo model (e.g. Navarro et al. 2004). There is no well-defined constant central density down to the resolution limit of XMM-Newton for the CCCs. However, the surface brightness profiles are self-similar at  $r > 0.1r_{\text{vir}}$  for the REFLEX-DXL sample.

- After the redshift evolution correction, the entropies at  $0.1r_{200}$  and entropy profiles for the REFLEX-DXL clusters are consistent with those for the nearby clusters in Ponman et al. (2003). The entropies at  $0.1r_{200}$  for the REFLEX-DXL sample agree with the scaling,  $\propto T^{0.65}$ . The entropy profiles at  $r > 0.1r_{\text{vir}}$  show a similar slope as observed in Ettori et al. (2002b),  $S \propto r^{0.97}$ . However, this is slightly shallower than the predicted slope from a spherical accretion shock model,  $S \propto r^{1.1}$  (e.g. Tozzi & Norman 2001; Kay 2004). Merger clusters show higher central entropies. The relatively relaxed clusters show lower central entropies. The central entropy has been used to divide the REFLEX-DXL sample into two subsamples, the CCC ( $< 100 \text{ keV cm}^2$ ) and NCCC ( $\geq 100 \text{ keV cm}^2$ ) subsamples. The observational deviation from the  $S$ - $T$  relation for the individual cluster can be used to distinguish the relaxation stage.

- A self-similar gravitational mass distribution has been found for the REFLEX-DXL sample. The gas density and temperature profiles provide an excellent diagnostics of the cluster structure and yield precise determinations of the mass and gas mass fraction. In the outskirts, the generally adopted  $\beta$ -model ( $\beta \sim 2/3$ ) gives  $\rho(r) \propto r^{-2}$  and the extended NFW model gives  $\rho(r) \propto r^{-3}$ . The observational density provides an average of  $\rho(r) \propto r^{-2.42}$  for the REFLEX-DXL sample. The  $\beta$ -model and the extended NFW model give systematically different slopes of the mass distributions.

- A deviation around the self-similar model has been observed in the central region. This reveals some physical processes rather than simply being statistical fluctuations in the measurements (Zhang et al. 2004b, 2005b; Finoguenov et al. 2005). Many studies (e.g. Markevitch et al. 2002; Randall et al. 2002; Finoguenov et al. 2005) show that the X-ray property estimated in the center can be biased by phenomena such as ghost cavities, bubbles, shock, cold fronts and cooling cores, that may somehow invalidate the hydrostatic equilibrium hypothesis. Complex dynamical interactions with AGN activities have



been indicated by the coincidence of CCCs and radio sources (e.g. Clarke et al. 2005). RXCJ0658.5–5556 provides an example to test the effect of merger boosts on the X-ray luminosity and also multi-temperature structures (Matsushita et al. 2002).

- The REFLEX-DXL sample shows an almost universal metallicity profile. An average metallicity,  $0.23 \pm 0.07 Z_{\odot}$ , has been derived for the whole sample with  $0.27 \pm 0.07 Z_{\odot}$  and  $0.22 \pm 0.08 Z_{\odot}$  for the CCCs and NCCCs, respectively. The results confirm previous studies and reveal that massive clusters show a universal metallicity profile (e.g. De Grandi et al. 2004). No significant evolution up to  $z \sim 0.3$  was found in metallicity comparing the REFLEX-DXL sample to nearby and distant samples of galaxy clusters. This is consistent with the results in Tozzi et al. (2003) that there is no evolution of the iron abundance up to  $z \sim 1.1$ .

### 8.1.3 Correlations of the cluster properties

- The results in this work confirm the previous studies of correlations (e.g.  $L-T$ ,  $L-M$ ,  $M-T$ , and  $M_{\text{gas}}-T$ ) in observations (e.g. Reiprich & Böhringer 2002) and simulations (e.g. Borgani et al. 2004). Since the cluster temperatures of the REFLEX-DXL sample are in a narrow temperature range, the whole sample provides a unique means to constrain the normalization with a higher accuracy.

- The CCCs and NCCCs give different normalizations in the correlations. For example, for the  $M_{500}-T$  relation, the value from the best power law fit is  $10^{13.61 \pm 0.07} M_{\odot}$  ( $10^{13.46 \pm 0.03} M_{\odot}$ ) for the CCCs (NCCCs), which is 2% higher (28% lower) than the value derived for the whole sample. The normalizations of the correlations are dependent on the variety in the cluster morphologies.

- The intrinsic scatter of the main correlations which, for example, gives  $(0.30 | 0.17)$  for  $(M | T)$  in the  $M-T$  relation, confirms the recent studies in observations (e.g. Reiprich & Böhringer 2002) and simulations (e.g. Stanek et al. 2005).

- No deviation in the correlations such as  $L-T$ ,  $L-M$ ,  $M-T$  and  $M_{\text{gas}}-T$  has been found comparing the REFLEX-DXL sample to the nearby samples. Therefore the results in this work confirm the general conclusion (e.g. Maughan et al. 2003; Vikhlinin et al. 2005a) that the evolution of galaxy clusters up to  $z \sim 1.2$  is well described by a self-similar model in the scenarios of hierarchical structure formation for massive clusters ( $> 5$  keV).

## 8.2 Summary of CL0024+17

For the lensing cluster CL0024+17 at redshift  $z = 0.395$ , the X-ray measured gravitational mass marginally agrees with the weak lensing results. However, the strong lensing measurements give larger values than the X-ray results at the lensing arc radii. The spatially resolved X-ray images and 2-dimensional hardness ratio maps show that this disagreement is most probably due to the complex merger with a long filament along the line-of-sight. The results are summarized as follows.

### 8.2.1 X-ray properties of CL0024+17

- The image shows overlapping mass concentrations in the XMM-Newton X-ray data and HST optical data. The substructure observed by HST in Kneib et al. (2003) is confirmed in the X-ray hardness ratio map showing an elongation in the northwest-southeast direction on a scale of  $3.3'$ . Further spectroscopy of this region confirms the temperature map suggesting a high temperature region with  $k_{\text{B}}T = 5.8 \pm 1.0$  keV. Similar to Sersic 159–03, the observed temperature distribution shows a temperature gradient at  $1.3' < r < 3'$ . The modeling of the temperature distribution yields a polytropic index of 1.17, lower than the adiabatic index of  $\gamma = 5/3$ . This indicates a convectively stable state in the outskirts of CL0024+17.
- CL0024+17 does not show a pronounced cooling flow in spite of a dominant central galaxy. Therefore we suggest that a merger in the cluster center ( $< 0.1h_{70}^{-1}$  Mpc) has disrupted any previous cooling flow.

### 8.2.2 Mass estimates and the discrepancy

- The mass estimate based on the precise measurements of the distributions of the temperature and gas density is lower by a factor of  $\sim 20$ –25% than the mass obtained under the assumption of isothermality in the outskirts. The NFW model does not fit the X-ray derived mass profile very well in the center ( $r < 0.1h_{70}^{-1}$  Mpc). The extended NFW model fits the data but yields a negative index ( $\alpha < 0$ ). This is most probably due to the disturbance of the core.
- The discrepancy remains between the X-ray gravitational mass and optical strong lensing mass at the arc radii ( $0.143h_{70}^{-1}$  Mpc and  $0.153h_{70}^{-1}$  Mpc) by a factor of up to 4. The XMM-Newton results are marginally consistent within  $2\sigma$  with the weak lensing measurement in Kneib et al. (2003). CL0024+17 is an example of a cluster for which weak lensing masses and X-ray masses are in acceptable agreement at large radii but for which the strong lensing masses disagree with the X-ray derived values at small radii (also e.g. A1689, Xue & Wu 2002; Dye et al. 2001; Clowe & Schneider 2001).
- The XMM-Newton measured parameters for CL0024+17 deviate slightly from the empirical  $M$ – $T$  and  $L$ – $T$  relations. CL0024+17 has a bright central galaxy and a compact lensing core but does not show a significant cooling flow. Similar to A2218 (Girardi et al. 1997; Pratt et al. 2005), the apparent discrepancy between the X-ray and gravitational lensing determined mass for CL0024+17 is most probably due to a line-of-sight merger of two almost mass comparable subsystems. In addition, filamentary structures could contribute to the projected mass detected by lensing, but since this mass does not lie within the cluster core, it would not be included in the X-ray mass measurement. The line-of-sight orientation makes it difficult to reveal the merger structure in the X-ray data, but on the other hand it enhances the probability of finding strong lensing features. The application of the hydrostatic equilibrium assumption might break down in the central region. On global scales the agreement becomes better. The galaxy distribution, lensing mass maps, and X-ray data all provide a consistent description of the cluster morphology.

### 8.3 Conclusions and future prospective

A complete diagnostics, the double background subtraction method, has been developed for a systematic study of the sample. This technique has been cross-calibrated using the high quality observations of XMM-Newton and Chandra (Zhang et al. 2005a). It provides an accurate cluster temperature measure and thus mass estimate at large radii (Zhang et al. 2005c).

This work is mainly based on the high quality data of a well defined, unbiased sample, the REFLEX-DXL sample (a flux-limited and almost volume-complete sample), observed by XMM-Newton. This sample provides a new insight into the scaling relations and their uncertainties based on the precise measure of the cluster structure. The results fit into the general picture that galaxy clusters are self-similar up to redshift  $z \sim 1.2$  excluding the cooling cores. However, the results in this work also illustrate that galaxy clusters are not completely self-similar by, e.g. the steep slope of the  $L-T$  relation. A combination of the high quality observations with simulations and theories would be the only choice to a comprehensive understanding of cluster formation and evolution in the Universe.

The average gas mass fraction (Zhang et al. 2005c) and the preliminary temperature function (Böhringer et al. 2005a, Fig. 8.1) of the REFLEX-DXL sample is in good agreement with the prediction of a low matter density universe. The REFLEX-DXL sample, as a well-defined, unbiased sample at medium redshifts, can be combined with other samples at different redshift bins (e.g. “XMM-Newton Legacy-Type Program for the Study of Galaxy Cluster Structure”, XMM-LP, PI: Hans Böhringer) to study the evolutionary effect in galaxy clusters.

The uncertainty of the temperature determination in the cluster outskirts is very high (50–100%) for the merging clusters in the REFLEX-DXL sample. Four merging clusters in the REFLEX-DXL sample were observed by Chandra with higher spatial resolution, better point-spread function and longer exposure time. The analysis of these data which is in progress will provide an improvement on the accuracy of the observed X-ray parameters such as temperature. Since the uncertainty in the mass determination is dominated by the uncertainty in the temperature measure, a deeper exposure allows a reduced uncertainty in the derived mass and thus enables a better understanding of the systematic errors and intrinsic scatter in the mass–observable relations.

A joint analysis based on the multi-wavelength observations will be performed as an extension of this work. All of the REFLEX-DXL clusters were observed by ESO/MPIA WFI in multi-colors. RXCJ0232.2–4420 and RXCJ0307.0–2840 were observed by ESO-NTT in two colors (V, I). Seven clusters were observed by ESO-VLT-VIMOS. The combined analysis of the optical and X-ray observations will shed light on (i) the relation between the X-ray and optical cluster properties, (ii) the determination of the mass-to-light ratio, (iii) the substructure and dynamical state, (iv) the relation of the heavy element abundance distribution with respect to the gas and galaxy density distributions, and (v) the nature of the galaxy distribution in colors and spectra as a function of the galaxy cluster environment.

XMM-Newton and Chandra with their advanced imaging spectroscopic capability bring X-ray astrophysics of galaxy clusters to a stage of precision. A comprehensive knowledge of the self-similar behavior of galaxy clusters makes them ideal objects to study structure formation and evolution and to constrain cosmological parameters. A close look at the

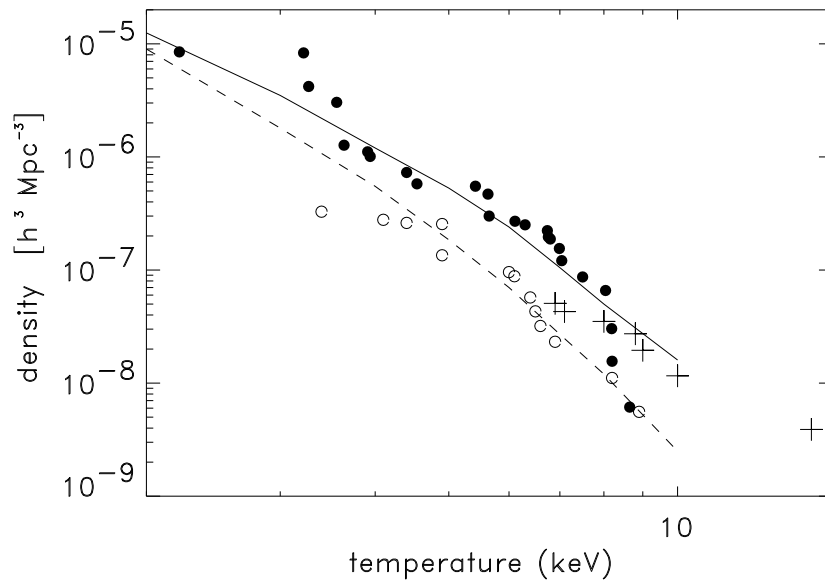


**Figure 8.1:** Preliminary temperature function of the REFLEX-DXL sample using 7 REFLEX-DXL clusters (cross) in Böhringer et al. (2005a). The samples at  $z \sim 0.05$  (open circle) and  $z \sim 0.32$  (filled circle) in Henry (1997) are shown for comparison.

complexity in galaxy clusters opens an interesting field to study the astrophysics. The next generation X-ray observatories, e.g. Constellation-X and XEUS, are particularly powerful to bring a continuous success of X-ray studies of galaxy clusters.

# Bibliography

- Akimoto, F., Kondou, K., Furuzawa, A., Tawara, Y., & Yamashita, K. 2003, *ApJ*, 596, 170
- Akritas, M. G., & Bershadsky, M. A. 1996, *ApJ*, 470, 706
- Allen, S. W., & Fabian, A. C. 1998, *MNRAS*, 297, L63
- Allen, S. W., Schmidt, R. W., & Fabian, A. C. 2002, *MNRAS*, 334, L11
- Allen, S. W., Schmidt, R. W., Fabian, A. C., & Ebeling, H. 2003, *MNRAS*, 334, 43
- Allen, S. W., Schmidt, R. W., Ebeling, H., Fabian, A. C., & van Speybroeck, L. 2004, *MNRAS*, 353, 457
- Anders, E., & Grevesse, N. 1989, *Geochimica et Cosmochimica Acta*, 53, 197
- Andersson, K. E., & Madejski, G. M. 2004, *ApJ*, 607, 190
- Andreani, P., Böhringer, H., dall'Oglio, G., et al. 1999, *ApJ*, 513, 23
- Arnaud, M., & Rothenflug, M. 1985, *A&AS*, 60, 425
- Arnaud, M., & Raymond, J. 1992, *ApJ*, 398, 394
- Arnaud, M., & Evrard, A. E. 1999, *MNRAS*, 305, 631
- Arnaud, M., Aghanim, N., & Neumann, M. 2002a, *A&A*, 389, 1
- Arnaud, M., Majerowicz, S., Lumb, D., et al. 2002b, *A&A*, 390, 27
- Bahcall, N. A. 1999, *Formation of Structure in the Universe*, eds. J. P. Ostriker & A. Dekel, Cambridge Univ. Press, p135
- Bahcall, N. A., Dong, F., Bode, P., et al. 2003, *ApJ*, 585, 182
- Bailey, M. E. 1982, *MNRAS*, 201, 271
- Bardeen, J., Bond, J. R., Kaiser, N., Szalay, A., S. 1986, *ApJ*, 304, 15
- Bartelmann, M., Dolag, K., Perrotta, F., et al. 2005, *New Astronomy Reviews*, 49, 199
- Benitez, N., Broadhurst, T. J., Ford, H., et al. 2002, *AAS*, 201, 8006
- Bennett, C. L., Halpern, G. R., Hinshaw, G., et al. 2003, *ApJS*, 148, 1

## Bibliography

---

- Böhringer, H., Soucail, G., Mellier, Y., Ikebe, Y., & Schuecker, P. 2000, A&A, 353, 124
- Böhringer, H., Schuecker, P., Guzzo, L., et al. 2001a, A&A, 369, 826
- Böhringer, H., Belsole, E., Kennea, J., et al. 2001b, A&A, 365, L181
- Böhringer, H., Schuecker, P., Lynam, P., et al. 2001c, Msngr, 106, 24
- Böhringer, H., Collins, C. A., Guzzo, L., et al. 2002a, ApJ, 566, 93
- Böhringer, H., Matsushita, K., Churazov, E., Ikebe, Y. & Chen, Y. 2002b, A&A, 382, 804
- Böhringer, H., Schuecker, P., Guzzo, L., et al. 2004a, A&A, 425, 367
- Böhringer, H., Matsushita, K., Churazov, E., Finoguenov, A., & Ikebe, Y. 2004b, A&A, 416, L21
- Böhringer, H., Schuecker, P., Zhang, Y.-Y., et al. 2005a, A&A, in press (Paper I)
- Böhringer, H., Burwitz, V., Zhang, Y.-Y., et al. 2005b, ApJ, 633, 148
- Bond, J. R., Kaiser, N., Cole, S., & Efstathiou, G. 1991, ApJ, 379, 440
- Bonnet, H., Mellier, Y., & Fort, B. 1994, ApJ, 427, L83
- Borgani, S., Rosati, P., Tozzi, P., et al. 2001, ApJ, 561, 13
- Borgani, S. 2004, Proc. *The Riddle of Cooling Flows in Galaxies and Clusters of Galaxies: E4.*, eds. T. H. Reiprich, J. C. Kempner, & N. Soker, in press
- Borgani, S., Murante, G., Springel, V., et al. 2004, MNRAS, 348, 1078
- Briel, U. G., Finoguenov, A., & Henry, J. P. 2004, A&A, 426, 1
- Broadhurst, T., Huang, X., Frye, B., & Ellis, R. 2000, ApJ, 534, L15
- Bryan, G. L., & Norman, M. L. 1998, ApJ, 495, 80
- Burkert, A. 1995, ApJ, 447, L25
- Burkert, A. 2000, ApJ, 534, L143
- Burles, S., Nollett, K. M., & Turner, M. S. 2001, ApJ, 552, L1
- Butcher, H., & Oemler, A. 1978, ApJ, 219, 18
- Carroll, S. M., Press, W. H., & Turner, E. L. 1992, ARA&A, 30, 499
- Castillo-Morales, A., & Schindler, S. 2003, Proc. *Frontier Objects in Astrophysics and Particle Physics*, ed. F. Giovannelli, in press, astro-ph/0303609
- Cavaliere, A., & Fusco-Femiano, R. 1976, A&A, 49, 137
- Chen, G. & Ratra, B. 2004, ApJ, 612, L1

- Chen, Y., Ikebe, Y., & Böhringer, H. 2003, *A&A*, 407, 41
- Cheng, L.-M., & Wu, X.-P. 2001, *A&A*, 372, 381
- Clarke, T. E., Sarazin, C. L., Blanton, E. L., Neumann, D. M., & Kassim, N. E. 2005, *ApJ*, in press, astro-ph/0503274
- Clowe, D., & Schneider, P. 2001, *A&A*, 379, 384
- Coia, D., McBreen, B., Metcalfe, et al. 2003, *A&A*, in press, astro-ph/0310317
- Colafrancesco, S. 2003, *Proc. The Frontiers of Cosmology*, eds. A. Blanchard, & M. Signore, p75
- Colley, W. N., Tyson, J. A., & Turner, E. L. 1996, *ApJ*, 461, L83
- Cypriano, E. S., Sodr e Jr. L., Kneib, J.-P., & Campusano, L. E. 2004, *ApJ*, 613, 95
- Czoske, O., Kneib, J.-P., Soucail, G., et al. 2001, *A&A*, 372, 391
- Czoske, O., Moore, B., Kneib, J.-P., & Soucail, G. 2002, *A&A*, 386, 31
- Davis, M., Geller, M. J., & Huchra, J. 1978, *ApJ*, 221, 1
- De Grandi, S., & Molendi, S. 2002, *ApJ*, 567, 163
- De Grandi, S., Ettori, S., Longhetti, M., & Molendi, S. 2004, *A&A*, 419, 7
- De Luca, A. & Molendi, S. 2001, in *Symp. New Visions of the X-ray Universe in the XMM-Newton and Chandra Era* (Noordwijk: ESA), in press
- De Luca, A., & Molendi, S. 2004, *A&A*, 419, 837
- Dickey, J. M., & Lockman, F. J. 1990, *ARA&A*, 28, 215
- Diemand, J., Moore, B., & Stadel, J. 2004, *MNRAS* 353, 624
- Dressler, A., & Gunn, J. E. 1982, *ApJ*, 263, 533
- Dressler, A., Gunn, J. E., & Schneider, D. P. 1985, *ApJ*, 294, 70
- Dye, S., Taylor, A. N., Thommes, E. M., et al. 2001, *MNRAS*, 321, 685
- Edge, A. C., & Stewart, G. C. 1991, *MNRAS*, 252, 414
- Eisenstein, D. J., & Hu, W. 1998, *ApJ*, 496, 605
- Eke, V. R., Navarro, J. F., & Frenk, C. S. 1998, *ApJ*, 503,569
- Ettori, S., De Grandi, S., & Molendi, S. 2002a, *A&A*, 391, 841
- Ettori, S., Fabian, A. C., Allen, S. W., & Johnstone, R. M. 2002b, *MNRAS*, 331, 635
- Ettori, S., Tozzi, P., & Rosati, P. 2003, *A&A*, 398, 879

## Bibliography

---

- Ettori, S., Tozzi, P., Borgani, S., & Rosati, P. 2004, *A&A*, 417, 13
- Evrard, A. E., Metzler, C. A., & Navarro, J. F. 1996, *ApJ*, 469, 494
- Evrard, A. E. 1997, *MNRAS*, 292, 289
- Evrard, A. E., & Gioia, I. M. 2002, *Merging Processes in Galaxy Clusters*, eds. L. Feretti, I.M. Gioia, & G. Giovannini, p253
- Fabian, A. C., & Nulsen, P. E. J. 1977, *MNRAS*, 180, 479
- Fabian, A. C., Hu, E. M., Cowie, L. L., & Grindlay, J. 1981, *ApJ*, 248, 47
- Fabian, A. C., Sanders, J. S., Allen, S. W., et al. 2003, *MNRAS*, 344, L43
- Fabricant, D., Lecar, M., & Gorenstein, P. 1980, *ApJ*, 241, 552
- Feigelson, E. D., & Babu, G. J. 1992, *ApJ*, 397, 55
- Feretti, L., & Venturi, T. 2002, *Proc. Merging processes of galaxy clusters*, eds. L. Feretti, I. M. Gioia, & G. Giovannini, p109
- Finoguenov, A., Arnaud, M., & David, L. P. 2001a, *ApJ*, 555, 191
- Finoguenov, A., Reiprich, T. H., & Böhringer, H. 2001b, *A&A*, 368, 749
- Finoguenov, A., Jones, C., Böhringer, H., & Ponman, T. J. 2002, *ApJ*, 578, 74
- Finoguenov, A., Briel, U. G., & Henry, J. P. 2003, *A&A*, 410, 777
- Finoguenov, A., Böhringer, H., Zhang, Y.-Y., et al. 2005, *A&A*, 442, 827
- Forman, W., & Jones, C. 1991, *Proc. Clusters and Superclusters of Galaxies*, eds. M.M. Colless, A. Babul, A.C. Edge, R.M. Johnstone, & S. Raychaudhury, p113
- Forman, W. 2003, *Proc. The Frontiers of Cosmology*, eds. A. Blanchard, & M. Signore, p23
- Forman, W., churazov, E., David, L., et al. 2003, *Proc. ASP Conference Series, IAU Symposium 214*, in press, astro-ph/0301476
- Freedman, W. L., Madore, B. F., Gibson, B. K., et al. 2001, *ApJ*, 553, 47
- Freyberg, M. J., Pfeffermann, E., & Briel, U. G. 2001, in *Symp. New Visions of the X-ray Universe in the XMM-Newton and Chandra Era* (Noordwijk: ESA), in press
- Fukazawa, Y., Makishima, K., Tamura, T., et al. 2000, *MNRAS*, 313, 21
- Fukazawa, Y., Kawano, N., & Kawashima, K. 2004, *ApJ*, 606, L109
- Fusco-Femiano, R., dal Fiume, D., Feretti, L., et al. 1999, *ApJ*, 513, L21
- Garnett, D. R. 2002, *ApJ*, 581, 1019



- Ghizzardi, S. 2001, In-flight calibration of the PSF for the MOS1 and MOS2 cameras, EPIC-MCT-TN-011 (Internal report)
- Girardi, M., Fadda, D., Escalera, E., et al. 1997, ApJ, 490, 56
- Girardi, M., Giuricin, G., Mardirossian, F., Mezzetti, M., & Boschin, W. 1998, ApJ, 505, 74
- Girardi, M., & Mezzetti, M. 2001, ApJ, 548, 79
- Governato, F., Babul, A., Quinn, T., et al. 1999, MNRAS, 307, 949
- Gunn, J. E., & Oke, J. B., 1975, ApJ, 195, 255
- Haiman, Z., Allen, S., Bahcall, N., et al. 2005, White paper submitted to the Dark Energy Task Force, astro-ph/0507013
- Hansen, F. K., Banday, A. J., & Gorski, K. M. 2004, MNRAS, 354, 641
- Henriksen, M. J., & Mushotzky, R. F. 1986, ApJ, 302, 287
- Henry, J. P., & Arnaud, K. A. 1991, ApJ, 372, 410
- Henry, J. P. 1997, ApJ, 489, L1
- Henry, J. P. 2004, ApJ, 609, 603
- Hernquist, L. 1990, ApJ, 356, 359
- Horner, D. J. 2001, Ph.D. thesis, *X-ray Scaling Laws for Galaxy Clusters and Groups*
- Hu, W., & Sugiyama, N. 1996, ApJ, 471, 542
- Humason, M. L., & Sandage, A., 1957, in Carnegie Yearbook 1956, p61
- Ikebe, Y., Reiprich, T. H., & Böhringer, H. 2002, A&A, 383, 773
- Ikebe, Y., Böhringer, H., & Kitayama, T. 2004, ApJ, 611, 175
- Isobe, T., Feigelson, E. D., Akritas, M. G., & Babu, G. J. 1990, ApJ, 364, 104
- Jeans, J. H. 1902, Phil. Trans. R. Soc. Lond. A, 199, 1
- Jeltema, T. E., Canizares, C. R., Bautz, M. W., & Buote, D. A. 2005, ApJ, in press, astro-ph/0501360
- Jenkins, A., Frenk, C. S., White, S. D. M., et al. 2001, MNRAS, 321, 372
- Jing, Y.-P. 2000, ApJ, 535, 30
- Jones, C., & Forman, W. 1984, ApJ, 276, 38
- Kaastra, J. S. 1992, An X-Ray Spectral Code for Optically Thin Plasmas, Internal SRON-Leiden Report, updated version 2.0

## Bibliography

---

- Kaastra J. S., Ferrigno, C., Tamura, T., et al. 2001, A&A, 365, L99
- Kaiser, N. 1986, MNRAS, 222,323
- Kaiser, N. 1991, ApJ, 383, 104
- Kassiola, A., Kovner, I., & Fort, B. 1992, ApJ, 400, 41
- Kassiola, A., Kovner, I., Fort, B., & Mellier, Y. 1994, ApJ, 429, L9
- Kay, S. T. 2004, MNRAS, 347, L13
- Kay, S. T., Thomas, P. A., Jenkins, A., & Pearce, F. R. 2004, MNRAS, 355, 1091
- Kempner, J. C., & David, L. P. 2004, MNRAS, 349, 385
- Kneib, J.-P., Hudelot, P., Ellis, R. S., et al. 2003, ApJ, 598, 804
- Kobayashi, C. 2004, MNRAS, 347, 740
- Koo, D. C. 1988, *Large-Scale Motions in the Universe*, eds. V. G. Rubin, & G. V. Gayne, Princeton Univ. Press, p513
- Kotov, O., & Vikhlinin, A. 2005, ApJ, in press, astro-ph/0504233
- Kravtsov, A. V., Nagai, D., & Vikhlinin, A., 2005, ApJ, in press, astro-ph/0501227
- Kriss, G. A., Cioffi, D. F., & Canizares, C. R. 1983, ApJ, 272, 439
- Lemonon, L., Pierre, M., Hunstead, R., et al. 1997, A&A, 326, 34
- Liedahl, D. A., Osterheld, A. L., & Goldstein, W. H. 1995, ApJ, 438, L115
- Lloyd-Davies, E. J., Ponman, T. J., & Cannon, D. B. 2000, MNRAS, 315, 689
- Lumb, D. H., Warwick, R. S., Page, M., & De Luca, A. 2002, A&A, 389, 93
- Makino, N., Sasaki, S., & Suto, Y. 1998, ApJ, 497, 555
- Markevitch, M., Forman, W. R., Sarazin, C. L., & Vikhlinin, A. 1998, ApJ, 503, 77
- Markevitch, M. 1998, ApJ, 504, 27
- Markevitch, M., Gonzalez, A. H., David, L., et al. 2002, ApJ, 567, L27
- Markevitch, M., Gonzalez, A. H., Clowe, D., et al. 2004, ApJ, 606, 819
- Matsushita, K., Belsole, E., Finoguenov, A., & Böhringer, H. 2002, A&A, 386, 77
- Maughan, B. J., Jones, L. R., Ebeling, H., et al. 2003, ApJ, 587, 589
- Mellier, Y., Fort, B., Soucail, G., Mathez, G., & Cailloux, M. 1991, ApJ, 380, 334
- Mewe, R., Gronenschild, E. H. B. M., & van den Oord, G. H. J. 1985, A&AS, 62, 197

- Mewe, R., Lemen, J. R., & van den Oord, G. H. J. 1986, *A&AS*, 65, 511
- Mohr, J., Evrard, A., Fabricant, D. & Geller, M. 1995, *ApJ*, 447, 8
- Mohr, J. J., Mathiesen, B., & Evrard, A. E. 1999, *ApJ*, 517, 627
- Molendi, S., & De Grandi, S. 1999, *A&A*, 351, L41
- Moore, B., Ghigna, S., Governato, F., et al. 1999, *ApJ*, 524, 19
- Morris, R. G., & Fabian, A. C. 2005, *MNRAS*, 358, 585
- Mushotzky, R. F. & Loewenstein, M. 1997, *ApJ*, 481, L63
- Mushotzky, R. F. & Scharf, C. A. 1997, *ApJ*, 482, L13
- Navarro, J. F., Frenk, C. S., & White, S. D. M. 1996, *ApJ*, 462, 563
- Navarro, J. F., Frenk, C. S., & White, S. D. M. 1997, *ApJ*, 490, 493
- Navarro, J. F., Hayashi, E., Power, C., et al. 2004, *MNRAS*, 349, 1039 (ext-NFW)
- Neumann, D., & Arnaud, M. 2001, *A&A*, 373, L33
- Nevalainen, J., Markevitch, M., & Forman, W. 2000, *ApJ*, 532, 694
- Nevalainen, J., Lieu, R., Bonamente, M., & Lumb, D. 2003, *ApJ*, 584, 716
- Oguri, M., Takada, M., Umetsu, K., & Broadhurst, T. 2005, *ApJ*, in press
- Ota, N., Pointecouteau, E., Hattori, M., & Mitsuda, K. 2004, *ApJ*, 601, 120
- Ota, N. & Mitsuda, K. 2005, *A&A*, 428, 757
- Padmanabhan, T. 1993, *Structure Formation in the Universe*, Cambridge Univ. Press
- Peebles, P. J. E. 1980, *The large Scale Structure of the Universe*, Princeton Univ. Press
- Pen, U.-L. 1997, *New Astronomy*, 2, 309
- Peterson, J. R., Paerels, F. B. S., Kaastra, J. S., et al. 2001, *A&A*, 365, L104
- Pierpaoli, E., Scott, D., & White, M. 2001, *MNRAS*, 325, 77
- Pierpaoli, E., Borgani, S., Scott, D., & White, M. 2003, *MNRAS*, 342, L63
- Piffaretti, R., Jetzer, Ph., Kaastra, J. S., & Tamura, T. 2005, *A&A*, 433, 101
- Pizzolato, F., Molendi, S., Ghizzardi, S., & De Grandi, S. 2003, *ApJ*, 592, 62
- Pointecouteau, E., Arnaud, M., Kaastra, J., & de Plaa, J. 2004, *A&A*, 423, 33
- Ponman, T. J., Cannon, D. B., & Navarro, J. F. 1999, *Natur*, 397, 135

## Bibliography

---

- Ponman, T. J., Sanderson, A. J. R., & Finoguenov, A. 2003, MNRAS, 343, 331
- Popesso, P., Biviano, A., Böhringer, H., Romaniello, M., & Voges, W. 2005, A&A, 433, 431
- Pratt, G. W., & Arnaud, M. 2002, A&A, 394, 375
- Pratt, G. W., & Arnaud, M. 2005, A&A, 429, 791
- Pratt, G. W., Böhringer, H., & Finoguenov, A. 2005, A&A, 433, 777
- Press, W. H., & Schechter, P. 1974, ApJ, 187, 425
- Randall, S. W., Sarazin, C. L., & Ricker, P. M. 2002, AAS, 201, 6706
- Read, A. M. 2002, preprint, astro-ph/0212436
- Read, A. M., & Ponman, T. J. 2003, A&A, 409, 395
- Reed, D., Gardner, J., Quinn, T., et al. 2003, MNRAS, 346, 565
- Reiprich, T. H. 2001, Ph.D. thesis, *Cosmological Implications and Physical Properties of an X-Ray Flux-Limited Sample of Galaxy Cluster*
- Reiprich, T. H., & Böhringer, H. 2002, ApJ, 567, 716
- Rosati, P., della Ceca, R., Norman, C., & Giacconi, R. 1998, ApJ, 492, L21
- Rosati, P., Tozzi, P., Giacconi, R., et al. 2002, ApJ, 566, 667
- Rowley, D. R., Thomas, P. A., & Kay, S. T. 2004, MNRAS, 352, 508
- Sanders, J. S., & Fabian, A. C. 2001, MNRAS, 325, 178
- Sanders, J. S., Fabian, A. C., Allen, S. W., & Schmidt, R. W. 2004, MNRAS, 349, 952
- Sanderson, A. J. R., Ponman, T. J., Finoguenov, A., Lloyd-Davies, E. J., & Markevitch, M. 2003, MNRAS, 340, 989
- Sarazin, C. L. 1988, *X-ray Emission from Clusters of Galaxies*, Cambridge Univ. Press
- Schindler, S., & Mueller, E. 1993, A&A, 272, 137
- Schindler, S. 1996, A&A, 305, 756
- Schneider, D. P., Dressler, A., & Gunn, J. E. 1986, AJ, 92, 523
- Schuecker, P., Böhringer, H., Reiprich, T. H., & Feretti, L. 2001, A&A, 378, 408
- Schuecker, P., Böhringer, H., Collins, C. A., & Guzzo, L. 2003, A&A, 398, 867
- Schuecker, P. 2005, Proc. *From Cosmological Structures to the Milky Way*, ed. S. Roeser, in press, astro-ph/0502234

- Seljak, U., & Zaldarriaga, M. 1996, *ApJ*, 469, 437
- Serio, S., Peres, G., Vaiana, G. S., Golub, L., & Rosner, R. 1981, *ApJ*, 243, 288
- Shapiro, P. R., & Iliev, I. T. 2000, *ApJ*, 542, L1
- Sheth, R. K., & Tormen, G. 1999, *MNRAS*, 308, 119
- Shimizu, M., Kitayama, T., Sasaki, S., & Suto, Y. 2003, *ApJ*, 590, 197
- Smail, I., Ellis, R. S., Dressler, A., et al. 1997, *ApJ*, 479, 70
- Soucail, G., Ota, N., Böhringer, H., Czoske, O., & Mellier, Y. 2000, *A&A*, 355, 433
- Spergel, D. N., Verde, L., Peiris, H. V., et al. 2003, *ApJS*, 148, 175
- Springel, V., White, S. D. M., & Herquist, L. 2001, *ApJ*, 549, 681
- StanekStanek, R., Evrard, A. E., Böhringer, H., & Schuecker, P. 2005, *ApJ*, in press
- Sugiyama, N. 1995, *ApJS*, 100, 281
- Sunyaev, R. A., & Zeldovich, Y. B. 1972, *Comm. on Ap. Sp. Phys.* 4, 173
- Sussman, R. A., & Hernandez, X. 2003, *MNRAS*, 345,871
- Suto, Y., Sasaki, S., & Makino, N. 1998, *ApJ*, 509, 544
- Tamura, T., Kaastra, J. S., Peterson, J. R., et al. 2001, *A&A*, 365, L87
- Tozzi, P., & Norman, C. 2001, *ApJ*, 546, 63
- Tozzi, P., Rosati, P., Ettori, S., Borgani, S., Mainieri, V., & Norman, C. 2003, *ApJ*, 593, 705
- Treu, T., Ellis, R.S., Kneib, J.-P., et al. 2003, *ApJ*, 591, 53
- Tucker, W. H., Tananbaum, H., & Remillard, R. A. 1995, *ApJ*, 444, 532
- Tucker, W., Blanco, P., Rappoport, S., et al. 1998, *ApJ*, 496, L5
- Tyson, J. A. 1988, *AAS*, 20, 980
- Tyson, J. A., Kochanski, G. P., & Dell'Antonio, I. P. 1998, *ApJ*, 498, L107
- Vikhlinin, A., Forman, W., & Jones, C. 1999, *ApJ*, 525, 47
- Vikhlinin, A., Markevitch, M., & Murray, S. S. 2001a, *ApJ*, 549, L47
- Vikhlinin, A., Markevitch, M., & Murray, S. S. 2001b, *ApJ*, 551, 160
- Vikhlinin, A., VanSpeybroeck, L., Markevitch, M., Forman, W., & Grego, L. 2002, *ApJ*, 578, L107

## Bibliography

---

- Vikhlinin, A., Voevodkin, A., Mullis, C. R., et al. 2003, *ApJ*, 590, 15
- Vikhlinin, A., Markevitch, M., Murray, S. S., et al. 2005a, *ApJ*, in press
- Vikhlinin, A., Kravtsov, A., Forman, W., et al. 2005b, *ApJ*, in press, astro-ph/0507092
- Voges, W., Aschenbach, B., Boller, T., et al. 1999, *A&A*, 349, 389
- Voit, G. M. 2000, *ApJ*, 543, 113
- Voit, G. M., & Bryan, G. L. 2001, *Nature*, 414, 425
- Voit, G. M., Bryan, G. L., Balogh, M. L., & Bower, R. G. 2002, *ApJ*, 576, 601
- Voit, G. M. 2005, *Rev. Mod. Phys.* 77, 207
- Wallington, S., Kochanek, C. S., & Koo, D. C. 1995, *ApJ*, 441, 58
- Watt, M. P., Ponman, T. J., Bertram, D., et al. 1992, *MNRAS*, 258, 738
- White, D. A., Jones, C., & Forman, W. 1997, *MNRAS*, 292, 419
- White, D. A. 2000, *MNRAS*, 312, 663
- White, S. D. M., Navarro, J. F., Evrard, A. E., & Frenk, C. S. 1993, *Natur*, 366, 429
- Wu, X.-P., Chiueh, T., Fang, L.-Z., & Xue, Y.-J. 1998, *MNRAS*, 301, 861
- Wu, X.-P., Xue, Y.-J., & Fang, L.-Z. 1999, *ApJ*, 524, 22
- Wu, X.-P. 2000, *MNRAS*, 316, 299
- Wu, X.-P., & Xue, Y.-J. 2000, *ApJ*, 542, 578
- Xu, H.-G., Jin, G.-X., & Wu, X.-P. 2001, *ApJ*, 553, 78
- Xue, S.-J., & Wu, X.-P. 2002, *ApJ*, 576, 152
- Xue, Y.-J., & Wu, X.-P. 2000a, *ApJ*, 538, 65
- Xue, Y.-J., & Wu, X.-P. 2000b, *MNRAS*, 318, 715
- Yang, J., Schramm, D. N., Steigman, G. & Rood, R. T. 1979, *ApJ*, 227, 697
- Yaqoob, T. 1999, *ApJ*, 511, L75
- Zakamska, N. L., & Narayan, R. 2003, *ApJ*, 582, 162
- Zhang, Y.-Y. 2001, *ChJAA*, 1, 29
- Zhang, Y.-Y., & Wu, X.-P. 2003, *ApJ*, 583, 529
- Zhang, Y.-Y., Finoguenov, A., Böhringer, H., et al. 2004a, *A&A*, 413, 49

- Zhang, Y.-Y., Finoguenov, A., Böhringer, H., et al. 2004b, Proc. *Memorie della Societa Astronomica Italiana - Supplementi*, ed. Antonuccio-Delogu, V., in press, astro-ph/0402533
- Zhang, Y.-Y., Böhringer, H., Mellier, Y., Soucail, G., & Forman, W. 2005a, A&A, 429, 85
- Zhang, Y.-Y., Böhringer, H., Finoguenov, A., et al. 2005b, Adv. Space Res., 36, 667
- Zhang, Y.-Y., Böhringer, H., Finoguenov, A., et al. 2005c, A&A, in press
- Zhao, H.-S. 1996, MNRAS, 278, 488
- Zwicky, F. 1933, Helv. Phys. Acta, 6, 110

## Bibliography

---



# Acknowledgements

Many thanks to my supervisor, Hans Böhringer, for giving me the opportunity to work on such a fascinating project in a friendly working atmosphere, and for providing all kinds of supports and suggestions with the greatest patience. I have received benefit from the continuous advice, encouragement of independent initiatives, and chances to participate in exciting related projects.

I am very grateful to Prof. Gregor Morfill and Prof. Guenther Hasinger for receiving the fellowship to start and continue this work and for supporting me to present my work at many conferences during the past three years.

I am obliged to the ROSAT and XMM-Newton hardware, software, and calibration teams at MPE for the dedicated work of and the helpful discussions. This work has benefited a lot from the use of the catalog from the REFLEX team. The observations were obtained with XMM-Newton, an ESA science mission with instruments and contributions directly funded by ESA Member States and the USA (NASA). I acknowledge Jacqueline Bergeron, PI of the XMM-Newton observation of the CDFS, and Martin Turner, PI of the XMM-Newton observation of RXCJ0658.5-5556. Thanks to Keith Arnaud for the XSPEC software support.

I appreciate the privilege of working with the following people in our institute, Guenther Hasinger, Alexis Finoguenov, Peter Schuecker, Werner Becker, Kyoko Matsushita, Ulrich G. Briel, Gabriel Pratt, Michael Freyberg, Hermann Brunner, Frank Haberl, Yas Hashimoto, Paul Lynam, Harald Baumgartner, Paola Popesso and Marc Zimer. Many thanks for their sincere friendship, extensive help, great patience and enthusiasm in many respects. I really benefit a lot from discussing with them during the tea break and group meetings. I am especially grateful to Peter Schuecker, Alexis Finoguenov and Gabriel Pratt for sharing their experience, carefully reading through my draft and giving a lot of practical suggestions in detail. I also want to thank Werner Becker for offering friendly and efficient help in the International Max-Planck Research School in last three years.

Thanks to my collaborators and friends, whom I consider to be among the best in this field, Xiang-Ping Wu, Mark Henriksen, Bill Forman, Alexey Vikhlinin, Yannick Mellier, Genevieve Soucail, Monique Arnaud, Stefano Borgani, Patrick J. Henry, Thomas Reiprich, Takaya Ohashi, Yasushi Ikebe, Luigi Guzzo, Chris A. Collins, Tae Furusho, Naomi Ota, and Maxim Markevitch. I acknowledge Xiang-Ping Wu for helpful suggestions and kind hospitality at NAOC and Mark Henriksen for useful discussion and kind hospitality at UMBC.

## Acknowledgements

---

I am so grateful to my parents for their infinite care regardless of the long distance. Very special thanks go to my friend, Rasmus Voss, for giving encouragement, providing corrections, discussing questions, and offering all kinds of convenience in both work and life. I also want to thank Yan-Jie Xue, Yanchun Liang and Dawei Xu for generous help and an interesting life. Many thanks to my friends, Zdenka Misanovic, Alina Streblyanskaya, Katya Dimova, Nina Nowak, Rene Fassbender, Luigi Gallo, Darren Croton, Linda Pittroff, Stefanie Komossa, Minzhi Kong, Bin Cui, Liang Gao, Yaxin Xiong, Binrong Xie, Jie Wang, Xiang-Zhong Zheng, Zhi-Ying Huo, and Yan Xu for useful help, sincere friendship, continuous encouragement, and a great life.

# Curriculum Vitae

## Personal data

- Name: Yu-Ying Zhang
- Date of birth: 10. June 1978
- Place of birth: Nei Mongol, China
- Gender: F
- Nationality: Chinese
- Current address: Max-Planck-Institut für extraterrestrische Physik  
Giessenbach Strasse 1, D-85741, Garching, Germany
- E-mail: yyzhang@mpe.mpg.de

## Education

- 1985–1990 Ground school, Baotou, China
- 1990–1993 Middle school, Baotou, China
- 1993–1996 High school, Baotou, China
- 1996–2000 Inner Mongolia University, Huhhot, China, Department of Physics  
Bachelor of Science (Credit A)  
BSc thesis topic: “Element Abundance Analysis of Red Clumpy Giants”  
Supervisor: Prof. Dr. Gang Zhao
- 2000–2002 Peking University, Beijing, China, Department of Astrophysics  
National Astronomy Observatories, Chinese Academic of Science  
Master of Science (by research)  
MSc thesis topic: “Cosmological Applications of X-Ray Properties and SZ Effect of  
Galaxy Clusters”  
Supervisor: Prof. Dr. Xiang-Ping Wu
- 2002–2005 Ludwig-Maximilians-Universität, München, Germany, Department of Physics  
International Max Planck Research School on Astrophysics (IMPRS) at  
Max-Planck-Institut für extraterrestrische Physik  
PhD on Astrophysics  
PhD thesis topic: “The Structure of Galaxy Clusters and Their Intracluster Medium  
as Observed with XMM-Newton”  
Supervisor: Prof. Dr. Hans Böhringer

## Honors and Awards

- 2005- Max-Planck-Institute Fellowship
- 2002-2005 Max-Planck-Institute International Fellowship
- 2000-2002 National Astronomy Observatories Graduate Scholarship
- 1999-2000 Inner Mongolia University Undergraduate Scholarship



# Publications and Proceedings

## Publications as first author:

- Zhang, Y. -Y., Böhringer, H., Finoguenov, et al. “X-ray properties in massive galaxy clusters: XMM-Newton observations of the REFLEX-DXL sample”, A&A, in press
- Zhang, Y. -Y., Böhringer, H., Finoguenov, et al. “Exploring the Structure of Galaxy Clusters: XMM-Newton observations of the REFLEX-DXL clusters at  $z \sim 0.3$ ”, 2005, Adv. Space Res., 36, 667
- Zhang, Y.-Y., Böhringer, H., Mellier, Y., Soucail, D., & Forman, W. “XMM-Newton study of the lensing cluster of galaxies CL0024+17”, 2005, A&A, 429, 85
- Zhang, Y.-Y., Finoguenov, A., Böhringer, H., et al. “Temperature gradients in XMM-Newton observed REFLEX-DXL galaxy clusters at  $z \sim 0.3$ ”, 2004, A&A, 413, 49
- Zhang, Y.-Y., & Wu, X.-P. “The Effect of Radiative Cooling on the Sunyaev-Zeldovich Cluster Counts and Angular Power Spectra: Analytic Treatment”, 2003, ApJ, 583, 529
- Zhang, Y.-Y. “The Sunyaev-Zel’dovich effect cluster surveys and their cosmological significance”, PAbei, 2002, 20, 265
- Zhang, Y.-Y. “Testing the Universality of the TIS Model on Cluster Scales from the X-ray Surface Brightness Profiles”, 2001, ChJAA, 1, 29

## Proceedings as first author:

- Zhang, Y. -Y., Böhringer, H., Finoguenov, et al. “X-ray Properties in Galaxy Clusters”, Proc. The X-ray Universe 2005, in press
- Zhang, Y. -Y., Böhringer, H., Finoguenov, et al. “Exploring Massive Galaxy Clusters: XMM-Newton observations of the REFLEX-DXL sample at  $z \sim 0.3$ ”, Proc. EPIC-XMM-Newton Consortium Meeting 5 Years of Science with XMM-Newton, eds. U. G. Briel, S. Sembay and A. Read, 2005, MPE Report, 288, 131
- Zhang, Y.-Y., Finoguenov, A., Böhringer, H., et al. “Spatial distributions of the REFLEX-DXL galaxy clusters at  $z \sim 0.3$  observed by XMM-Newton”, Proc. Modelling the Intergalactic and Intracluster Media, eds. V. Antonuccio-Delogu, S. Borgani and A. Ferrara, Memorie della Societa Astronomica Italiana - Supplementi, in press, arXiv: astro-ph/0402533

## Publications as co-author:

- Böhringer, Schuecker, P., Zhang, Y.-Y., et al. “REFLEX-DXL sample and its temperature function”, A&A, in press
- Böhringer, Burwitz, V., Zhang, Y.-Y. et al. “CHANDRA reveals galaxy cluster with the most massive nearby cooling core, RXCJ1504–0248”, 2005, ApJ, 633, 148

## Publications and Proceedings

---

- Finoguenov, A., Böhringer, H., & Zhang, Y.-Y. “XMM-Newton study of the two-dimensional structure of the REFLEX-DXL galaxy clusters”, 2005, *A&A*, 442, 827
- Finoguenov, A., Böhringer, H., Osmond, J.P.F., Ponman, T.J., Sanderson, A.J.R, Zhang, Y.-Y., & Zimer, M “Cluster scaling and its redshift evolution from XMM-Newton”, 2005, *Adv. Space Res.*, 36, 622